Ministry of Education and Science of the Russian Federation
Saint Petersburg National Research University of Information Technologies, Mechanics, and Optics

NANOSYSTEMS:

PHYSICS, CHEMISTRY, MATHEMATICS

2021, volume 12(6)

Наносистемы: физика, химия, математика

2021, том 12, № 6

NANO
Ф&Х&М

NANOSYSTEMS:

PHYSICS, CHEMISTRY, MATHEMATICS

ADVISORY BOARD MEMBERS

Chairman: V.N. Vasiliev *(St. Petersburg, Russia)*,
V.M. Buznik *(Moscow, Russia)*; V.M. Ievlev *(Voronezh, Russia)*, P.S. Kop'ev*(St. Petersburg, Russia)*, N.F. Morozov *(St. Petersburg, Russia)*, V.N. Parmon *(Novosibirsk, Russia)*, A.I. Rusanov *(St. Petersburg, Russia)*,

EDITORIAL BOARD

Editor-in-Chief: I.Yu. Popov *(St. Petersburg, Russia)*

Section Co-Editors:
Physics – V.M. Uzdin *(St. Petersburg, Russia)*,
Material science – V.V. Gusarov *(St. Petersburg, Russia)*,
Chemistry – V.K. Ivanov *(Moscow, Russia)*,
Mathematics – I.Yu. Popov *(St. Petersburg, Russia)*.

Editorial Board Members:
V.M. Adamyan *(Odessa, Ukraine)*; O.V. Al'myasheva *(St. Petersburg, Russia)*; A.P. Alodjants *(Vladimir, Russia)*; S. Bechta *(Stockholm, Sweden)*; J. Behrndt *(Graz, Austria)*; M.B. Belonenko *(Volgograd, Russia)*; A. Chatterjee (*Hyderabad, India)*; A.V. Chizhov *(Dubna, Russia)*; A.N. Enyashin *(Ekaterinburg, Russia)*, P.P. Fedorov *(Moscow, Russia)*; E.A. Gudilin *(Moscow, Russia)*; H. Jónsson *(Reykjavik, Iceland)*; A.A. Kiselev *(Durham, USA)*; Yu.S. Kivshar *(Canberra, Australia)*; S.A. Kozlov *(St. Petersburg, Russia)*; P.A. Kurasov *(Stockholm, Sweden)*; A.V. Lukashin *(Moscow, Russia)*; I.V. Melikhov *(Moscow, Russia)*; G.P. Miroshnichenko *(St. Petersburg, Russia)*; I.Ya. Mittova *(Voronezh, Russia)*; Nguyen Anh Tien *(Ho Chi Minh, Vietnam)*; V.V. Pankov *(Minsk, Belarus)*; K. Pankrashkin *(Orsay, France)*; A.V. Ragulya *(Kiev, Ukraine)*; V. Rajendran *(Tamil Nadu, India)*; A.A. Rempel *(Ekaterinburg, Russia)*; V.Ya. Rudyak *(Novosibirsk, Russia)*; H.M. Sedighi (*Ahvaz, Iran*); D Shoikhet *(Karmiel, Israel)*; P Stovicek *(Prague, Czech Republic)*; V.M. Talanov *(Novocherkassk, Russia)*; A.Ya. Vul' *(St. Petersburg, Russia)*; A.V. Yakimansky (*St. Petersburg, Russia*), V.A. Zagrebnov *(Marseille, France)*.

Editors:
I.V. Blinova; A.I. Popov; A.I. Trifanov; E.S. Trifanova *(St. Petersburg, Russia)*,
R. Simoneaux *(Philadelphia, Pennsylvania, USA)*.

Address: ITMO University, Kronverkskiy pr., 49, St. Petersburg 197101, Russia.
Phone: +7(812)607-02-54, **Journal site:** http://nanojournal.ifmo.ru/,
E-mail: nanojournal.ifmo@gmail.com

AIM AND SCOPE

The scope of the journal includes all areas of nano-sciences. Papers devoted to basic problems of physics, chemistry, material science and mathematics inspired by nanosystems investigations are welcomed. Both theoretical and experimental works concerning the properties and behavior of nanosystems, problems of its creation and application, mathematical methods of nanosystem studies are considered.

The journal publishes scientific reviews (up to 30 journal pages), research papers (up to 15 pages) and letters (up to 5 pages). All manuscripts are peer-reviewed. Authors are informed about the referee opinion and the Editorial decision.

CONTENT

MATHEMATICS

PHYSICS

CHEMISTRY AND MATERIAL SCIENCE

NANOSYSTEMS: PHYSICS, CHEMISTRY, MATHEMATICS, 2021, 12 (6), P. 657–663

Monotonicity of the eigenvalues of the two-particle Schrödinger operatoron a lattice

J. I. Abdullaev[1,2], A. M. Khalkhuzhaev[1,2], L. S. Usmonov[2]

[1]Institute of Mathematics of the Academy of Sciences of the Republic of Uzbekistan,
Mirzo Ulugbek 81, Tashkent 100170, Uzbekistan

[2] Samarkand State University, University Boulevard 15, Samarkand 140104, Uzbekistan

jabdullaev@mail.ru, ahmad_x@mail.ru, u.lochinbek@bk.ru

PACS 02.30.Tb **DOI 10.17586/2220-8054-2021-12-6-657-663**

We consider the two-particle Schrödinger operator $H(\mathbf{k})$, ($\mathbf{k} \in \mathbf{T}^3 \equiv (-\pi, \pi]^3$ is the total quasimomentum of a system of two particles) corresponding to the Hamiltonian of the two-particle system on the three-dimensional lattice $\mathbf{Z}^3$. It is proved that the number $N(\mathbf{k}) \equiv N(k^{(1)}, k^{(2)}, k^{(3)})$ of eigenvalues below the essential spectrum of the operator $H(\mathbf{k})$ is nondecreasing function in each $k^{(i)} \in [0, \pi]$, $i = 1, 2, 3$. Under some additional conditions potential $\hat{v}$, the monotonicity of each eigenvalue $z_n(\mathbf{k}) \equiv z_n(k^{(1)}, k^{(2)}, k^{(3)})$ of the operator $H(\mathbf{k})$ in $k^{(i)} \in [0, \pi]$ with other coordinates $\mathbf{k}$ being fixed is proved.

Keywords: two-particle Schrödinger operator, Birman-Schwinger principle, total quasimomentum, monotonicity of the eigenvalues.

Received: 22 October 2021

Revised: 20 November 2021

1. Introduction

Coherent optical fields provide a strong tool for manipulating ultracold atoms and a unique setting for quantum simulations of interacting many-body systems because of high-degree of controllable parameters such as optical lattice geometry and dimensionality, particle masses, tunneling, two-body potentials, temperature etc. [1–4]. However, in such manipulations, due to diffraction, there is a fundamental limit for the length scale, given by the wavelength of light [5] and therefore, the corresponding models are naturally restricted to the short-range case. However, recent experimental and theoretical results show that integrating plasmonic systems with cold atoms, especially using optical potential fields formed from the near field scattering of light by an array of plasmonic nanoparticles allows one to considerably increase the energy scales in the realization of Hubbard models and engineer effective long-range interaction in many body dynamics [5–7].

Hamiltonians, corresponding to systems of particles on a lattice, were first considered in the 1990s by D. S. Mattis [8], A. I. Mogilner [9], and after that, research has rapidly developed. The kinematics of quantum quasiparticles on a lattice is rather peculiar, even in the two-particle case. For example, because the discrete analog of the Laplacian or of its generalization is not translation invariant, the Hamiltonian of the system cannot be divided into two parts with one part corresponding to the motion of the center and the other corresponding to the internal degrees of freedom. This is the so-called phenomenon of “excess mass” for lattice systems: the effective mass of the two-particle bound state exceeds the sum of the effective masses of the quasiparticles constituting the system (see, e.g., [8, 9]). In contrast to the continuous case, where the center-of-mass motion can be separated, the two-particle problem on a lattice reduces to studying the one-particle problem using the Gelfand transformation. Namely, the Hilbert space $\ell_2((\mathbf{Z}^3)^2)$ can be decomposed into the direct (continuous) von Neumann integral associated with the representation of the Abelian (discrete) group $\mathbf{Z}^3$ formed by commutative operators on the lattice. Then the two-particle Hamiltonian can also be decomposed into the direct (continuous) von Neumann integral. In contrast to the continuous case, the corresponding fiber operators $H(\mathbf{k})$, $\mathbf{k} \in \mathbf{T}^3$, associated with the decomposition of the direct integral depend parametrically on the quasimomentum $\mathbf{k}$, which ranges the first Brillouin zone $\mathbf{R}^3 \setminus (2\pi\mathbf{Z})^3$. Because the spherical symmetry of the problem is lost, the spectra of the family $H(\mathbf{k}), \mathbf{k} \in \mathbf{T}^3$, become rather sensitive to variations in the quasimomentum $\mathbf{k}$.

Spectral properties of the two-particle discrete Schrödinger operator $H(\mathbf{k}) = H_0(\mathbf{k}) - V$, $\mathbf{k} \in \mathbf{T}^3$ are studied in the more works (see.i.e. [10–13]). In work [13] a two-particle discrete Schrödinger operator $H(\mathbf{k})$, $\mathbf{k} \in \mathbf{T}^3$ with zero range potential $\hat{v}(\mathbf{n_1} - \mathbf{n_2}) = \mu\delta_{\mathbf{n_1}\mathbf{n_2}}$ was considered and the existence of a unique eigenvalue $z(\mathbf{k})$ of the operator $H(\mathbf{k})$ was established. In [13] it is proved that the eigenvalue $z(\mathbf{k}) = z(k^{(1)}, k^{(2)}, k^{(3)})$, $\mathbf{k} \in \mathbf{T}^3$ is symmetric and even in each variable $k^{(i)} \in [-\pi, \pi]$, $i = 1, 2, 3$ and strictly increases in each $k^{(i)} \in [0, \pi]$, $i = 1, 2, 3$. In particular, it was shown that the two-particle operator $H(\mathbf{k})$, $\mathbf{k} \neq \mathbf{0}$ has a positive eigenvalue below the essential spectrum, provided that $H(\mathbf{0})$ has a virtual level at zero.

The following effect was discovered in [14] for a wide class of two-particle Schrödinger operators $H(\mathbf{k})$, associated with the Hamiltonian of the system of two arbitrary particles. If the discrete Schrödinger operator $H(\mathbf{0})$, $\mathbf{0} = (0,0,0) \in \mathbf{T}^3$, has a virtual level or an eigenvalue on the lower threshold of the essential spectrum, then the operator $H(\mathbf{k})$, has an eigenvalue below the threshold of the essential spectrum for all nonzero values of the quasimomentum $\mathbf{k} \in \mathbf{T}^3$. Similar results was discussed in [15] for $d-$ dimensional lattice case. In [16] was studied the discrete spectrum of the two-particle Schrödinger operator $H_{\mu,\lambda}(\mathbf{k}), \mathbf{k} \in \mathbf{T}^2$, associated to the Bose–Hubbard Hamiltonian $\hat{H}_{\mu,\lambda}$ of a system of two identical bosons interacting on site and nearest-neighbor sites in the two dimensional lattice $\mathbf{Z}^2$, with interaction magnitudes $\mu \in \mathbb{R}$ and $\lambda \in \mathbb{R}$, respectively, and completely described the spectrum of $H_{\mu,\lambda}(\mathbf{0})$ and established the optimal lower bound for the number of eigenvalues of $H_{\mu,\lambda}(\mathbf{k})$ outside its essential spectrum for all values of $\mathbf{k} \in \mathbf{T}^2$. Namely, the (μ, λ) -plane was partitioned that in each connected component of the partition, the number of bound states of below or above its essential spectrum cannot be less than the corresponding number of bound states of $H_{\mu,\lambda}(\mathbf{0})$ below or above its essential spectrum. In [17] a two-particle Schrödinger operator H on the $d-$ dimensional diamond lattice was considered and a sufficiency condition of finiteness for discrete spectrum eigenvalues of H was found.

In this note, we consider the two-particle operator $H(\mathbf{k}) = H_0(\mathbf{k}) - V$, $\mathbf{k} \in \mathbf{T}^3$ with general potential v. For the potential $\hat{v}(\mathbf{x}) = (\mathcal{F}v)(\mathbf{x})$ we assume:

$$\hat{v}(\mathbf{x}) \geq 0, \ \forall \mathbf{x} \in \mathbf{Z}^3, \quad \hat{v} \in \ell_1(\mathbf{Z}^3). \tag{1.1}$$

Non-negativity $\hat{v}(\mathbf{x}) \geq 0$ will ensure the positivity interaction operator V. We denote by $V^{1/2}$ its positive square root.When proving monotonicity the eigenvalue $z_n(\mathbf{k})$ of the operator $H(\mathbf{k})$ with respect to $k^{(i)} \in [0,\pi]$, we will use the monotonicity property of the operator-valued function:

$$G(\mathbf{k}, z) = V^{\frac{1}{2}}(H_0(\mathbf{k}) - zI)^{-1}V^{\frac{1}{2}}$$

by $z \in (-\infty, \mathcal{E}_{\min}(\mathbf{k}))$ and $k^{(i)} \in [0,\pi]$, where the number $\mathcal{E}_{\min}(\mathbf{k})$ is the left edge of the essential spectrum of the operator $H(\mathbf{k})$. For any $\mathbf{k} \in (-\pi,\pi)^3$ the operator $G(\mathbf{k}, z)$ converges uniformly to the limit operator $G(\mathbf{k}, \mathcal{E}_{\min}(\mathbf{k}))$ as $z \to \mathcal{E}_{\min}(\mathbf{k})$. Under the condition (1.1), it is proved that $G(\mathbf{k}, \mathcal{E}_{\min}(\mathbf{k}))$ belongs to the class Σ_1 (see. proof of the Lemma 3.1.) Since $G(\mathbf{k}, \mathcal{E}_{\min}(\mathbf{k}))$ is monotonic in each $k^{(i)} \in [0,\pi]$, $i = 1,2,3$ it follows that the number $N(\mathbf{k})$ of eigenvalues lying below the essential spectrum of the operator $H(\mathbf{k})$ is nondecreasing function with respect in each $k^{(i)} \in [0,\pi]$, $i = 1,2,3$ (Theorem 2.1).

We will prove the monotonicity $G(\mathbf{k}, z)$ by $z \in (-\infty, \mathcal{E}_{\min}(\mathbf{k}))$, that is $G(\mathbf{k}, z_1) \leq G(\mathbf{k}, z_2)$ at $z_1 < z_2$. This implies that each eigenvalue $\lambda_n(\mathbf{k}, z)$ of the operator $G(\mathbf{k}, z)$ is increasing function with respect to $z \in (-\infty, \mathcal{E}_{\min}(\mathbf{k}))$ (Lemma 3.4). Given $\hat{v}(2s, n^{(2)}, n^{(3)}) \equiv 0, \forall s \in \mathbf{Z}$ or $\hat{v}(2s+1, n^{(2)}, n^{(3)}) \equiv 0, \forall s \in \mathbf{Z}$ the operator-valued function $G(\mathbf{k}, z)$ decreases by $k^{(1)} \in [0,\pi]$ (Lemma 3.5). It follows that each eigenvalue $z_n(\mathbf{k})$ of the two-particle operator $H(\mathbf{k})$ increases in $k^{(1)} \in [0,\pi]$ (Theorem 2.3).

2. Representation of Hamiltonian associated to a system of two particle on a lattice. Statement of the main result

Energy operator $\hat{H}$ of a system of two quantum particles on a three-dimensional lattice $\mathbf{Z}^3$ acts in the Hilbert space $\ell_2((\mathbf{Z}^3)^2)$ by:

$$\hat{H} = \hat{H}_0 - \hat{V},$$

where the free energy operator $\hat{H}_0$ acts in $\ell_2((\mathbf{Z}^3)^2)$ as:

$$\hat{H}_0 = -\frac{1}{2m_1}\Delta_{x_1} - \frac{1}{2m_2}\Delta_{x_2}.$$

Here, $m_1, m_2 > 0$ are denoted the masses of particles, which in the future are considered equal to one, $\Delta_{x_1} = \Delta \otimes I$ and $\Delta_{x_2} = I \otimes \Delta$, lattice Laplacian Δ is a difference operator describing the transfer of a particle from a site to neighboring site:

$$(\Delta\hat{\psi})(\mathbf{x}) = \sum_{i=1}^{3}[\hat{\psi}(\mathbf{x}+\mathbf{e}_i) + \hat{\psi}(\mathbf{x}-\mathbf{e}_i) - 2\hat{\psi}(\mathbf{x})], \quad \hat{\psi} \in \ell_2(\mathbf{Z}^3),$$

where $\mathbf{e}_1 = (1,0,0)$, $\mathbf{e}_2 = (0,1,0)$, $\mathbf{e}_3 = (0,0,1)$ are the unit vectors in $\mathbf{Z}^3$.

The interaction of two particles is described by the operator $\hat{V}$:

$$(\hat{V}\hat{\psi})(\mathbf{x_1}, \mathbf{x_2}) = \hat{v}(\mathbf{x_1} - \mathbf{x_2})\hat{\psi}(\mathbf{x_1}, \mathbf{x_2}), \quad \hat{\psi} \in \ell_2((\mathbf{Z}^3)^2).$$

Under the conditions (1.1), the energy operator $\hat{H}$ is the bounded self-adjoint operator in the space $\ell_2((\mathbf{Z}^3)^2)$. Transition to momentum representation is performed by using the Fourier transform $\mathcal{F} : L_2((\mathbf{T}^3)^2) \to \ell_2((\mathbf{Z}^3)^2)$. Operator energy $H = \mathcal{F}^{-1}\hat{H}\mathcal{F}$ in the momentum representation commutes with the group of unitary operators $U_{\mathbf{s}}, \mathbf{s} \in \mathbf{Z}^3$:

$$(U_{\mathbf{s}}f)(\mathbf{k_1}, \mathbf{k_2}) = \exp\big(-i(\mathbf{s}, \mathbf{k_1} + \mathbf{k_2})\big)f(\mathbf{k_1}, \mathbf{k_2}), \quad f \in L_2((\mathbf{T}^3)^2).$$

From the last fact we obtain [18] that there are decompositions of the space $L_2((\mathbf{T}^3)^2)$, operators $U_{\mathbf{s}}$ and H into direct integrals:

$$L_2((\mathbf{T}^3)^2) = \int\limits_{\mathbf{T}^3} \oplus L_2(F_{\mathbf{k}})d\mathbf{k}, \quad U_{\mathbf{s}} = \int\limits_{\mathbf{T}^3} \oplus U_{\mathbf{s}}(\mathbf{k})d\mathbf{k}, \quad H = \int\limits_{\mathbf{T}^3} \oplus \tilde{H}(\mathbf{k})d\mathbf{k}.$$

Here

$$F_{\mathbf{k}} = \{(\mathbf{k_1}, \mathbf{k_2}) \in (\mathbf{T}^3)^2 : \quad \mathbf{k_1} + \mathbf{k_2} = \mathbf{k}\};$$

$U_{\mathbf{s}}(\mathbf{k}), \mathbf{k} \in \mathbf{T}^3$ is the multiplication operator by the function $\exp(-i(\mathbf{s}, \mathbf{k}))$ in the space $L_2(F_{\mathbf{k}})$, and fiber operators $\tilde{H}(\mathbf{k}), \mathbf{k} \in \mathbf{T}^3$ in $L_2(F_{\mathbf{k}})$ are defined according to the formula

$$(\tilde{H}(\mathbf{k})f)(\mathbf{q}, \mathbf{k} - \mathbf{q}) = (\mathcal{E}(\mathbf{q}) + \mathcal{E}(\mathbf{k} - \mathbf{q}))f(\mathbf{q}, \mathbf{k} - \mathbf{q}) - (2\pi)^{-\frac{3}{2}} \int\limits_{\mathbf{T}^3} v(\mathbf{q} - \mathbf{s})f(\mathbf{s}, \mathbf{k} - \mathbf{s})d\mathbf{s}$$

and it is unitarily equivalent to the operator $H(\mathbf{k}) = H_0(\mathbf{k}) - V$, the so-called the Schrödinger operator. Unitarity is carried out using the unitary transformation:

$$u_{\mathbf{k}} : L_2(F_{\mathbf{k}}) \to L_2(\mathbf{T}^3), \quad (u_{\mathbf{k}}g)(\mathbf{q}) = g(\frac{\mathbf{k}}{2} - \mathbf{q}, \frac{\mathbf{k}}{2} + \mathbf{q}).$$

$H_0(\mathbf{k})$ is the multiplication operator by the function:

$$\mathcal{E}_{\mathbf{k}}(\mathbf{q}) = \mathcal{E}(\frac{\mathbf{k}}{2} + \mathbf{q}) + \mathcal{E}(\frac{\mathbf{k}}{2} - \mathbf{q}),$$

where:

$$\mathcal{E}(\mathbf{q}) = \sum_{j=1}^{3}(1 - \cos q^{(j)})$$

and V is the integral operator in $L_2(\mathbf{T}^3)$, generated by the kernel $(2\pi)^{-3/2}v(\mathbf{q} - \mathbf{s})$. The kernel v of the integral operator V is the Fourier transform of the potential $\hat{v}$. The potential $\hat{v}$ satisfies the conditions (1.1), therefore, the function v is continuous on $\mathbf{T}^3$.

We denote by $N(\mathbf{k})$ the number of eigenvalues of the operator $H(\mathbf{k})$, lying to the left $\mathcal{E}_{\min}(\mathbf{k}) = \min_{\mathbf{q} \in \mathbf{T}^3} \mathcal{E}_{\mathbf{k}}(\mathbf{q})$.

Theorem 2.1. *$N(\mathbf{k}) \equiv N(k^{(1)}, k^{(2)}, k^{(3)})$ is nondecreasing function in each $k^{(i)} \in [0, \pi]$ with other coordinates of $\mathbf{k} \in \mathbf{T}^3$ being fixed.*

Assumption 2.2. *Let:*

$$\hat{v}(2s, n^{(2)}, n^{(3)}) = 0, \forall s \in \mathbf{Z} \tag{2.1}$$

or:

$$\hat{v}(2s + 1, n^{(2)}, n^{(3)}) = 0, \forall s \in \mathbf{Z}. \tag{2.2}$$

Theorem 2.3. *Let assumption 2.2 be fulfilled. Then, each eigenvalue $z_n(\mathbf{k}) \equiv z_n(k^{(1)}, k^{(2)}, k^{(3)})-$ of the operator $H(\mathbf{k})$ increases in $k^{(1)} \in [0, \pi]$.*

Remark 2.4. *Let:*

$$\hat{v}(n^{(1)}, 2s, n^{(3)}) = 0, \forall s \in \mathbf{Z}$$

or:

$$\hat{v}(n^{(1)}, 2s + 1, n^{(3)}) = 0, \forall s \in \mathbf{Z}$$

(respectively

$$\hat{v}(n^{(1)}, n^{(2)}, 2s) = 0, \forall s \in \mathbf{Z}$$

or:

$$\hat{v}(n^{(1)}, n^{(2)}, 2s + 1) = 0, \forall s \in \mathbf{Z}).$$

Then, each eigenvalue $z_n(\mathbf{k})$ of the operator $H(\mathbf{k})$ increases in $k^{(2)} \in [0, \pi]$ (respectively in $k^{(3)} \in [0, \pi]$).

3. Eigenvalues of the two-particle operator

Let us investigate the essential and discrete spectra of families of two-particle discrete Schrödinger operator $H(\mathbf{k})$, $\mathbf{k} \in \mathbf{T}^3$. Here, we will study the number $N(\mathbf{k})$ of eigenvalues of the operator $H(\mathbf{k})$, lying below the essential spectrum and dependence of the eigenvalues $z_n(\mathbf{k})$ on the total quasi-momentum $\mathbf{k} \in \mathbf{T}^3$.

We introduce the following notation: for a self-adjoint operator B acting in a Hilbert space $\mathcal{H}$ and not having any essential spectrum on the right from the point μ, denote by $\mathcal{H}_B(\mu) \subset \mathcal{H}$, $\mu \in \mathbb{R}$ subspaces such that nonzero elements $f \in \mathcal{H}_B(\mu)$ satisfy the inequality $(Bf, f) > \mu(f, f)$ and put:

$$n(\mu, B) = \sup_{\mathcal{H}_B(\mu)} \dim \mathcal{H}_B(\mu).$$

If some point of the essential spectrum B is greater μ, then $n(\mu, B)$ is equal to infinity, and if $n(\mu, B)$ finite, then it is equal to the number of eigenvalues of the operator B, which is greater than μ (see., for example, Glazman's lemma [19])

The number $n(\mu, B)$ is the same as the number of eigenvalues of the operator B lying to the right of μ. For any $\mathbf{k} \in (-\pi, \pi)^3$ and $z \leq \mathcal{E}_{\min}(\mathbf{k})$ we define the integral operators $G(\mathbf{k}, z)$ and $Q(\mathbf{k}, z)$, acting in the space $L_2(\mathbf{T}^3)$ with the kernels:

$$G(\mathbf{k}, z; \mathbf{p}, \mathbf{q}) = \frac{1}{(2\pi)^3} \int\limits_{\mathbf{T}^3} v^{\frac{1}{2}}(\mathbf{p} - \mathbf{t})(\mathcal{E}_{\mathbf{k}}(\mathbf{t}) - z)^{-1} v^{\frac{1}{2}}(\mathbf{t} - \mathbf{q}) d\mathbf{t}$$

and:

$$Q(\mathbf{k}, z; \mathbf{p}, \mathbf{q}) = (2\pi)^{-\frac{3}{2}} v^{\frac{1}{2}}(\mathbf{p} - \mathbf{q})((\mathcal{E}_{\mathbf{k}}(\mathbf{q}) - z)^{\frac{1}{2}})^{-1},$$

where:

$$v^{\frac{1}{2}}(\mathbf{p}) = (F\hat{v}^{\frac{1}{2}})(\mathbf{p}) = \frac{1}{(2\pi)^{3/2}} \sum_{\mathbf{n} \in \mathbf{Z}^3} \sqrt{\hat{v}(\mathbf{n})} \exp(i(\mathbf{n}, \mathbf{p})).$$

Note that for any $z < \mathcal{E}_{\min}(\mathbf{k})$ the equalities

$$G(\mathbf{k}, z) = V^{\frac{1}{2}} r_0(\mathbf{k}, z) V^{\frac{1}{2}}, \qquad Q(\mathbf{k}, z) = V^{\frac{1}{2}} r_0^{\frac{1}{2}}(\mathbf{k}, z),$$

hold, where $r_0(\mathbf{k}, z)$ is the resolvent of the unperturbed operator $H_0(\mathbf{k})$, and $V^{\frac{1}{2}}$ is the positive square root of the positive operator V. In the limiting case $z = \mathcal{E}_{\min}(\mathbf{k})$, we have the following assertion.

Lemma 3.1. *For any* $\mathbf{k} \in (-\pi, \pi)^3$ *the operator* $Q(\mathbf{k}, \mathcal{E}_{\min}(\mathbf{k}))$ *belongs the Hilbert-Schmidt class* Σ_2.

Proof. By virtue of conditions (1.1) for the potensial $\hat{v}(\cdot)$ the function $v^{\frac{1}{2}}(\cdot)$ belongs to $L_2(\mathbf{T}^3)$. The function $\mathcal{E}_{\mathbf{k}}(\mathbf{p}) - \mathcal{E}_{\min}(\mathbf{k})$ can be represented as:

$$\mathcal{E}_{\mathbf{k}}(\mathbf{p}) - \mathcal{E}_{\min}(\mathbf{k}) = 2 \sum_{i=1}^{3} \cos \frac{k^{(i)}}{2} (1 - \cos p^{(i)}), \quad \mathbf{k} \in (-\pi, \pi)^3, \tag{3.1}$$

and it has only nondegenerate minimum at the point $\mathbf{p} = \mathbf{0}$, therefore:

$$\int\limits_{\mathbf{T}^3} \int\limits_{\mathbf{T}^3} |Q(\mathbf{k}, \mathcal{E}_{\min}(\mathbf{k}); \mathbf{p}, \mathbf{q})|^2 d\mathbf{p} d\mathbf{q} = \frac{1}{(2\pi)^3} \int\limits_{\mathbf{T}^3} |v^{\frac{1}{2}}(\mathbf{p})|^2 d\mathbf{p} \int\limits_{\mathbf{T}^3} \frac{d\mathbf{q}}{\mathcal{E}_{\mathbf{k}}(\mathbf{q}) - \mathcal{E}_{\min}(\mathbf{k})} < \infty.$$

It means that $Q(\mathbf{k}, \mathcal{E}_{\min}(\mathbf{k}))$ belongs to the Hilbert-Schmidt class Σ_2. □

From the representation $G(\mathbf{k}, z) = Q(\mathbf{k}, z)(Q(\mathbf{k}, z))^*$ it follows positivity and the operator $G(\mathbf{k}, z)$ belongs to the class Σ_1 with all $\mathbf{k} \in (-\pi, \pi)^3$ and $z \leq \mathcal{E}_{\min}(\mathbf{k})$.

Lemma 3.2. *The number* $z < \mathcal{E}_{\min}(\mathbf{k})$ *is an eigenvalue of the operator* $H(\mathbf{k})$ *if and only if* $\lambda = 1$ *is an eigenvalue of the operator* $G(\mathbf{k}, z)$.

Proof of Theorem 2.1. Using the view (3.1) we get that the function:

$$(G(\mathbf{k}, \mathcal{E}_{\min}(\mathbf{k}))\psi, \psi) = \int\limits_{\mathbf{T}^3} \frac{|(V^{1/2}\psi)(\mathbf{p})|^2 d\mathbf{p}}{\mathcal{E}_{\mathbf{k}}(\mathbf{p}) - \mathcal{E}_{\min}(\mathbf{k})} = \int\limits_{\mathbf{T}^3} \frac{|(V^{1/2}\psi)(\mathbf{p})|^2 d\mathbf{p}}{2 \sum_{i=1}^{3} \cos \frac{k^{(i)}}{2} (1 - \cos p^{(i)})}$$

is non-decreasing in each $k^{(i)} \in [0, \pi]$ with fixed other coordinates. This means that the function $N(\mathbf{k})$ also has this property. □

Let us denote by $\lambda_1(\mathbf{k}, z) \geq \lambda_2(\mathbf{k}, z) \geq \cdots \geq \lambda_n(\mathbf{k}, z) \geq \cdots$ eigenvalues of the compact positive operator $G(\mathbf{k}, z)$. Each eigenvalue $\lambda_n(\mathbf{k}, z)$ is the even function by $k^{(i)} \in [-\pi, \pi]$. Now we will prove the monotonicity of each eigenvalue $\lambda_n(\mathbf{k}, z)$ by $z \in (-\infty, \mathcal{E}_{\min}(\mathbf{k}))$ and $k^{(i)} \in [0, \pi]$.

The following lemma is a Birman-Schwinger principle for the operator $H(\mathbf{k})$.

Lemma 3.3. *For any* $\mathbf{k}\in(-\pi,\pi)^3$ *and* $z\le\mathcal{E}_{\min}(\mathbf{k})$ *the equality:*

$$n(-z,-H(\mathbf{k}))=n(1,G(\mathbf{k},z)), \tag{3.2}$$

holds.

Proof. A proof of a similar lemma is given in the paper [15]. □

Lemma 3.4. *For any* $\mathbf{k}\in(-\pi,\pi)^3$ *each positive eigenvalue* $\lambda_n(\mathbf{k},z)$ *of the operator* $G(\mathbf{k},z)$ *increases by* $z\in(-\infty,\mathcal{E}_{\min}(\mathbf{k}))$.

Proof. For any $\psi\in L_2(\mathbf{T}^3)$ and $z_1<z_2\in(-\infty,\mathcal{E}_{\min}(\mathbf{k}))$ the inequality holds

$$\int\limits_{\mathbf{T}^3}\frac{|(V^{1/2}\psi)(\mathbf{p})|^2d\mathbf{p}}{\mathcal{E}_{\mathbf{k}}(\mathbf{p})-z_1}\le\int\limits_{\mathbf{T}^3}\frac{|(V^{1/2}\psi)(\mathbf{p})|^2d\mathbf{p}}{\mathcal{E}_{\mathbf{k}}(\mathbf{p})-z_2}.$$

Hence $(G(\mathbf{k},z_1)\psi,\psi)\le(G(\mathbf{k},z_2)\psi,\psi)$, so $\lambda_n(\mathbf{k},z_1)\le\lambda_n(\mathbf{k},z_2)$. Now, we show the strict inequality:

$$\lambda_n(\mathbf{k},z_1)<\lambda_n(\mathbf{k},z_2). \tag{3.3}$$

Let $\mathcal{H}_{[\lambda_n,\infty)}(G(\mathbf{k},z_1))$ be subspace generated by the eigenfunctions of the operator $G(\mathbf{k},z_1)$, corresponding eigenvalues $\lambda_1(\mathbf{k},z_1)\ge\lambda_2(\mathbf{k},z_1)\ge...\ge\lambda_n(\mathbf{k},z_1)>0$. For any non-zero $\psi\in\mathcal{H}_{[\lambda_n,\infty)}(G(\mathbf{k},z_1))$ we obtain:

$$(G(\mathbf{k},z_2)\psi,\psi)=\int\limits_{\mathbf{T}^3}\frac{|(V^{1/2}\psi)(\mathbf{p})|^2d\mathbf{p}}{\mathcal{E}_{\mathbf{k}}(\mathbf{p})-z_2}>\int\limits_{\mathbf{T}^3}\frac{|(V^{1/2}\psi)(\mathbf{p})|^2d\mathbf{p}}{\mathcal{E}_{\mathbf{k}}(\mathbf{p})-z_1}=(G(\mathbf{k},z_1)\psi,\psi)\ge\lambda_n(\mathbf{k},z_1)(\psi,\psi).$$

Hence, strict inequality (3.3) holds. □

Lemma 3.5. *Let assumption 2.2 be fulfilled. Then, for any* $z\in(-\infty,\mathcal{E}_{\min}(\mathbf{k}))$, *each positive eigenvalue* $\lambda_n(\mathbf{k},z)$ *of the operator* $G(\mathbf{k},z)$ *decreases in* $k^{(1)}\in[0,\pi]$.

Proof. Let the condition (2.1) be satisfied. Then for the function $v^{\frac{1}{2}}(\mathbf{p})$, the following equality

$$v^{\frac{1}{2}}(p^{(1)}+\pi,p^{(2)},p^{(3)})=-v^{\frac{1}{2}}(p^{(1)},p^{(2)},p^{(3)})$$

holds. Similarly, if satisfing the condition (2.2), then

$$v^{\frac{1}{2}}(p^{(1)}+\pi,p^{(2)},p^{(3)})=v^{\frac{1}{2}}(p^{(1)},p^{(2)},p^{(3)}).$$

Therefore, in both cases $|(V^{\frac{1}{2}}\psi)(\mathbf{p})|=|\varphi(\mathbf{p})|$ is a π - periodic function by argument $p^{(1)}$. For any $\psi\in L_2(\mathbf{T}^3)$ we have

$$(G(\mathbf{k},z)\psi,\psi)=\int\limits_{\mathbf{T}^3}\frac{|\varphi(\mathbf{p})|^2d\mathbf{p}}{\mathcal{E}_{\mathbf{k}}(\mathbf{p})-z}=\int\limits_{\mathbf{T}^2}\Bigg\{\int\limits_{-\pi}^{\pi}\frac{|\varphi(\mathbf{p})|^2dp^{(1)}}{B('\mathbf{k},'\mathbf{p};z)-2\cos\frac{k^{(1)}}{2}\cos p^{(1)}}\Bigg\}d'\mathbf{p}. \tag{3.4}$$

Here, $'\mathbf{k}=(k^{(2)},k^{(3)})$, $'\mathbf{p}=(p^{(2)},p^{(3)})\in\mathbf{T}^2$,

$$B('\mathbf{k},'\mathbf{p};z)=6-2\cos\frac{k^{(2)}}{2}\cos p^{(2)}-2\cos\frac{k^{(3)}}{2}\cos p^{(3)}-z>0,\qquad z<\mathcal{E}_{\min}(\mathbf{k}).$$

The inner integral of the right-hand side of the equality (3.4) is represented as the sum of two integrals over the intervals $[-\pi,0]$ and $[0,\pi]$. In the first integral, making the replacement variable $p^{(1)}=\pi+q^{(1)}$ and using the identity $\cos(\pi+x)=-\cos x$ and property
$|\varphi(p^{(1)}+\pi,'\mathbf{p})|=|\varphi(\mathbf{p})|$ we have:

$$(G(\mathbf{k},z)\psi,\psi)=2\int\limits_{\mathbf{T}^2}B('\mathbf{k},'\mathbf{p};z)\Bigg\{\int\limits_{0}^{\pi}\frac{|\varphi(\mathbf{p})|^2dp^{(1)}}{B^2('\mathbf{k},'\mathbf{p};z)-4\cos^2\frac{k^{(1)}}{2}\cos^2p^{(1)}}\Bigg\}d'\mathbf{p}. \tag{3.5}$$

Since $B('\mathbf{k},'\mathbf{p};z)>0$ with all $'\mathbf{p}\in\mathbf{T}^2$, $z<\mathcal{E}_{\min}(\mathbf{k})$, the inner integral in (3.5) strictly decreases with increasing $k^{(1)}\in[0,\pi]$. The monotonicity of the integral implies that:

$$(G(\mathbf{k},z)\psi,\psi)>(G(\mathbf{k}',z)\psi,\psi) \tag{3.6}$$

if $\varphi=V^{1/2}\psi$ is a nonzero element in $L_2(\mathbf{T}^3)$ and $\mathbf{k}=(k^{(1)},k^{(2)},k^{(3)})$, $\mathbf{k}'=(k_1^{(1)},k^{(2)},k^{(3)})$ at $0\le k^{(1)}<k_1^{(1)}\le\pi$. Note that from the inclusion $\psi\in\mathcal{H}_{[\lambda_n,\infty)}(G(\mathbf{k}',z))\setminus\{0\}$ it follows that $V^{1/2}\psi\ne0$. Therefore, from

the inequality (3.6), the assertion $(G(\mathbf{k},z)\psi,\psi) \geq \lambda_n(\mathbf{k}',z)(\psi,\psi)$ holds for all $\psi \in \mathcal{H}_{[\lambda_n,\infty)}(G(\mathbf{k}',z)) \setminus \{0\}$. This proves that $\lambda_n(\mathbf{k},z) > \lambda_n(\mathbf{k}',z)$ by $0 \leq k^{(1)} < k_1^{(1)} \leq \pi$. □

Proof of Theorem 2.3. Let $\mathbf{k} = (k^{(1)},k^{(2)},k^{(3)})$ and $\mathbf{k_1} = (k_1^{(1)},k^{(2)},k^{(3)})$ be two arbitrary points such that $0 \leq k^{(1)} < k_1^{(1)} \leq \pi$. Let the operator $H(\mathbf{k})$ has $N = N(\mathbf{k})$ eigenvalues $z_1(\mathbf{k}) \leq z_2(\mathbf{k}) \leq \cdots \leq z_N(\mathbf{k})$, lying below $\mathcal{E}_{\min}(\mathbf{k})$. Existence is not less than $N(\mathbf{k})$ eigenvalues of the operator $H(\mathbf{k_1})$ follows from Theorem 2.1. From here, it follows that the operator $G(\mathbf{k},z)$ has $N(\mathbf{k})$ eigenvalues:

$$\lambda_1(\mathbf{k},z) \geq \lambda_2(\mathbf{k},z) \geq \cdots \geq \lambda_N(\mathbf{k},z) > 1$$

by $z \in (z_N(\mathbf{k}),\mathcal{E}_{\min}(\mathbf{k})]$. The continuity of $G(\mathbf{k},z)$ with respect to the totality of variables $\mathbf{k} \in \mathbf{T}^3$ and $z < \mathcal{E}_{\min}(\mathbf{k})$ implies the continuity of $\lambda_n(\mathbf{k},z), 1 \leq n \leq N$, with respect such arguments $\mathbf{k}$ and z. It is easy to show that

$$\lim_{z\to-\infty} ||G(\mathbf{k},z)|| = 0. \tag{3.7}$$

From the inequality $\lambda_n(\mathbf{k},z) \leq ||G(\mathbf{k},z)||$ it follows that for any $n \in \{1,2,...,N\}$ the equation $\lambda_n(\mathbf{k},z) = 1$ has a unique solution $z = z_n(\mathbf{k}) \in (-\infty,\mathcal{E}_{\min}(\mathbf{k}))$. Uniqueness follows from the monotonicity of $\lambda_n(\mathbf{k},\cdot)$ in $(-\infty,\mathcal{E}_{\min}(\mathbf{k}))$. By virtue of Lemma 3.2, the number $z_n(\mathbf{k})$ is the eigenvalue of the operator $H(\mathbf{k})$. Using the definition of $z_n(\mathbf{k})$, the inequality $\lambda_n(\mathbf{k},z) \geq \lambda_{n+1}(\mathbf{k},z)$ and monotonicity of the function $\lambda_n(\mathbf{k},\cdot)$ we obtain that $z_n(\mathbf{k}) \leq z_{n+1}(\mathbf{k}), n = \overline{1,N-1}$. Now, let's show the monotonicity of $z_n(\mathbf{k})$ in each $k^{(1)} \in [0,\pi]$. By virtue of Lemma 3.5 an eigenvalue $\lambda_n(\mathbf{k},z)$ is the decreasing function with respect to $k^{(1)} \in [0,\pi]$, and hence:

$$1 = \lambda_n(\mathbf{k},z_n(\mathbf{k})) > \lambda_n(\mathbf{k_1},z_n(\mathbf{k})).$$

On the other side:

$$1 = \lambda_n(\mathbf{k_1},z_n(\mathbf{k_1})) > \lambda_n(\mathbf{k_1},z_n(\mathbf{k})).$$

Since $\lambda_n(\mathbf{k},\cdot)$ is an increasing function in $(-\infty,\mathcal{E}_{\min}(\mathbf{k}))$, we get $z_n(\mathbf{k_1}) > z_n(\mathbf{k})$. □

Notice that the assumption (2.1) is essential. The following example shows that if the assumption (2.1) is not satisfied, then there is a potential $\hat{v}$ and the segment $[\pi-\delta,\pi]$, such that the eigenvalue $E_0(\mathbf{k})$ of the operator $H(\mathbf{k})$ strictly decreases in $k^{(1)} \in [\pi-\delta,\pi]$.

Example 3.6. *Let $\hat{v}(\mathbf{0}) = 2\hat{v}(\mathbf{e}_1) = 2\hat{v}(-\mathbf{e}_1) = 2, \hat{v}(\mathbf{n}) = 0$ at $\mathbf{n} \neq \mathbf{0}, \mathbf{n} \neq \pm\mathbf{e}_1$. Then the operator $H(\pi,\pi,\pi)$ has simple eigenvalue $E_0 = 4$. Using perturbation theory, we obtain that the operator $H(\pi-\beta,\pi,\pi)$ has a unique simple eigenvalue $E_0(\pi-\beta,\pi,\pi)$ in the neighborhood of E_0 for small β, and for $E_0(\pi-\beta,\pi,\pi)$ the following asymptotic formula holds [20]:*

$$E_0(\pi-\beta,\pi,\pi) = E_0 - \frac{\hat{v}(\mathbf{0}) - 3\hat{v}(\mathbf{e}_1)}{\hat{v}(\mathbf{0}) - \hat{v}(\mathbf{e}_1)}\frac{1}{4}\beta^2 + O(\beta^4) \quad at \quad \beta \to 0.$$

This implies the existence of the segment $[\pi-\delta,\pi]$, where $E_0(k^{(1)},\pi,\pi)$ strictly decreases.

4. Conclusion

We study the two-particle Schrödinger operator $H(\mathbf{k})$, ($\mathbf{k} \in \mathbf{T}^3 \equiv (-\pi,\pi]^3$ is the total quasimomentum of a system of two particles) corresponding to the Hamiltonian of the two-particle system on the three-dimensional lattice $\mathbf{Z}^3$. We prove that the number $N(\mathbf{k}) \equiv N(k^{(1)},k^{(2)},k^{(3)})$ of eigenvalues below the essential spectrum of the operator $H(\mathbf{k})$ is nondecreasing function in each $k^{(i)} \in [0,\pi]$, $i = 1,2,3$. We show the monotonicity property of each eigenvalue $z_n(\mathbf{k}) \equiv z_n(k^{(1)},k^{(2)},k^{(3)})$ of the operator $H(\mathbf{k})$ in $k^{(i)} \in [0,\pi]$ with other coordinates $\mathbf{k}$ being fixed.

In [21], for the case $d = 1$ and $card\{n \in \mathbf{Z} : \hat{v}(n) > 0\} = \infty$, the limit result:

$$\lim_{k\to\pi-} N(k) = +\infty,$$

for the number $N(k)$ of the eigenvalues of the operator $H(k)$ was proved. We remark that in our case if $card\{\mathbf{n} \in \mathbf{Z}^3 : \hat{v}(\mathbf{n}) > 0\} = \infty$, then one can prove the above limit result.

In the following, we give some generalizations of the statement of Theorem 2.3. If the potential $\hat{v}$ satisfies one of the conditions:

$$\hat{v}(2s^{(1)}+1,2s^{(2)}+1,2s^{(3)}+1) = 0, \quad \forall s = (s^{(1)},s^{(2)},s^{(3)}) \in \mathbf{Z^3},$$
$$\hat{v}(2s^{(1)},2s^{(2)},2s^{(3)}) = 0, \quad \forall s = (s^{(1)},s^{(2)},s^{(3)}) \in \mathbf{Z^3},$$

then the eigenvalue $z_n(k^{(1)},k^{(2)},k^{(3)})$ of the operator $H(\mathbf{k})$ increases with respect to each argument $k^{(1)}$, $k^{(2)}$ and $k^{(3)}$ in $[0,\pi]$.

One can show that the statement of Theorem 2.3 is preserved, if the dimension d of the lattice $\mathbf{Z}^d$ is greater than three. It is clear that for $d = 1, 2$, is impossible to define the Birman-Schwinger operator $G(\mathbf{k}, z)$ in the whole space at the point $z = \mathcal{E}_{\min}(\mathbf{k})$. Let us denote by:

$$L_2^e(\mathbf{T}^d) = \{f \in L_2(\mathbf{T}^d) : f(-\mathbf{p}) = f(\mathbf{p})\} \quad \text{and} \quad L_2^o(\mathbf{T}^d) = \{f \in L_2(\mathbf{T}^d) : f(-\mathbf{p}) = -f(\mathbf{p})\}.$$

For the even potential $\hat{v}$, the subspaces $L_2^e(\mathbf{T}^d)$ and $L_2^o(\mathbf{T}^d)$ are invariant under the operator $H(\mathbf{k})$. The operator $G^o(\mathbf{k}, z)$, corresponding to the operator $H^o(\mathbf{k}) = H(\mathbf{k})|_{L_2^o(\mathbf{T}^d)}$, can be defined as a compact operator on the boundary $z = \mathcal{E}_{\min}(\mathbf{k})$ of the essential spectrum. In this case, one can prove a similar result concerning to the monotonicity of the eigenvalues of the operator $H^o(\mathbf{k})$ with respect to $k^{(i)} \in [0, \pi]$.

Acknowledgement

The authors expresses gratitude to the referee for valuable remarks.

References

[1] Bloch I., Dalibard J., and Nascimbene S. Quantum simulations with ultracold quantum gases, *Nature Physics*, 2012, **8**, P. 267–276.

[2] Jaksch D., Zoller P. The cold atom Hubbard toolbox, *Annals of Physics*, 2005, **315**, P. 52-79.

[3] Lewenstein M., Sanpera A., Ahufinger V. Ultracold Atoms in Optical Lattices: Simulating Quantum Many-body Systems, 2012, Oxford University Press.

[4] Gullans M., Tiecke T.G., Chang D.E., Feist J., Thompson J.D., Cirac J.I., Zoller P., Lukin M.D. Nanoplasmonic Lattices for Ultracold Atoms, *Phys. Rev. Lett.*, 2012, **109**, P. 235309.

[5] Hecht E. Optics. Addison-Wesley, Reading, MA, 1998.

[6] Murphy B., Hau L.V. Electro-optical nanotraps for neutral atoms, *Phys. Rev. Lett.*, 2009, **102**, P. 033003.

[7] N.P. de Leon, Lukin M D., and Park H. Quantum plasmonic circuits, IEEE *J. Sel. Top. Quantum Electron.*, 2012, **18**, P. 1781–1791.

[8] Mattis D.C. The few-body problem on a lattice. *Rev. Modern Phys.*, 1986, **58**, P. 361–379.

[9] Mogilner A.I. Hamiltonians in solid-state physics as multiparticle discrete Schrödinger operators: Problems and results, in: Many Particle Hamiltonians: Spectra and Scattering (Adv. Soviet Math., Vol. 5, R. A. Minlos, ed.), Amer. Math. Soc., Providence, R.I., 1991, P. 139–194.

[10] Graf G.M., Schenker D. 2-magnon scattering in the Heisenberg model, *Ann. Inst. H. Poincare' Phys. The'or.*, 1997, **67**(1), P. 91–107.

[11] Muminov M.I., Ghoshal S.K. Spectral features of two-particle Schrödinger operator on d-dimensiional lattice. *Complex Analysis and Operator Theory*, 2020, **14**(1).

[12] Lakaev S.N., Khalkhuzhaev A.M. The number of eigenvalues of the two-particle discrete Schrödinger operator. *Theor. Math. Phys.*, 2009, **158**(2), P. 221–232.

[13] Abdullaev J.I., Lakaev S.N. Asymptotics of the discrete spectrum of the three-particle Schrödinger difference operator on lattice, *Theor. Math. Phys.*, 2003, **136**(2), P. 1096–1109.

[14] Albeverio S., Lakaev S.N., Makarov K.A., Muminov Z.I. The threshold effects for the two-particle Hamiltonians on lattices, *Commun. Math. Phys.*, 2006, **262**(1), P. 91–115.

[15] Lakaev S.N., Khalkhuzhaev A.M. Spectrum of the two-particle Schrödinger Operator on a lattice, *Theor. Math. Phys.*, 2008, **155**(2), P. 753–764.

[16] Lakaev S., Kholmatov Sh., Khamidov Sh. Bose-Hubbard models with on-site and nearest-neighbor interactions: Exactly solvable case. *J. Phys. A: Math. Theor.*, 2021, **54**, P. 245201(22).

[17] Muminov M., Lokman C. Finiteness of discrete spectrum of the two-particle Schrödinger operator on diamond lattices, *Nanosystems: physics, chemistry, mathematics,* 2017, **8**(3), P. 310–316.

[18] M. Reed and B. Simon, Methods of modern mathematical physics. IV: Analysis of operators. Academic Press, N.Y., 1979.

[19] Pankov A.A. Lecture Notes on Schrödinger equations. Nova Science, New York, 2007.

[20] Abdullaev Zh.I., Kuliev K.D. Bound States of a two-boson system on a two-dimensional lattice, *Theor. Math. Phys.*, 2016, **186**(2), P. 231–250.

[21] Abdullaev Zh.I. Bound states of a system of two fermions on a one-dimensional lattice. *Theor. and Math. Phys.*, 2006, **147**(1), P. 486–495.

NANOSYSTEMS: PHYSICS, CHEMISTRY, MATHEMATICS, 2021, 12 (6), P. 664–671

Domination topological properties of polyhydroxybutyrate and polycaprolactone with QSPR analysis

Hanan Ahmed[1], Anwar Alwardi[2], Suha A. Wazzan[3]

[1]Department of Mathematics, Yuvarajas College, University of Mysore, Mysore, India
[2]Department of Mathematics, University of Aden, Yemen
[3]Department of Mathematics, Science Faculty, King Abdulaziz University, Jeddah, Saudi Arabia
hananahmed1a@gmail.com, a_wardi@hotmail.com, swazzan@kau.edu.sa

DOI 10.17586/2220-8054-2021-12-6-664-671

Polyhydroxyalkanoates (PHAs) are biopolymers, which are stored inside cells as energy storage materials by various microorganisms. PHAs are plastic materials that have a positive environmental impact when compared to regular plastics in terms of production methods and recyclabillity. In addition, PHAs are characterized by biocompatibility, biodegradability and thus have a wide range of applications such as biomedicine, surgery, etc. The most common PHAs are Polyhydroxybutyrate, Polyhydroxyvalerate, and copolymer. In this paper, we calculate the domination topological indices of these polymers; also, we discuss the quantitative structure property relationships (QSPR) analysis of these domination topological indices. Further, we show that the characteristics have a good correlation with the physico-chemical characteristics of polymers.

Keywords: polyhydroxybutyrate, polyhydroxyvalerate, domination topological indices, domination degree, QSPR analysis.

Received: 18 November 2021

Revised: 27 November 2021

Final revision: 29 November 2021

1. Introduction

Polyhydroxyalkanoates (PHAs) are biologically produced in various biological organisms. There are several microorganisms known as the gatherer of PHAs such as Pseudomonas sp., Bacillus sp., etc [1]. Where the PHAs are stored and mixed as granules in the cytoplasm [2]. PHAs have a wide range of applications such as biomedicine [3,4]. PHAs are similar in terms of their physical and chemical properties to oil-based plastics such as polypropylene [5–7]. Let $G = (V, E)$ be a connected, simple graph with vertex set V and edge set E. A set $D \subseteq V$ is said to be a dominating set of a graph G, if for any vertex $v \in V - D$, there exists a vertex $u \in D$ such that u and v are adjacent. The domination number $\gamma(G)$ of a graph G is the minimum cardinality of a minimal dominating set in G. A dominating set $D = \{v_1, v_2, ..., v_r\}$ is minimal if $D - v_i$ is not a dominating set [8]. A dominating set of G of minimum cardinality is said to be a minimum dominating set. Topological indices are the numerical parameters of a graph, and these parameters are the same for graphs which are isomorphic. A variety of topological indices have been created and developed, and many studies have been conducted on them in various fields of molecular graphs and networks [9–14]. A. M. Hanan Ahmed et al. [15], have introduced new degree-based topological indices called domination topological indices which are based on the minimal dominating sets. The domination degree is defined as:

Definition 1.1. [15] For each vertex $v \in V(G)$, the domination degree denotes by $d_d(v)$ and define as the number of minimal dominating sets of G which contains v.

The first and second domination Zagreb indices and modified first Zagreb domination indices are defined as:

$$DM_1(G) = \sum_{v \in V(G)} d_d^2(v),$$

$$DM_2(G) = \sum_{uv \in E(G)} d_d(u)\, d_d(v),$$

$$DM_1^*(G) = \sum_{uv \in E(G)} [d_d(u) + d_d(v)],$$

where $d_d(v)$ is the domination degree of the vertex v. The total number of minimal dominating sets of G is denoted as $T_m(G)$ [15]. The forgotten domination, hyper domination, and modified forgotten domination indices of graphs [16] are defined as:

$$DF(G) = \sum_{v \in V(G)} d_d^3(v),$$

$$DH(G) = \sum_{uv \in E(G)} [d_d(u) + d_d(v)]^2,$$

$$DF^*(G) = \sum_{uv \in E(G)} d_d^2(u) + d_d^2(v).$$

For more discussion about domination topological indices, refer to [10–12].

2. Materials and methods

In this paper, the results will be organized into two parts:the first part, in which the total number of minimal dominating sets are determined, and then the domination degree for all vertices is calculated. Using the domination degree, the exact values of the domination topological indices are calculated. In the second part, the quantitative structure property relationships (QSPR) analysis of these indicators is discussed, as well as the verification of the chemical applicability of the domination topological indicators. A set of physical and chemical properties of polymers were considered for such a test and the corresponding experimental values are given in Table 1.Analysis tools the linear structures of the models obtained by the program are drawn Excel. For the nonlinear regression analysis, we use R-software.

TABLE 1. Physiochemical properties of PHB, PHV, and PHBV such as Melting Point (M.P.)

Polymer name	M.P. C°
PHB[n]	170
PHV[n]	180
PHBV[n]	145

3. Main results

Polyhydroxybutyrate (PHB) is one type of PHA and, it is of great importance, as biologically derived plastics have the potential for biodegradability [17]. In this section, we calculate the domination topological indices of degradable plastics such as PHB. We will use the symbol PHB[n] (see Fig. 1) for one layer of this structure containing n connections together. The substance chart PHB[n] contains $12n$ vertices and $12n - 1$ edges, where n is the quantity of connections in a layer.

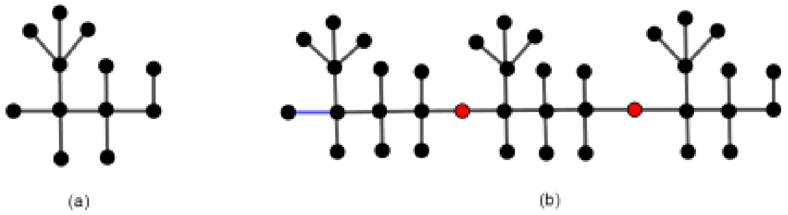

FIG. 1. Polyhydroxybutyrate PHB[n], (a) unit of PHB[n], (b) appear PHB[3]

Lemma 3.1. Let $G \cong PHB[n]$, for $n \geq 1$. Then $T_m(G) = 16n$, and

$$d_d(v) \begin{cases} 2^{4n-2}, & \text{if } v \text{ is the common vertex;} \\ 2^{4n-1}, & \text{otherwise.} \end{cases}$$

Proof. Let G be the molecular graph of Polyhydroxybutyrate PHB[n]. We first divide G into n components A_1, A_2, A_3,..., A_n. We calculate the minimal dominating sets of each component so that we get, $T_m(A_1) = 16$, $T_m(A_2) = 16$, $T_m(A_3) = 16$, ..., $T_m(A_n) = 16$. Every minimal dominating set of A_1 is added to each minimal dominating set of A_2 and we check for the minimality of the resulting dominating sets. As a result, we obtain 256 minimal dominating sets. Note that the common vertex will be removed if this vertex is present in the same minimal dominating set with that vertex in the first unit which is adjacent to it.

Next, every minimal dominating set of A_3 is added to each of these 256 minimal dominating sets and we check for the minimality of the resulting dominating sets. Similarly, the second common vertex will be removed if this vertex is present in the same minimal dominating set with that vertex in the previous unit which is adjacent to it. Here, we obtain $256 \times 16 = 4096$ minimal dominating sets. Continuing in this manner we get $T_m(G) = 16n$, and

$$d_d(v) = \begin{cases} 2^{4n-2}, & \text{if } v \text{ is the common vertex;} \\ 2^{4n-1}, & \text{otherwise.} \end{cases}$$

Theorem 3.2. Suppose G is the molecular graph of Polyhydroxybutyrate PHB[n], for $n \geq 1$. Then:

$$DM_1(G) = 2^{8n-4}(45n+3),$$
$$DM_2(G) = 2^{8n-2}(10n+1) + 2^{8n-3}(2n-2),$$
$$DM_1^*(G) = 2^{4n}(10n+1) + \left(2^{4n-1} + 2^{4n-2}\right)(n-1).$$

Proof. if $G \cong PHB[n]$, the set of vertices of G divides into two sets, C is the set of all common vertices, $|C| = n-1$ and B contains another vertex of G, $|B| = 11n+1$. By using Lemma 3.1, we have:

$$DM_1(G) = \sum_{v \in V(G)} d_d^2(v) = \sum_{v \in V(B)} ((2^{4n-1})^2 + \sum_{v \in V(C)} (2^{4n-2})^2 = 2^{8n-4}(45n+3).$$

From Table 2, we get:

$$DM_2(G) = \sum_{uv \in E(G)} d_d(u)\, d_d(v) = 2^{8n-2}(10n+1) + 2^{8n-3}(2n-2),$$

$$DM_1^*(G) = \sum_{uv \in E(G)} d_d(u) + d_d(v) = 2 \times 2^{4n-1} + \left(2^{4n-1} + 2^{4n-2}\right)(2n-2) + 2 \times 2^{4n-1}(10n)$$
$$= 2^{4n}(10n+1) + \left(2^{4n-1} + 2^{4n-2}\right)(n-1).$$

The edges of G are separated as follows (Table 2).

TABLE 2. Edge partition of PHB[n]

$(d_d(u), d_d(v))$	Number of edges
$\left(2^{4n-1}, 2^{4n-1}\right)$	1 (First edge in first unit)
$\left(2^{4n-1}, 2^{4n-2}\right)$	$2n-2$
$\left(2^{4n-1}, 2^{4n-1}\right)$	$10n$

Theorem 3.3. If $G \cong$ PHB[n], for $n \geq 1$, then:

$$DF(G) = 2^{12n-6}(89n+7),$$
$$DH(G) = 2^{8n}(10n+1) + \left(2^{8n} + 2^{8n-3}\right)(n-1),$$
$$DF^*(G) = 2^{8n-1}(10n+1) + \left(2^{8n-1} + 2^{8n-3}\right)(n-1).$$

Proof. Let $G \cong$PHB[n], for $n \geq 1$. By using the partition of vertices of G as in proof of Theorem 3.2, and Lemma 3.1, we get:

$$DF(G) = \sum_{v \in V(G)} d_d^3(v) = \sum_{v \in V(B)} ((2^{4n-1})^3 + \sum_{v \in V(C)} (2^{4n-2})^3$$
$$= \left[\frac{88 \times 2^{12n-6} + 2^{12n-6}}{64}\right] n + 7 \times 2^{12n-6} = 2^{12n-6}(89n+7).$$

From Table 2, we have:

$$DH(G) = \sum_{uv \in E(G)} (d_d(u) + d_d(v))^2 = 2^{8n}(10n+1) + \left(2^{8n} + 2^{8n-3}\right)(n-1),$$

$$DF^*(G) = \sum_{uv \in E(G)} d_d^2(u) + d_d^2(v) = 2^{8n-1}(10n+1) + \left(2^{8n-1} + 2^{8n-3}\right)(n-1).$$

Now, we compute domination topological indices of Polyhydroxyvalerate (PHV) biodegradable plastic, we use the notation PHV[n] (see Fig. 2) for one layer of this structure contains n unites. The chemical structure of PHV[n] consists of $15n$ vertices and $15n-1$ edges, where n is the number of units in a layer.

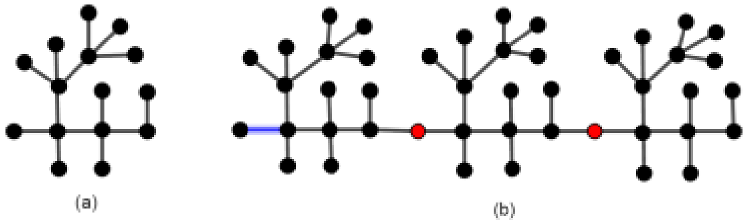

FIG. 2. Polyhydroxyvalerate PHV[n], (a) unit of PHV[n], (b) represents PHV[3]

Lemma 3.4. Let $G \cong$PHV[n], for $n \geq 1$. Then $T_m(G) = 32n$ and:

$$d_d(v) = \begin{cases} 2^{5n-2}, & \text{if } v \text{ is the center vertex;} \\ 2^{5n-1}, & \text{otherwise.} \end{cases}$$

Proof. The proof of this lemma is on the same line as that of Lemma 3.1.

Theorem 3.5. Let G be the chemical structure of PHV[n], for $n \geq 1$. Then:

$$DM_1(G) = \left(7 \times 2^{10n-1} + 2^{10n-4}\right) n + 3 \times 2^{10n-4},$$

$$DM_2(G) = 7 \times 2^{10n-1} n,$$

$$DM_1^*(G) = 2^{5n}(13n+1) + 3 \times 2^{5n-1}(n-1).$$

Proof. Let $G \cong$ PHV[n], we can divide the vertices of G into two sets: the set C which contains the common vertices, $|C| = n-1$ and the set B, which contains the other vertices of G, $|B| = 14n+1$ by using Lemma 3.4, we get:

$$DM_1(G) = \sum_{v \in V(G)} d_d^2(v) = \sum_{v \in V(B)} ((2^{5n-1})^2 + \sum_{v \in V(C)} (2^{5n-2})^2$$

$$= \left(\frac{7 \times 2^{10n+3} + 2^{10n}}{16}\right) n + 4 \times 2^{10n-4} - 2^{10n-4} = \left(7 \times 2^{10n-1} + 2^{10n-4}\right) n + 3 \times 2^{10n-4}.$$

From Table 3, we get:

$$DM_2(G) = \sum_{uv \in E(G)} d_d(u) d_d(v) = 7 \times 2^{10n-1} n,$$

$$DM_1^*(G) = \sum_{uv \in E(G)} d_d(u) + d_d(v) = 2^{5n}(13n+1) + 3 \times 2^{5n-1}(n-1).$$

The edges of G are separated as follows (Table 3).

TABLE 3. Edge partition of PHV[n]

$(d_d(u), d_d(v))$	Number of edges
$\left(2^{5n-1}, 2^{5n-1}\right)$	1 (first edge in the first unit)
$\left(2^{5n-1}, 2^{5n-2}\right)$	$2n-2$
$\left(2^{5n-1}, 2^{5n-1}\right)$	$13n$

Theorem 3.6. Suppose G is the molecular structure of PHV[n], then:

$$DF(G) = \left(7 \times 2^{15n-2} + 2^{15n-6}\right) n + 7 \times 2^{15n-6},$$

$$DH(G) = 2^{10n}(13n+1) + \left(2^{10n} + 2^{10n-3}\right)(n-1),$$

$$DF^*(G) = 2^{10n-1}(13n+1) + 2^{10n-3}(5n-5).$$

Proof. Let $G \cong$PHV[n], for $n \geq 1$. By using the partition of vertices of G as in the proof of Theorem 3.5 and Lemma 3.4, we get:

$$\begin{aligned} DF(G) &= \sum_{v\in V(G)} d_d^3(v) = \sum_{v\in V(B)} ((2^{5n-1})^3 + \sum_{v\in V(C)} (2^{5n-2})^3 \\ &= \left(\frac{7\times 2^{15n+4}+2^{15n}}{64}\right) n + 7\times 2^{15n-6} = \left(7\times 2^{15n-2}+2^{15n-6}\right) n + 7\times 2^{15n-6}. \end{aligned}$$

From Table 3, we have:

$$DH(G) = \sum_{uv\in E(G)} (d_d(u)+d_d(v))^2 = 2^{10n}(13n+1) + \left(2^{10n}+2^{10n-3}\right)(n-1),$$

$$DF^*(G) = \sum_{uv\in E(G)} d_d^2(u)+d_d^2(v) = 2^{10n-1}(13n+1) + 2^{10n-3}(5n-5).$$

In this part we shall compute domination topological indices of chemical structure of the co-polymer of PHB and PHV. One layer of this structure we denote it by PHBV[n] (see Fig. 3) containing n units. The chemical graph PHBV[n] contains $27n$ vertices and $27n-1$ edges.

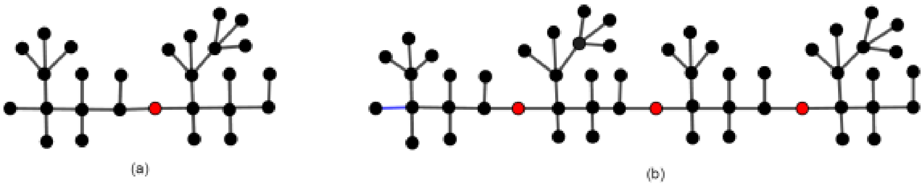

FIG. 3. Polyhydroxybutyrovalerate for the co-polymer PHBV[n], (a) unit of PHBV[n], (b) appear PHBV[2]

Lemma 3.7. Let $G \cong$ PHBV[n], for $n \geq 1$. Then $T_m(G) = 512n$ and

$$d_d(v) = \begin{cases} 2^{9n-2}, & \text{if } v \text{ is the center vertex;} \\ 2^{9n-1}, & \text{otherwise.} \end{cases}$$

Proof. The proof of this lemma is on the same line as that of Lemma 3.1.

Theorem 3.8. Suppose G is the molecular structure of PHBV[n]. Then:

$$\begin{aligned} DM_1(G) &= 51\times 2^{18n-3}n + 3\times 2^{18n-4}, \\ DM_2(G) &= \left(23\times 2^{18n-2}+2^{18n-1}\right) n, \\ DM_1^*(G) &= 2^{9n}(23n+4) - 3\times 2^{9n-1}. \end{aligned}$$

Proof. Let $G \cong$PHBV[n]. The set of vertices of G can be divided into two sets: the set C contains all center vertices, $|C| = 2n-1$ and the set B contains the remaining vertices of G, $|B| = 25n+1$. By using Lemma 3.7, we get:

$$\begin{aligned} DM_1(G) &= \sum_{v\in V(G)} d_d^2(v) = \sum_{v\in V(B)} ((2^{9n-1})^2 + \sum_{v\in V(C)} (2^{9n-2})^2 \\ &= \left(\frac{50\times 2^{18n}+2^{18n}}{8}\right) n + 3\times 2^{18n-4} = 51\times 2^{18n-3}n + 3\times 2^{18n-4}. \end{aligned}$$

From Table 4, we have:

$$DM_2(G) = \sum_{uv\in E(G)} d_d(u)\,d_d(v), = \left(23\times 2^{18n-2}+2^{18n-1}\right) n,$$

$$DM_1^*(G) = \sum_{uv\in E(G)} d_d(u)+d_d(v) = 2^{9n}(23n+4) - 3\times 2^{9n-1}.$$

The edges of G are separated as follows (Table 4).

Theorem 3.9. Let $G \cong$ chemical structure of PHBV[n], for $n \geq 1$. Then:

$$DF(G) = 101\times 2^{27n-5}n + 7\times 2^{27n-6},$$

TABLE 4. Edge partition of PHBV[n]

$(d_d(u), d_d(v))$	Number of edges
$(2^{9n-1}, 2^{9n-1})$	1 (first edge in the first unit)
$(2^{9n-1}, 2^{9n-2})$	$4n-2$
$(2^{9n-1}, 2^{9n-1})$	$23n$

$$DH(G) = 2^{18n}(23n+1) + 9\left(2^{18n-2}n - 2^{18n-3}\right),$$
$$DF^*(G) = 2^{18n-1}(23n+1) + 5\left(2^{18n-2} - 2^{18n-3}\right).$$

Proof. Suppose $G \cong$PHBV[n], for $n \geq 1$. By using the partition of vertices of G as in the proof of Theorem 3.8 and Lemma 3.7, we get:

$$DF(G) = \sum_{v\in V(G)} d_d^3(v) = \sum_{v\in V(B)} ((2^{9n-1})^3 + \sum_{v\in V(C)} (2^{9n-2})^3 = 101 \times 2^{27n-5}n + 7 \times 2^{27n-6}.$$

Now, from Table 4, we have:

$$DH(G) = \sum_{uv\in E(G)} (d_d(u) + d_d(v))^2 = 2^{18n}(23n+1) + 9\left(2^{18n-2}n - 2^{18n-3}\right),$$

$$DF^*(G) = \sum_{uv\in E(G)} d_d^2(u) + d_d^2(v) = 2^{18n-1}(23n+1) + 5\left(2^{18n-2} - 2^{18n-3}\right).$$

4. QSPR Analysis

QSPR analysis remains the focus of many studies aimed at the modeling and prediction of physicochemical and biological properties of molecules. A powerful tool to help in this task is chemometrics, which uses statistical and mathematical methods to extract maximum information from a data set. QSPR uses chemometric methods to describe how a given physicochemical property varies as a function of molecular descriptors relevant to the chemical structure of a molecule. Thus, it is possible to replace costly biological tests or experiments of a given physicochemical property with calculated descriptors, which can, in turn, be used to predict the properties of interest for new compounds. The basic strategy of QSPR is to find an optimum quantitative relationship, which can be used for the prediction of the properties of compounds, including those unmeasured. It is obvious that the performance of QSPR model mostly depends on the parameters used to describe the molecular structure. Many efforts have been made to develop alternative molecular descriptors which can be derived using only the information encoded in the chemical structure. Much attention has been concentrated on “topological indices” derived from the connectivity and composition of a molecule which has made significant contributions in QSPR studies. The topological index has advantages of simplicity and quick speed of computation and so attracts the attention of scientists.

In this section, we are going to discuss the QSPR analysis of the domination topological indices. Further, we show that the characteristics have a good correlation with the physico-chemical characteristics of polymers. In this part, we will show the importance of domination topological indices to predict the physiochemical property in Table 1. In this study, we used the nonlinear regression analysis modelled as: $\log(y) = a + b\log(x)$, where y is the physicochemical property of the chemical compounds and x represents the domination topological indices. These were calculated using R-software for the values of one physicochemical property and the six domination topological indices of PHB, PHV, and Copolymer (PHBV) for $n = 1$, $n = 2$ and $n = 3$.

By using the above model of nonlinear regression analysis, we can obtain different nonlinear models for the domination topological indicesas follows:

$$\log(\text{M.P.}) = 5.2 - 0.005\log DM_1,$$
$$\log(\text{M.P.}) = 5.2 - 0.0053\log DM_2,$$
$$\log(\text{M.P.}) = 5.2 - 0.01\log DM_1^*,$$
$$\log(\text{M.P.}) = 5.2 - 0.004\log DF,$$
$$\log(\text{M.P.}) = 5.2 - 0.005\log DH,$$
$$\log(\text{M.P.}) = 5.2 - 0.0052\log DF^*.$$

Now, the predicted values of physiochemical property are given in Table 5.

TABLE 5. The values of M.P. Predicted by domination topological indices

Polymer name	M.P. – Predicted by					
	DM_1	DM_2	DM_1^*	DF	DH	DF^*
PHB[1]	175.3	175.1	172.1378	175.1	174.2	174.6
PHV[1]	173.9	173.5	170.537	173.4	172.8	173.1
PHBV[1]	168.7	168.03	164.882	167.4	167.58	167.7
PHB[2]	169.9	169.3	166.2931	168.88	168.86	168.9
PHV[2]	167.5	166.7	163.561	165.94	166.3	166.3
PHBV[2]	157.9	156.7	153.9177	154.9	156.9	156.6
PHB[3]	165.01	164.1	161.0975	163.11	163.9	163.8
PHV[3]	161.4	160.3	157.3411	158.9	160.3	160.2
PHBV[3]	148.11	146.3	144.0490	143.5	147.2	146.5

Figure 4 indicates how much the predicted values of physio-chemical properties are correlated with the well-known physio-chemical properties. The degree of correlation between any two data sets is measured by the correlation coefficient (R). When the value of R becomes close to unity, two data sets are more correlated. The QSPR study of domination indices reveals that these domination indices can be helpful in predicting the Melting Point (M.P.). From Fig. 4, the range of the correlation is $0.56 < R < 0.57$ which shows a good correlation of predicted values of Melting Point (M.P.) with exact values of M.P. In fact, these obtained values for the correlation coefficient for these domination indices are satisfactory. On another hand, all domination indices are good to predict the M.P. of these polymers. Melting Point is an important physicochemical property using these domination indices to predict the values of this property is very useful and saves time and money. It has been shown that these indices can be considered useful molecular descriptors in QSPR research of polymers.

The correlation coefficient values of predicted physicochemical properties with the exact values of physio-chemical properties of the chemical compounds used in this study are given in Table 6.

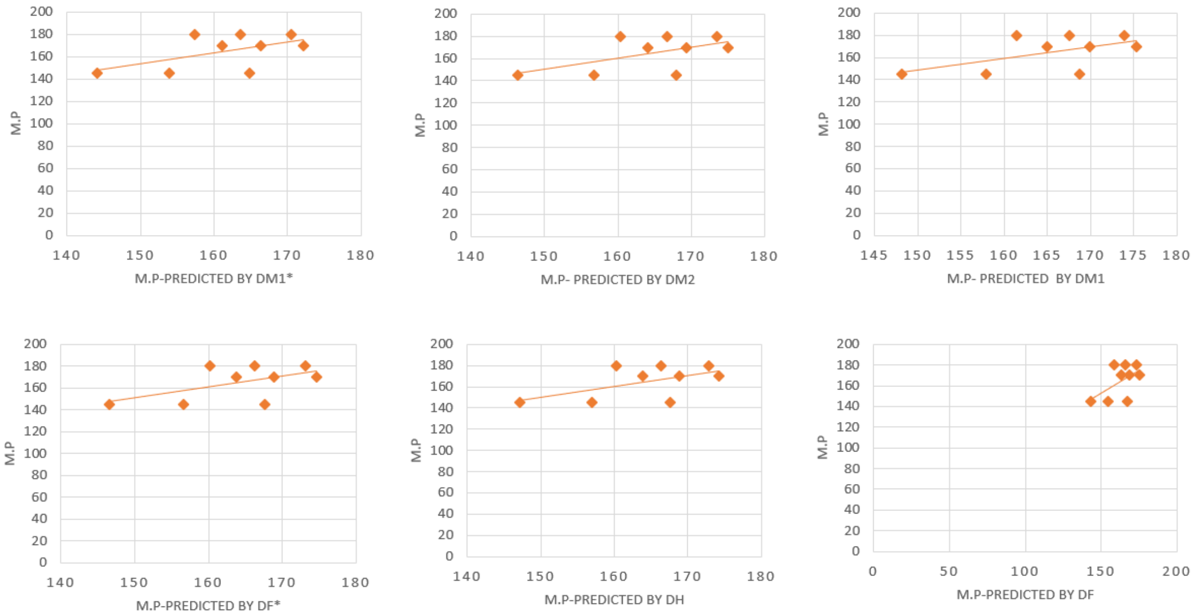

FIG. 4. Graphical relationships between predicted values of M.P., and the exact values of M.P.

TABLE 6. The correlation coefficient values of predicted physicochemical properties with the exact values of physio-chemical properties

Physicochemical property	M.P. – Predicted by					
	DM_1	DM_2	DM_1^*	DF	DH	DF^*
M.P.	0.57	0.562	0.56	0.563	0.562	0.562

5. Conclusion

We calculated domination topological indices for PHB, PHV, and their copolymer, PHBV. There are many different applications of these polymers that resemble petroleum-based plastic such as polypropylene, which is useful in kinking many of the physical and chemical properties of these polymers with domination topological indices. We have also discussed the QSPR analysis of PHB, PHV, and their copolymer, PHBV. The cases in which good correlations were obtained suggested the validity of the calculated topological indices to be further used to predict the physicochemical properties of chemical compounds.

Acknowledgements

The authors would like to thank the reviewer for his constructive suggestions and useful comments which resulted in an improved version of this paper.

References

[1] Lemoigne M. Produits de deshydration et de polymerisation de lacide-oxybutyrique. *Bull. Soc. Chim. Biol.*, 1926, **8**, P. 770–782.

[2] Shrivastav A., Kim H.Y., Kim Y.R. Advances in the applications of polyhydroxyalkanoate nanoparticles for novel drug delivery system. *Biomed. Res. Int.*, 2013, **12**, P. 1–12.

[3] Hazer B. Amphiphilic poly(3-hydroxy alkanoate)s: potential candidates for medical applications. *Int. J. of Polymer Science*, 2010, 423460.

[4] Lau N.S., Sudesh K. Revelation of the ability of Burkholderi a sp, USM (JCM 15050) PHAs syn-thase to polymerize 4-hydroxybutyrate monomer. *AMB Express*, 2012, **2** (1), 41.

[5] Brigham C.J., Bhubalan K., et al. Characterization of the highly active polyhydroxyalkanoate synthase of Chromobacterium sp.strain USM2. *Appl. Environ. Microbiol.*, 2011, **77** (9), P. 2926–2933.

[6] Budde C.F., Riedel S.L., et al. Growth and polyhydroxybutyrate production by Ralstonia eutropha in emulsi ed plant oil medium. *Appl. Microbiol. Biotechnol.*, 2011, **89** (5), P. 1611–1619.

[7] Sudesh K., Abe H., Doi Y. Synthesis, structure and properties of polyhydroxyalkanoates: biological polyesters. *Progress in Polymer Science*, 2000, **25**, P. 1503–1555.

[8] François J., Couturier A., Letourneur R., Liedloff M. On the number of minimal dominating sets on some graph classes. *Theor. Computer Science*, 2015, **562**, P. 634–642.

[9] Akhter S., Imran M., Farahani M.R., Javaid I. On topological properties of hexagonal and silicate networks. *Hacettepe J. of Mathematics and Statistics*, 2019, **48** (3), P. 711–723.

[10] Ahmed H., Alwardi A., Salestina R.M. Domination Topological Indices and Polynomial of Some Chemical Structures Applied for the Treatment of COVID-19 Patients. *Biointerface Research in Applide Chemistry*, 2021, **5**, P. 13290–13302.

[11] Ahmed H., Farahani M.R., Alwardi A., Salestina R.M. Domination topological properties of some chemical structures using polynomial approach. *Eurasian Chemical Communications*, 2021, **3** (4), P. 210–218.

[12] Ahmed H., Alwardi A., Salestina R.M. Domination topological indices and their polynomials of a firefly graph. *J. of Discrete Mathematical Sciences and Cryptography*, 2021, **24** (2) P. 325–341.

[13] Wazzan S., Saleh A. On the First and Second Locating Zagreb Indices of Graphs. *Applied Mathematics*, 2019, **10** (10), P. 805–816.

[14] Wazzan S., Saleh A. Locating and Multiplicative Locating Indices of Graphs with QSPR Analysis. *J. of Mathematics*, 2021, 5516321.

[15] Hanan Ahmed A.M., Alwardi A., Salestina R.M. On Domination Topological Indices of Graphs. *Int. J. Anal. Appl.*, 2021, **19** (1), P. 47–64.

[16] Ahmed H., Alwardi A., Salestina R.M., Soner N.D. Forgotten domination, hyper domination and modified forgotten domination indices of graphs. *J. of Discrete Mathematical Sciences and Cryptography*, 2021, **24** (2), P. 353–368.

[17] Lichtenthaler F.W. Carbohydrates as Organic Raw Materials. Ullmann's Encyclopedia of Industrial Chemistry, 2010, Wiley-VCH Verlag GmbH & Co. KGaA.

NANOSYSTEMS: PHYSICS, CHEMISTRY, MATHEMATICS, 2021, 12 (6), P. 672–679

Ab initio calculations of layered compounds consisting of sp^3 or $sp+sp^2$ hybridized carbon atoms

E. A. Belenkov[1], V. A. Greshnyakov[1], V. V. Mavrinskii[2]

[1]Chelyabinsk State University, Bratiev Kashirinykh, 129, Chelyabinsk, 454001, Russia
[2]Nosov Magnitogorsk State Technical University, Lenin Street, 38, Magnitogorsk, 455000, Russia
greshnyakov@csu.ru, gefest80@gmail.com

PACS 61.50.Ah, 81.05.ug **DOI 10.17586/2220-8054-2021-12-6-672-679**

The density functional theory method was used to study new layered carbon nanostructures consisting of sp^3- and $sp+sp^2$-hybridized atoms. The nanostructures are theoretically built on the basis of graphene 5 – 7 layers. As a result of calculations, it is found that the structures of two diamond-like bilayers and twenty-one graphyne layers are stable. The diamond-like bilayers have a band gap of $\sim$ 1.8 eV, so their properties should be semiconducting. For fourteen graphyne layers, the band gap is zero and their properties are metallic. Seven graphyne layers have band gaps ranging from 0.05 to 0.2 eV.

Keywords: graphene, diamond-like bilayers, graphyne layers, computer simulation.

Received: 8 November 2021

1. Introduction

There are three crystalline allotropic forms of carbon, such as carbyne, graphite and diamond, which consist of carbon atoms in two-, three- and four-coordinated states in the corresponding crystal structure [1]. The orbitals of valence electrons of carbon atoms in these compounds are sp-, sp^2- or sp^3-hybridized [2]. There are also various carbon nanostructures such as fullerenes, nanotubes, graphene layers, and others [3–5]. In most of these nanostructures, carbon atoms are in the states of sp^2-hybridization. It is necessary to investigate the possibility of the existence of diamond-like and carbyne-like carbon nanostructures consisting of sp^3- and sp-hybridized atoms, respectively. The theoretical analysis performed earlier showed that the existence of diamond-like layers of sp^3-hybridized atoms, as well as graphyne layers of $sp+sp^2$ atoms, is possible [6–13]. The structure of such layered carbon nanostructures can theoretically be constructed on the basis of polymorphic varieties of graphene [6, 10]. Earlier, we studied diamond-like bilayers and graphyne monolayers formed on the basis of the main polymorphic graphene varieties L_6, L_{4-8}, L_{3-12}, and L_{4-6-12} [6, 8, 10, 13]. The stability of diamond-like and graphyne-like layers correlates well with the stability of graphene layer precursors. Therefore, nanostructures formed from the most stable graphene polymorphs must be stable. According to theoretical calculations, one of the most stable structural varieties of graphene is L_{5-7} graphene [14, 15]. Graphenes, whose layers consist of pentagons and heptagons, has several polymorphic varieties of which L_{5-7a} and L_{5-7b} are the most stable [15]. Therefore, the study of diamond-like and graphyne layers formed from L_{5-7a} and L_{5-7b} graphenes was carried out in this work.

2. Calculation methods

To obtain the initial structures of diamond-like layers, the theoretical technique described in [1, 6] was used. The structures of these layers were obtained as a result of the formation of covalent bonds between atoms of parallel two-dimensional graphene-like precursors (Fig. 1). Six polymorphic graphene varieties were considered as precursors of diamond-like layers (Fig. 2).

Graphyne $sp+sp^2$ layers were built on the basis of two polymorphs of 5 – 7 graphene by replacing carbon-carbon bonds with fragments of diatomic carbyne chains according to the method described in [10,13]. Fig. 3 shows a diagram illustrating the construction of a structure of one graphyne layer based on the graphene L_{5-7a} layer. Each carbon atom in the graphene layer is covalently bonded to three neighboring atoms, so one, two, or three bonds can be replaced with a carbine chain. If each three-coordinated atom has all bonds with neighboring two-coordinated atoms, then layers of α-graphyne were obtained. When two bonds or one bond were replaced, the structure of β- and γ-graphyne varieties was formed, respectively.

Further calculations of the structure and electronic properties of layered carbon nanostructures were performed using the density functional theory (DFT) method in the Quantum ESPRESSO software package [16]. The calculations were performed using the generalized gradient approximation [17] only for valence electrons. The influence of ionic cores was taken into account by the method of the norm-conserving pseudopotential. For integration in the Brillouin

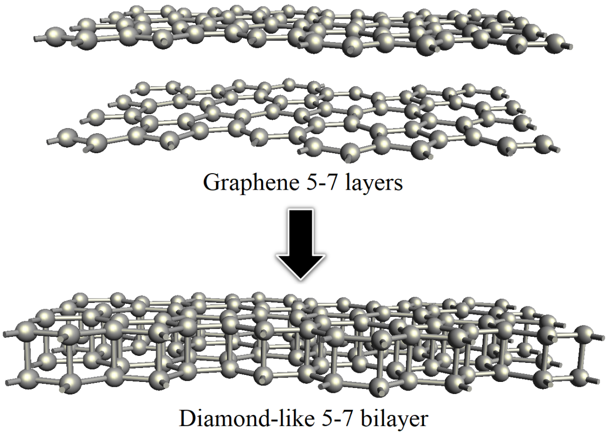

FIG. 1. Scheme of model obtaining of diamond-like bilayer from two graphene layers

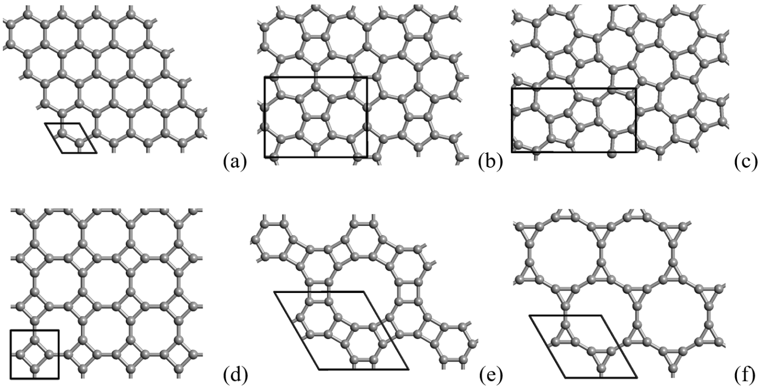

FIG. 2. Structures of graphene layers: (a) L_6; (b) L_{5-7a}; (c) L_{5-7b}; (d) L_{4-8}; (e) L_{4-6-12}; (f) L_{3-12}

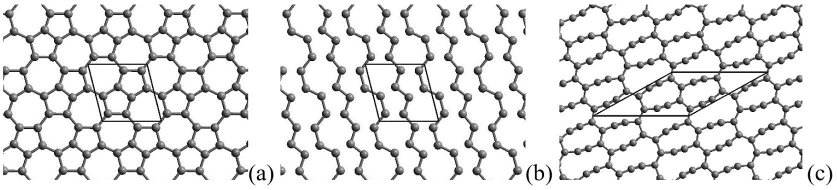

FIG. 3. Diagram of the structure formation of a graphyne $\gamma 1$-L_{5-7a} layer: (a) the initial graphene L_{5-7a} layer; (b) cutting some of the interatomic bonds in the initial graphene and replacing them with fragments of diatomic carbine chains; (c) the optimized graphyne $\gamma 1$-L_{5-7a} layer structure

zones, $20 \times 20 \times 1$ k-point grids were used. The kinetic energy cutoff value was taken equal to 800 eV. To reduce the mutual influence of neighboring carbon layers, unit cells with the parameter $c = 15$ Å were chosen. Modeling of phase transitions was carried out on the basis of the technique described in [6].

3. Results and discussion

3.1. Diamond-like bilayers

As a result of the DFT calculations of the cross-linked graphene L_{5-7} layer structures, the possibility of stable existence of two new structural varieties of diamond-like bilayers was established. The new DL_{5-7a} and DL_{5-7b} bilayers have orthorhombic unit cells, in contrast to the hexagonal or tetragonal DL_6, DL_{4-8}, DL_{4-6-12} and DL_{3-12} bilayers (Table 1). The unit cell parameters of the initial graphene layers and diamond-like bilayers are given in Table 1. The lengths of the elementary translation vectors of diamond-like DL_{5-7a} and DL_{5-7b} bilayers are 10 – 13 % longer than the corresponding values for the initial graphene layers. The bilayer thickness is ~ 1.608 Å. The interatomic bond lengths are in the range from 1.5376 to 1.6268 Å in the bilayer structures. The angles between covalent bonds in the diamond-like DL$_{5-7a}$ and DL$_{5-7b}$ bilayers vary from 89.56 to 140.83 °, while the smallest (60 °) and largest (150 °) angles are observed in the DL$_{3-12}$ and DL$_{4-6-12}$ bilayers. The pores of the maximum diameter are approximately 2.08 Å. The structures of the DL$_{5-7a}$, DL$_{5-7b}$, and DL$_6$ bilayers are the least stressed in comparison with the structure of cubic diamond, since the total deviations of the bond angles from the diamond angle (109.47 °) take the smallest values. The most stressed layered nanostructures are the DL$_{4-6-12}$ and DL$_{3-12}$ bilayers.

TABLE 1. Calculated structural parameters and properties of the initial graphene layers, cubic diamond, and diamond-like bilayers (a, b, and N are the unit cell parameters; Δ_{Ed} is the difference total energy relative to the diamond total energy)

Structure	Symmetry group	a, Å	b, Å	N, atoms	Density, mg/m^2	Δ_{Ed}, eV/atom	Band gap, eV
L$_6$	*p6/mmm*	2.4872	2.4872	2	0.745	−0.04	—
L$_{5-7a}$	*cmmm*	7.5183	5.8942	16	0.720	0.22	—
L$_{5-7b}$	*pbam*	8.9919	4.6430	16	0.764	0.20	—
L$_{4-8}$	*p4/mmm*	3.4687	3.4687	4	0.663	0.52	—
L$_{4-6-12}$	*p6/mmm*	6.8116	6.8116	12	0.596	0.66	—
L$_{3-12}$	*p6/mmm*	5.2563	5.2563	6	0.500	1.09	—
Diamond	$Fd\bar{3}m$	3.5969	3.5969	8	—	0.00	5.61
DL$_6$	*p6/mmm*	2.7369	2.7369	4	1.230	1.22	1.86
DL$_{5-7a}$	*cmmm*	8.2607	6.4825	32	1.192	1.32	1.88
DL$_{5-7b}$	*pbam*	10.1451	5.2704	32	1.194	1.31	1.68
DL$_{4-8}$	*p4/mmm*	3.8218	3.8218	8	1.092	1.55	2.38
DL$_{4-6-12}$	*p6/mmm*	7.5116	7.5116	24	0.980	1.65	1.41
DL$_{3-12}$	*p6/mmm*	5.8204	5.8204	12	0.816	2.00	1.36

The surface densities of the diamond-like DL$_{5-7a}$ and DL$_{5-7b}$ bilayers are 1.192 and 1.194 mg/m^2, respectively, and exceed that for hexagonal L$_6$ graphene by 65 % (Table 1). The total energy calculations of the bilayers showed that the most stable layers should be the diamond-like DL$_6$, DL$_{5-7a}$, and DL$_{5-7b}$ bilayers, since their total energies are higher than those for cubic diamond by 1.22 – 1.32 eV/atom. The least stable bilayer is DL$_{3-12}$, for which the difference total energy (Δ_{Ed}) is 2.00 eV/atom. Diamond-like bilayers with minimum total energies are formed from the most stable graphene layers (Table 1). The calculated data analysis showed that the value of Δ_{Ed} decreases linearly with an increase in the surface density of the bilayer. It should be noted that the DL$_{5-7a}$ and DL$_{5-7b}$ bilayers should be less stable than thirty-three three-dimensional diamond polymorphs studied in [18], since the different energies of these bilayers are higher than the corresponding energies of these diamond polymorphs by at least 0.19 eV. However, the two new bilayers are more stable than diamond-like CA1 (T-carbon) and CA12 phases, which consist of polymerized tetrahedranes [18, 19].

To study the electronic properties of the diamond-like bilayers, the band structures and the density of electronic states were calculated. For all bilayers, the calculations of the electron energies in the Brillouin zones were carried out in the planes specified by the vectors k_1 and k_2. Fig. 4 shows the calculated band structure for the most stable DL$_{5-7b}$ bilayer. It was found that the widths of the direct band gap in the DL$_{5-7a}$ and DL$_{5-7b}$ bilayers are 1.88 and 1.68 eV, respectively, which are 66 – 70 % less than that for cubic diamond (Table 1). The spectrum of electronic states in the Brillouin zone of the diamond-like DL$_{5-7b}$ bilayer is also shown in Fig. 4. The minimum band gap, determined as the difference between the electron energies of the bottom of the conduction band and the top of the valence band, for the diamond-like DL$_{5-7a}$ bilayer is 1.40 eV, which is 10 % less than the corresponding value for the DL$_{5-7b}$ bilayer. Only for the diamond-like DL$_{4-6-12}$ bilayer, the band gap values determined from the band structure and the spectrum of electronic states coincide. Therefore, the new DL$_{5-7a}$ and DL$_{5-7b}$ bilayers must be semiconductors with an indirect band gap.

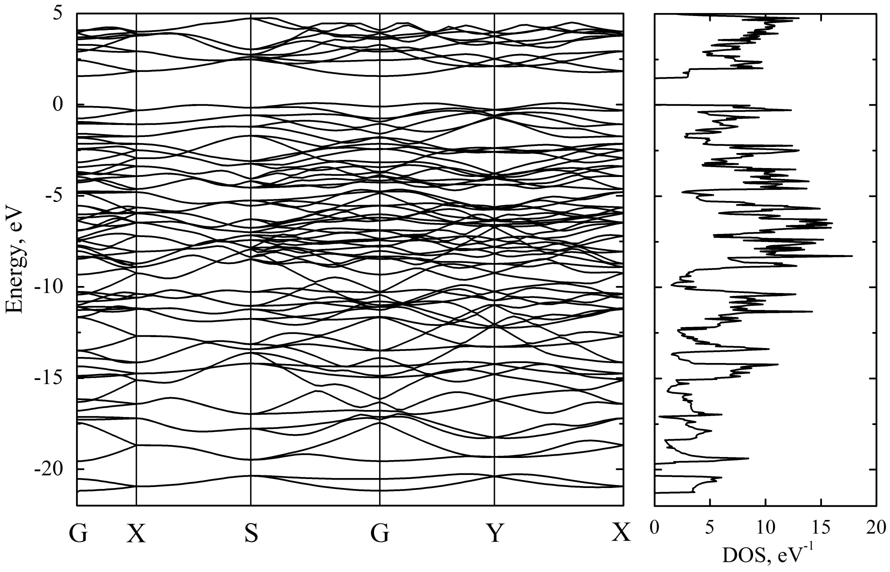

FIG. 4. Electronic band structure and density of states (DOS) of the diamond-like DL_{5-7b} bilayer

One of the ways to experimentally obtain diamond-like materials is strong compression of precursors consisting of sp^2-hybridized atoms [2, 20, 21], therefore, the phase transitions of bilayer graphenes into diamond-like bilayers under uniaxial compression were simulated. As a result of the compression of the initial graphene L_{5-7} layers along the 001 crystallographic axis, the formation of covalent bonds between adjacent graphene layers occurs. Fig. 5 shows the graphs of the dependences of the difference in total energy on the distance between adjacent layers, illustrating the first order phase transitions. The diamond-like DL_{5-7a} and DL_{5-7b} bilayer structures are formed when the initial graphene layers approach each other at a distance of 1.758 Å (Fig. 5). The pressure at which the "bilayer graphene $L_{5-7a} \rightarrow DL_{5-7a}$ bilayer" structural transformation occurs is 12.9 GPa, while the pressure for the "$L_{5-7b} \rightarrow DL_{5-7b}$" phase transition is 10.0 GPa. These values are much less than the calculated values of the formation pressures of cubic and hexagonal diamonds [22].

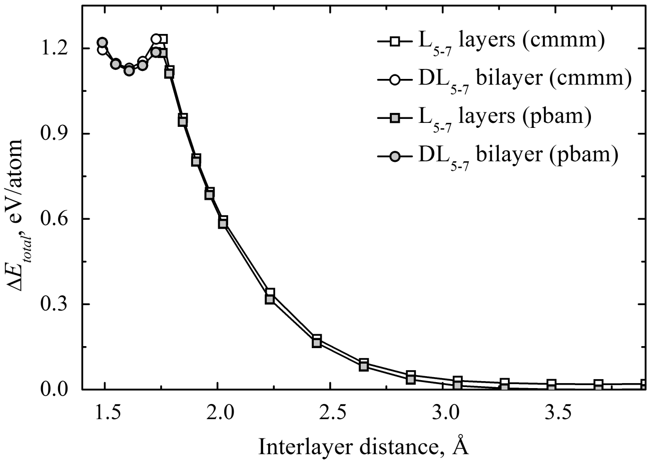

FIG. 5. Dependences of the difference total energy (ΔE_{total}) on the interlayer distance for the phase transitions of graphene layers into diamond-like bilayers

3.2. Graphyne-like layers

Based on the graphene L_{5-7a} layer, the initial structures of one α-, four β- and four γ-graphyne layers were theoretically constructed. Twenty-eight original graphyne layers of γ- and β-structured varieties, as well as one α-structure were built on the basis of the graphene L_{5-7b} layer. Calculations by the DFT-GGA method of the geometrically optimized structure of graphyne layers showed that only two α-layers, one γ-layer, and eighteen structural varieties of β-layers retained the original graphyne structure (Table 2). Images of the structures of these stable layers are shown in Figs. 6 and 7. In the course of optimization, the structures of unstable γ-type layers were transformed into structures of different graphene layers or into structures of graphyne layers with a smaller relative number of sp-hybridized atoms (Fig. 8).

TABLE 2. The structural, energy and electronic characteristics of graphyne L_{5-7} layers (P is the number of non-equivalent structural positions of atoms; N is the number of atoms in the unit cell; ρ is the layer density; ΔE_{total} calculated as E_{total} minus total energy of the hexagonal graphene layer; E_{sub} is the sublimation energy; Δ is the band gap width at the Fermi energy level E_F)

Graphyne layer	P	N, atoms	ρ, mg/m^2	ΔE_{total}, eV/atom	E_{sub}, eV/atom	Δ, eV	E_F, eV
α-L_{5-7a}	10	32	0.37	1.10	6.66	0.00	−4.69
β1-L_{5-7a}	12	24	0.46	1.10	6.66	0.00	−4.71
β2-L_{5-7a}	12	24	0.46	1.05	6.71	0.00	−4.64
β3-L_{5-7a}	12	24	0.48	0.98	6.78	0.00	−4.84
β4-L_{5-7a}	7	24	0.48	0.98	6.78	0.00	−4.83
α-L_{5-7b}	16	64	0.36	1.10	6.66	0.00	−4.64
β1-L_{5-7b}	12	48	0.47	1.03	6.73	0.00	−4.58
β2-L_{5-7b}	24	48	0.46	1.10	6.66	0.00	−4.60
β3-L_{5-7b}	24	48	0.46	1.22	6.54	0.00	−4.55
β4-L_{5-7b}	24	48	0.47	1.01	6.75	0.17	−4.78
β5-L_{5-7b}	24	48	0.47	1.01	6.75	0.08	−4.59
β6-L_{5-7b}	24	48	0.46	1.08	6.68	0.00	−4.57
β7-L_{5-7b}	12	48	0.46	1.05	6.71	0.11	−4.57
β8-L_{5-7b}	48	48	0.47	1.04	6.72	0.18	−4.66
β9-L_{5-7b}	24	48	0.47	1.04	6.72	0.20	−4.70
β10-L_{5-7b}	10	48	0.48	0.98	6.78	0.00	−4.91
β11-L_{5-7b}	10	48	0.48	0.98	6.78	0.11	−4.99
β12-L_{5-7b}	12	48	0.46	1.10	6.66	0.00	−4.59
β13-L_{5-7b}	24	48	0.47	1.03	6.73	0.05	−4.68
β14-L_{5-7b}	10	48	0.48	0.98	6.78	0.00	−4.91
γ1-L_{5-7b}	8	32	0.62	1.03	6.73	0.00	−4.24

The numerical values of some structural parameters characterizing the layers of L_{5-7} graphyne are shown in Table 2. The unit cells of the layers are orthorhombic and monoclinic, containing from 24 to 64 atoms. The values of the vectors of elementary translations a and b vary in the range from 8.0 to 25.9 Å. The number of different structural positions (P) of atoms in the unit cells is minimal for the β4-L_{5-7a} layer ($P = 7$), the maximum value of this parameter is observed for the β8-L_{5-7b} layer ($P = 48$). The ratio of the number of atoms in the sp- and sp^2-hybridization states varies from 1:1 in the graphyne γ1-L_{5-7b} layer to 2:1 in the β-type layers and 3:1 in the α-graphyne layers. The layer density is minimal for the α-type layers (0.36 – 0.37 mg/m^2), the maximum density (0.62 mg/m^2) is observed for the γ1-L_{5-7b} graphyne layer. For the β-type graphyne layers, the density is $\sim$ 0.47 mg/m^2. The layer density of the graphyne layers is lower than the layer density of 0.74 mg/m^2 for hexagonal graphene (Table 2).

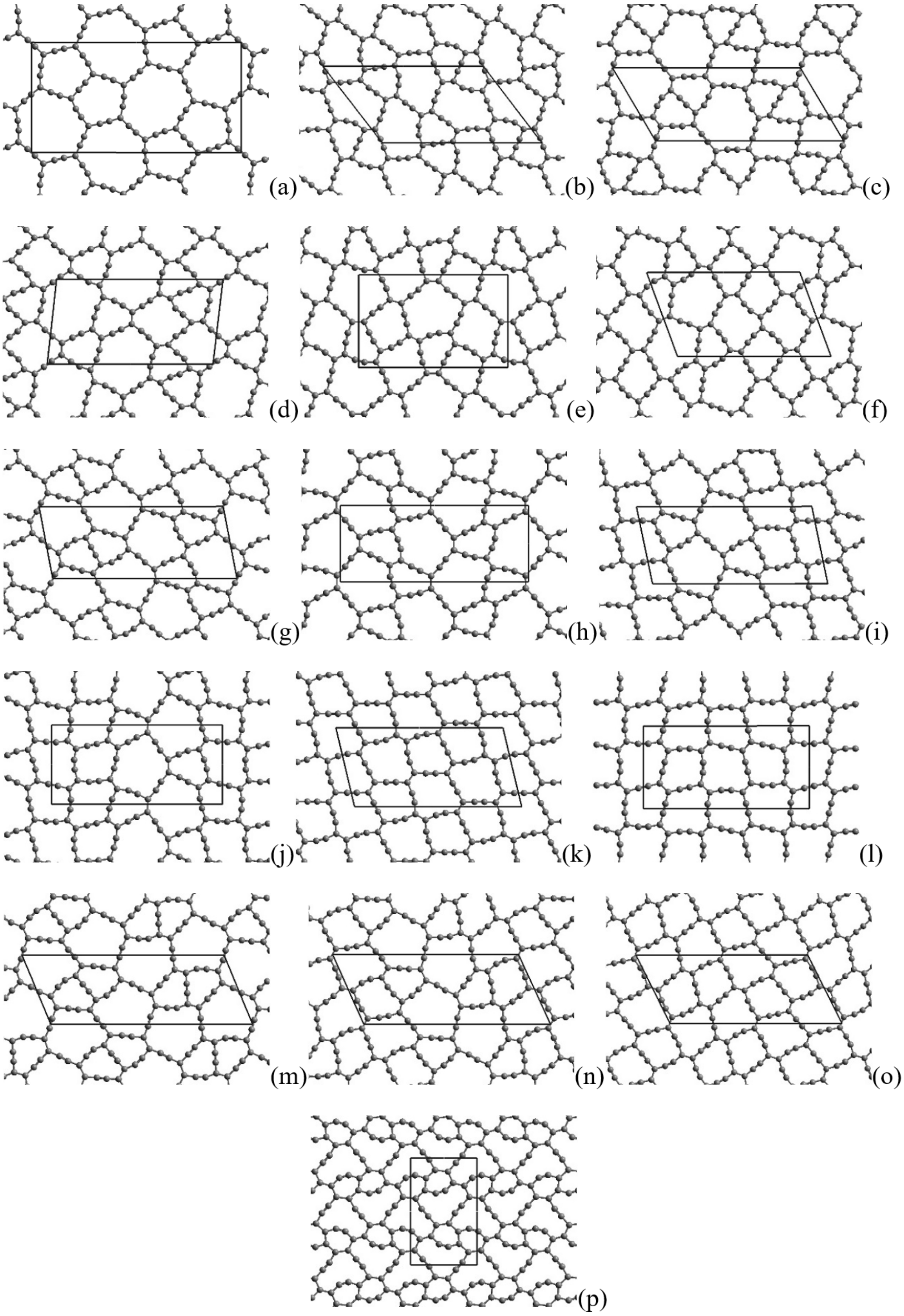

FIG. 6. Geometrically optimized structures of stable graphyne layers: (a) α-L$_{5-7b}$; (b) β1-L$_{5-7b}$; (c) β2-L$_{5-7b}$; (d) β3-L$_{5-7b}$; (e) β4-L$_{5-7b}$; (f) β5-L$_{5-7b}$; (g) β6-L$_{5-7b}$; (h) β7-L$_{5-7b}$; (i) β8-L$_{5-7b}$; (j) β9-L$_{5-7b}$; (k) β10-L$_{5-7b}$; (l) β11-L$_{5-7b}$; (m) β12-L$_{5-7b}$; (n) β13-L$_{5-7b}$; (o) β14-L$_{5-7b}$; (p) γ1-L$_{5-7b}$

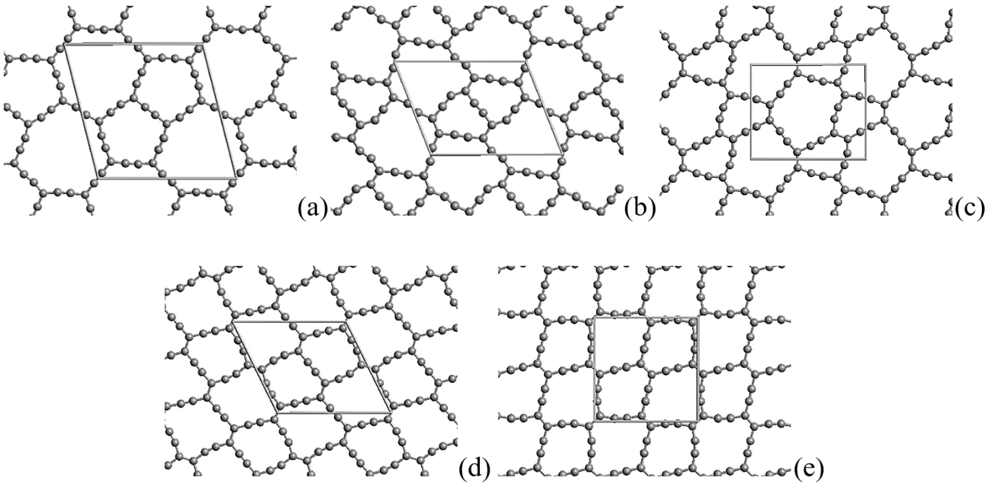

FIG. 7. Geometrically optimized structures of stable graphyne layers: (a) α-L$_{5-7a}$; (b) β1- L$_{5-7a}$; (c) β2- L$_{5-7a}$; (d) β3- L$_{5-7a}$; (e) β4-L$_{5-7a}$

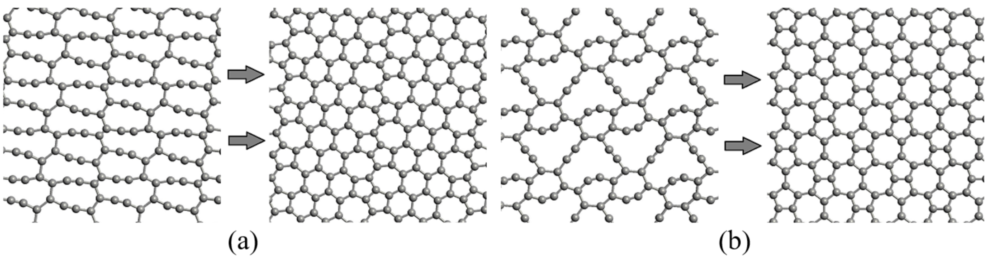

FIG. 8. Transformation of the structure of graphyne γ-L$_{5-7a}$ layers during geometric optimization: (a) a graphyne γ1-L$_{5-7a}$ layer is transformed to a graphene L$_{5-6-7a}$ layer; (b) a graphyne γ3-L$_{5-7a}$ layer is transformed to a graphene L$_{5-7a}$ layer

The difference energy ΔE_{total}, calculated as the difference between the total energies in the graphyne layers and the hexagonal graphene layer, varies from 0.98 to 1.22 eV/atom. This indicates a lower stability of graphyne layers compared to graphene layers. However, the sublimation energies of 6.66 – 6.78 eV/atom for the graphyne L$_{5-7b}$ layers fall within the range of values typical for carbon compounds that stably exist under normal conditions. The maximum sublimation energy is observed for the β3-L$_{5-7a}$, β4-L$_{5-7a}$, β10-L$_{5-7b}$, β11-L$_{5-7b}$, and β14-L$_{5-7b}$ layers (Table 2). Apparently, these graphyne layers should be the most stable.

The DFT-GGA calculations of the band structure and density of electronic states of the graphyne L$_{5-7}$ layers showed that the density of electronic states is zero at the Fermi energy for seven layers, and the band gap varies from 0.05 to 0.20 eV. The band gap for the remaining fourteen layers is zero. The Fermi energy (E_F) varies in the range from -4.99 to -4.24 eV (Table 2).

4. Conclusions

Thus, a number of new carbon nanostructures according to specially developed algorithms were theoretically built on the basis of graphene L$_{5-7a}$ and L$_{5-7b}$ layers. These new nanostructures were two diamond bilayers and thirty-eight graphyne layers. As a result of the DFT-GGA calculations, it was found that diamond-like bilayers and twenty-one graphyne layers have stable structures. After geometric optimization, the structure of seventeen graphyne layers turned out to be unstable. These layers, consisting of sp+sp^2-hybridized atoms, tend to transform their structure into the structure of graphene layers, consisting only of sp^2-hybridized atoms. The band gap for most of the stable graphyne layers is zero, while for the rest of the graphyne layers, it does not exceed 0.2 eV. Diamond-like layers have a direct band gap of 1.88 and 1.68 eV for the DL$_{5-7a}$ and DL$_{5-7b}$ bilayers, respectively. The new polymorphic varieties of graphyne, apparently, can be experimentally obtained by polymerization of molecules, the structure of the carbon framework of which is close to the structure of the corresponding graphyne layers [23]. The diamond-like bilayers based on L$_{5-7}$ graphene can be obtained by uniaxial compression of these graphene bilayers at pressures of $\sim$ 11 GPa.

The practical application of the new carbon nanostructures with a layered structure is possible in electronics and as molecular sieves [24, 25].

References

[1] Belenkov E.A., Greshnyakov V.A. Classification schemes of carbon phases and nanostructures. *New Carbon Materials*, 2013, **28** (4), P. 273–283.

[2] Pierson H.O. *Handbook of carbon, graphite, diamond, and fullerenes: properties, processing, and application*. Noyes, Park Ridge, New Jersey, 1993, 402 p.

[3] Kroto H.W., Heath J.R., et al. C_{60}: Buckmimsterfullerene. *Nature*, 1985, **318** (6042), P. 162–163.

[4] Iijima S. Helical microtubules of graphitic carbon. *Nature*, 1991, **354** (6348), P. 56–58.

[5] Novoselov K.S., Geim A.K., et al. Electric field effect in atomically thin carbon films. *Science*, 2004, **306** (5696), P. 666–669.

[6] Greshnyakov V.A., Belenkov E.A. Ab initio calculations of carbon bilayers with diamond-like structures. *J. of Structural Chemistry*, 2020, **61** (6), P. 835–843.

[7] Ohno K., Satoh H., et al. Exploration of carbon allotropes with four-membered ring structures on quantum chemical potential energy surfaces. *J. of Computational Chemistry*, 2019, **40** (1), P. 14–28.

[8] Greshnyakov V.A., Belenkov E.A. Theoretical study of the stability and formation methods of layer diamond-like nanostructures. *Letters on Materials*, 2020, **10** (4), P. 457–462.

[9] Baughman R.H., Eckhardt H., Kertesz M. Structure-property predictions for new planar forms of carbon: Layered phases containing sp^2 and sp atoms. *The J. of Chemical Physics*, 1987, **87** (11), P. 6687–6699.

[10] Belenkov E., Brzhezinskaya M., Mavrinskii V. Graphynes: Advanced carbon materials with layered structure. In book: *Handbook of graphene. Volume 3: Graphene-like 2D materials*, Chapter 4, ed. Mei Zhang. Wiley, Tallahassee, 2019, P. 113–150.

[11] Li G., Li Y., et al. Architecture of graphdiyne nanoscale films. *Chemical Communications*, 2010, **46** (19), 3256.

[12] Gao X., Liu H., Wang D., Zhang J. Graphdiyne: synthesis, properties, and applications. *Chemical Society Reviews*, 2019, **48** (3), P. 908–936.

[13] Belenkov E.A., Mavrinskii V.V., Belenkova T.E. Chernov V.M. Structural modifications of graphyne layers consisting of carbon atoms in the sp and sp^2-hybridized states. *J. of Experimental and Theoretical Physics*, 2015, **120** (5), P. 820–830.

[14] Deza M., Fowler P.W., Shtogrin M., Vietze K. Pentaheptite modifications of the graphite sheet. *J. of Chemical Information and Computer Sciences*, 2000, **40** (6), P. 1325–1332.

[15] Belenkov M.E., Kochengin A.E., Chernov V.M., Belenkov E.A. Graphene polymorphs. *J. of Physics: Conference Series*, 2019, **1399**, 022024.

[16] Giannozzi P., Andreussi O., et al. Advanced capabilities for materials modelling with Quantum ESPRESSO. *J. of Physics: Condensed Matter*, 2017, **29** (46), 465901.

[17] Perdew J.P., Burke K., Ernzerhof M. Generalized Gradient approximation made simple. *Physical Review Letters*, 1996, **77** (18), P. 3865–3868.

[18] Belenkov E.A., Greshnyakov V.A. Structure, properties, and possible mechanisms of formation of diamond-like phases. *Physics of the Solid State*, 2016, **58** (10), P. 2145–2454.

[19] Sheng X.-L., Yan Q.-B., et al. T-carbon: A novel carbon allotrope. *Physical Review Letters*, 2011, **106** (15), 155703.

[20] Bundy F.P. Direct conversion of graphite to diamond in static pressure apparatus. *The J. of Chemical Physics*, 1963, **38** (3), P. 631–643.

[21] Wang Z.W., Zhao Y.S., et al. A quenchable superhard carbon phase synthesized by cold compression of carbon nanotubes. *Proceedings of the National Academy of Sciences*, 2004, **101** (38), P. 13699–13702.

[22] Greshnyakov V.A., Belenkov E.A., Brzhezinskaya M.M. Theoretical investigation of phase transitions of graphite and cubic 3C diamond into hexagonal 2H diamond under high pressures. *Physica Status Solidi B*, 2019, **256** (7), 1800575.

[23] Diederich F. Carbon scaffolding: Building acetylenic all-carbon and carbon-rich compounds. *Nature*, 1994, **369** (6477), P. 199–207.

[24] Zhang H., He X., et al. Tunable hydrogen separation in sp-sp^2 hybridized carbon membranes: A first-principles prediction. *The J. of Physical Chemistry C*, 2012, **116** (31), P. 16634–16638.

[25] He X.J., Tan J., et al. The roles of π electrons in the electronic structures and optical properties of graphyne. *Chinese Science Bulletin*, 2012, **57** (23), P. 3080–3085.

NANOSYSTEMS: PHYSICS, CHEMISTRY, MATHEMATICS, 2021, 12 (6), P. 680–689

Temperature dependence of recombination radiation in semiconductor nanostructures with quantum dots containing impurity complexes

V. D. Krevchik[1], A. V. Razumov[1], M. B. Semenov[1], I. M. Moyko[1], A. V. Shorokhov[1,2]

[1]Penza State University, Krasnaya, 40, Penza, 440026, Russia
[2]University of Jyväskylä, PO Box 35, Jyväskylä, FI-40014, Finland

physics@pnzgu.ru, alex.shorokhov@gmail.com

PACS 73.40.Gk, 03.65.Xp **DOI 10.17586/2220-8054-2021-12-6-680-689**

Temperature dependence of the spectral intensity of recombination radiation in a quasi-zero-dimensional structure, containing impurity complexes "$A^+ + e$" (a hole localized on a neutral acceptor, interacting with an electron localized in the ground state of a quantum dot), has been investigated in an external electric field in the presence of tunneling decay of a quasistationary A^+-state. Probability of dissipative tunneling of a hole has been calculated in the one-instanton approximation, and the influence of tunneling decay and of an external electric field on the A^+-state binding energy and on the spectra of recombination radiation, associated with the optical transition of an electron from the ground state of a quantum dot to the A^+-state of the impurity center, has been investigated in the adiabatic approximation. "Dips" in the temperature dependence of the SIRR have been revealed, which are associated with the presence of resonant tunneling at certain values of temperature and strength of the external electric field, for which the double-well oscillatory potential becomes symmetric.

Keywords: spectral intensity of recombination radiation, quasi-zero-dimensional structure, impurity complexes, quantum dots.

Received: 15 November 2021

Revised: 19 November 2021

1. Introduction

The relevance of studies of the spectral intensity of recombination radiation (SIRR) temperature dependence in quasi-zero-dimensional structures is determined by the fact that, first, electro-optical systems based on quantum dots (QD)s have significantly better parameters compared to similar devices based on quantum wells. Second, the temperature quenching of luminescence is usually associated with the presence of a nonradiative channel caused by a defect located in a QD [1, 2] or at the barrier boundary. In this work, we would like to draw attention to the possible existence of one more channel of temperature quenching of luminescence associated with tunneling processes, in particular, with the process of dissipative tunneling of a hole localized at the A^+-center into the matrix, surrounding the QD. As will be shown below, the temperature "spreading" of the wave function for the quasi-stationary A^+-state under tunnel decay conditions is accompanied by an increase in the energy of the radiative transition of an electron and a corresponding decrease in the overlap integral of the wave functions of a hole and an electron, which leads to temperature quenching of the recombination radiation. The aim of this work is to study theoretically the temperature effect, associated with the electron – phonon interaction, on the binding energy of a hole in the "$A^+ + e$"-impurity complex in a spherically symmetric QD, as well as on the spectral intensity of the recombination radiation of a quasi-zero-dimensional structure in the presence of a dissipative tunneling.

2. Binding energy of a quasi-stationary A^+-state in a quantum dot in the presence of dissipative tunneling in an external electric field

Let us consider the problem of quasi-stationary states of a hole in an impurity complex $A^+ + e$ in a semiconductor spherically symmetric QD. The interaction of an electron in the QD ground state with a hole, localized at the A^0-center, will be considered in the framework of the adiabatic approximation [3]. In this case, the electron potential $V_{n,l,m}(\vec{r})$ acting on the hole can be considered averaged over the electron motion:

$$V_{nlm}\left(\vec{r}\right) = -\frac{e^2}{4\pi\varepsilon_0\varepsilon}\int\limits_0^{R_0}\frac{\left|\Psi_{nlm}\left(\vec{r}_e\right)\right|^2}{\left|\vec{r}-\vec{r}_e\right|}d\vec{r}_e, \tag{1}$$

where e is the the electron charge; ε is the dielectric permittivity of QD material; ε_0 is the electrical constant; $m = 0, \pm1, \pm2, ...$ is the magnetic quantum number; $l = 0, 1, 2...$ is the orbital quantum number, $\Psi_{nlm}\left(\vec{r}_e\right)$ is the wave function of an electron in a QD determined by the expression (2):

$$\Psi_{nlm}\left(\vec{r}_e\right) = Y_{lm}\left(\theta_e, \varphi_e\right) \frac{J_{l+\frac{3}{2}}\left(K_{nl} r_e\right)}{\sqrt{2\pi} R_0 \sqrt{r} J_{l+\frac{3}{2}}\left(K_{nl} R_0\right)}, \tag{2}$$

where K_{nl} is defined by an expression of the following form:

$$K_{nl} = \sqrt{\frac{\tilde{X}_{n,l}^2}{R_0^{*2}} + \frac{kT}{E_h} \ln\left[4 \sinh\left(\frac{\Omega}{v_{LA}\sqrt{kT}}\right) \sinh\left(\frac{2\Omega}{v_{TA}\sqrt{kT}}\right)\right]}. \tag{3}$$

Here ν_{LA}, ν_{TA} are the velocities of longitudinal and transverse phonons; $\Omega = \dfrac{\pi\hbar\Theta G}{a}\sqrt{\dfrac{2}{\rho V}}$, G is the overlap integral, Θ is the deformation potential, a is the lattice constant, ρ is the QD material density, V is the QD volume, E_h is the Bohr hole energy, $\tilde{X}_{n,l}$ is the half-integer root of the Bessel function $l + 1/2$.

Let us consider the case corresponding to the p-state of an electron, in this case $l = 1$, $m = 0$, then expression (1) can be represented in the form

$$V_{n10}(\vec{r}_h) = \\ -\frac{e^2}{4\pi\varepsilon_0\varepsilon} \int\limits_0^{\pi} \sin\theta_e d\theta_e \int\limits_0^{2\pi} d\varphi_e \left(\int\limits_0^{r_h} \frac{\left|\Psi_{n10}\left(r_e, \theta_e, \varphi_e\right)\right|^2 {r_e}^2 dr_e}{\sqrt{{r_h}^2 + {r_e}^2 - 2 r_h r_e \cos\theta_e}} + \int\limits_{r_h}^{R_0} \frac{\left|\Psi_{n10}\left(r_e, \theta_e, \varphi_e\right)\right|^2 {r_e}^2 dr_e}{\sqrt{{r_h}^2 + {r_e}^2 - 2 r_h r_e \cos\theta_e}} \right). \tag{4}$$

Or, taking into account the explicit expression for the wave function:

$$V_{n10}(\vec{r}_h) = -\frac{3e^2}{32\pi^3 \varepsilon_0 \varepsilon R_0^2 J_{\frac{5}{2}}^2\left(K_{n1} R_0\right)} \int\limits_0^{\pi} \sin\theta_e \cos^2\theta_e d\theta_e \int\limits_0^{2\pi} d\varphi_e \left(\int\limits_0^{r_h} \frac{J_{\frac{5}{2}}^2\left(K_{n1} r_e\right) r_e dr_e}{\sqrt{{r_h}^2 + {r_e}^2 - 2 r_h r_e \cos\theta_e}} \right. \\ \left. + \int\limits_{r_h}^{R_0} \frac{J_{\frac{5}{2}}^2\left(K_{nl} r_e\right) r_e dr_e}{\sqrt{{r_h}^2 + {r_e}^2 - 2 r_h r_e \cos\theta_e}} \right). \tag{5}$$

After integration over the angular variables φ_e, θ_e and over the radial coordinate of the electron r_e, we obtain:

$$V_{n10}(r_h) = \frac{e^2}{2^7 \pi^3 \varepsilon_0 \varepsilon R_0^{*6} K_{n1}^{*5} r_h^{*4} J_{\frac{5}{2}}^2\left(K_{n1}^* r_h^*\right)} \left[3R_0^{*4} + 6K_{n1}^{*2} R_0^{*4} r_h^{*2} + 9r_h^{*4} + 6K_{n1}^{*2} R_0^{*2} r_h^{*4} \right. \\ - 4K_{n1}^{*4} R_0^{*4} r_h^{*4} - 9r_h^{*4} \cos\left(2K_{n1}^* R_0^*\right) + 12K_{n1}^{*2} R_0^{*2} r_h^{*4} \cos\left(2K_{n1}^* R_0^*\right) \\ - 3R_0^{*4} \cos\left(2K_{n1}^* R_0^*\right) + 4K_{n1}^{*4} R_0^{*4} r_h^{*4} \left(\mathrm{Ci}\left(2K_{n1}^* R_0^*\right) - \mathrm{Ci}\left(2K_{n1}^* r_h^*\right)\right) \\ \left. -4K_{n1}^{*4} R_0^{*4} r_h^{*4} \ln\left(\frac{R_0^*}{r_h^*}\right) - \left(9r_h^{*3} + 3R_0^{*3} - K_{n1}^{*2} R_0^{*3} r_h^{*2}\right) 2K_{n1}^* R_0^* r_h^* \sin\left(2K_{n1}^* R_0^*\right) \right]. \tag{6}$$

Here, $r_h^* = r_h/a_h$, $R_0^* = R_0/a_h$,

$$K_n^* = \sqrt{\frac{X_{n,l}^2}{R_0^{*2}} + \frac{kT}{E_h R_0^{*2}} \ln\left[4 \sinh\left(\frac{\Omega}{v_{LA}\sqrt{kT}}\right) \sinh\left(\frac{2\Omega}{v_{TA}\sqrt{kT}}\right)\right]},$$

$\mathrm{Ci}\,(x)$ is the cosine integral.

In the case under consideration, p-state with $m = 0$, the potential energy minimum is shifted relative to the QD center. Position of the minimum $r_{h\,\min}$ is determined from the solution of the transcendental equation, which is obtained by equating the first derivative of expression (6) to zero:

$$\frac{dV_{n,1,0}(r_h)}{dr_h} = 0. \tag{7}$$

Expanding expression (6) in a Taylor series near $r_{h\,\min}$ and limiting ourselves to the quadratic term in the radial coordinate of the hole r_h, we obtain:

$$\begin{aligned} V_{n10}(r_h) = {} & \frac{e^2 2^{-7}\pi^{-3}}{\varepsilon_0\varepsilon R_0^{*6} K_{n1}^{*5} r_{h\,\min}^{*6} J_{5/2}^2\left(K_{n1}^{*}R_0^{*}\right)}\Biggl[r_{h\,\min}^{*2}\Bigl(2K_{n1}^{*2}R_0^{*2}r_{h\,\min}^{*2}\left(3R_0^{*2}+3r_{h\,\min}^{*2}-2K_{n1}^{*2}R_0^{*2}r_{h\,\min}^{*2}\right)\Bigr)+ \\ & + 4K_{n1}^{*4}R_0^{*4}r_{h\,\min}^{*4}\left(\mathrm{Ci}\left(2K_{n1}^{*}R_0^{*}\right)-\mathrm{Ci}\left(2K_{n1}^{*}r_{h\,\min}^{*}\right)-\ln\left(\frac{R_0^{*}}{r_{h\,\min}^{*}}\right)\right)- \\ & - 2K_{n1}^{*}r_{h\,\min}^{*}R_0^{*}\Bigl(K_{n1}^{*2}R_0^{*3}r_{h\,\min}^{*2}\sin\left(2K_{n1}^{*}r_{h\,\min}^{*}\right)-9r_{h\,\min}^{*3}\sin\left(2K_{n1}^{*}R_0^{*}\right)-3R_0^{*3}\sin\left(2K_{n1}^{*}r_{h\,\min}^{*}\right)\Bigr)+ \\ & + \left(r_h^{*}-r_{h\,\min}^{*}\right)2R_0^{*4}r_{h\,\min}^{*}\Bigl(-6-6K_{n1}^{*2}r_{h\,\min}^{*2}+2K_{n1}^{*4}r_{h\,\min}^{*4}+6\left(1-K_{n1}^{*2}r_{h\,\min}^{*2}\right)\cos\left(2K_{n1}^{*}r_{h\,\min}^{*}\right)+ \\ & + K_{n1}^{*}r_{h\,\min}^{*}\left(K_{n1}^{*2}r_{h\,\min}^{*2}-12\right)\sin\left(2K_{n1}^{*}r_{h\,\min}^{*}\right)\Bigr)- \\ & - \left(r_h^{*}-r_{h\,\min}^{*}\right)^2 2R_0^{*4}\Bigl(-15-9K_{n1}^{*2}r_{h\,\min}^{*2}+K_{n1}^{*4}r_{h\,\min}^{*4}+ \\ & + \left(15-21K_{n1}^{*2}r_{h\,\min}^{*2}+K_{n1}^{*4}r_{h\,\min}^{*4}\right)\cos\left(2K_{n1}^{*}r_{h\,\min}^{*}\right)+\left(30K_{n1}^{*}r_{h\,\min}^{*}-7K_{n1}^{*3}r_{h\,\min}^{*3}\right)\sin\left(2K_{n1}^{*}r_{h\,\min}^{*}\right)\Bigr)\Biggr], \end{aligned} \tag{8}$$

where $r_{h\,\min}^{*} = r_{h\,\min}/a_h$.

Within the framework of the adiabatic approximation for the p-state of an electron, we obtain:

$$V_{n10}(r_h^{*}) = -\frac{e^2}{\varepsilon R_0^{*}}\beta_n - \frac{m_h\omega_n^2\left(r_h^{*}-r_T^{*}\right)^2}{2}, \tag{9}$$

where values β_n, ω_n and r_T^{*} are defined as follows:

$$\begin{aligned} \beta_n = {} & \frac{2^{-7}\pi^{-3}}{R_0^{*5} K_{n1}^{*5} r_{h\,\min}^{*6} J_{5/2}^2\left(K_{n1}^{*}R_0^{*}\right)}\Biggl[r_{h\,\min}^{*2}\Bigl(2K_{n1}^{*2}R_0^{*2}r_{h\,\min}^{*2}\left(3R_0^{*2}+3r_{h\,\min}^{*2}-2K_{n1}^{*2}R_0^{*2}r_{h\,\min}^{*2}\right)\Bigr)+ \\ & + 3R_0^{*4}+9r_{h\,\min}^{*4}+3r_{h\,\min}^{*4}\cos\left(2K_{n1}^{*}R_0^{*}\right)\left(6K_{n1}^{*2}R_0^{*2}-3\right)-3R_0^{*4}\cos\left(2K_{n1}^{*}r_{h\,\min}^{*}\right)+ \\ & + 4K_{n1}^{*4}R_0^{*4}r_{h\,\min}^{*4}\left(\mathrm{Ci}\left(2K_{n1}^{*}R_0^{*}\right)-\mathrm{Ci}\left(2K_{n1}^{*}r_{h\,\min}^{*}\right)-\ln\left(\frac{R_0^{*}}{r_{h\,\min}^{*}}\right)\right)- \\ & - 2K_{n1}^{*}r_{h\,\min}^{*}R_0^{*}\Bigl(K_{n1}^{*2}R_0^{*3}r_{h\,\min}^{*2}\sin\left(2K_{n1}^{*}r_{h\,\min}^{*}\right)-9r_{h\,\min}^{*3}\sin\left(2K_{n1}^{*}R_0^{*}\right)-3R_0^{*3}\sin\left(2K_{n1}^{*}r_{h\,\min}^{*}\right)\Bigr)+ \\ & + 2R_0^{*4}r_{h\,\min}^{*2}\Bigl(-6-6K_{n1}^{*2}r_{h\,\min}^{*2}+2K_{n1}^{*4}r_{h\,\min}^{*4}+6\left(1-K_{n1}^{*2}r_{h\,\min}^{*2}\right)\cos\left(2K_{n1}^{*}r_{h\,\min}^{*}\right)+ \\ & + K_{n1}^{*}r_{h\,\min}^{*}\left(K_{n1}^{*2}r_{h\,\min}^{*2}-12\right)\sin\left(2K_{n1}^{*}r_{h\,\min}^{*}\right)\Bigr)^2\times\Bigl(15+9K_{n1}^{*2}r_{h\,\min}^{*2}-K_{n1}^{*4}r_{h\,\min}^{*4}- \\ & - \cos\left(2K_{n1}^{*}r_{h\,\min}^{*}\right)\left(15-21K_{n1}^{*2}r_{h\,\min}^{*2}+K_{n1}^{*4}r_{h\,\min}^{*4}\right)-\left(30K_{n1}^{*}r_{h\,\min}^{*}-7K_{n1}^{*3}r_{h\,\min}^{*3}\right)\sin\left(2K_{n1}^{*}r_{h\,\min}^{*}\right)\Bigr)^{-1}\Biggr], \end{aligned} \tag{10}$$

$$\begin{aligned} \hbar\omega_n = {} & \Biggl[\frac{\hbar^2 e^2 2^{-5}\pi^{-3}}{m_h^{*}\varepsilon_0\varepsilon R_0^{*2} K_{n1}^{*5} r_{h\,\min}^{*6} J_{5/2}^2\left(K_{n1}R_0^{*}\right)}\Bigl(15+9K_{n1}^{*2}r_{h\,\min}^{*2}-K_{n1}^{*4}r_{h\,\min}^{*4}- \\ & - \cos\left(2K_{n1}^{*}r_{h\,\min}^{*}\right)\left(15-21K_{n1}^{*2}r_{h\,\min}^{*2}+K_{n1}^{*4}r_{h\,\min}^{*4}\right)-\left(30K_{n1}^{*}r_{h\,\min}^{*}-7K_{n1}^{*3}r_{h\,\min}^{*3}\right)\sin\left(2K_{n1}^{*}r_{h\,\min}^{*}\right)\Bigr)\Biggr]^{1/2}, \end{aligned} \tag{11}$$

and

$$\begin{aligned} r_T^{*} = {} & -r_{h\,\min}^{*}-\frac{r_{h\,\min}^{*}}{2}\Bigl(-6-6K_{n1}^{*2}r_{h\,\min}^{*2}+2K_{n1}^{*4}r_{h\,\min}^{*4}+6\left(1-K_{n1}^{*2}r_{h\,\min}^{*2}\right)\cos\left(2K_{n1}^{*}r_{h\,\min}^{*}\right)+ \\ & + K_{n1}^{*}r_{h\,\min}^{*}\left(K_{n1}^{*2}r_{h\,\min}^{*2}-12\right)\sin\left(2K_{n1}^{*}r_{h\,\min}^{*}\right)\Bigr)\times\Bigl[-15-9K_{n1}^{*2}r_{h\,\min}^{*2}+K_{n1}^{*4}r_{h\,\min}^{*4}+ \\ & + \left(15-21K_{n1}^{*2}r_{h\,\min}^{*2}+K_{n1}^{*4}r_{h\,\min}^{*4}\right)\cos\left(2K_{n1}^{*}r_{h\,\min}^{*}\right)+\left(30K_{n1}^{*}r_{h\,\min}^{*}-7K_{n1}^{*3}r_{h\,\min}^{*3}\right)\sin\left(2K_{n1}^{*}r_{h\,\min}^{*}\right)\Bigr]^{-1}. \end{aligned} \tag{12}$$

Since the confining potential of a QD, generally speaking, should have a finite depth, then in our model of the hole potential of confinement (9), the amplitude of the potential U_0 is an empirical parameter and satisfies the relation

$$U_0 = -e^2\beta_n/4\pi\varepsilon_0\varepsilon R_0 + m_h^*\omega_n^2 R_0^2/2 = m_h^*\omega_0^2 R_0^2/2,$$

whence $\omega_0 = \sqrt{\omega_n^2 - e^2\beta_n/2\pi\varepsilon_0\varepsilon m_h R_0^3}$ is the characteristic frequency of the hole confining potential of a QD within the adiabatic approximation, and in this case $U_0/\left(\hbar\omega_0\right) \gg 1$.

Usage of the adiabatic approximation makes it possible to take into account the effect of an external electric field on the bound state of the hole. Let the electric field strength vector $\vec{E}_0$ be directed along the x coordinate axis, then the energy levels of the oscillatory potential (9) will have the form:

$$E_{n_1 n_2 n_3}^{n,0,0}(T) = -\frac{e^2}{\varepsilon R_0}\beta_h - \frac{|e|^2 E_0^2}{2m_h\omega_n^2} + \hbar\omega_n\left(n_1 + n_2 + n_3 + \frac{3}{2}\right) + \\ + kT\ln\left[4\sinh\left(\frac{\Omega}{v_{LA}\sqrt{kT}}\right)\sinh\left(\frac{2\Omega}{v_{TA}\sqrt{kT}}\right)\right], \quad (13)$$

and the corresponding one-particle wave functions are written as:

$$\Psi_{n_1 n_2 n_3}^{n}(x,y,z) = C_n \exp\left(-\frac{(x-x_0)^2 + y^2 + z^2}{2a_n^2}\right) H_{n_1}\left(\frac{x-x_0}{a_n}\right) H_{n_2}\left(\frac{y}{a_n}\right) H_{n_3}\left(\frac{z}{a_n}\right). \quad (14)$$

Here, $C_n = \left[2^{n1+n2+n3} n_1! n_2! n_3! \pi^{3/2} a_n^3\right]^{-1/2}$; $a_n = \sqrt{\hbar/\left(m_h^*\omega_n\right)}$; $x_0 = |e|\,E_0/\left(m_h^*\omega_n^2\right)$; $H_n(x)$ are the Hermite polynomials; n_1, n_2, n_3 are the quantum numbers corresponding to energy levels of a harmonic oscillator. We will assume that the process of decay of the quasi-stationary level of the A^+-center is due to dissipative tunneling. It should be noted that in the one-instanton approximation, the decay probability Γ_0 (dissipative tunneling), under conditions of an external electric field, can be represented in the form $\Gamma_0 = B\exp(-S)$, where the expressions for S and B were obtained in our previous papers (in the Bohr units) [4, 5]:

$$S = \frac{1}{2}\left(\frac{b_0' + x_0^*}{a_0' + x_0^*} + 1\right)\left(3 - \frac{b_0' + x_0^*}{a_0' + x_0^*}\right)\tau_0^* - \frac{1}{2\beta^*}\left(\frac{b_0' + x_0^*}{a_0' + x_0^*} + 1\right)^2 \tau_0^{*2} - \frac{1}{2\gamma^*}\left(\frac{b_0' + x_0^*}{a_0' + x_0^*} + 1\right)^2 \times \\ \times \left(\frac{(1 - x_2^*)}{\sqrt{x_1^*}}\left[\coth\left(\beta^*\sqrt{x_1^*}\right) - \frac{\cosh\left((\beta^* - \tau_0^*)\sqrt{x_1^*}\right) - \cosh\left(\beta^*\sqrt{x_1^*}\right)}{\sinh\left(\beta^*\sqrt{x_1^*}\right)} + \cosh\left((\beta^* - \tau_0^*)\sqrt{x_1^*}\right)\right] - \right. \\ \left. - \frac{(1 - x_1^*)}{\sqrt{x_2^*}}\left[\coth\left(\beta^*\sqrt{x_2^*}\right) - \frac{\cosh\left((\beta^* - \tau_0^*)\sqrt{x_2^*}\right) - \cosh\left(\beta^*\sqrt{x_2^*}\right)}{\sinh\left(\beta^*\sqrt{x_2^*}\right)} + \cosh\left((\beta^* - \tau_0^*)\sqrt{x_2^*}\right)\right]\right), \quad (15)$$

$$B = \frac{2E_d\sqrt{U_0^*}}{\hbar\sqrt{\pi}}\left(\frac{b_0' + x_0^*}{a_0' + x_0^*} + 1\right)\sqrt{\varepsilon_T^*} \times \left\{A^*\left[\beta_1^*\cosh\left(\frac{\beta_1^*}{2}\right) - 1\right] + D^*\left[\beta_2^*\cosh\left(\frac{\beta_2^*}{2}\right) - 1\right] + \right. \\ \left. + A^*\left(1 - \frac{\beta_1^*}{2}\frac{\left(\frac{\beta_1^*}{2} - \tau_{01}{}^*\right)}{\sinh\left(\frac{\beta_1^*}{2}\right)}\right) + D^*\left(\frac{\beta_2^*}{2}\frac{\cosh\left(\frac{\beta_2^*}{2} - \tau_{02}{}^*\right)}{\sinh\left(\frac{\beta_2^*}{2}\right)} - 1\right)\right\} \times \\ \left(A^*\left[\frac{\beta_1^*}{2}\frac{\cosh\left(\frac{\beta_1^*}{2} - \tau_{01}{}^*\right)}{\sinh\left(\frac{\beta_1^*}{2}\right)} - 1\right] + D^*\left[\frac{\beta_2^*}{2}\frac{\cosh\left(\frac{\beta_2^*}{2} - \tau_{02}{}^*\right)}{\sinh\left(\frac{\beta_2^*}{2}\right)} - 1\right]\right)^{-1/2}, \quad (16)$$

where

$$x_{1,2}^* = \frac{1}{2}\left[\frac{\varepsilon_L^{*2}a^{*2}}{4U_0^*} + 1 + \frac{\varepsilon_c^4 a^{*2}}{4\varepsilon_L^{*2}U_0^*} \mp \sqrt{\left(\frac{\varepsilon_L^{*2}a^{*2}}{4U_0^*} + 1 + \frac{\varepsilon_c^4 a^{*2}}{4\varepsilon_L^{*2}U_0^*}\right)^2 - \frac{\varepsilon_L^{*2}a^{*2}}{U_0^*}}\right],$$

$$\gamma^* = \sqrt{\left(\varepsilon_L^{*2}a^{*2}/\left(4U_0^*\right) + 1 + \varepsilon_c^{*\,4}a^{*2}/\left(4\varepsilon_L^{*2}U_0^*\right)\right)^2 - \varepsilon_L^{*2}a^{*2}/U_0^*},$$

$$\tau_0^* = \operatorname{arsinh}\left[\left(1 - \frac{b_0' + x_0^*}{a_0' + x_0^*}\right)\sinh(\beta^*)/\left(1 + \frac{b_0' + x_0^*}{a_0' + x_0^*}\right)\right] + \beta_{„}^*,$$

$\varepsilon_T^* = kT/E_h$, $\quad\varepsilon_L^* = \hbar\omega_L/E_h$, $\quad\varepsilon_c^* = \hbar\sqrt{c}/E_d$, $\quad\beta_{„}^* = \sqrt{U_0^*}/a^*\varepsilon_T^*$, $\quad b_0' = b_0/a_h$, $\quad a_0' = a_0/a_h$, $\quad x_0{}^* = x_0/a_h$;

E_h and a_h are the Bohr energy and the hole radius correspondingly;

$$A^* = \left(2\varepsilon_L^{*2} a^{*2} - x_1^*\right) / \left(\left(x_1^* - x_2^*\right) x_1^*\right), \quad D^* = \left(2\varepsilon_L^{*2} a^{*2} - x_2^*\right) / \left(\left(x_1^* - x_2^*\right) x_2^*\right),$$

$$\beta_1^* = \sqrt{2\, U_0^* x_1^*} / \left(a^* \varepsilon_T^*\right), \quad \beta_2^* = \sqrt{2\, U_0^* x_2^*} / \left(a^* \varepsilon_T^*\right), \quad \tau_{01}^* = \tau_0^* \sqrt{x_1^*}/\sqrt{2}, \quad \tau_{02}^* = \tau_0^* \sqrt{x_2^*}/\sqrt{2}.$$

Using the zero-range potential procedure (see, for example, [3]), in combination with the one-instanton approximation [5], we obtain an equation that determines the dependence of the hole energy in the complex $A^+ + e$ on temperature T, QD parameters, and dissipative tunneling.

The short-range potential of an impurity is simulated by a potential of zero radius with a power $\gamma = 2\pi\hbar^2/(\alpha m_h^*)$, which has the form:

$$V_\delta\left(x, y, z; x_a, y_a, z_a\right) = \gamma \delta\left(x - x_a\right) \delta\left(y - y_a\right) \delta\left(z - z_a\right) \left[1 + \left(r - r_a\right) \frac{\partial}{\partial r}\right], \tag{17}$$

where α is determined by the binding energy E_i of the same A^+-center in a bulk semiconductor.

In the effective mass approximation, the wave function $\Psi_{\lambda h}\left(x, y, z; x_a, y_a, z_a\right)$ of an electron localized at a short-range potential satisfies the Schrödinger equation:

$$\left(E_{\lambda h} - H\right) \Psi_{\lambda h}\left(x, y, z; x_a, y_a, z_a\right) = V_\delta\left(x, y, z; x_a, y_a, z_a\right) \Psi_{\lambda h}\left(x, y, z; x_a, y_a, z_a\right), \tag{18}$$

where $E_h^{QD} = -\hbar^2 \lambda^2 / \left(2m_h^*\right)$ – the eigenvalues of the Hamilton operator $H^\delta = H + V_\delta\left(x, y, z; x_a, y_a, z_a\right)$; $H = -\hbar^2/\left(2m_h^*\right) \nabla^2 + m_h^* \omega_0^2 \left(x^2 + y^2 + z^2\right)/2 - |e| E_0 x$.

To determine the binding energy of a hole in a complex $A^+ + e$ in the adiabatic approximation, it is necessary to construct a one-particle Green's function $G\left(x, y, z; x_a, y_a, z_a; E_{\lambda n}\right)$ to the Schrödinger equation with a Hamiltonian, containing potential (17):

$$G\left(x, y, z; x_a, y_a, z_a; E_{\lambda h}\right) = -\sum_{n1, n2, n3} \frac{\Psi_{n_1, n_2, n_3}^{n*}\left(x_a, y_a, z_a\right) \Psi_{n_1, n_2, n_3}^{n}\left(x, y, z\right)}{-E_h^{QD} + i\hbar\Gamma_0 + E_{n_1, n_2, n_3}^{n, 0, 0}\left(T\right)}. \tag{19}$$

The Lippmann–Schwinger equation for a A^+-state in a QD with a parabolic confinement potential can be written as:

$$\Psi_h\left(x, y, z; x_a, y_a, z_a\right) = \int\limits_{-\infty}^{+\infty} \int\limits_{-\infty}^{+\infty} \int\limits_{-\infty}^{+\infty} dx_1 dy_1 dz_1 G\left(x, y, z; x_a, y_a, z_a; E_{\lambda h}\right) \times$$
$$\times V_\delta\left(x, y, z; x_a, y_a, z_a\right) \Psi_{\lambda h}\left(x_1, y_1, z_1, x_a, y_a, z_a\right). \tag{20}$$

Substituting (17) into (20), we obtain:

$$\Psi_h\left(x, y, z; x_a, y_a, z_a\right) = \gamma G\left(x, y, z; x_a, y_a, z_a; E_{\lambda h}\right) \left(T\Psi_h\right)\left(x, y, z; x_a, y_a, z_a\right), \tag{21}$$

where:

$$\left(T\Psi_{\lambda h}\right)\left(x, y, z; x_a, y_a, z_a\right) \equiv \lim_{\substack{r \to r_a \\ \varphi \to \varphi_a \\ \theta \to \theta_a}} \left[1 + \left(r - r_a\right) \frac{\partial}{\partial r}\right] \Psi_{\lambda h}\left(x, y, z; x_a, y_a, z_a\right). \tag{22}$$

Acting by the operator T on both sides of relation (21), we obtain an equation that determines dependence of the energy $E_{\lambda h}$ of the bound state of the A^+-center on the parameters of the QD, on the position of the impurity $R_a = \left(x_a, y_a, z_a\right)$, and on the temperature T:

$$\alpha = \frac{2\pi\hbar^2}{m_h^*} \left(TG\right)\left(x_a, y_a, z_a; x_a, y_a, z_a; E_{\lambda h}\right), \tag{23}$$

here, α is determined by the energy E_i of the bound state of the same A^+-center in a massive semiconductor.

Then, for Green's function (29), taking into account (23) and (24), we obtain in the Bohr units:

$$G\left(x, y, z, x_a, y_a, z_a; \eta_{\lambda h}^2\right) = -\frac{1}{\pi^{3/2} a_n^2 E_h} \exp\left(-\frac{\left(x^* - x_0^*\right)^2 + y^{*2} + z^{*2} + \left(x_a^* - x_0^*\right)^2 + y_a^{*2} + z_a^{*2}}{2}\right) \times$$
$$\times \sum_{n_1, n_2, n_3} \frac{H_{n_1}\left(x^* - x_0^*\right) H_{n_1}\left(x_a^* - x_0^*\right)}{2^{n_1} ! n_1 !} \frac{H_{n_2}\left(y^*\right) H_{n_2}\left(y_a^*\right)}{2^{n_2} ! n_2 !} \frac{H_{n_3}\left(z^*\right) H_{n_3}\left(z_a^*\right)}{2^{n_3} ! n_3 !} \times$$
$$\left\{-\eta_h^2 - \beta_h^* - \frac{x_0^{*2}}{4\beta^{-2}} + i4\Gamma_0^* + \beta^{-1}\left(n_1 + n_2 + n_3 + \frac{3}{2}\right) + \frac{kT}{E_h} \ln\left[4 \sinh\left(\frac{\Omega}{v_{LA}\sqrt{kT}}\right) \sinh\left(\frac{2\Omega}{v_{TA}\sqrt{kT}}\right)\right]\right\}^{-1}, \tag{24}$$

where the next notations are introduced: $\eta_h^2 = E_h^{QD}/E_h$; $R_0^* = R_0/a_h$; $\beta = E_h/\hbar\omega_n$; $a_n^* = a_n/a_h$; $\beta_h^* = e^2\beta_h/\varepsilon R_0^* E_h a_h$; $\Gamma_0^* = \hbar\Gamma_0/4E_h$.

Further, given that:

$$\left(-\eta_h^2 - \beta_h^* - \frac{x_0^{*2}\beta^{-2}}{4a_h^{*2}} + i4\Gamma_0^* + \frac{kT}{E_h}\ln\left[4\sinh\left(\frac{\Omega}{v_{LA}\sqrt{kT}}\right)\sinh\left(\frac{2\Omega}{v_{TA}\sqrt{kT}}\right)\right] + n_1 + n_2 + n_3 + \frac{3}{2}\right)^{-1} =$$
$$\beta^{-1}\int_0^\infty dt\exp\left[-t\left(-\beta\left(\eta_h^2 + \beta_h^* + \frac{x_0^{*2}\beta^{-2}}{4a_h^{*2}} - i4\Gamma_0^*\right) + \right.\right.$$
$$\left.\left. + n_1 + n_2 + n_3 + \frac{3}{2} + \frac{kT\beta}{E_h}\ln\left[4\sinh\left(\frac{\Omega}{v_{LA}\sqrt{kT}}\right)\sinh\left(\frac{2\Omega}{v_{TA}\sqrt{kT}}\right)\right]\right]\right], \quad (25)$$

the expression for the Green's function takes the following form:

$$G\left(x, y, z, x_a, y_a, z_a, \eta_h^2\right) = -\frac{1}{\pi^{\frac{3}{2}}a_n^2\beta E_h}\exp\left(-\frac{\left(x^* - x_0^*\right)^2 + \left(x_a^* - x_0^*\right)^2 + y^2 + y_a^2 + z^2 + z_a^2}{2a_n}\right)\times$$
$$\times\int_0^\infty dt\exp\left[-t\left(-\beta\left(\eta_h^2 + \beta_h^* + \frac{x_0^{*2}\beta^{-2}}{4a_h^{*2}} - i4\Gamma_0^*\right) + \frac{kT\beta}{E_h}\ln\left[4\sinh\left(\frac{\Omega}{v_{LA}\sqrt{kT}}\right)\sinh\left(\frac{2\Omega}{v_{TA}\sqrt{kT}}\right)\right] + \frac{3}{2}\right)\right]\times$$
$$\times\sum_{n_1=0}^{\infty}\left(\frac{e^{-t}}{2}\right)^{n_1}\frac{H_{n_1}\left(\frac{x-x_0}{a_n}\right)H_{n_1}\left(\frac{x_a-x_0}{a_n}\right)}{n_1!}\sum_{n_2=0}^{\infty}\left(\frac{e^{-t}}{2}\right)^{n_2}\frac{H_{n_2}\left(\frac{y}{a_n}\right)H_{n_2}\left(\frac{y_a}{a_n}\right)}{n_2!}\times$$
$$\times\sum_{n_3=0}^{\infty}\left(\frac{e^{-t}}{2}\right)^{n_3}\frac{H_{n_3}\left(\frac{z}{a_n}\right)H_{n_3}\left(\frac{z_a}{a_n}\right)}{n_3!}. \quad (26)$$

Making summation over the quantum numbers n_1, n_2, n_3, and separating the divergent part of the expression for the Green's function (26), we obtain:

$$G\left(r, R_a, \eta_h^2\right) = -\frac{1}{\pi^{\frac{3}{2}}a_n^2\beta E_h}\int_0^\infty dt\exp\left[-t\left(-\beta\left(\eta_h^2 + \beta_h^* + \frac{x_0^{*2}\beta^{-2}}{4a_h^{*2}} - i4\Gamma_0^*\right) + \frac{3}{2} + \right.\right.$$
$$\left.\left. + \frac{kT\beta}{E_h}\ln\left[4\sinh\left(\frac{\Omega}{v_{LA}\sqrt{kT}}\right)\sinh\left(\frac{2\Omega}{v_{TA}\sqrt{kT}}\right)\right]\right)\right]\times$$
$$\times\left\{\left(1 - \exp\left(-t\right)\right)^{-\frac{3}{2}}\exp\left(-\frac{r^2 + R_a^2}{2a_n}\right)\exp\left(\frac{2\left(rR_a\right)e^{-t} - \left(r^2 + R_a^2\right)e^{-2t}}{a_n\left(1 - e^{-2t}\right)}\right) - \frac{1}{t\sqrt{t}}\exp\left[-\frac{\left(r - R_a\right)^2}{2a_n^2 t}\right]\right\} -$$
$$-\frac{\exp\left(-\sqrt{2\left(-\eta_h^2 - \beta_h^* - \frac{x_0^{*2}\beta^{-2}}{4a_h^{*2}} + i4\Gamma_0^* + \frac{kT}{E_h}\ln\left[4\sinh\left(\frac{\Omega}{v_{LA}\sqrt{kT}}\right)\sinh\left(\frac{2\Omega}{v_{TA}\sqrt{kT}}\right)\right] + \frac{3}{2}\right)}\frac{\left|r-R_a\right|}{a_n}\right)}{2\pi^{\frac{3}{2}}a_n\beta E_h\left|r - R_a\right|}. \quad (27)$$

Substituting (27) into (23) we obtain the dispersion equation that determines the dependence of the binding energy of a hole E_h^{QD} in the complex $A^+ + e$ on the parameters of the QD, on temperature T, and on the electron quantum number n. Using the procedure of the zero-range potential method (see, for example, [3]) in combination with the one-instanton approximation [5], we obtain the dispersion equation that determines dependence of the hole binding energy in the complex $A^+ + e$ on the temperature T and on parameters of dissipative tunneling:

$$\eta_i = \sqrt{-\eta_h^2 - \beta_h^* - \frac{x_0^{*2}\beta^{-2}}{4a_h^{*2}} + i4\Gamma_0^* + \frac{kT}{E_h}\ln\left[4\sinh\left(\frac{\Omega}{v_{LA}\sqrt{kT}}\right)\sinh\left(\frac{2\Omega}{v_{TA}\sqrt{kT}}\right)\right] + \frac{3}{2}} +$$
$$+\sqrt{\frac{2}{\beta\pi}}\int_0^\infty dt\exp\left\{-t\beta\left(-\eta_h^2 - \beta_h^* - \frac{x_0^{*2}\beta^{-2}}{4a_h^{*2}} + i4\Gamma_0^* + \frac{3}{2\beta} + \frac{kT}{E_h}\times\right.\right.$$
$$\left.\left.\times\ln\left[4\sinh\left(\frac{\Omega}{v_{LA}\sqrt{kT}}\right)\sinh\left(\frac{2\Omega}{v_{TA}\sqrt{kT}}\right)\right]\right)\right\}\left[\frac{1}{2t\sqrt{2t}} - \left(1 - e^{-2t}\right)^{-\frac{3}{2}}\exp\left(-\frac{R_a^{*^2}\beta^{-1}}{2}\times\frac{1 - e^{-t}}{1 + e^{-t}}\right)\right], \quad (28)$$

where $R_a^* = R_a/a_n$; $\eta_i = \sqrt{|E_i|/E_h}$, $\eta_h = \sqrt{E_h^{(QD)}/E_h}$.

It should be noted that the binding energy of a hole in the case under consideration is a complex quantity. Its real part determines the average binding energy of the resonant state of the A^+-center $\overline{E_h^{(QD)}} = \operatorname{Re} E_h^{(QD)}$, and the doubled imaginary part determines the broadening of the corresponding energy level $\Delta E_h = 2 \operatorname{Im} E_h^{(QD)}$. Fig. 1 shows the result of a numerical analysis of the dispersion equation for the case of a centered A^+-center ($R_a^* = 0$) at different values of the QD radius R_0^*. It was taken into account that the binding energy of the A^+-state is measured from the level of the ground state of the adiabatic oscillatory well.

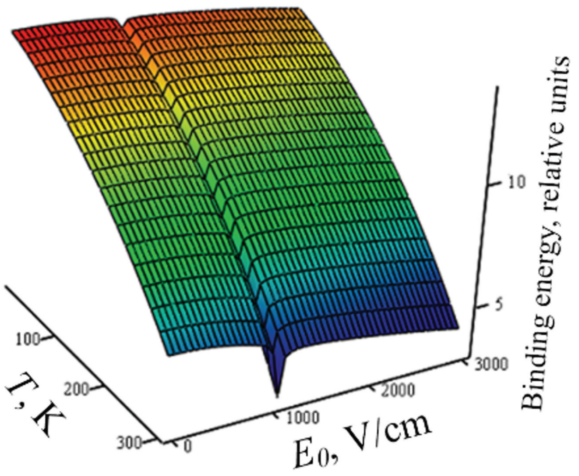

FIG. 1. Dependence of the binding energy of quasi-stationary states of a hole in the complex $A^+ + e$ on the temperature T and the magnitude of the external electric field E_0, for the following values of the QD parameters and dissipative tunneling $R_0^* = 1$ ($R_0^* = R_0/a_h$ – QD radius R_0 in units of the effective Bohr radius of the hole a_h); $U_0^* = 350$ ($U_0^* = U_0/E_h$ is the amplitude of the adiabatic potential U_0 of an electron in units of the effective Bohr energy of a hole E_h), $\eta_i = 3$.

As can be seen from Fig. 1, that in the field dependence of the binding energy of the A^+-state, there are "dips" at a certain temperature. This is due to the effect of "tuning" the starting energy level of the A^+-state to the states caused by the hole-phonon interaction in the matrix surrounding the quantum dot, i.e. with the effect of resonant tunneling. The depth of the dip increases with increasing temperature, which is due to the dynamics of the temperature-dependent peak in the field dependence of the probability of dissipative tunneling [5]. A decrease in the binding energy of the A^+-state with an increase in the external electric field strength is associated with the Stark shift in energy and with the polarization of the A^+-center, and with an increase in temperature – with the broadening of energy levels and the corresponding "spreading" of the wave function of the A^+-state.

3. Temperature and field dependences of the spectral intensity of recombination radiation in a quasi-zero-dimensional structure with impurity complexes

Let us consider the process of radiative transition of an excited electron to the level of A^+-center. The Coulomb interaction of an electron with a hole is accompanied by a radiative transition of an electron to the energy level of A^+-center under conditions of tunneling decay of a quasi-stationary A^+-state. The energy spectrum of an electron in the size-quantized band can be represented as [6, 7]:

$$E_{n,l} = \frac{\tilde{X}_{n,l}^2 E_h}{R_0^{*2}} + kT \ln\left[4 \sinh\left(\frac{\Omega}{v_{LA}\sqrt{kT}}\right) \sinh\left(\frac{2\Omega}{v_{TA}\sqrt{kT}}\right)\right], \tag{29}$$

here $\tilde{X}_{n,l}$ is the root of the Bessel function of half-integer order $l + 1/2$.

The wave function of an electron is given by expression (2).

The SIRR, taking into account the dispersion of QD sizes and the finite lifetime of the resonant A^+-state, is determined by an expression of the next form [8]:

$$\Phi(\omega) = \frac{4\omega^2 \sqrt{\varepsilon} e^2}{c^3 V} \left|\frac{P_{eh} e_0}{m_0}\right| \int \sum_{nlm} |M|^2 P(u) \frac{\Gamma_0}{\frac{\hbar^2 \Gamma_0^2}{4} + (E_{nlm} - E_{\lambda h} - \hbar\omega)^2} du, \tag{30}$$

where m_0 – the free electron mass; P_{eh} is the matrix element of the momentum operator at the Bloch amplitudes of band carriers; ω is the frequency of the emitted electromagnetic wave with polarization e_0; V is the QD volume; $P\left(u\right)$ – the Lifshitz–Slezov function [9]:

$$P\left(u\right)=\begin{cases}\dfrac{3^4eu^2\exp\left[-1/\left(1-2u/3\right)\right]}{2^{5/3}\left(u+3\right)^{7/3}\left(3/2-u\right)^{11/3}}, & u<\dfrac{3}{2},\\ 0, & u>\dfrac{3}{2}.\end{cases} \tag{31}$$

The wave function of A^+-state, in the case of a central location of the A^+ center in the QD, has the form:

$$\Psi_h\left(r\right)=-C\int\limits_0^\infty dt\exp\left\{-\beta t\left(-\eta_h^2-\beta_h^*-\frac{x_0^{*2}}{a_n^{*4}}+i4\Gamma_0^*+\frac{kT}{E_h\beta}\ln\left[4\sinh\left(\frac{\Omega}{v_{LA}\sqrt{kT}}\right)\sinh\left(\frac{2\Omega}{v_{TA}\sqrt{kT}}\right)\right]+\right.\right.$$
$$\left.\left.+\frac{3}{2\beta}\right)\right\}\times\left(1-\exp\left(-t\right)\right)^{-3/2}\exp\left(-\frac{\left(1+e^{-2t}\right)}{\left(1-e^{-2t}\right)}\times\frac{r^2}{2a_n^2}\right), \tag{32}$$

where C is the normalization factor, determined by an expression of the next form:

$$C=\left\{\frac{2\sqrt{\pi}}{\left[\eta_h^2\left(T\right)\right]^2}\frac{\Gamma\left(1+\frac{\eta_h^2(T)}{2}\right)\cdot a_n^3}{\Gamma\left(\frac{\eta_h^2(T)-1}{2}\right)}\left[\frac{\eta_h^2\left(T\right)}{2}\left(\Psi\left(\frac{\eta_h^2\left(T\right)}{2}+1\right)-\Psi\left(\frac{\eta_h^2\left(T\right)}{2}-\frac{1}{2}\right)-1\right)\right]\right\}^{-\frac{1}{2}}. \tag{33}$$

Here, $\eta_{\lambda h}^2\left(T\right)$ is determined by the dispersion equation (28).

The matrix element of the radiative transition of an excited electron to the level of A^+-center in the dipole approximation has the form:

$$M=i\lambda_0\sqrt{\frac{2\pi\alpha^*I_0}{\omega}}\left(E_{n,l,m}-E_h\right)\left\langle\Psi_h\left(r\right)\left|\left(\vec{e}_\lambda,\vec{r}\right)\right|\Psi_{n,l,m}\left(\rho,\theta,\varphi\right)\right\rangle. \tag{34}$$

Taking into account (2), (28) and (32), the matrix element of the radiative recombination transition of an electron from the ground state of the size-quantized band to the level of A^+-center in the QD can be represented as:

$$M=\frac{a_h^{-1}2^{-\frac{3}{2}}\pi^{-\frac{5}{4}}\sqrt{3}\beta^{\frac{1}{2}}}{\sqrt{2\pi}R_0^{*4}J_{\frac{3}{2}}\left(\tilde{X}_{n,1}\right)}\left[\frac{\Gamma\left(1+\frac{\eta_h^2(T)}{2}\right)}{\left[\eta_h^2\left(T\right)\right]^2\Gamma\left(\frac{\eta_h^2(T)-1}{2}\right)}\times\right.$$
$$\left.\times\left[\frac{\eta_h^2\left(T\right)}{2}\left(\Psi\left(\frac{\eta_h^2\left(T\right)}{2}+1\right)-\Psi\left(\frac{\eta_h^2\left(T\right)}{2}-\frac{1}{2}\right)-1\right)\right]\right]^{-\frac{1}{2}}\int\limits_0^{+\infty}\int\limits_0^{\pi}\int\limits_0^{2\pi}r^{*2}dr^*\cos\theta\sin\theta d\theta d\varphi\times$$
$$\times\int\limits_0^\infty dt\exp\left[-t\left(-\eta_h^2\beta-\beta\beta_h^*-\frac{x_0^{*2}\beta}{a_n^{*4}}+i4\beta\Gamma_0^*+\frac{kT\beta}{E_h}\ln\left[4\sinh\left(\frac{\Omega_n}{v_{LA}\sqrt{kT}}\right)\sinh\left(\frac{2\Omega_n}{v_{TA}\sqrt{kT}}\right)\right]+\frac{3}{2}\right)\right]\times,$$
$$\times\left(1-\exp\left(-t\right)\right)^{-\frac{3}{2}}\exp\left(-\frac{\left(1+e^{-2t}\right)}{\left(1-e^{-2t}\right)}\times\frac{r^{*2}}{2}\right)Y_{l,m}\left(\theta,\varphi\right)\frac{J_{l+\frac{3}{2}}\left(\frac{\tilde{X}_{n,l}}{R_0^*}r^*\right)}{\sqrt{r^*}J_{l+\frac{3}{2}}\left(\tilde{X}_{n,l}\right)}, \tag{35}$$

where $R_0^*=R_0/a_h$.

Calculation of (35) leads to integrals giving selection rules for quantum numbers m and l:

$$\int\limits_0^{2\pi}\exp\left(im\varphi\right)d\varphi=\begin{cases}2\pi, & \text{if } m=0,\\ 0, & \text{if } m\neq 0,\end{cases} \tag{36}$$

$$\int\limits_0^{\pi}P_l\left(\cos\theta\right)\cos\theta\sin\theta d\theta=\begin{cases}\dfrac{2}{3}, & \text{if } l=1,\\ 0, & \text{if } l\neq 1.\end{cases} \tag{37}$$

Thus, the radiative transition of an electron to the level of the A^+-center is possible only from states with the values of quantum numbers $l=0$ and $m=0$.

The remaining integral over the radial coordinate r^* has the form:

$$\int\limits_0^\infty dr^* r^{*3/2} J_{l+\frac{3}{2}}\left(\frac{\tilde{X}_{n,l} r^*}{R_0^*}\right) \exp\left(-\frac{\left(1+e^{-2t}\right)}{2\left(1-e^{-2t}\right)} r^{*2}\right) = \\ \sqrt{\frac{\tilde{X}_{n,l}}{R_0^*}} \exp\left(-\frac{1}{2}\left(\frac{1-e^{-2t}}{1+e^{-2t}}\right)\left(\frac{\tilde{X}_{n,l}}{R_0^*}\right)^2\right)\left(\frac{1-e^{-2t}}{1+e^{-2t}}\right)^{3/2}. \quad (38)$$

Taking into account (36), (37), and (38), for the square of the matrix element (35), we have:

$$|M|^2 = \frac{2^{-2}\pi^{-5/2}\beta_h \tilde{X}_{n,1}}{a_h^2 R_0^{*9} \left|J_{\frac{3}{2}}\left(\tilde{X}_{n,1}\right) J_{\frac{5}{2}}\left(\tilde{X}_{n,1}\right)\right|^2} \left|\frac{\Gamma\left(1+\frac{\eta_h^2}{2}\right)}{\left[\eta_h^2\right]^2 \Gamma\left(\frac{\eta_h^2-1}{2}\right)} \left[\frac{\eta_h^2}{2}\left(\Psi\left(\frac{\eta_h^2}{2}+1\right) - \Psi\left(\frac{\eta_h^2}{2}-\frac{1}{2}\right) - 1\right)\right]\right|^{-1} \times \\ \times \left|\int\limits_0^\infty dt \exp\left[-t\left(-\eta_h^2\beta - \beta\beta_h^* - \frac{x_0^{*2}\beta}{a_n^{*4}} + i4\beta\Gamma_0^* + \frac{kT\beta}{E_h} \ln\left[4\sinh\left(\frac{\Omega}{v_{LA}\sqrt{kT}}\right)\sinh\left(\frac{2\Omega}{v_{TA}\sqrt{kT}}\right)\right] + \frac{3}{2}\right)\right] \times \right. \\ \left. \times \left(1-\exp\left(-t\right)\right)^{-3/2} \exp\left(-\frac{1}{2}\left(\frac{1-e^{-2t}}{1+e^{-2t}}\right)\left(\frac{\tilde{X}_{n,1}}{R_0^*}\right)^2\right)\left(\frac{1-e^{-2t}}{1+e^{-2t}}\right)^{3/2}\right|^2. \quad (39)$$

Taking into account (31) and (39) for the spectral intensity of recombination radiation (SIRR) in QD (30), we can write:

$$\Phi\left(X,T\right) = \Phi_0 \times \frac{a_h^4 \beta_h \tilde{X}_{n,1} X^2}{R_0^{*12}\left|J_{\frac{3}{2}}\left(\tilde{X}_{n,1}\right) J_{\frac{5}{2}}\left(\tilde{X}_{n,1}\right)\right|^2} \times \int\limits_0^{3/2} du P\left(u\right) \times \\ \times \left|\frac{\Gamma\left(1+\frac{\eta_h^2}{2}\right)}{\left(\eta_h^2\right)^2 \Gamma\left(\frac{\eta_h^2-1}{2}\right)} \left[\frac{\eta_h^2}{2}\left(\Psi\left(\frac{\eta_h^2}{2}+1\right) - \Psi\left(\frac{\eta_h^2}{2}-\frac{1}{2}\right) - 1\right)\right]\right|^{-1} \times \\ \times \left|\int\limits_0^\infty dt \exp\left[-t\left(-\eta_h^2\beta - \beta\beta_h^* - \frac{x_0^{*2}\beta}{a_n^{*4}} + i4\beta\Gamma_0^* + \frac{kT\beta}{E_h} \ln\left[4\sinh\left(\frac{\Omega}{v_{LA}\sqrt{kT}}\right)\sinh\left(\frac{2\Omega}{v_{TA}\sqrt{kT}}\right)\right] + \frac{3}{2}\right)\right] \times \right. \\ \left. \times \left(1-\exp\left(-t\right)\right)^{-3/2} \exp\left(-\frac{1}{2}\left(\frac{1-e^{-2t}}{1+e^{-2t}}\right)\left(\frac{\tilde{X}_{n,1}}{R_0^*}\right)^2\right)\left(\frac{1-e^{-2t}}{1+e^{-2t}}\right)^{3/2}\right|^2 \times \\ \times \frac{\Gamma_0^*}{\Gamma_0^{*2} + \left(\frac{X_{n,1}^2}{R_0^{*2}} + \frac{kT}{E_h}\ln\left[4\sinh\left(\frac{\Omega}{v_{LA}\sqrt{kT}}\right)\sinh\left(\frac{2\Omega}{v_{TA}\sqrt{kT}}\right)\right] - \eta_{\lambda h}^2 - X\right)^2}, \quad (40)$$

where $X = \hbar\omega/E_h$; $\Phi_0 = \sqrt{\varepsilon} e^2 \left|P_{eh} e_0\right| / 4\pi^{\frac{5}{2}} \hbar^3 c^3 m_0$.

Figure 2 shows the SIRR dependence on the magnitude of the external electric field E_0. It can be seen that the decrease in the SIRR value with increasing of E_0 is accompanied by “dips”, that appear at certain values of the external electric field strength and temperature. In [5], it is shown that variation of the strength of the external electric field can lead to transformation of the shape of the double-well oscillatory potential, which simulates the system “QD – surrounding matrix”, while the transition to the symmetric shape of the double-well oscillatory potential is accompanied by the appearance of a peak in the field dependence of tunneling probability. Thus, the nature of the dip appears to be related to the effect of resonant tunneling, when the double-well oscillator potential becomes symmetric. An increase in the SIRR value with the temperature increasing (Fig. 2) is associated with an increase in the overlap integral of the wave functions of the initial and final states due to temperature smearing of energy levels. It should be noted that the presence of dissipative tunneling makes the optics of quantum dots very sensitive to the parameters of the surrounding matrix, which determine, respectively, the frequency of the phonon mode ϵ_L and the constant of interaction with the contact medium (with the heat-bath) ϵ_C. With an increase in the value of ϵ_L, the wave function of the A^+-state “spreads” due to the hole-phonon interaction, which is accompanied by a decrease in the SIRR value. An increase in the parameter ϵ_C leads to an increase in the “viscosity” of the surrounding matrix, i.e. to a decrease

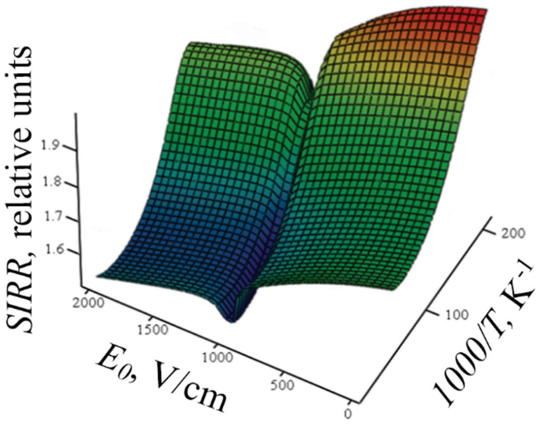

FIG. 2. The SIRR dependence on the inverse temperature $1000/T$ and the external electric field strength E_0 at $R_0^* = 1$; $U_0^* = 350$; $\eta_i = 3$.

in the probability of dissipative tunneling. As a result, the binding energy of the A^+-state increases, and the overlap integral of the wave functions of the initial and final states decreases, which leads to a decrease in the SIRR value.

4. Conclusion

The possibility of the existence of a luminescence temperature quenching channel in semiconductor quasi-zero-dimensional structures with "$A^+ + e$" impurity complexes associated with dissipative tunneling of a hole into the matrix, surrounding the QD, has been theoretically substantiated. It is shown that this channel "triggers" efficiently at the temperature and strength of the external electric field, for which the double-well oscillatory potential, simulating the "quantum dot – surrounding matrix" system, becomes symmetric (resonant tunneling effect).

Acknowledgements

The present study was supported by the Ministry of Education and Science of the Russian Federation (Project No. 0748-2020-0012).

References

[1] Shamirzaev T.S., Klochikhin A.A, et. al. Photoluminescence of germanium quantum dots grown in silicon on a SiO_2 monolayer. *Physics of the Solid State*, 2005, **47** (1), P. 82–85.

[2] Reznitsky A.N., Seksenbaev K.S, Permogorov S.A. Temperature dependence of the photoluminescence intensity of self-organized CdTe quantum dots in a ZnTe matrix under different excitation conditions. *Physics of the Solid State*, 2012, **54** (1), P. 123–133.

[3] Krevchik V.D., Levashov A.V. Energy spectrum of the complex $A^+ + e$ in a quantum dot in the adiabatic approximation. *Physics of the Solid State*, 2006, **48** (3), P. 589–592.

[4] Kusmartsev F.V., Krevchik V.D, et al. Phonon assisted resonant tunnelling and its phonons control. *JETP Letters*, 2016, **104**, P. 392–397.

[5] Leggett A.J., Krevchik V.D, et al. *Controllable dissipative tunneling. Tunnel transport in low-dimensional systems*. Fizmatlit, Moscow, 2011–2012. 496 p.

[6] Vainshtein I.A., Zatsepin A.F, Kortov V.S. Applicability of the empirical Varshni relation for the temperature dependence of the width of the band gap. *Physics of the Solid State*, 1999, **41** (6), P. 905–908.

[7] Ridley B. *Quantum processes in semiconductors*. Mir, Moscow, 1986.

[8] Zhou Hai-Yang, Gu Shi-Wei, Shi Yao-Ming. Electronic and shallow impurity states in semiconductor heterostructures under an applied electric field *Commun. Theor. Phys.*, 2005, **44**, P. 375–380.

[9] Lifshits I.M., Slezov V.V. On the kinetics of diffusion decomposition of supersaturated solid solutions. *JETP: Journal of Experimental and Theoretical Physics (ZhETF)*, 1958, **35** (2), P. 479–492.

NANOSYSTEMS: PHYSICS, CHEMISTRY, MATHEMATICS, 2021, 12 (6), P. 690–696

Polarization phenomena in coherent excitation of atomic systems: an overview of results

N. V. Sytenko

Mozhaisky Military Space Academy 13, Zhdanovskaya, St. Petersburg, 197198, Russia

vka@mil.ru

DOI 10.17586/2220-8054-2021-12-6-690-696

The article gives an overview of the main theoretical and experimental studies of the phenomena caused by the formation of coherent states – coherent population trapping, electromagnetically induced transparency, and laser generation without inversion.

Keywords: Λ-scheme, Liouville von Neumann equation, dark state, Hanle effect, Rabi frequency.

Received: 10 October 2021

Revised: 27 November 2021

1. Introduction

Many phenomena are known to be conditioned by the formation of coherent states. They include laser generation itself and the phenomena resulting from laser generation – coherent population trapping and electromagnetically induced transparency.

The phenomenon of coherent population trapping (CPT) was discovered in the 1980s and, therefore, it has been studied comprehensively. However, the studies on CPT gave impetus for research into the phenomena associated with coherent trapping, which led to the discovery of new phenomena as well as to the search for practical applications of CPT, such as frequency stabilization and ultrahigh resolution spectroscopy, lasers without inversion, obtaining “slow” light, and ultra-deep cooling of atoms, the phenomenon that may lead to the creation of electronic memory. In addition, it was proposed to use CPT as a basis for spatial superlocalization of atoms for dimensions that are much smaller than the light wavelength in caustics of inhomogeneously polarized wave fronts; also, a method for diagnosing the magnetic field in plasma was developed, etc. Since the research began, coherent population trapping has been showing itself in an increasing number of experimental situations. The “side effects” of this phenomenon lead to unexpected and surprising consequences, some of which are not fully understood.

2. Coherent population trapping

In the late 1990s, interest in the behavior of three-level systems in the fields of two electromagnetic waves increased. The research showed that three-level systems (in the general case, multilevel systems) cannot always be excited to the upper state. This phenomenon was first described in [1], [2]; the authors experimentally detected the disappearance of absorption in an ensemble of sodium atoms was when it was irradiated by a laser field. Subsequently, this phenomenon was called “coherent population trapping”. Further studies, the results of which are partially given in [3], showed that during excitation according to the Λ-scheme (see Fig. 1), special states are generated in the system that do not interact with the external electromagnetic field; these states arise at certain ratios between frequency detuning in each wave used for excitation.

In [4], a three-level system comprising two lower levels of the superfine structure of the ^{87}Rb atom ground state $5^2S_{1/2}$ and a lower level of the superfine structure of $5^2P_{1/2}$ state of that atom is considered. The authors compare the theoretical and experimental time dependences of absorption arising from a sudden change in the sign of the frequency detuning. The theoretically obtained dependence is accompanied by oscillations whose frequency increases with time, which agrees with the experimental results.

Consideration of the CPT phenomenon, not related to the solution of systems of differential equations, but based only on the symmetry properties, is presented in [5], where a system of three levels a, b and c, and level b is populated from levels $a$and c by the Λ-scheme. This paper shows that if the wave function of a system is expanded by eigenfunctions of states $|a\rangle$, $|b\rangle$ and $|c\rangle$, then, based on the symmetry properties of the differential equations for products of the form $c_i\dfrac{d}{dt}c_i$, $i = a, b, c$, where c_a, c_b and c_c are expansion coefficients, we can obtain a relation resembling the hyperboloid equation with complex coefficients determined by dipole moments. Further, using normalization of expansion coefficients, the relations linking the squares of the population modulus of states $|a\rangle$ and $|c\rangle$ through the functions describing the fields in the shoulders of the Λ-scheme and the population of state $|b\rangle$ are obtained in the paper. Finally,

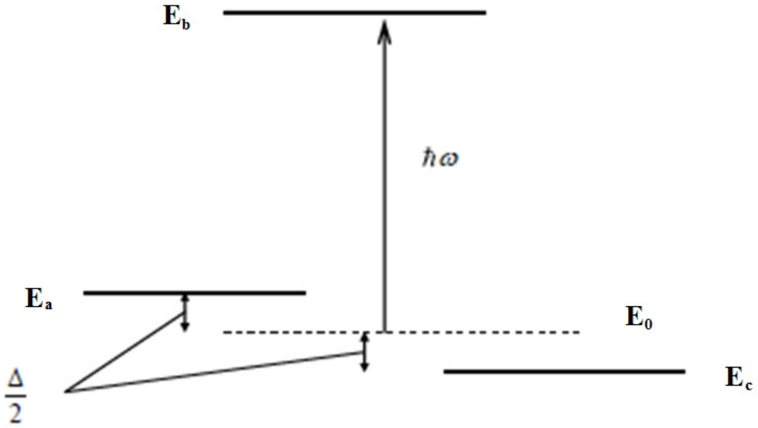

FIG. 1. Λ-scheme

assuming that the envelopes of these fields are described by Gaussian packets, the geometrical interpretation of the experimental results is performed.

It is essential that in experiments, the CPT phenomenon is often recorded in the form of the Hanle effect, which manifests itself in a sharp decrease in absorption depending on the magnitude of the magnetic field strength in the vicinity of the zero value of this field. Such a dip is often called "black resonance". The black resonance curves were observed in [6], [7], where transitions between the superfine levels of the sodium atom in a magnetic field were studied. In [7], using numerical integration of the Liouville von Neumann equation for closed and open systems, it was shown that in the general case, the width of the black resonance depends on the magnetic field $H$and the integration time (in the authors' terminology, "interaction time") t_{fin} or, in other words, $I = I\left(H, t_{fin}\right)$. Note that the width of resonance decreases with an increase in interaction time. The authors explain it by the population loss of the open system in the process of evolution. Thus, it follows from this work that an increase in the interaction time leads to dark resonance narrowing, and the main contribution to the intensity is made by the neighborhood of point $H = 0$, where the absence of absorption leads to the absence of the population loss. In a closed system, where the population remains, $I\left(H, t_{fin}\right)$ does not depend on time.

In [8], a method for diagnosing the magnetic field in plasma is proposed. It is based on the following idea: if the direction of the magnetic field coincides with the direction of the propagating electromagnetic wave ($\vec{H} \parallel \vec{k}$), the electric field will induce dipole moments in the direction perpendicular to the field, leading to transitions between magnetic sublevels with changes in the magnetic quantum number $\Delta m = \pm 1$ and transitions with frequency $2\omega_L$. If $\vec{H}$ and $\vec{k}$ directions do not coincide, then the system will have transitions with frequencies ω_L and $2\omega_L$. This circumstance allows us to judge about the magnetic field direction by the with respect to the radiation intensities at the frequencies ω_L and $2\omega_L$.

In [9], where, using the ^{87}Rb as an example, the influence of system parameters on the character of the three-level system transition to the CPT state is considered. It is shown that at high Rabi frequencies, the system's transition to the CPT state is accompanied by oscillations. In the opposite case of small Rabi frequencies, the system reaches this state smoothly, after a short transient process.

Because of superfine splitting, each of the two lower levels of the ^{87}Rb ($I = 3/2$)—^{2}S$_{1/2}$ and $^2P_{1/2}$—, splits into two levels characterized by the total moments $F_1 = 1$ and $F_2 = 2$. If we now place such a system in a magnetic field and excite it with light polarized along the left-hand circle of the upper level $F_{1e} = 2$ from the two lower levels $F_{2g} = 2$ and $F_{1g} = 1$, then a transition $M_{F_{1g}} = -2 \rightarrow M_{F_{2e}} = -1$ is formed, as well as a chain of three Λ- schemes:

$$\Lambda_1 : M_{F_{1g}} = 0 \rightarrow M_{F_{2e}} = -1; M_{F_{2g}} = 0 \rightarrow M_{F_{2e}} = 1;$$

$$\Lambda_2 : M_{F_{1g}} = 0 \rightarrow M_{F_{2e}} = 1; M_{F_{2g}} = 0 \rightarrow M_{F_{2e}} = 1;$$

$$\Lambda_3 : M_{F_{1g}} = 1 \rightarrow M_{F_{2e}} = 2; M_{F_{2g}} = 1 \rightarrow M_{F_{2e}} = 2.$$

If we now modulate the applied magnetic field according to the harmonic law $\cos\left(\frac{4\pi}{T}t + \phi\right)$, we will find Λ_2 system in the CPT state at point $t = \frac{T}{2}$. Due to the shift of magnetic sublevels in the magnetic field, Λ_1 and Λ_3 systems will reach the CPT state at a time somewhat later than Λ_2. The transition of Λ_2 to this state will be accompanied by oscillations, which, according to [9], are caused by a redistribution of the population in Λ_2 system. In the case of an increase in the detuning, systems Λ_1 and Λ_3 first go to the CPT state at certain but different times, and at very significant detuning, these two systems can be considered as one that goes to the CPT state near the point where the amplitude of the magnetic field modulation becomes zero.

Papers [10], [11], and [12] consider the effect of the field phases involved in the excitation process of multilevel systems closed in the excitation process, i.e., when the excitation process depends on the characteristics of only a pair of neighboring levels $\vec{E} = \sum\limits_i \vec{e}_i\varepsilon_i \cos(\omega_i t + \phi_i)$, where $\vec{e}_i$ is the polarization field vector with amplitude ε_i, frequency ω_i, and phase ϕ_i, which has the sense of the excitation frequency tuning. It is shown that if the condition $\omega_{1n} = \sum\limits_{i=1}^{n-1} \omega_{i,i+1}$ of system closure in the excitation process is fulfilled, the solution of the system of density matrix equations depends on some total phase $\Phi = \phi_{n,1} - \sum\limits_{i=1}^{n-1} \phi_{i+1,i}$. The results of theoretical studies are compared with those of the experiment in [4], where the absorption oscillations were observed with a sharp change in the detuning in the radio-frequency field arm. The experiment showed that the absorption signal oscillation frequency increased with an increase in the tuning, which agrees with the theoretical prediction.

In all of the above-mentioned publications, the width of the signal used for excitation was assumed to be much narrower than the width of the levels included in the excited system. In the opposite case, when considering the CPT problem, it should be assumed that the system in question interacts with a field the phases of which are random quantities. The presence of random phases leads to the fact that the system of equations for the density matrix contains random quantities and, therefore, is stochastic. Consequently, its solution does not give the quantities themselves, but only their values averaged over the phase distribution [13].

A theoretical study on the emission of $6s2^1S_0 \to 6s6p^1P_1$ transition in an ensemble of ^{137}Ba and ^{138}Ba atoms in the presence of a magnetic field used to separate the Zeeman sublevels is carried out in [14]. In this case, the system of $^1P_1$ state sublevels forms the upper state, while a similar set of $^1S_0$ state sublevels forms the lower state. All levels between the upper and lower states form a reservoir where the upper state decays radiatively. Both σ and π radiations were used for excitation. This paper also considers the shapes of the resonances resulting from the transitions from various Zeeman sublevels of the excited state to similar sublevels of the ground state.

Reference [15] considers the effect of a strong magnetic field on the polarization characteristics of the radiation of a multilevel system whose set of lower levels is populated from the ground state by axially symmetric excitation, while the upper levels are populated from the lower levels in a coherent manner. Specific calculations were made for $2p^3P_j - 3s^3S_1$ transition of the helium atom. Using the numerical solution of the Liouville von Neumann equation, it is shown that the system reaches the CPT state when the laser frequency becomes quite significant. At smaller values of detunings, a population-type ordering of angular momentums is induced on the excited state of the system, whereas an alignment-type ordering is absent. When the direction of excitation anisotropy makes a right angle with the magnetic field's direction, the system reaches the CPT state, i.e., the population and, consequently, the alignment of the system are zeroed out.

The description of the CPT phenomenon in complex polyatomic systems is, at least from the computational point of view, a rather complicated problem. When considering such problems, one has to resort to various approximations. For example, in [16], when considering a three-level system consisting of $6^2P_{1/2}$, $6^2P_{3/2}$ and $6^2S_{1/2}$ levels of Tl atom in the presence of a magnetic field, the wave function of the system was defined as an expansion in the eigenfunctions of these states. The resulting system of differential equations is solved in the resonance approximation, which reduces the problem to the solution of a system of differential equations with constant coefficients. As a result, the time dependence of the squares of the modulus of the expansion coefficients, the populations of the states in question, was obtained.

To conclude the discussion of the CPT phenomenon, it should be noted that in [17], where the problem of observing the CPT phenomenon in semiconductors was discussed theoretically using numerical integration of the Bloch equations, it was shown that despite the difficulties associated with the band structure and the strong multiparticle effects associated with excitons, signs of dark states can also be observed in these media.

3. Electromagnetically induced transparency

A phenomenon related to CPT is electromagnetically induced transparency (EIT), which was discovered in 1991 [18]. It consists in disappearance of absorption of a weak test field in one arm of the Λ-scheme, while a strong binding field acts in the other arm. Under the action of these two fields, the system becomes practically transparent with respect to the test field if the frequency difference of the fields acting in both shoulders coincides with the frequency difference of the transitions. From a computational point of view, the EIT problem is easier than the similar CPT problem, since in the latter case, the system's evolution can be found by numerical solution of the system of differential equations for the density matrix. In the EIT problem it is initially assumed that the binding field is much stronger than the test field, for which the Liouville von Neumann system of equations is to be solved based on perturbation theory.

A considerable number of works are devoted to the EIT phenomenon (see review [19]). In addition, Reference [20] experimentally and theoretically illustrates the disappearance of absorption in $5^2S_{1/2}\,(F=1) \leftrightarrow 5^2P_{1/2}\,(F=2)$ transition in an ensemble of ^{87}Rb atoms, while a strong binding field acts in $5^2S_{1/2}\,(F=2) \leftrightarrow 5^2P_{1/2}\,(F=1)$ shoulder. Reference [21] considers the EIT phenomenon in an optically dense medium, which is particularly interesting because both the absorption and dispersion properties of the medium can be controlled by the phase of the laser beam, which makes it possible to control the properties of the propagating radiation more efficiently than in a conventional experiment on EIT.

The system of three superfine levels of ^{87}Rb atom is considered in [22]. The test beam corresponded to the $5^2S_{1/2}\,(F=1) \leftrightarrow 5^2P_{1/2}\,(F=1)$ transition, and the binding one, to the $5^2S_{1/2}\,(F=2) \leftrightarrow 5^2P_{1/2}\,(F=1)$ transition. If we do not consider the influence of magnetic sublevels, the system under consideration is a classical Λ-scheme. In the case when this system is in the CPT state, it can be argued that, eventually, only $5^2S_{1/2}\,(F=1)$ level will be populated, since the Rabi frequency in the arm containing the binding beam is larger than the one in the arm containing the trial beam. The paper shows that the consideration of Zeeman sublevels has a strong influence on the behavior of the system, which is manifested by the fact that the set of Zeeman sublevels $5^2P_{1/2}\,(F=1)$ and $5^2S_{1/2}\,(F=2)$ forms a system in the CPT state, and all the population accumulates mainly at the $5^2S_{1/2}\,(F=2)$ level. Moreover, the CPT state is achieved at relatively weak binding fields and it weakly depends on detuning.

Along with the EIT phenomenon, which consists in enlightening the medium due to coherence, there is an opposite, in some sense, phenomenon – electromagnetically induced absorption (EIA) [23], [24], [25]. A prerequisite condition for the EIA is a strong difference in the excitation intensities of the test and binding beams. In [25] it is shown that the necessary conditions under which the EIA emerges are the following:

1. the quantum numbers of the upper and lower states e and g—respectively F_e and F_g—differ by one;
2. $g \to e$ transition is closed;
3. the ground state is degenerate, i.e., $F_g > 0$.

In [24] and [25], the EIA phenomenon is described in detail. In [24], the $5^2S_{1/2}\,(F=3) \to 5^2P_{1/2}\,(F=4)$ transition of ^{87}Rb atom is studied both experimentally and theoretically. In [25], the results of the experiment on the observation of resonance from the $5^2S_{1/2}\,(F=3) \to 5^2P_{3/2}$ transition are analyzed.

In [26], for a mixture of ^{87}Rb atoms and a buffer gas, neon, in particular, the effect of a test beam, polarized linearly and corresponding to the $F_0 = 2 \to F = 1$ transition, on the EIT signal was studied. The Hanle effect, which implies the presence of a sharp maximum in the bandwidth at zero magnetic field, was used to record the system's enlightening by the test beam. The observations showed that the EIT signal has the form of a Lorentz curve if the laser beam has the form of a broad Gaussian curve or has a low intensity. A similar situation is observed if the laser beam is U-shaped with the same width as the aforementioned Gaussian curve. For a narrow Gaussian beam or a beam of high intensity, the EIT signal has a non-Lorentzian shape.

In [27], the EIP phenomenon was considered experimentally and theoretically on a mixture of ^{87}Rb and ^{85}Rb isotopes. The theoretical consideration was based on a system of six superfine levels: two superfine structure levels of the ground $^2S_{1/2}$ state and four superfine structure levels of the first excited state $^2P_{3/2}$. The test and binding fields in this work are directed toward each other and have opposite linear polarizations. As a result of the experiment, the absorption dependences of the test field on the binding field detuning were obtained. The experimental results are compared with the data of numerical calculations made in the framework of the Liouville von Neumann solution. In so doing, nonuniformity of the populating levels of the superfine structure caused by the Doppler effect is taken into account. The paper also considers the possibility of describing the system within the framework of the traditional three-level excited by the Λ-scheme. It is shown that the resulting half-width of the EIT resonance strongly depends on the velocities and, after averaging over the velocities, can be used for the qualitative characteristics of the system under consideration.

An interesting way of creating coherent states is described in [28], which considers a system formed by three levels of the Pb atom: $6p7p\,[1/2,3/2]_1$ (level c), $6s7s\,[1/2,1/2]_1$ (level b), $6p^2\,[1/2,1/2]_0$ (level a). A strong field binds b and c levels, whereas the frequency of the test field is somewhat less than the transition frequency between b and a levels. The binding field forms a coherent state from $|b\rangle$ and $|c\rangle$ states. The experimental conditions are such that the considered levels are collisionally broadened, and the collisions broaden b and a levels to a greater extent. The interaction energy of atoms of the same element in the same states (resonance collisions) is inversely proportional to the third degree of inter-nuclear distance, whereas the similar value for collisions of the same atoms in different states is inversely proportional to the sixth degree of internuclear distance. Therefore, the Lorentzian lineshape corresponding to the $a \leftrightarrow b$ transition will widen and overlap with a similar lineshape corresponding to the $c \leftrightarrow b$ transition .

To conclude the overview of the works devoted to the EIT phenomenon, it is worth noting that in solids, where states are strongly broadened, the creation of coherent states may involve serious difficulties. These difficulties were partially overcome in [29], where absorption disappeared in a ruby crystal under the action of an external field.

4. Laser generation without inversion

Another phenomenon associated with induced coherence is laser generation without inversion. The assumptions about the feasibility of obtaining this phenomenon were first made in [30] and [31]. In [30], the authors point to a possibility of amplifying an ultrashort pulse in the Λ-scheme due to low-frequency coherence. In [31], the problem of the evolution of the system in question was solved in the framework of the Schrödinger equation, i.e., the wave function of the system was expanded by the system of wave functions of the states under consideration with coefficients a_1, a_2, a_3. The absorption coefficient $W_{ab} \sim -\dfrac{d}{dt}\left|a_1\right|^2$ was calculated under the initial condition of $a_1 = 1$. Similarly, the transmission coefficient was calculated under the initial condition of $a_2 = 1$.

The possibility of inversionless generation is considered in monograph [32]. Here, at arbitrary population of the levels of a three-level system at the initial moment of time, the Liouville von Neumann equation for the density matrix is solved in approximation linear on Rabi frequencies. It follows that one can choose the parameters of the problem so that the absorption will become zero.

The fundamental role of low-frequency coherence in laser generation without inversion was demonstrated in [33], where an ensemble of Sm atoms is considered. Its lower state has a total momentum $j = 1$, and the upper state has a total momentum $j = 0$. Due to Zeeman splitting, the superimposed magnetic field forms a four-level system. A sequence of picosecond pulses polarized in the right and left circles was used to induce low-frequency coherence at the Zeeman sublevels of the lower state according to the scheme $j = 1$; $m = -1 \leftrightarrow j = 0$; $m = 0 \leftrightarrow j = 1$; $m = 1$. After passing through the sequence of pulses, at a moment in time consistent with the sign and magnitude of the induced low-frequency coherence, a linearly polarized short pulse (π-pulse) is fed to provide the population of the upper state according to the scheme $j = 1$; $m = 0 \leftrightarrow j = 0$; $m = 0$. However, the population of the upper state was always less than the population of the lower state. The authors observed an abrupt increase in the signal if the π-pulse was formed at a time when the low-frequency coherence was maximal (the latter oscillated with the doubled Larmor frequency), and no signal enhancement was observed if the π-pulse was formed when this coherence was absent.

The feasibility of laser generation without inversion is discussed in many works (for example, [34], [35], [36]). However, Zibrov and others were the first to observe this phenomenon experimentally. In their work [37], the authors consider set of four levels of the ^{87}Rb atom superfine structure: two levels of the superfine structure of the ground state $^2S_{1/2}$ with $F = 1$ (level b) and $F = 1$ (level b'), the first excited state $^2P_{1/2}$ with $F = 2$ (level a), and one of the levels of the superfine structure of $^2P_{3/2}$ state with $F = 2$ (level c). Levels c and b are bound by a strong binding field with the Rabi frequency Ω_c, whereas levels a and b are bound by a weak test field. Since the set of a, b,c levels form a V-scheme, the joint action of the test and binding fields results in the highest population at b' level. If we introduce another field (pumping field) linking the levels b' and a, then the population balance will change due to the radiative decay of a level into b and b' levels.

When solving the system of equations for the density matrix in accordance with perturbation theory, being limited to the zero order by the test field, the relation for the absorption coefficient in $a - b$ shoulder is obtained:

$$\chi \sim -\frac{\left(\rho_{aa}^{(0)} - \rho_{bb}^{(0)}\right) + \dfrac{\left|\Omega_c\right|^2}{\gamma_{ac}\gamma_{bc}}\left(\rho_{bb}^{(0)} - \rho_{cc}^{(0)}\right)}{\gamma_{ac} + \dfrac{\left|\Omega_c\right|^2}{\gamma_{ac}}}.$$

The formula shows that negative absorption requires either a population inversion—$\rho_{aa}^{(0)} > \rho_{bb}^{(0)}$— or, in the case of large Rabi frequencies, $\rho_{bb}^{(0)} > \rho_{cc}^{(0)}$, which can be achieved for good ratios between the radiative decay efficiencies.

In that study, the authors confirmed both theoretically, using the numerical solution of the system of the Liouville von Neumann equations for the density matrix, and experimentally the presence of the test field frequency interval, at which the absorption coefficient becomes negative, that is, there is a generation.

Work [38] is similar to [37] with the difference that in the first one, the authors use the Λ- scheme formed by two levels of the superfine structure of the sodium atom in $^2S_{1/2}$ state with $F = 1$ and $F = 2$, as well as $^2P_{1/2}$ level of the first excited state of this atom to experimentally confirm generation without inversion. In this work, a strong binding field acts between $F = 2$ levels of $^2S_{1/2}$ state and $F = 1$ level of $^2P_{1/2}$ state. This field, together with a very weak test field binding the superfine structure levels of $^2S_{1/2}$ and $^2P_{1/2}$ states with $F = 1$, leads to the emergence of EIT resonance. The authors experimentally show that at a frequency close to the EIT frequency, the test signal in the system is amplified, which holds for a very short period of time at the same frequency as the test field. The system was placed in a ring resonator, wherein laser generation caused by vacuum fluctuations was observed.

In [39], the feasibility of laser generation without inversion at fine levels of the helium atom is considered. The approach to the generation problem in this work is fundamentally different from that proposed in [37], [38]. Within the framework of the built model, the possibility of generation is shown by reducing the broadening of the lower levels of the Λ-scheme. According to the Λ-scheme, excitation was carried out from the excited 2^3P_1 and 2^3P_2 helium atom states, which made it possible to avoid a significant broadening of the lower levels due to their interaction with the buffer gas. It is shown that although the frequency in one arm of the Λ-scheme is a hundred times greater than in the other, no less strong polarization field effect is obtained even at equal Rabi frequencies. In the paper it is noted that creation and maintenance of population at levels 2^3P_1 and 2^3P_2 in practice is most likely to involve certain difficulties.

In [40], an approach proposed to obtain laser generation without inversion does not require a quantum superposition of states in the active medium. The authors show that with periodically varying pumping, the generation is achievable even when the population inversion of the active medium is negative. This is possible due to the fact that the laser in the strong coupling mode is a nonhermetic system with an exceptional point existing at the negative value of the population inversion. It is shown that because of the nonorthogonality of the eigenstates near the exceptional point, a change in the pumping power over time can lead to laser parametric instability and excite autoscillations of the electromagnetic field. These oscillations take place even when the population inversion of the active medium is negative.

In standard lasers, light amplification requires a population inversion between the upper and lower states in order to break the reciprocity between absorption and stimulated emission. However, in a medium in a certain superposition state, quantum interference can completely suppress absorption, leaving the stimulated emission intact, which opens the possibility of radiation without inversion. Such a situation is considered in [41]. The authors show that radiation without inversion occurs naturally during the propagation of intense femtosecond laser pulses in air. It is caused by a combination of molecular ionization and molecular alignment, which are inevitable in intense light fields. This effect may allow for broadband radiation in many molecular gases without inversion, opening up unusual possibilities for remote sensing.

References

[1] Alzetta G., Moi L., Orriols G. Nonabsorbtion hyperfine resonance in sodium vapor irradiated by a Multimode dye-laser. *Novo. Chimento*, 1979, **52**(2), P. 209–217.

[2] Alzetta G., Gozzini A., Moi L., Orriols G. An experimental-method for the observation of Rf transitions and laser beat resonances in oriented Na vapor. *Novo. Chimento*, 1976, **36**, P. 5.

[3] Agapiev B.D., Gorny I.B., Matisov B.G., Rozhdestvensky Yu.V. Coherent population trapping in quantum systems. *UFN*, 1993, **183**(9), P. 1–36.

[4] Park Song Jong, Cho Hyuck, Kwon Taeg Yong, Lee Ho Seong. Transient coherence oscillation induced by a deturned Raman field in a rubidium Λ-system. *Phys. Rev. A*, 2004, **69**, P. 023806.

[5] Zhang G.P. Hidden identity in a generic Λ-system application to coherent population trapping. *J. Phys. B*, 2013, **46**, P. 035504.

[6] Renzoni F., Maichen W., Windholz L., Arimondo E. Coherent population trapping with losses observed on the Hanle effect of the D_1 sodium line. *Phys. Rev. A*, 1997, **55**, P. 3710–3718.

[7] Renzoni F., Arimondo E. Population-loss-ed narrowing of the dark resonance. *Phys. Rev. A*, 1998, **58**(6), P. 4717–4722.

[8] Akhmedzhanov R., SnplaceZlensky SnI., Kuznetsova E. Magnetic field diagnostics of plasma based on coherent population trapping: theory and experiment. *Phys. Rev. E*, 2004, **69**, P. 036409.

[9] Margalit L., Rosenbluh M., Wilson-Condon A.D. Coherence-population-trapping transients indused by the magnetic field. *Phys. Rev. A*, 2012, **52**, P. 063809.

[10] Kosachev D., Matisov B.G., Rozhdestvensky Yu.V. The coherent phenomena in multiplet systems with closed interaction contour. *J. Phys. B*, 1992, **25**, P. 2473–2488.

[11] Kosachev D., Matisov B.G., Rozhdestvensky Yu.V. Coherent population trepping: sensitivity of an atomic system to the relative phase of exciting fields. *Opt. Commun*, 1991, **85**, P. 209–212.

[12] Maichen W., Renzoni F., SnplaceMazets SnI., Korsunsky E., Windholz L. Transient coherent population trepping in a closed loop unteraction scheme. *Phys. Rev. A*, 1996, **53**(5), P. 3444–3453.

[13] Stenholm S. *Fundamentals of laser spectroscopy*. Nauka, CityplaceMoscow, 1986, 280 p.

[14] Kai-Shue-Lam. Coherent laser excitation of ^{137}Ba and ^{138}Ba. *Phys. Rev. A*, 1992, **45**(5), P. 3084–3092.

[15] Petrashen A.G., Sytenko N.V. Polarization phenomena during coherent excitation in the presence of a strong magnetic field. *Nanosystems: physics, chemistry, mathematics*, 2012, **3**(5), P. 62–69.

[16] Karagodova T.Ya. The influence of the orientation and strength of a magnetic field on the coherent population trapping in the Λ-system. *Optics and Spectroscopy*, 2002, **93**(2), P. 194–197.

[17] Lindberg M., Binder R. Dark states in coherent semiconductor spectroscopy. *Phys. Rev. Lett. A 45*, 1995, **75**(7), P. 1403–1406.

[18] Boller K-J., Imamoglu A., Harris S.E. Observation of electromagnetically induced transparency. *Phys. Rev. Lett.*, 1991, **66**(20), P. 2593–2596.

[19] Fleischhauer M. Electromagnetically induced transparency: Optics in coherent media. *Rev. Mod. Phys.*, 2005, **77**, P. 633–673.

[20] Yong-qing Li, Xiao Min Electromagnetically induced transparency in a three-level Λ-type system in rubidium atoms. *Phys. Rev. A*, 1995, **53**(4), P. 2703–2706.

[21] Korsunsky E.A., Leinfellner N., Hass A., Baluschev S., Windholz L. Phase-dependent electromagnetically induced transparency. *Phys. Rev. A*, 1999, **59**(3), P. 2303–2305.

[22] Hong Yuan Ling, Yong Oing Li, Min Xiao Coherent population trapping and electromagnetically induced transparency in multi-zeeman-sublevel atoms. *Phys. Rev. A*, 1996, **53**(2), P. 1014–1026.

[23] Valente D., Failache H., Lezmana A. Conparative study of the transient evolution of Hanle electromagnetically induced transparency and absorption resonance. *Phys. Rev. A*, 2002, **53**(2), P. 023814.

[24] Akulshin A.M., CityplaceBarreiro S., Lezama A. Electromagnetically induced absorption and transparency due to the resonant excitation of quasidegenerate levels of *Rb*vapor. *Phys. Rev. A*, 1998, **57**(4), P. 2996–3002.

[25] Lezama A., CityplaceBarreiro S., Akulshin A.M. Electromagnetically induced absorption. *Phys. Rev. A*, 1999, **59**(6), P. 4732-4735.

[26] Nicolic S.N., Radonjic M., Krmpot A.J., CityplaceLucic StateN.M., Zlatkovik B.V. Effects of laser beam profile on Zeeman electromagnetically induced transparency in the Rb buffer gas cell. *J. Phys. B: At. Mol. Opt. Phys.*, 2013, **46**, P. 075501.

[27] Bhattacharyya D., Ghosh A., Bandyopadhyay A., Saha S., De S. Observation of electromagnetically induced transparency in six-level Rb atoms and theoretical stimulation of the observed spectra. *J. Phys. B*, 2015, **48**, P. 175503.

[28] Field J.E., Hahn K.H., Harris S.E. Observation of electromagnetically induced transparency in collisionally broadened lead vapor. *Phys. Rev. Lett.*, 1991, **67**(22), P. 3062–3065.

[29] Yang Zhao, Cunckal Wu, Byoung-Seung Ham, Kim M.K., Microwave induced transparency in Ruby. *Phys. Rev. Lett.*, 1997, **79**(4), P. 641–644.

[30] Kocharovskaya O.A., Khanin Y.I. Coherent amplification of an ultrashort pulse in a three-level system without population inversion. *Letters to ZhETF*, 1988, **48**, P. 581–583.

[31] Harris S.E. Laser without inversion: interference of lifetime broaded resonances. *Phys. Rev. Lett.*, 1989, **62**(9), P. 1033–1036.

[32] Scully M.O., Zubairi M.S. *Quantum optics*. Fizmatlit, placeCityMoscow, 2003, 510 p.

[33] Nottelman A., Peters S., Lange W. Inversionless amplification of picosecond pulses due to Zeeman coherence. *Phys. Rev. Lett.*, 1993, **70**(12), P. 1783–1786.

[34] Imamoglu A., Harris S. Lasers without inversion: interference of dressed life-time broadened state. *Opt. Lett.*, 1989, **14**(24), P. 1033–1036.

[35] Agarwal G.S. Inhibition of spontaneous emission noise in lasers without inversion. *Phys. Rev. Lett.*, 1991, **67**(8), P. 980982.

[36] Gheri K.M., Walls D.F. Sub-Shot-Noise laser without inversion. *Phys. Rev. Lett.*, 1992, **68**(23), P. 3428–3431.

[37] Zibrov A.S., Lukin M.D., Niconov D.E., Holiberg L.,Scully M.O., Velichansky V.L., Robinson H.G. Experimental demonstration of laser oscillation without population inversion via quantum interference in *Rb. Phys. Rev. Lett.*, 1995, **75**(8), P. 1499–1501.

[38] Pandanabandu G.G., Welch G.R., Shubin I.N., Fry E.S., Nikonov D.E., Lukin M.D., Scully M.O. Laser oscillation without population inversion in sodium atomic beam. *Phys. Rev. Lett.*, 1996, **76**(12), P. 2053–2056.

[39] Petrashen A.G., Sytenko N.V. Laser generation without inversion on the fine levels of the helium atom. *Nanosystems: physics, chemistry, mathematics*, 2016, **7**(2), P. 384–393.

[40] Doronin I.V, Zyablovsky A.A., Andrianov E.S., Pukhov A.A., Vinogradov A.P. Lasing without inversion due to parametric instability of the laser near the exceptional point. *Phys. Rev. A*, 2019, **100**, P. 021801.

[41] Lytova M., Morales F., Haessler S., Smirnova O., Spanner M., Ivanov M. Rotational quantum beat lasing without inversion. Optica, Optical Society of placecountry-regionAmerica - OSA Publishing, 2020, **7**(6), P. 586–592.

NANOSYSTEMS: PHYSICS, CHEMISTRY, MATHEMATICS, 2021, 12 (6), P. 697–702

Discrimination and decoherence of Schrödinger cat states in lossy quantum channels

R. K. Goncharov[1,2], A. D. Kiselev[1,2], N. G. Veselkova[1], Ranim Ali[3], F. D. Kiselev[1,2]

[1]Quantum Information Laboratory, ITMO University, Kadetskaya Line, 3,
199034 Saint Petersburg, Russia

[2]Laboratory of Quantum Processes and Measurements, ITMO University, Kadetskaya Line, 3,
199034 Saint Petersburg, Russia

[3]Faculty of Photonics, ITMO University, Kronverksky Pr. 49, bldg. A,
197101 Saint Petersburg, Russia

rkgoncharov@itmo.ru

PACS 03.67.Bg, 03.67.Hk **DOI 10.17586/2220-8054-2021-12-6-697-702**

We investigate environment induced effects of decoherence in discrimination between the Schrödinger cat states transmitted through noisy quantum channels such as optical fibers. We calculate the fidelity and the statistics of photocounts for both even and odd coherent states. The method that uses the beam splitter-like transformation acting in the enlarged Hilbert space to model the quantum channel is compared with the approach based on the Lindblad dynamics of one-mode bosonic systems.

Keywords: Schrödinger cat states, decoherence, quantum state discrimination.

Received: 20 November 2021

Revised: 30 November 2021

1. Introduction

Quantum states known as the even (odd) Schrödinger cat states, $|\alpha_+\rangle$ ($|\alpha_-\rangle$), are represented by symmetric (antisymmetric) superpositions of the coherent states:

$$|\alpha_\pm\rangle = \frac{1}{\sqrt{M_\pm(\alpha)}}\big(|\alpha\rangle \pm |{-\alpha}\rangle\big), \tag{1}$$

where

$$M_\pm(\alpha) = 2(1 \pm \langle\alpha| - \alpha\rangle) = 2(1 \pm \exp(-2|\alpha|^2). \tag{2}$$

These states have a long history dating back to the original paper by Dodonov, Malkin and Man'ko [1]. and, apart from the fundamental interest, are shown to be technologically useful.

In metrology, even coherent states in combination with parity detection method are used to realize super-resolving angular rotation measurements [2]. Optical Schrödinger cat states can also serve as a basis for quantum computations [3], teleportation and cryptography [4–7]. These states have been produced experimentally using the optical Kerr effect in 1986 by Yurke and Stoler [8]. Among more recent experimental procedures suggested for generation of optical cat states are the method based on photon subtraction of an optical squeezed state [9–12] and the protocol that uses homodyne detection and photon number states [13] (see [14] for a review on generating cat states).

In this paper, our goal is to assess the fragility of the cat states propagating in noisy quantum channels. More specifically, we consider the statistics of photocounts underlying the method to discriminate between the parity of the cat states and examine its sensitivity to environment induced decoherence effects. We shall also calculate the fidelity of the states depending on the amplitude and the transmission of the fiber channel. In addition to the model of the quantum channel based on the beam splitter-like transformation acting in the enlarged Hilbert space, we employ Lindblad dynamics of an one-mode bosonic system to model a lossy optical fiber.

2. Results

Following [6,7,15], we begin with the simplest model of the noisy channel representing the fiber. In this model, the lossy mode is combined with the beam splitter of the transmission, τ, along with the input vacuum state in additional environmental (ancillary) mode E:

$$\begin{aligned} |\alpha_\pm\rangle \to |\Psi_\pm\rangle &= \hat{T}_{BS}(\tau)|\alpha_\pm\rangle \otimes |0\rangle_E \\ &= \frac{1}{\sqrt{M_\pm(\alpha)}}\Big\{|\sqrt{\tau}\alpha\rangle \otimes |\sqrt{1-\tau}\alpha\rangle_E \pm |-\sqrt{\tau}\alpha\rangle \otimes |-\sqrt{1-\tau}\alpha\rangle_E\Big\}, \end{aligned} \tag{3}$$

where $\hat{T}_{BS}(\tau)$ is the unitary describing the beam splitter with the transmittance τ. Clearly, $|\Psi_\pm\rangle$ is the entangled two-mode state generated by the beam splitter. Note that, according to Ref. [16], the phase modulator can be regarded as a multiport beam splitter that transforms a one-mode Schrödinger cat state into entangled multimode state.

The density operators can now be readily derived by tracing out the ancillary mode. The result:

$$\hat{\rho}_\pm = \mathrm{Tr}_E\, |\Psi_\pm\rangle\langle\Psi_\pm| = P_\pm|\gamma_\pm\rangle\langle\gamma_\pm| + Q_\pm|\gamma_\mp\rangle\langle\gamma_\mp|, \tag{4}$$

where $\gamma \equiv \sqrt{\tau}\alpha$, shows that the density matrices are mixtures of even and odd cat states with the coefficients given by:

$$\begin{aligned} P_+ &= \cosh((1-\tau)|\alpha|^2)\frac{\cosh(\tau|\alpha|^2)}{\cosh(|\alpha|^2)}, \quad Q_+ = 1 - P_+ = \sinh((1-\tau)|\alpha|^2)\frac{\sinh(\tau|\alpha|^2)}{\cosh(|\alpha|^2)}, \\ P_- &= \cosh((1-\tau)|\alpha|^2)\frac{\sinh(\tau|\alpha|^2)}{\sinh(|\alpha|^2)}, \quad Q_- = 1 - P_- = \sinh((1-\tau)|\alpha|^2)\frac{\cosh(\tau|\alpha|^2)}{\sinh(|\alpha|^2)}. \end{aligned} \tag{5}$$

Since $\langle\gamma_\mu|\gamma_\nu\rangle = \delta_{\mu\nu}$, the above coefficients P_ν and Q_ν are the eigenvalues of the density operator $\hat{\rho}_\nu$.

The effect of decoherence for even and odd cat states is characterized by the probabilities Q_+ and Q_-. It is not difficult to see that, $Q_\pm$ tends to 1/2 as $|\alpha|$ becomes infinitely large, and thus the operators $\hat{\rho}_+$ and $\hat{\rho}_-$ are both approaching the limit of the completely chaotic (equiprobable) mixture as $|\alpha|$ increases. For small $|\alpha|$ with $\alpha \approx 0$, $\hat{\rho}_+$ and $\hat{\rho}_-$ are close to the vacuum state $|0\rangle\langle 0|$ and the mixed state $(1-\tau)|0\rangle\langle 0| + \tau|1\rangle\langle 1|$, respectively.

Given the density operator (4), we can now evaluate the fidelity:

$$F_\pm = \langle\alpha_\pm|\hat{\rho}_\pm|\alpha_\pm\rangle \tag{6}$$

characterizing the difference between the mixed and pure states: $\hat{\rho}_\pm$ and $|\alpha_\pm\rangle\langle\alpha_\pm|$. For even and odd cat states, we have:

$$\begin{aligned} F_+ &= \frac{\cosh((1-\tau)|\alpha|^2)}{\cosh^2(|\alpha|^2)}\cosh^2(\sqrt{\tau}|\alpha|^2), \\ F_- &= \frac{\cosh((1-\tau)|\alpha|^2)}{\sinh^2(|\alpha|^2)}\sinh^2(\sqrt{\tau}|\alpha|^2). \end{aligned} \tag{7}$$

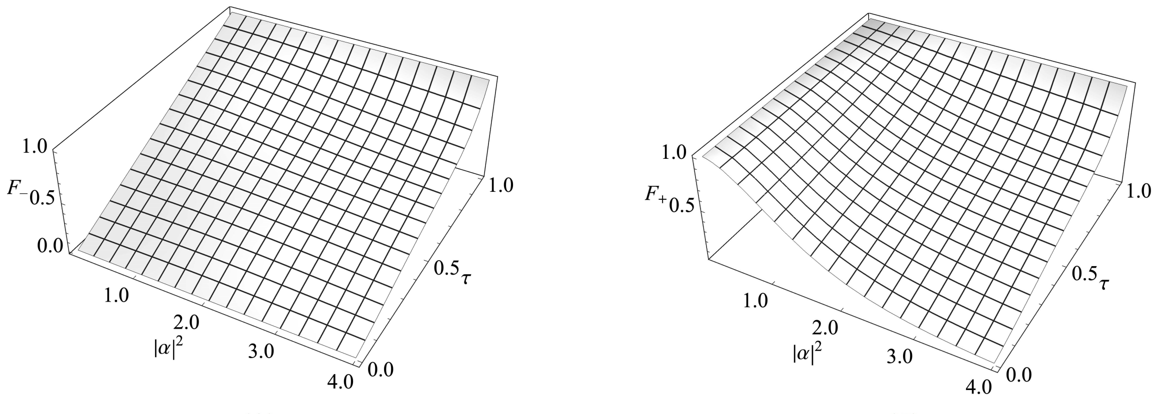

(A) **(B)**

FIG. 1. Fidelity as a function of the transmittance coefficient τ and the mean photon number $|\alpha|^2$ for (A) odd and (B) even cat states

Fig. 1 shows the fidelities F_- and F_+ as an function of the transmittance τ the mean photon number $|\alpha|^2$. It is seen that, in the zero amplitude limit where the symmetric cat state is close the vacuum state, the fidelity F_+ approaches unity. The corresponding value for the fidelity of the antisymmetric cats equals τ. At large $|\alpha|$, the fidelitites are exponentially decaying functions of the mean photon number: $F_\pm \approx \exp(-(1-\sqrt{\tau})^2|\alpha|^2)$.

Our next step is to study how decoherence that has a detrimental effect on the fidelity will affect the distinguishability of the cat states. For this purpose, we shall discuss performing photocounting measurements as the means to discriminate between the even and odd cat states based on the parity of the photon number registered by a photon-number resolving photodetector.

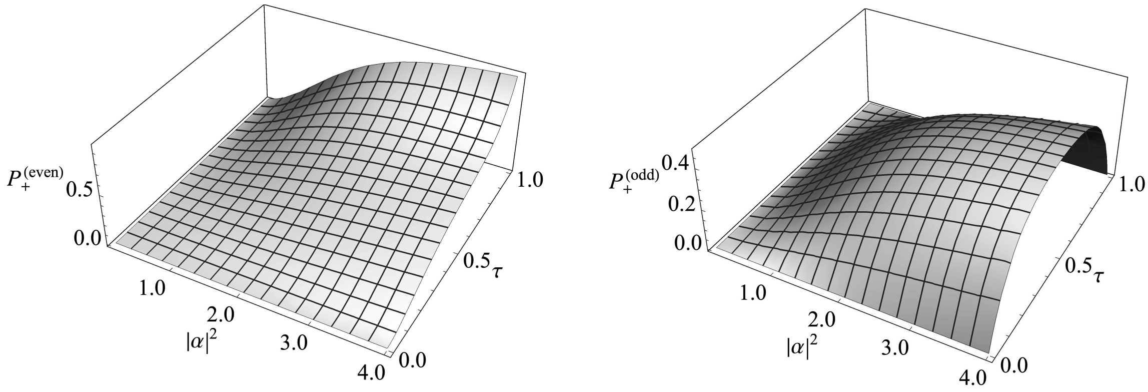

(A) **(B)**

FIG. 2. Probabilities to detect (A) even and (B) odd number of photocounts as a function of the transmittance coefficient τ and the mean photon number $|\alpha|^2$ for the symmetric (even) Schrödinger cat

In order to evaluate the statistics of photocounts for the quantum cat states, $\hat{\rho}_+$ and $\hat{\rho}_-$, we shall use the well-known Kelley-Kleiner formula [17] and deduce the following expression for the probability to detect k photons:

$$\Pr_\nu(k) = \frac{1}{k!}\operatorname{Tr}\bigl[:(\eta_\mathrm{d}\hat{a}^\dagger\hat{a})^k e^{-\eta_\mathrm{d}\hat{a}^\dagger\hat{a}}: \rho_\nu\bigr] = P_\nu C_\nu(k) + Q_\nu C_{-\nu}(k), \tag{8}$$

where

$$\begin{aligned} C_\nu(k) &\equiv \frac{1}{k!}\langle\gamma_\nu| :(\eta_\mathrm{d}\hat{a}^\dagger\hat{a})^k e^{-\eta_\mathrm{d}\hat{a}^\dagger\hat{a}}: |\gamma_\nu\rangle \\ &= \frac{(\eta_\mathrm{d}\tau|\alpha|^2)^k}{k!}\frac{\exp((1-\eta_\mathrm{d})\tau|\alpha|^2) + (-1)^k\nu\exp(-(1-\eta_\mathrm{d})\tau|\alpha|^2)}{\exp(\tau|\alpha|^2)+\nu\exp(-\tau|\alpha|^2)}, \end{aligned} \tag{9}$$

η_d is the efficiency of the photodetector.

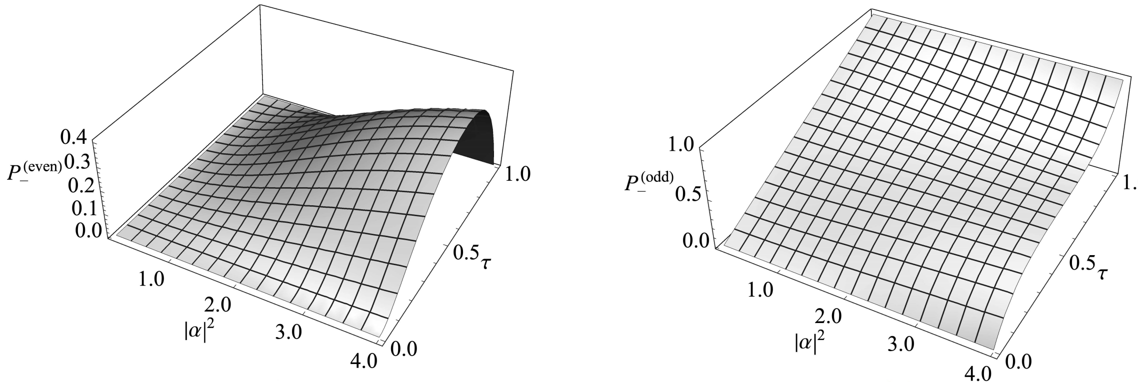

(A) **(B)**

FIG. 3. Probabilities to detect (A) even and (B) odd number of photocounts as a function of the transmittance coefficient τ and the mean photon number $|\alpha|^2$ for the antisymmetric (odd) Schrödinger cat

From Eq. (9) it can be readily seen that, in the case where the efficiency and the transmittance are both equal to unity, $\eta_{\mathrm{d}} = \tau = 1$, the probability of odd (even) number of clicks:

$$P_\nu^{(\mathrm{odd})} = \sum_{k=0}^{\infty} \mathrm{Pr}_\nu(2k+1), \quad P_\nu^{(\mathrm{even})} = \sum_{k=1}^{\infty} \mathrm{Pr}_\nu(2k) \tag{10}$$

vanishes for the even (odd) states, $P_+^{(\mathrm{odd})} = 0$ ($P_-^{(\mathrm{even})} = 0$), and thus the cat states are perfectly distinguishable. Note that, in contrast to the case of pure odd cat state, where the no-click probabilty is zero, $P_-(0) = 0$, for the pure even cat state, this probability decays with $|\alpha|^2$, $P_+(0) = 1 - P_+^{(\mathrm{even})} = 1/\cosh(|\alpha|^2)$, and represents the non-vanishing contribution of the vacuum state.

As is shown in Figs. 2 and 3, dependence of the decoherence induced probabilities $P_+^{(\mathrm{odd})}$ and $P_-^{(\mathrm{even})}$ on the channel transmittance reveal nonmonotonic behavior. From the above discussion, these probabilities equal zero in the limit of the lossless channel with $\tau = 1$. In the opposite case, with $\tau = 0$, the density operators are projectors on the vacuum state $|0\rangle$ and $P_\pm^{(\mathrm{odd})} = P_\pm^{(\mathrm{even})} = 0$. So, referring to Fig. 4, the no-click probabilities $P_+(0)$ and $P_-(0)$ are both equal to unity in the no-signal limit with $\tau = 0$.

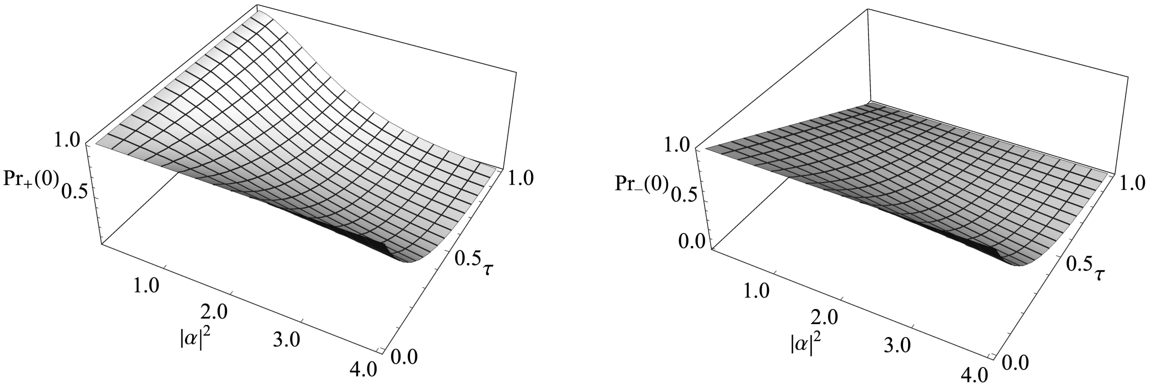

(A) **(B)**

FIG. 4. No-click probability as a function of the transmittance coefficient τ and the mean photon number $|\alpha|^2$ for (A) symmetric (even) and (B) antisymmetric (odd) Schrödinger cats

The results indicate that the statistics of photocounts for the odd cat state at small $|\alpha|^2$ are less sensitive to the decoherence effects as compared to the even states. Interestingly, there is the optimal value of $|\alpha|$ that gives the greatest possible difference $P_+^{(\mathrm{even})} - P_+^{(\mathrm{odd})}$, whereas $P_-^{(\mathrm{odd})} - P_-^{(\mathrm{even})}$ monotonically decreases with $|\alpha|$.

An alternative approach to modelling of the quantum channel representing a noisy fiber is based on the master equation method [16, 18, 19]. In our case we can start from the one-mode Markovian thermal bath version of the Lindblad equation for the density matrix given by:

$$\begin{aligned} &\frac{\partial \hat{\rho}}{\partial t} = \mathcal{L}\hat{\rho} = -i\Omega[\hat{n}, \hat{\rho}] + \kappa\big(\mathcal{D}_{\hat{a}\hat{a}^\dagger}\hat{\rho} + \mathrm{e}^{-z_T}\mathcal{D}_{\hat{a}^\dagger\hat{a}}\hat{\rho}\big), \\ &\hat{n} = \hat{a}^\dagger\hat{a}, \quad \mathcal{D}_{\hat{A}\hat{B}}\hat{\rho} \equiv 2\hat{A}\hat{\rho}\hat{B} - \hat{B}\hat{A}\hat{\rho} - \hat{\rho}\hat{B}\hat{A}, \end{aligned} \tag{11}$$

where the dagger denotes Hermitian conjugation, $\hat{\rho}$ is the density matrix representing the quantum state; $\hat{a}^\dagger$ ($\hat{a}$) is the creation (annihilation) operator; $[\hat{A}, \hat{B}] = \hat{A}\hat{B} - \hat{B}\hat{A}$ stands for the commutator; Ω (κ) is the element of the frequency (relaxation) constant, $z_T = \dfrac{\hbar\Omega_0}{k_B T}$ is the dimensionless inverse temperature parameter, where Ω_0 is the bare frequency, $\hbar$ is the reduced Planck constant, k_B is the Boltzmann constant and T is the temperature of the environment.

By using the method of characteristics, it can be shown that temporal evolution of the normally ordered characteristic function is described by the relation [20]:

$$\chi_N(\beta, t) = \mathrm{Tr}[\mathrm{e}^{\beta\hat{a}^\dagger}\mathrm{e}^{-\beta^*\hat{a}}\hat{\rho}(t)] = \mathrm{e}^{-\langle n\rangle|\beta|^2}\chi_{\mathrm{ini}}(\mathrm{e}^{(i\Omega-\Gamma)t}\beta), \quad \langle n\rangle = (1 - \mathrm{e}^{-2\Gamma t})n_T \tag{12}$$

where $\Gamma = (1 - \mathrm{e}^{-z_T})\kappa$ is the relaxation rate; $n_T = (\mathrm{e}^{z_T} - 1)^{-1}$ is the mean number of thermal photons; and $\chi_{\mathrm{ini}}(\beta)$ is determined by the initial condition $\hat{\rho}(0) = |\alpha_\nu\rangle\langle\alpha_\nu|$ as follows:

$$\begin{aligned} \chi_{\mathrm{ini}}(\beta) &= \chi_\nu(\beta) = \langle\alpha_\nu|\mathrm{e}^{\beta\hat{a}^\dagger}\mathrm{e}^{-\beta^*\hat{a}}|\alpha_\nu\rangle \\ &= \frac{\cosh(\beta\alpha^* - \beta^*\alpha) + \nu\mathrm{e}^{-2|\alpha|^2}\cosh(\beta\alpha^* + \beta^*\alpha)}{1 + \nu\mathrm{e}^{-2|\alpha|^2}}. \end{aligned} \tag{13}$$

An important point is that the probability of clicks (8) is expressed in terms of the moments $\langle : \hat{n}^m : \rangle$:

$$\mathrm{Pr}_\nu(k) = \sum_{m=0}^{\infty} \frac{(-1)^m \eta_{\mathrm{d}}^{m+k}}{k!m!} \langle : \hat{n}^{m+k} : \rangle. \tag{14}$$

In particular, for the cat states, generating function of the moments:

$$\begin{aligned} &\tilde{\chi}_\nu(|\beta|) = \frac{1}{2\pi}\int_0^{2\pi} \chi_\nu(|\beta|\mathrm{e}^{i\phi})\mathrm{d}\phi = \sum_{m=0}^{\infty} \frac{(-1)^m|\beta|^{2m}}{(m!)^2}\langle : \hat{n}^m : \rangle_\nu, \\ &\langle : \hat{n}^m : \rangle_\nu = \frac{1 + (-1)^m\nu\mathrm{e}^{-2|\alpha|^2}}{1 + \nu\mathrm{e}^{-2|\alpha|^2}}|\alpha|^{2m} \end{aligned} \tag{15}$$

is obtained by averaging $\chi_\nu(\beta)$ over the phase of β and leads to the expression for the probability of photocounts given by Eq. (9). Then the phase averaged characteristic function (12):

$$\tilde{\chi}_N(|\beta|, t) = \frac{1}{2\pi}\int_0^{2\pi} \chi_N(|\beta|\mathrm{e}^{i\phi}, t)\mathrm{d}\phi = \mathrm{e}^{-\langle n\rangle|\beta|^2}\tilde{\chi}_\nu(\sqrt{T}|\beta|) = \sum_{m=0}^{\infty} \frac{(-1)^m|\beta|^{2m}}{(m!)^2}\langle : \hat{n}^m : \rangle \tag{16}$$

gives the expression for the normally ordered moments of the photon number operator

$$\langle : \hat{n}^m : \rangle = \sum_{l=0}^{m}\Big[\frac{m!}{(m-l)!}\Big]^2 \frac{\langle n\rangle^l}{l!} T^{m-l}\langle : \hat{n}^{m-l} : \rangle_\nu, \tag{17}$$

where $T = \mathrm{e}^{-2\Gamma t}$ is the channel transmittance. Formula (17) can now be combined with Eq. (14) to compute the probability of photocounts (10). It is not difficult to see that, at $\eta_{\mathrm{d}} = 1$, the probabilities $P_+^{(\mathrm{odd})}$ and $P_-^{(\mathrm{even})}$ vanish in the zero-temperature limit with $n_T = 0$. Thus we arrive at the conclusion that within the framework of Lindblad dynamics distinguishability of the Schrödinger cat states is solely governed by the mean number of thermal photons $\langle n\rangle \propto n_T$ rather than the channel transmittance.

3. Conclusion and discussion

We have studied the fidelity and the statistics of photocounts for the even and odd Shrödinger cat states subjected to the effects of decoherence in the noisy quantum channel representing a lossy optical fiber. For the beam splitter model of the quantum channel characterized by the transmittance τ, the probabilities that determine the photocounting statistics are computed in realtion to τ and the mean photon number $|\alpha|^2$. By contrast to this model, exact results describing Lindblad dynamics of photon states show that the key parameter governing decoherence induced effects on photocounting is the mean number of thermal photons n_T.

In our analysis, the criterion used to discriminate between the even and odd states is based on the parity of photocounts registered by a photodetector. Since the vacuum state contribution to the even Schrödinger cat states is found to reduce their distinguishability, the odd coherent states present the most robust case.

In general, from our results, it might be concluded that, despite daunting nature of the task to utilize Schrödinger cat states for quantum communications, these states can be used in entanglement distribution (swapping) protocols at sufficiently short distances.

Acknowledgements

The work was done by Leading Research Center "National Center of Quantum Internet" of ITMO University during the implementation of the government support program, with the financial support of Ministry of Digital Development, Communications and Mass Media of the Russian Federation and RVC JSC; Grant Agreement ID: 0000000007119P190002, agreement No. 006-20 dated 27.03.2020. A.D.K. acknowledges financial support by the Ministry of Education and Science of the Russian Federation (Grant No. 2019-0903).

References

[1] Dodonov V.V., Malkin I.A., Man'ko V.I. Even and odd coherent states and excitations of a singular oscillator, *Physica*, 1974, **72**(3), P. 597–615.

[2] Hao L., Tang H., Wang Q. Resolution improvement of angular rotation measurement through even coherent states coupled with parity detection strategy. *Journal of Optics*, 2020, **22**(2), P. 025203.

[3] Lund A.P., Ralph T.C., Haselgrove H.L. Fault-tolerant linear optical quantum computing with small-amplitude coherent states. *Phys. Rev. Lett.*, 2008, **100**, P. 030503.

[4] Sangouard N., Simon C., Gisin N., Laurat J., Tualle-Brouri R., Grangier P. Quantum repeaters with entangled coherent states. *J. Opt. Soc. Am. B*, 2010, **27**(6), P. A137–A145.

[5] Brask J.B., Rigas I., Polzik E.S., Andersen U.L., Sørensen A.S. Hybrid long-distance entanglement distribution protocol. *Phys. Rev. Lett.*, 2010, **105**, P. 160501.

[6] Ghasemi M., Tavassoly M.K. Toward a quantum repeater protocol based on the coherent state approach. *Laser Physics*, 2019, **29**.

[7] Parker R.C., Joo J., Spiller T.P. Photonic hybrid state entanglement swapping using cat state superpositions. *Proceedings of the Royal Society A: Mathematical, Physical and Engineering Sciences*, 2020, **476**(2243), P. 20200237.

[8] Yurke B., Stoler D. Generating quantum mechanical superpositions of macroscopically distinguishable states via amplitude dispersion. *Phys. Rev. Lett.*, 1986, **57**, P. 13–16.

[9] Neergaard-Nielsen J.S., Nielsen B.M., Hettich C., Mølmer K., Polzik E.S., Generation of a superposition of odd photon number states for quantum information networks. *Phys. Rev. Lett.*, 2006, **97**, P. 083604.

[10] Ourjoumtsev A., Ferreyrol F., Tualle-Brouri R., Grangier P. Preparation of non-local superpositions of quasi-classical light states. *Nature Physics*, 2009, **5**, P. 189–192.

[11] Serikawa T., Yoshikawa J.-i., Takeda S., Yonezawa H., Ralph T.C., Huntington E.H., Furusawa A. Generation of a cat state in an optical sideband. *Phys. Rev. Lett.*, 2018, **121**, P. 143602.

[12] Takase K., Yoshikawa J.-i., Asavanant W., Endo M., Furusawa A. Generation of optical Schrödinger cat states by generalized photon subtraction. *Phys. Rev. A*, 2021, **103**, P. 013710.

[13] Ourjoumtsev A., Jeong H., Tualle-Brouri R., Grangier P. Generation of optical "Schrödinger cats" from photon number states. *Nature*, 2007, **448**, P. 784–786.

[14] Glancy S., de Vasconcelos H.M. Methods for producing optical coherent state superpositions. *J. Opt. Soc. Am. B*, 2008, **25**(5), P. 712–733.

[15] S.J. van Enk, Hirota O. Entangled coherent states: Teleportation and decoherence. *Phys. Rev. A*, 2001, **64**, P. 022313.

[16] Miroshnichenko G.P., Kiselev A.D., Trifanov A.I., Gleim A.V. Algebraic approach to electro-optic modulation of light: exactly solvable multimode quantum model. *J. Opt. Soc. Am. B*, 2017, **34**(6), P. 1177–1190.

[17] Kelley P.L., Kleiner W.H. Theory of electromagnetic field measurement and photoelectron counting. *Phys. Rev.*, 1964, **136**, P. A316–A334.

[18] Kozubov A., Gaidash A., Miroshnichenko G. Quantum model of decoherence in the polarization domain for the fiber channel. *Phys. Rev. A*, 2019, **99**, P. 053842.

[19] Gaidash A., Kozubov A., Miroshnichenko G. Dissipative dynamics of quantum states in the fiber channel. *Phys. Rev. A*, 2020, **102**, P. 023711.

[20] Kiselev A.D., Ali R., Rybin A.V. Lindblad dynamics and disentanglement in multi-mode bosonic systems. *Entropy*, 2021, **23**(11).

NANOSYSTEMS: PHYSICS, CHEMISTRY, MATHEMATICS, 2021, 12 (6), P. 703–710

Review on NiO thin film as hole transport layer in perovskite solar cell

Kamal Bhujel[1,2]*, Suman Rai[2], Ningthoujam Surajkumar Singh[1]

[1]Physical Sciences Research Center, Pachhunga University College, Aizawl, 796001, India
[2]Laser and Photonics Laboratory, Department of Physics, Mizoram University, Aizawl, 796004, India
*kamalaawaz@gmail.com

DOI 10.17586/2220-8054-2021-12-6-703-710

The saturation in increasing the power conversion efficiency (PCE) of silicon-based solar cells made researchers around world to look for the alternatives. An alternative solar cell would possess some basic requirements like cost effectiveness, reproducible, durable (stability), non-toxicity and higher efficiency. Perovskite solar cell (PSC) opened the new realm of hope for this alternative, consisting of perovskite absorber sandwich between the hole transport layer (HTL) and the electron transport layer (ETL). Good performance of PSCs can be achieved by optimizing many parameters of the components of PSC for obtaining the highest PCE. Among them, the HTL also plays a very vital role. Previously, organic poly (3,4-ethylenedioxythiophene):poly (styrene sulfonic acid) PEDOT:PSS was being widely used as the HTL in PSCs, but due to its hygroscopic nature and acidic properties, it lowered the stability and the life time of the PSCs. Later it was replaced mostly by NiO, a p-type transparent conducting oxide (TCO) enhancing the PCE of PSCs. Its excellent stability and electrical/optical properties attracted the interest of many researchers. Different types of PSCs used NiO thin films prepared from different synthesis routes and obtained variation in efficiency of PSCs. Different parameters of NiO thin films like thickness, annealing temperature (AT) and duration, precursor combinations and more in synthesis processes, have a significant role in optimizing the PCE. Though there are many routes for obtaining NiO thin film, here we are trying to focus more on sol-gel method, as this route is very cost effective and employs basic equipment. Its evolution, present status and the future perspectives will also be discussed.

Keywords: power conversion efficiency, organic photovoltaic device, annealing temperature, sol-gel method.

Received: 19 December 2020

Revised: 4 April 2021

Final revision: 3 December 2021

1. Introduction

In human civilization, energy has played an important role in societal evolution. The trend of social development and many more dimensions of human civilization depend upon the availability of the energy resources and its rational utilization. The limited sources of energy materials and the ever-increasing demand for energy create a situation of scarcity over the resources. Sources of energy materials directly affect the global economy. So, the whole world is concerned about the permanent solution of the energy crisis.

Ultimately researchers are interested in solar energy. Solar energy can be converted into electrical energy and can be used as alternative to conventional carbon-based sources of energy. Gradual development took place from the initial discovery of the solar photovoltaic effect in 1839 by French Scientist Edmond Becquerel [1]. Since the world's first Photovoltaic solar cell by Chapin et al. [3], solar cells have been based on silicon, selenium, cadmium, copper, dye-sensitized photochemical cell, thin film solar cell based on different materials with solar storage [2], to perovskite solar cells at present. Perovskite based solar cell shave recently reached an efficiency > 25 % [4].

Many elements and compounds have photovoltaic properties which allow conversion of solar energy into electrical energy. Historically, the silicon-based solar cells have gained the popularity, but due to their limited efficiency, scientists are finding alternatives. The perovskite solar cell is currently popular. Lead-based perovskite solar cells have almost attained the efficiency of the silicon-based solar cells. As Pb is toxic to the environment, its commercialization became the hurdle in the development of high efficiency solar cell. So, now an alternative to the Pb-PSCs is currently a topic of research interest. Pb-free PSCs seem to be promising alternatives for replacing the conventional Si-based solar cells [5].

2. Perovskite and NiO in the solar cell

Perovskite is a crystal named after the Russian mineralogist Lev Perovski. Its crystal structure generalized as ABX_3 form, in which A is a $2+$ metal cation, B is a $4+$ metal cation and X is a $2-$ oxygen anion or halogens. Common examples are $CaTiO_3$, $BaTiO_3$, and $CsSnI_3$, etc. Gradually, many more perovskite materials were discovered and halide perovskite, organic perovskite, mixed organic-inorganic perovskite, double and triple perovskite materials were also introduced. In 2009, the first perovskite based Dye Sensitized Solar Cell (DSSC) was reported by Kojima et al. [6] and first solid state solar cell based on perovskite was reported by Kim et al. [7]. Currently, the organo-lead-halide perovskite has achieved the highest efficiency in comparison to the Si-Solar Cells. Pb is mostly replaced by Sn and achieved the comparable efficiency. Since, the oxide of Sn is unstable in ambient environment; it has become a serious issue to be resolved. Inorganic and double perovskites are also an other possibility for research.

The general architecture of the thin film based PSCs has a multi-layer structure of its components like electrodes, ETL, perovskite absorbers, HTL and back contact. Perovskite absorbers are mainly sandwiched between the HTL and ETL (Fig. 1) [42]. The variation in the ETL and HTL has shown improvement in increasing the efficiency of the PSCs. ETLs are the n-type semiconductors vis phenyl-C61- butyric acid methyl ester (PCBM), ZnO, SnO_2, TiO_2, etc. and HTLs are the p-type semiconductors namely, 2,2',7,7'-tetrakis(N,N-pdimethoxyphenylamino)-9,9'-spirobifluorene (Spiro-OMeTAD), poly(3,4-ethylenedioxythiophene)/poly(styrenesulfonicacid) (PEDOT:PSS), NiO_x, CuSCN, etc. Previously the organic HTL PEDOT:PSS was very common in PSCs, but due to its hygroscopic and poor electron blocking nature, significant degradation in PCE occurred. If the electrons are not blocked properly, then the recombination at the interface layer will be increased, leading to low cell efficiency [8]. PEDOT:PSS also has an acidic nature. Transport materials need to be transparent, able to block the electron, should possess Ohmic contact with the electrodes and good stability. NiO thin film was the next candidate with all these properties. It was found that the inorganic materials provide good stability and carrier mobility [10].

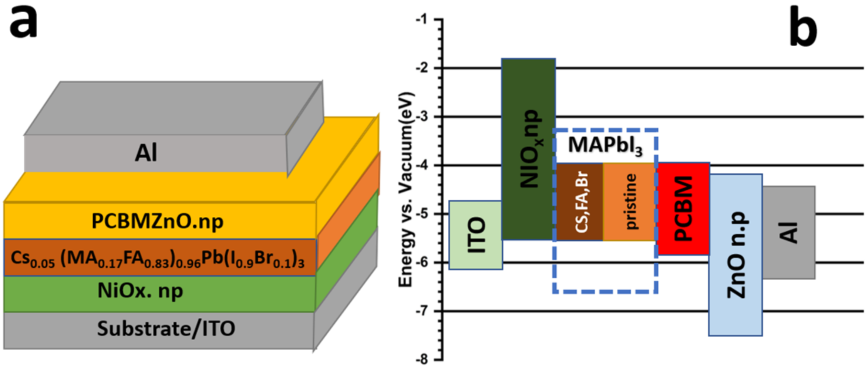

FIG. 1. a) Typical device architecture of the inverted planar PSCs. b) Energy levels of layers in the stack (Copyright permission taken from ref. [42])

Electron-hole pairs (E–H) are generated when light is incident upon the absorber. To extract the E–H and to transport to the corresponding electrodes, ETL and HTL are required respectively. In general, PSCs, ETL is deposited on the TCO (mainly FTO/ITO) followed by the perovskite absorber. HTL is deposited above the absorber to extract the holes efficiently. On the top of the hole, metal layer of silver (Ag) or gold (Au) is deposited (TCO/ETL/Perovskite/HTL/Ag) and in inverted configuration, just the position of HTL and ETL are interchanged (TCO/HTL/Perovskite/ETL/Ag). Previously, the ETL and HTL were incorporated with some meso-porous layers also.

This review mainly concentrates on development in synthesis process of NiO thin film for the application as HTL in PSCs. With the introduction of NiO as HTL in PSCs, many possibilities have been seen in improving the efficiency of the PSCs. NiO thin films have been synthesized varying many synthesis routes and parameters like thickness, different precursors or solvents [9], annealing time and temperature and influenced the properties of the solar cell. There are many routes for depositing the NiO thin film, including: sol-gel route (Fig. 2) [10, 11], direct spin coating from pre-synthesized nanocrystals [12], combustion method [13], electrodeposition [14], sputtering [15], pulsed laser deposition (PLD) [16], atomic layer deposition (ALD) [17], spray pyrolysis [18], chemical precipitation methods [19] and many more have been used for the thin film deposition.

Nickel oxide (NiO) has a basic cubic structure with the space group Fm3M which is similar to that of NaCl. Its lattice parameter is 0.4173 nm [20]. NiO is a wide bandgap material having the band gap in the range of 3.6 – 4.0 eV with the work function of 5.4 eV. It is a highly transparent nano thin film enabling it to be a good p-type TCO [21,22].

3. Literature survey

Jimenze et al. synthesized NiO thin film via a dip-coating sol-gel route using Ni-acetate as precursor. They studied the effect of AT on crystal structure and found the films to be amorphous when annealed between 175 – 250 °C and above 250 °C it was crystalline with a good surface homogeneity. They found the dependency of electrical conductivity with the thickness in the range of 2×10^{-5} to 6.5×10^{-3} $(\Omega \cdot \mathrm{cm})^{-1}$ and similarly the energy band gap E_g was from

FIG. 2. Schematic sol-gel route for NiO thin film synthesis following the method of ref [11]

3.9 to 3.8 eV for the corresponding film thickness varying from 49 to 191.8 nm. The transmittance of films decreased with increased thickness and the films with thickness > 100 nm had very low optical transmittance. Slower growth rate resulted in good morphology and uniform homogeneity with increasing electrical conductivity [23]. The effect of precursor on the grain size of the thin film was observed as 2 – 3 nm in case of Ni-sulfate precursor than Ni-acetate (average 5 nm) via SG route [24]. The electrical resistivity decreased with an increase in temperature (semiconductor behavior) and thickness was calibrated graphically for chemical bath-deposited films [25]. AT changes the surface roughness and the crystal structure. At an AT up to 300 °C good surface morphology was not observed, and it was found to be amorphous in nature. However, above 300 °C, the surface roughness also started improving with the proper crystal structure. The correlation between the deposition parameters and optical properties of the NiO thin film was also established. The AT and dipping speed also affected the refractive index and the extinction coefficient of the films [26]. Ghamadi et al. prepared thin film by the SGSC method using Ni-Ac as precursor with an optimum AT of 600 °C. Their study showed that the volume energy loss is greater than the surface energy loss at all incident photon energies. The optical band gap was 3.44 eV. They used single electronic oscillator mode to obtain the values for the oscillator strength, oscillator energy. They also calculated dielectric and refractive index of the film with values of 4.04 and 2.01 respectively. The value of third order susceptibility was estimated using Frumer model as 1.62×10^{-13} esu [27]. Patil et al. synthesized NiO nanopowder via chemical precipitation route using nickel acetate as a precursor. Further, the NiO powder was mixed with m-cresol and prepared as a thin film using a spin-coater. They observed the decrease in band gap energy from 3.86 to 3.47 eV and increase in electrical conductivity from 10^{-4} to 10^{-2} $(\Omega\cdot\text{cm})^{-1}$ after annealing the NiO films from 400 to 700 °C [28]. With increasing AT from 400 – 700 °C there was an increase in mean grain size. Increasing the grain size (40 – 60 nm) caused a decrease in the grain boundary density of a film and decrease in scattering of carriers at grain boundaries. With an increase in AT, the absorption coefficient of the film also increased. This could be assumed due to increase in the density of states of holes with increase in AT [29]. Annealing (600 °C) in different environments (air and N_2) showed that grain size increased with the increased in number of layers for annealing at aerobic environment but in N_2 environment there was a decrease in grain size. Even the optical band gap energy decreased from 3.76 to 3.52 eV and 3.75 to 3.49 eV annealed in air and N_2 respectively. The resistivity of air annealed film was more than that of N_2 as 900×10^3 and 40 $\Omega\cdot$cm respectively. Aerobic annealing leads to production of larger grains and better crystalline structure with lower oxygen vacancies, which can be the predominant factor of conductivity with higher resistivity [10]. Thermal analysis showed that below an AT of 400 °C there was continuous decomposition and weight loss and after reaching 400 °C, the weight loss became constant, leading to the formation of NiO crystal [30]. Annealing increased the surface roughness and it might be due to the fact that the annealing process would enlarge the NiO particle sizes [31]. Sahoo et al. showed the influence of AT on morphological, optical and electrical properties of SGSC synthesized NiO thin film. AT affected the current at light and dark mode from 9.9 to 3.3 mA and 7.9 to 3.6 mA respectively [11]. Kayani et al. synthesized NiO powder via SG route varying the AT from 400 to 1000 °C. The crystalline sizes increased with increased AT from 12 to 32 nm from 400 – 1000 °C respectively. The dislocation density decreased from 6.5×10^{-3} to 2.3×10^{-3} nm^{-2} with an increase in AT. The transmittance decreased with increasing AT, but the band gap increased from 3.02 to 3.14 eV. This increase in the band gap may be due to an increase in the defect levels. When magnetic field was applied on NiO nanoparticles the magnetization showed a more or less linear dependence. Therefore, NiO nanoparticles showed paramagnetic behavior. NiO also showed ferromagnetic behavior above the critical diameter of 55 nm, below which, the nanoparticles became single magnetic domains [32]. The transmittance decreased with increasing the thickness but couldn't find the proper correlation of reflectance with the thickness. Band gap energy increased from 3.87 to 3.94 eV as thickness increased from 124 to 166 nm. Electrical conductivity which was increased from 7.94×10^{-3} to 27.89×10^{-3} $(\Omega\cdot\text{cm})^{-1}$ when film thickness increased from 124 to 137 nm but again decreased at 145 nm and at 166 nm showed a good electrical conductivity with 84×10^{-3} $(\Omega\cdot\text{cm})^{-1}$ [33]. Average crystalline size increased with increasing AT whereas dislocation density decreased. Annealing reduced the lattice defects of the film and increased the crystalline quality by modifying the periodic arrangement of atoms in the crystal lattice [34].

4. NiO as hole transport layer

HTL serves as an electron blocking layer in bulk heterojunction (BHJ) solar cell. Previously used HTL PEDOT:PSS degraded so early and had a limited performance. Aqueous solution of PEDOT:PSS was highly acidic in nature with pH 1.2. Due to its hygroscopic nature, moisture may get absorbed leading to proton release and anode corrosion [8]. As a result, it leads to the degradation of device, lowering lifetime and overall performance of the device. For an ideal candidate to be used as HTL, it should have $E_g > 3$ eV, p-type transparent conducting material, it should be chemically stable and possess good conductivity.

Steirer et al. introduced NiO thin film replacing the PEDOT:PSS in OPV. The NiO thin film was deposited by a solution based Ni-organic inkjet technique. Although the work function of NiO was tailored by O_2-plasma treatment but the real effect was not understood properly. Thicker films produced uniform devices with lower open-circuit voltage (V_{oc}), lower short-circuit current density (J_{sc}) and higher series resistance (R_s). Thinner films failed to produce uniform device on a substrate causing inconsistent performance, perhaps due to incomplete surface coverage. But the optimum thickness varied from device to device. The device ITO/NiO/P3HT:PCBM/Ca/Al, attained the PCE of 3.6 %. In comparison,the performance of NiO was as good as that of PEDOT:PSS [16]. Films synthesized via PLD technique was applied in BHJ solar cell improved the performance with work function of $\sim$ 5.3 eV, optical transmittance of $>$ 80 %. The problem in forming good Ohmic contact caused lowering of efficiency to some extent [35]. Hsu et al. demonstrated, for the first time, the fabrication of uniform, defect-free, and conformal NiO ultra-thin films for use as HTL in BHJ polymer solar cell via ALD optimizing its processing parameters. ALD offers unparalleled advantages owing to its unique capabilities, including defect-free deposition, complete and uniform coverage over large-area/high-aspect-ratio surface features, precise control over deposited thickness, and low deposition temperatures. Thickness was optimized and 4 nm seemed to be the optimum one giving comparable PCE of 3.38 % comparable to PEDOT:PSS [17]. You et al. improved the air stability of the PSC using solution processed NiO as HTL. The maximum PCE obtained was 14.6±1.5% with device architecture glass/ITO/NiO_x/$CH_3NH_3PbI_3$/PCBM/Al. The crystallinity of perovskite on NiO was also improved compared to the that of formed on PEDOT:PSS. The number of grain boundaries was reduced with an increase in crystal size, leading to a decrease in the recombination process. These factors may affect the higher open circuit voltage in case of NiO than PEDOT:PSS. The thickness also changed the device efficiency as the thinner NiO film ($<$ 40 nm) showed current leakage and low shunt resistance, resulting in a low open-circuit voltage and fill factor. Perhaps in thinner films the coverage of NiO could be very low, while for thicker films (120 nm), the series resistance also seemed to be increasing, leading to a decrease in the fill factor. Thus, the optimized film with 80 nm thickness showed the best performance. The air stability of device in ambient environment without encapsulation with NiO as HTL remained good for 60 days, but the device with organic HTL started degrading only after 5 days [36]. Singh et al. applied NiO thin film as HTL in organic solar cell viaan inkjet printing technique. With device structure ITO/NiO(IJ)/P3HT:PC_{60}BM (70 nm)/LiF(1 nm)/Al obtained maximum PCE of $\sim$ 2.60 %. Parameters such as AT, surface treatment, thickness of NiO thin film played key roles in optimization [37]. Loi developed a direct method of NiO film deposition from NiO nanopowder mixing with HCl. He mainly optimized the AT of the NiO thin film with 350, 400, and 450 °C and the corresponding obtained PCE were 16.23, 15.48, and 14.18 % respectively. The completed perovskite solar cell structures were FTO/PEDOT:PSS or NiO_x/$MAPbI_{3-x}Cl_x$/PCBM/C_{60} + C/Ag [12]. Electron beam physical vapor deposition (EBPVD) based NiO HTL was incorporated into FTO/EBNiO/$CH_3NH_3PbI_3$/PCBM/BCP solar cell showed faster charge transfer and more effectively suppressed recombination and fewer surface trap states with a PCE of 10.80 % [38]. Kim used polyethylene glycol (PEG)-assisted sol-gel synthesis of the compact NiO as HTL. There was a significant improvement in the uniformity and smoothness of the film morphology of the compact NiO, which modified the interfacial properties between the layers. It helped in the good extraction of charge and suppression of charge recombination. He also incorporated PEDOT:PSS onto NiO layer as a hybrid HTL, which facilitated efficient cascade charge migration and passivation of the tiny pinholes. The introduction of compact NiO HTL improved the PCE from 5.68 to 6.91 % and for the hybrid PEDOT:PSS and NiO HTL, PCE improved from 7.26 to 7.93 %. Thus, optimizing the interfacial properties also improved the overall PCE of the solar cells [39]. Akhtaruzzaman et al. used the EBPVD technique to synthesize NiO thin film and incorporated in PSC as HTL with structure glass/FTO/NiO_x/$CH_3NH_3PbI_3$/PC_{61}BM/BCP/Ag. There was a difference in PCE for the HTLs which was normal NiO and annealed NiO thin film as 13.20 and 13.24 % respectively. Their optimized AT was 500 °C with a thickness of 18 nm. There was a difference in degradation in efficiency with time for normal and annealed device. In ambient environment normal device retained 72.2 % and annealed device retained 76.96 % of the initial efficiency after 28 days of fabrication of the PSCs [40]. The comparative performance of the PSCs with NiO as HTL is given in Table 1.

TABLE 1. Overall Performance of the PSCs with NiO as HTL based on SGSC method

Device Configuration	V_{oc} [V]	J_{sc} [mA/cm^2]	FF	PCE	Ref.
FTO/NiO_x/$CH_3NH_3PbI_3$/C_{60}/SnO_2 NCs/Ag	1.12	23.7	0.76	18.8 %	[41]
ITO/NiO/$Cs_{0.05}(MA_{0.17}FA_{0.83})_{0.95}Pb(I_{0.9}Br_{0.1})_3$/ PCBM/ZnO/Al	1/023	22/2	0/82	18.6 %	[42]
ITO/NiO/$CH_3NH_3PbI_3$/PCBM/Ti(Nb)O_x/Ag	1.07	21.88	0.79	18.49 %	[43]
FTO/NiO/$CH_3NH_3PbI_3$/PCBM/BCP/Ag	0.99	22.92	0.803	18.15 %	[44]
ITO/NiO/$CH_3NH_3PbI_3$/C_{60}/Bis-C_{60}/Ag	1.03	21.80	0.784	17.70 %	[45]
FTO/NiO/Perovksite/PCBM/Bis-C_{60}/Ag	1.10	21.67	0.75	17.64 %	[46]
ITO/NiO/Perovskite/PCBM/PDINO/Ag	1.11	20.57	0.765	17.5 %	[47]
ITO/NiO/$CH_3NH_3PbI_3$/PCBM/Ag	1.04	23.51	0.69	16.91 %	[48]
NiO_x/$MAPbI_{3-x}Cl_x$/PCBM/C_{60}+C/Ag	1.08	24.25	0.66	16.76 %	[12]
ITO/NiO/$CH_3NH_3PbI_3$/PCBM/Ag	1.103	21.28	0.714	16.74 %	[49]
TO/NiO/$CH_3NH_3PbI_3$/PCBM/Ag	1.09	19.9	0.769	16.68 %	[50]
TO/NiO/$CH_3NH_3PbI_3$/PCBM/Ag	1.07	20.58	0.748	16.47 %	[51]
ITO/NiO_x/$CH_3NH_3PbI_3$/PCBM/Al	1.01	21.0	0.76	14.5 ± 1.6 %	[36]
FTO/NiO_x/$CH_3NH_3PbI_3$/PCBM/BCP/Ag	0.99	17.16	0.78	13.24 %	[40]
ITO/NiO/$CH_3NH_3PbI_{3-x}Cl_x$/PCBM/BCP/Al	0.92	12.43	0.68	7.80 %	[52]
ITO/NiO/P3HT:PCBM/Ca/Al	0.58	8.6	0.66	3.60 %	[16]
ITO/NiO/P3HT/PCBM/Ca/Al	0.58	10	0.58	3.38 %	[17]
ITO/NiO(IJ)/P3HT:$PC_{60}BM$/LiF/Al	0.60	8.57	0.50	2.60	[37]

5. Doping

Improvement in the efficiency of the cell is the main concern, so doping of some metals into NiO was also applied to enhance the HTL property. Jung et al. incorporated Cu doped NiO in PSCs consisting of methylammonium lead halide perovskite. Synthesis via low temperature combustion method (150 °C) and conventional solution based high temperature method (500 °C) achieved the highest PCE of 17.8 and 15.52 % respectively. ITO-free Cu-NiO based PSC showed PCE of 13.42 % [13]. Li doping in NiO thin film affected the grain size to decrease and variation in transmittance. Li doping also decreased the band gap but there was no such difference in crystallinity due to AT [53]. Addition of Cu-dopant increased the grain size influencing the surface morphology and decrease in transmittance. The optical band gap value of the Cu-doped NiO film (3.69 eV) was lower than that of the undoped NiO film (3.73 eV) and the resistivity of the Cu-doped NiO film was 23 Ω·m, which was significantly lower than that of the undoped NiO film (320 Ω·m) [54]. The doping effect has also been observed in conductivity at lower AT of 700 °C as increasing in conductivity [55]. Cs:NiO_x HTL achieved 16 – 19 % PCE [56] and molecule F6TCNNQ dopingachieved PCE of 20.86 % [57]. So, doping also enhanced the PCE of the PSCs. The comparative performance of the PSCs of doped NiO as HTL is given in Table 2.

6. Conclusion

The exploration of different properties of NiO nanoparticles and thin films led to the potential use in various applications. Incorporation of inorganic HTL showed a sound improvement in the overall performance of the PSCs. Different synthetic routes had its own advantages and disadvantages. The best route will be the one which is very cost effective and provides higher efficiency while leaving the other properties intact. Although the sol-gel method has its own limitations, it is very accessible for everyone. So, more improvement can be met using this method. The

TABLE 2. Overall Performance of the PSCs with doped-NiO as HTL based on SGSC method

Device Configuration	V_{oc} [V]	J_{sc} [mA/cm^{-2}]	FF	PCE	Ref.
ITO/F6TCNNQ:NiO$_x$/CsFAMAperovskite/ PCBM/ZrAcac/Ag	1.12	23.18	0.80	20.86 %	[57]
ITO/Cu:NiO/CH$_3$NH$_3$PbI$_3$/C$_{60}$/BCP/Ag	1.12	22.28	0.81	20.26 %	[57]
FTO/Cu:NiO/meso-Cu:NiO/CH$_3$NH$_3$PbI$_3$/ PCBM/bis-C$_{60}$/Ag	1.11	21.58	0.81	19.62 %	[58]
FTO/Cs:NiO$_x$/MAPbI$_3$/PCBM/ZrAcac/Ag	1.12	21.77	0.79	19.35 %	[56]
ITO/Cu:NiO/CH$_3$NH$_3$PbI$_3$/PCBM/BCP/Ag	1.11	20.76	0.81	18.66 %	[59]
ITO/Cu:NiO/CH$_3$NH$_3$PbI$_3$/Bis-C$_{60}$/C$_{60}$/Ag	1.05	21.60	0.77	17.46 %	[13]
ITO/Li:NiO/CH$_3$NH$_3$PbI$_3$/PCBM/Ag	1.05	22.8	0.64	15.51 %	[60]
FTO/Cu:NiO/CH$_3$NH$_3$PbI$_3$/PCBM/Ag	1.11	18.75	0.72	14.98 %	[61]
FTO/LiCu:NiO/CH$_3$NH$_3$PbI$_3$/PCBM/Ag	0.965	20.28	0.71	14.04 %	[62]

doping has also showed good improvement. In most of the findings, variation in annealing temperature was done for optimization. The SGSC method is very facile for low cost synthesis and can sustain good method for higher PCE of the PSCs in future also.

Conflicts of interest

The authors declare there is no conflict of interest.

Acknowledgements

This work was supported by Science & Engineering Research Board (SERB), New Delhi, Sanction Order No. EEQ/2017/000435 dated 17 March, 2018.

References

[1] Fatet J. Recreating Edmond Becquerel's electrochemical actinometer. *Arch. Des Sci.*, 2005, **58**, P. 149–158.

[2] Timeline of solar cells, Wikipedia.org, 2013. URL: http://en.wikipedia.org/w/index.php?title=Timeline_of_solar_cells&oldid=577975981.

[3] Bellis M. History and Definition of a Solar Cell. ThoughtCo, 2020, URL: thoughtco.com/history-of-solar-cells-1992435.

[4] N.R.E.L. (NREL), Best Research Efficiency, 2016, URL: https://www.nrel.gov/pv/cell-efficiency.html.

[5] Kour R., Arya S., et al. Potential Substitutes for Replacement of Lead in Perovskite Solar Cells: A Review, Glob. *Challenges*, 2019, **3**, 1900050.

[6] Kojima A., Teshima K., Shirai Y.,, Miyasaka T. Organometal halide perovskites as visible-light sensitizers for photovoltaic cells. *J. Am. Chem. Soc.*, 2009, **131**, 6050–1.

[7] Kim H.S., Lee C.R., et al. Lead iodide perovskite sensitized all-solid-state submicron thin film mesoscopic solar cell with efficiency exceeding 9%. *Sci. Rep.*, 2012, **2**, P. 1–7.

[8] Yin X., Guo Y., et al. Nickel Oxide as Efficient Hole Transport Materials for Perovskite Solar Cells. *Sol. RRL*, 2019, **3**, P. 1–27.

[9] Ningsih S.K.W. Effect of various solvent on the synthesis of nio nanopowders by simple sol-gel methods and its characterization. *Indones. J. Chem.*, 2015, **15**, P. 50–55.

[10] Jlassi M., Sta I., Hajji M., Ezzaouia H. Optical and electrical properties of nickel oxide thin films synthesized by sol-gel spin coating. *Mater. Sci. Semicond. Process*, 2014, **21**, P. 7–13.

[11] Sahoo P., Thangavel R. Effect of annealing temperature on physical properties of solution processed nickel oxide thin films. *AIP Conf. Proc.*, 2018, **1961** (1), 030041.

[12] Loi Nguyen. New Method of Nickel Oxide as Hole Transport Layer and Characteristics of Nickel Oxide Based Perovskite Solar Cell. ProQuest Dissertations And Theses, 2018, **57-06**, 59 p.

[13] Jung J.W., Chueh C.C., Jen A.K.Y. A Low-Temperature, Solution-Processable, Cu-Doped Nickel Oxide Hole-Transporting Layer via the Combustion Method for High-Performance Thin-Film Perovskite Solar Cells. *Adv. Mater.*, 2015, **27**, P. 7874–7880.

[14] Wu M.S., Yang C.H., Wang M.J. Morphological and structural studies of nanoporous nickel oxide films fabricated by anodic electrochemical deposition techniques. *Electrochim. Acta*, 2008, **54**, P. 155–161.

[15] Zhao Y., Wang H., et al. Structures, electrical and optical properties of nickel oxide films by radio frequency magnetron sputtering. *Vacuum*, 2014, **103**, P. 14–16.

[16] Steirer K.X., Chesin J.P., et al. Olson, Solution deposited NiO thin-films as hole transport layers in organic photovoltaics. I , 2010, **11**, P. 1414–1418.

[17] Hsu C.C., Su H.W., et al. Atomic layer deposition of NiO hole-transporting layers for polymer solar cells. *Nanotechnology*, 2015, **26**, 385201.

[18] Zaouche C., Aoun Y., Benramache S., Gahtar A. Synthesis and Characterization of Deposited NiO Thin Films by Spray Pyrolysis Technique. *Sci. Bull. Valahia Univ. – Mater. Mech.*, 2020, **17**, P. 27–32.

[19] Jeevanandam P., Pulimi V.R.R. Synthesis of nanocrystalline NiO by sol-gel and homogeneous precipitation methods. *Indian J. Chem. – Sect. A Inorganic, Phys. Theor. Anal. Chem.*, 2012, **51**, P. 586–590.

[20] Soonmin H. Preparation and characterization of nickel oxide thin films: A review. *Int. J. Appl. Chem.*, 2016, **12**, P. 87–93.

[21] Ukoba K.O., Eloka-Eboka A.C., Inambao F.L. Review of nanostructured NiO thin film deposition using the spray pyrolysis technique. *Renew. Sustain. Energy Rev.*, 2018, **82**, P. 2900–2915.

[22] Zhang P.P., Zhou Z.J., Kou D.X., Wu S.X. Perovskite Thin Film Solar Cells Based on Inorganic Hole Conducting Materials. *Int. J. Photoenergy*, 2017, **2017**, 6109092.

[23] Jiménez-González A.E., Cambray J.G. Deposition of NiO_x thin films by sol-gel technique. *Surf. Eng.*, 2000, **16**, P. 73–76.

[24] Korošec R.C., Bukovec P. Sol-Gel Prepared NiO Thin Films for electrochromic applications. *Acta Chim. Slov.*, 2006, **53** (2), P. 136–147.

[25] Chavan U.J., Yadav A.A. Structural, Optical and Electrical Properties of Chemical Bath Deposited NiO Thin Films. *Int. J. of Engineering Sciences & Research Technology*, 2016, **5** (10), P. 282–287.

[26] Ghodsi F.E., Khayatiyan S.A. Preparation and determination of optical properties of NiO thin films deposited by DIP coating technique. *Surf. Rev. Lett.*, 2007, **14**, P. 219–224.

[27] Al-Ghamdi A.A., Mahmoud W.E., Yaghmour S.J., Al-Marzouki F.M. Structure and optical properties of nanocrystalline NiO thin film synthesized by sol-gel spin-coating method. *J. Alloys Compd.*, 2009, **486**, P. 9–13.

[28] Patil V.P., Pawar S., et al. Effect of Annealing on Structural, Morphological, Electrical and Optical Studies of Nickel Oxide Thin Films. *J. Surf. Eng. Mater. Adv. Technol.*, 2011, **01**, P. 35–41.

[29] Nalage S.R., Chougule M.A., et al. Sol-gel synthesis of nickel oxide thin films and their characterization. *Thin Solid Films*, 2012, **520**, P. 4835–4840.

[30] Zorkipli N.N.M., Kaus N.H.M., Mohamad A.A. Synthesis of NiO Nanoparticles through Sol-gel Method. *Procedia Chem.*, 2016, **19**, P. 626–631.

[31] Abdullah M.A.R., Mamat M.H., et al. Preparation of nickel oxide thin films at different annealing temperature by sol-gel spin coating method. *AIP Conf. Proc.*, 2016, **1733**, 020013.

[32] Kayani Z.N., Butt M.Z., Riaz S., Naseem S. Synthesis of NiO nanoparticles by sol-gel technique. *Mater. Sci. Pol.*, 2018, **36**, P. 547–552.

[33] Benramache S., Aoun Y., Arif A. The film thickness effect on the physical properties of NiO thin films elaborated by Sol-gel method. *J. Sci. Technol.*, 2020, **12**, P. 7–14.

[34] Aswathy N.R., Varghese J., Vinodkumar R. Effect of annealing temperature on the structural, optical, magnetic and electrochemical properties of NiO thin films prepared by sol-gel spin coating. *J. Mater. Sci. Mater. Electron.*, 2020, **31**, P. 16634–16648.

[35] Irwin M.D., Servaites J.D., et al. Structural and electrical functionality of NiO interfacial films in bulk heterojunction organic solar cells. *Chem. Mater.*, 2011, **23**, P. 2218–2226.

[36] You J., Meng L., et al. Improved air stability of perovskite solar cells via solution-processed metal oxide transport layers. *Nat. Nanotechnol.*, 2016, **11**, P. 75–81.

[37] Singh A., Gupta S.K., Garg A. Inkjet printing of NiO films and integration as hole transporting layers in polymer solar cells. *Sci. Rep.*, 2017, **7**, P. 1–12.

[38] Mahmud Hasan A.K., Jamal M.S., et al. Integration of NiO Layer as Hole Transport Material in Perovskite Solar Cells. *Int. Conf. Sp. Sci. Commun. Iconsp.*, 2019, P. 267–270.

[39] Kim J.K. PEG-assisted sol-gel synthesis of compact nickel oxide hole-selective layer with modified interfacial properties for organic solar cells. *Polymers (Basel)*, 2019, **11**, P. 1–8.

[40] Akhtaruzzaman M., Hasan A.K.M., et al. Air-Stable Perovskite Photovoltaic Cells with Low Temperature Deposited NiO_x as Efficient Hole-Transporting Material. *Opt. Mater. Express*, 2020, **10**, P. 1801–1816.

[41] Zhu Z., Bai Y., et al. Enhanced Efficiency and Stability of Inverted Perovskite Solar Cells Using Highly Crystalline $\mathrm{SnO_2}$Nanocrystals as the Robust Electron-Transporting Layer. *Adv. Mater.*, 2016, **28**, P. 6478–6484.

[42] Najafi M., Di Giacomo F., et al. Highly Efficient and Stable Flexible Perovskite Solar Cells with Metal Oxides Nanoparticle Charge Extraction Layers. *Small*, 2018, **14**, P. 1–10.

[43] He J., Bi E., et al. Ligand-Free, Highly Dispersed NiO_x Nanocrystal for Efficient, Stable, Low-Temperature Processable Perovskite Solar Cells. *Sol. RRL*, 2018, **2**, P. 1–7.

[44] Tang L.J., Chen X., et al. A Solution-Processed Transparent NiO Hole-Extraction Layer for High-Performance Inverted Perovskite Solar Cells. *Chem. – A Eur. J.*, 2018, **24**, P. 2845–2849.

[45] Zhang H., Cheng J., et al. Pinhole-free and surface-nanostructured niox film by room-Temperature solution process for high-performance flexible perovskite solar cells with good stability and reproducibility. *ACS Nano*, 2016, **10**, 1503–1511.

[46] Vinet L., Zhedanov A. A "missing" family of classical orthogonal polynomials. *J. Phys. A Math. Theor.*, 2011, **44**, P. 1689–1699.

[47] Hou Y., Chen W., et al. Overcoming the Interface Losses in Planar Heterojunction Perovskite-Based Solar Cells. *Adv. Mater.*, 2016, **28**, P. 5112–5120.

[48] Guo X., Luo G., et al. A 16.5 % efficient perovskite solar cells with inorganic NiO film as hole transport material. *IEEE J. Photovoltaics*, 2018, **8**, P. 1039–1043.

[49] Yoon S., Kang D.W. Solution-processed nickel oxide hole transport layer for highly efficient perovskite-based photovoltaics. *Ceram. Int.*, 2018, **44**, P. 9347–9352.

[50] Yin X., Liu J., et al. Solvothermal derived crystalline NiO_x nanoparticles for high performance perovskite solar cells. *J. Power Sources*, 2016, **329**, P. 398–405.

[51] Yin X., Chen P., et al. Highly Efficient Flexible Perovskite Solar Cells Using Solution-Derived NiO_x Hole Contacts. *ACS Nano*, 2016, **10**, P. 3630–3636.

[52] Jeng J.Y., Chen K.C., et al. Nickel oxide electrode interlayer in $\mathrm{CH_3NH_3PbI_3}$ perovskite/PCBM planar-heterojunction hybrid solar cells. *Adv. Mater.*, 2014, **26**, P. 4107–4113.

[53] Jesuraj S.A., Haris M., Immanuel P. Structural and Optical Properties of Pure NiO and Li-Doped Nickel Oxide Thin Films by Sol-Gel Spin Coating Method. *Int. J. Sci. Res.*, 2014, P. 8–9.

[54] Kim K.H., Takahashi C., Abe Y., Kawamura M. Effects of Cu doping on nickel oxide thin film prepared by sol-gel solution process. *Optik (Stuttg)*, 2014, **125**, P. 2899–2901.

[55] Ehara T., Sasaki K., Abe M., Nakanishi T. Preparation of copper-doped nickel oxide thin films by sol-gel method using nickel and copper acetate. *Mater. Sci. Forum*, 2017, **909**, P. 213–218.

[56] Chen W., Liu F.Z., et al. Cesium Doped NiO_x as an Efficient Hole Extraction Layer for Inverted Planar Perovskite Solar Cells. *Adv. Energy Mater.*, 2017, **7**, P. 1–8.

[57] Chen W., Zhou Y., et al. Molecule-Doped Nickel Oxide: Verified Charge Transfer and Planar Inverted Mixed Cation Perovskite Solar Cell. *Adv. Mater.*, 2018, **30**, P. 1–9.

[58] Yao K., Li F., et al. A copper-doped nickel oxide bilayer for enhancing efficiency and stability of hysteresis-free inverted mesoporous perovskite solar cells. *Nano Energy*, 2017, **40**, P. 155–162.

[59] He Q., Yao K., et al. Room-Temperature and Solution-Processable Cu-Doped Nickel Oxide Nanoparticles for Efficient Hole-Transport Layers of Flexible Large-Area Perovskite Solar Cells. *ACS Appl. Mater. Interfaces*, 2017, **9**, P. 41887–41897.

[60] Qiu Z., Gong H., et al. Enhanced physical properties of pulsed laser deposited NiO films via annealing and lithium doping for improving perovskite solar cell efficiency. *J. Mater. Chem. C*, 2017, **5**, P. 7084–7094.

[61] Kim J.H., Liang P.W., et al. High-performance and environmentally stable planar heterojunction perovskite solar cells based on a solution-processed copper-doped nickel oxide hole-transporting layer. *Adv. Mater.*, 2015, **27**, P. 695–701.

[62] Liu M.-H., Zhou Z.-J., et al. P-type Li, Cu-codoped NiO_x hole-transporting layer for efficient planar perovskite solar cells. *Opt. Express*, 2016, **24**, A1349.

NANOSYSTEMS: PHYSICS, CHEMISTRY, MATHEMATICS, 2021, 12 (6), P. 711–727

Phase equilibria and materials in the TiO_2–SiO_2–ZrO_2 system: a review

S. A. Kirillova[1,2], V. I. Almjashev[1,2,3], V. L. Stolyarova[1,4]

[1]I. V. Grebenshchikov Institute of Silicate Chemistry of RAS, Emb. Makarova, 2,
St. Petersburg, 199034, Russia

[2]St. Petersburg Electrotechnical University "LETI", Professor Popov St., 5,
St. Petersburg, 197376, Russia

[3]FSUE "Alexandrov Research Institute of Technology", Koporskoye sh., 72,
Sosnovy Bor LR, 188540, Russia

[4]St. Petersburg State University, Universitetskaya nab., 7/9, St. Petersburg, 199034, Russia

refractory-sveta@mail.ru, vac@mail.ru, stolyarova.v@iscras.ru

PACS 64.75.-g; 28.52.Fa; 28.52.Nh **DOI 10.17586/2220-8054-2021-12-6-711-727**

This paper analyzes the available data on phase equilibria in the TiO_2–SiO_2–ZrO_2 system. The advantages of specialized databases and software systems for the analysis of information on phase equilibria are pointed. Phase diagrams are kind of a roadmap for the design of materials. As shown in the review, nanomaterials are no exception to this. Data on phase equilibria, such as eutectic points, solubility limits, binodal and spinodal curves, make it possible to predict the possibility of the formation of nanoscale structures and materials based on them. In its turn during the transition to the nanoscale state, the mutual component solubility, the temperature of phase transformation may change significantly, and other features may become observable. This provides additional variability when choosing compositions and material design based on the phases of a given system. As an example, for design of nuclear fuel assemblies that are tolerant to severe accidents at nuclear power plants, mixed carbides (so-called MAX-phases) are considered as one of the most promising options as nanoscale layers on fuel cladding. It is suggested that the materials of the TiO_2–SiO_2–ZrO_2 system, which are the product of oxidation of some MAX-phases, can serve as an inhibitor of their further corrosion. Ensuring the stability of materials based on MAX-phases expands their prospects in nuclear power. This requires comprehensive information about phase equilibria and formation conditions of nanostructured states in the analyzed system.

Keywords: phase equilibria, zirconia, silica, titania, nanomaterials, MAX-phases, nuclear safety.

Received: 3 February 2021

Revised: 25 September 2021

1. Introduction

Nuclear power safety directly depends on the choice of reactor materials. The core materials are especially critical. In particular, the zirconium as a fuel cladding material, which has proven itself well under normal operating conditions, turns out to be extremely dangerous in beyond design basis accidents [1]. For this reason, there is an active search for a safer material to replace zirconium all over the world. One of these options is MAX-phases – a family of ternary layered compounds corresponding to the conditional formula $M_{n+1}AX_n$ ($n = 1, 2, 3, ...$), where M is a transition d-metal (Sc, Ti, V, Cr, Zr, Nb, Mo, Hf, Ta); A – p-element (Si, Ge, Al, Ga, S, P, Sn, As, Cd, I, Tl, Pb); X is carbon or nitrogen. These materials exhibit a unique combination of properties common to both metals and ceramics [2,3]. They are of low density; high thermal and electrical conductivity; high strength; excellent corrosion resistance in aggressive liquid media, resistance to high-temperature oxidation and thermal shock; easily machined; high melting point and are quite stable at temperatures up to 1000 °C and above [2–5]. That is, according to the combination of characteristics, the MAX-phases can be ideal for the fuel cladding material of nuclear reactors. However, the prospects of their use cannot be assessed without a comprehensive study of their stability, especially in the Nuclear Power Plants accident conditions. In this case, their unique features can be used to the full, leading to a decrease in the likelihood of severe accidents or, at least, to mitigate their consequences.

One of the aspects of such investigations is the study of the oxidation products of MAX-phases, in particular, zirconia, silica and titania. Materials based on these components, presenting certain combinations of phases and features of their dimensional parameters and mutual arrangement, can both contribute to the destruction of claddings based on MAX-phases and serve as good protectors against their further corrosion. To assess the boundaries of stability and predict the properties of these materials, it is necessary to know the phase equilibria in the TiO_2–SiO_2–ZrO_2 system, as well as to know the features of the formation of structures that have the physicochemical and mechanical properties necessary to create a protective layer.

So, for example, on the basis of the system under consideration, the formation of nested glass-crystalline structures is possible. Interest in materials with a hierarchically organized spatial distribution of phases, including nanostructured materials, is associated with their unique characteristics. For such materials, it becomes possible to fine-tune their properties in a very wide range [6–9].

The study of the formation of hierarchical structures deserves special attention. One of these processes is phase decay and, in particular, separation in the liquid phase – miscibility gap [10–20]. The structures that appear upon rapid cooling of samples from the miscibility gap can be classified as hierarchical due to the appearance of a number of sublevels with rounded inclusions ranging in size from 0.01 to 10 μm [11].

Materials with a hierarchical structure arising during the crystallization of immiscible viscous oxide liquids can be classified as nanomaterials containing nanosized blocks (crystallites) at the lowest levels of the hierarchy, included in a glassy or crystalline matrix [7]. In addition to the size factor, the shape and spatial distribution of phases have a significant effect on the properties of such materials. The hierarchical structure formed during the cooling of immiscible melts is associated with the boundaries of phase stability and reflects the history of the decay of primary and formation of secondary phases [21]. This determines, as a rule, the characteristics of the materials thus formed [18, 19, 22–25].

Thereby, to solve the problem of creating and studying the physicochemical features and stability of materials, it is necessary to analyze the available information on phase equilibria. In the review, we are performed such an analysis for the TiO_2–SiO_2–ZrO_2 system. It also provides information on materials based on the TiO_2–SiO_2–ZrO_2 system and their relationship with data on phase equilibria.

2. TiO_2–SiO_2 system

The TiO_2–SiO_2 system is important for interpreting the interaction of titanium and silicon dioxides in the production of ceramics, glass ceramics, and glasses. Based on the components of the system, it is possible to create fundamentally new materials with unique mechanical, optical and catalytic properties [26–37]. In addition, the components of the system themselves have a variety of properties that are promising for modern technology [38–40].

The data given in the literature on the TiO_2–SiO_2 system are contradictory [4, 41–43, 45–53]. In particular, the authors of [41–43] carried out experiments in a reducing atmosphere, and in this connection, possibly, in addition to TiO_2, the samples contained the oxides Ti_2O_3 and Ti_3O_5. The authors of [42] found that this system is characterized by the presence of a region of immiscibility of two liquid phases, which was not noted in [44]. In [45], contrary to previous studies, two series of solid solutions were found in the system, the existence of which was not confirmed later in [46]. The authors of [46] clarified the position of the eutectic point defined in [44]. According to those authors [46], the eutectic in the TiO_2–SiO_2 system corresponds to a composition of 8.1 mol. % TiO_2 and a temperature of 1550±4 °C. In [46], data on the position in the system of the region of immiscibility of two liquid phases arising at 1780±10 °C in the range from 15.0 to 90.9 mol. % TiO_2, i.e., significantly different from the data of [42].

Other research [47] shows the calculated diagram of the state of the system obtained on the basis of previously published data on phase equilibria in the system and thermodynamic data on SiO_2 and TiO_2 [48]. It is noted that the experimental data on the boundaries of the region of immiscibility of two liquid phases are unknown, and the critical point of the miscibility gap is 56.3 mol. % TiO_2 and 2618 °C, was obtained only from the data of thermodynamic modeling of the region of immiscibility of liquid phases. In addition, the existence of solid solutions from the side of TiO_2 is taken into account. It should be noted that the work [47] used an approach based on combining the available experimental information for phase equilibria and thermodynamic properties of the phases of the system. Then it is describing the properties of each phase by a mathematical model containing a set of tunable parameters, and carrying out the procedure for finding the parameters of the phase models that best suit all available information about the phase equilibria of the system of interest to the researcher. This approach has become widespread and has actually become the standard for thermodynamic optimization of phase diagrams. In the literature, the method has the abbreviation CALPHAD (from the CALculation of PHAse Diagrams) [54].

In works [49, 50] on the basis of experimental data [46, 51–53] and their own data on the boundaries of the region of immiscibility of two liquid phases, a variant of the thermodynamically optimized diagram of phase equilibria in the TiO_2–SiO_2 system based on the sub-regular model was proposed. In the case when the thermodynamic parameters of the used model are taken to be independent of temperature, the critical point of the miscibility gap is 50.8 mol. % TiO_2 and 2374 °C, and for the linear dependence of the model parameters on temperature – 54.7 mol. % and TiO_2 2339 °C.

In [55], the eutectic and monotectic nature of the phase diagram of the TiO_2–SiO_2 system was confirmed by the Differential Thermal Analysis method (DTA) on an original setup. The temperature of the eutectic (1543±3 °C) and monotectic (1780±7 °C) transformations has been specified. The temperature of the eutectic is somewhat at odds with the previously obtained literature data, however, in general, it can be considered that the experimental data are in good agreement with the previously obtained results in [44, 46]. Scanning electron microscopy proved the presence of a region of two immiscible melts. The data obtained for the temperature of monotectic transformation coincided with the results of [46], and the results for the liquidus line above the monotectic temperature also do not contradict them. Based on the coordinates of the liquidus line and the points of invariant transformations, the parameters of the model of subregular ionic solutions [56] for melts of the TiO_2–SiO_2 system were determined and a thermodynamically optimized phase diagram was constructed in the temperature range of 1500–1900 °C.

In [57], phase equilibria in the TiO_2–SiO_2 system in the region of liquid phase separation were experimentally investigated. It is shown that in the experimental study of silicon-containing immiscible melts, an important factor that determines the microstructure and complicates the interpretation of the data is the dynamics of system cooling. Along with the rate of cooling of the melt, it is necessary to take into account such parameters of the system as the viscosity and density of coexisting liquid phases, diffusion of components, etc. Thus, for a melt based on SiO_2 at temperatures below monotectic, due to high viscosity, the liquid phase is slowly freed from the solid phase based on TiO_2, and at temperatures above monotectic, the release of the liquid phase from TiO_2 occurs at a significantly higher rate. Also, the work carried out a critical analysis of the available and obtained experimental data. A thermodynamically optimized phase diagram of the TiO_2–SiO_2 system based on the model of subregular solutions has been constructed. The phase diagram obtained by optimization by the CALPHAD method differs markedly from the diagram given in [50], which was constructed using experimental data on the composition of liquid phases at the boundary of the miscibility gap at temperatures significantly higher than the monotectic temperature. Apparently, in [50], the microstructure of samples quenched from temperatures of 2185 and 2260 °C was unreasonably interpreted as corresponding to the state of equilibrium immiscibility at these temperatures (Fig. 1*a*). Such a character of the microstructure may be a consequence of the decomposition of a homogeneous melt during quenching. This assumption is supported by the fact that a uniform pattern of phase decomposition is observed over the entire volume of the sample.

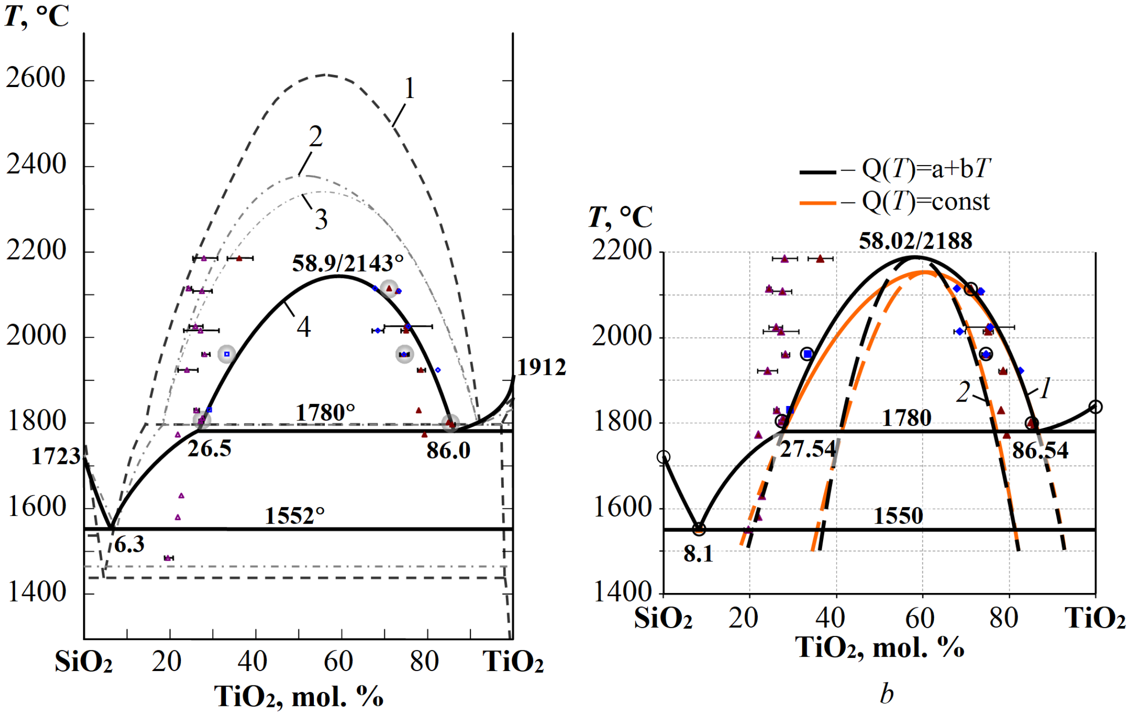

a *b*

FIG. 1. Phase diagram of the TiO_2–SiO_2 system: *a* – 1 – [47], 2 – [49], 3 – [50], 4 – [57]; *b* – [58]: *1* – binodal curves; *2* – spinodal curves

In [58], on the basis of experimental data obtained in [57], the parameters of the subregular melt model were determined without and taking into account the temperature dependence of the mixing energies of the components. Using the obtained parameter values, as well as thermodynamic data for the pure components [59–61], and taking into account the absence of miscibility of the components in the solid phase, the binodal and liquidus lines in the TiO_2–SiO_2 system were constructed. On the basis of the obtained thermodynamic model, the curves of spinodal decomposition of the liquid phase were also constructed (Fig. 1*b*). Comparison of the experimental data with the curves of binodal separation and spinodal phase decomposition showed that, upon rapid cooling of the melt, the phase decomposition in the liquid-phase region proceeds according to the spinodal mechanism [48] with the formation of materials with a hierarchically organized structure down to the nanometer scale. There are at least three levels of the hierarchy (Fig. 2). Thus, there is a fundamental possibility of experimentally constructing the spinodal of the system from data on the composition, shape, and spatial distribution of the solid regions of the phases over the volume of the material, obtained upon rapid cooling of the melt from the region of existence of two immiscible liquids.

In addition to determining the boundaries of phase equilibria and the features of phase separation and decomposition during cooling of immiscible oxide liquids in the TiO_2–SiO_2 system, the dependence of the microstructure on heating and cooling conditions was investigated. The results of the studies performed indicate that the parameters of the microstructure can be controlled at all levels of the hierarchy.

The authors of [63] draw attention to the fact that in the phase diagram of TiO_2–SiO_2 system, there are large discrepancies between the calculated and experimental data (Fig. 3). They suggest that these discrepancies are likely due to inherent difficulties in the system: the need to operate in an inert atmosphere to avoid the formation of Ti_2O_3 and Ti_3O_5, and the high temperature problems associated with miscibility gap and high SiO_2 content. For example, in [46], it is indicated that difficulties arose with the determination of the eutectic in the SiO_2-rich region, since it was impossible to reach equilibrium due to the high viscosity and the steep slope of the liquidus. In [57], the importance of the quenching rate for obtaining equilibrium data is also indicated. In general, it is necessary to implement new approaches for further experimental studies that will allow confirming the equilibrium data. As indicated, the experimental data from [57] are closest to the calculations. The critical temperature of the miscibility gap in the TiO_2–SiO_2 system is closer to [57]. The melting point of rutile is higher than that taken from [64]. The run of the liquidus curve correlates well with the new values from the Scientific Group Thermodata Europe (SGTE) substance database. Deviations from monotectic and eutectic points have not yet been explained and should be further investigated. The line going from pure rutile to the eutectic at 9 mol. % SiO_2 is parallel to that in [46] and the eutectic temperature is also higher than the experimental one. The calculated liquid level decreases towards SiO_2 enrichment. The discrepancy can be explained by the experimental difficulty in establishing equilibrium, and the kinetics can be very complex for such viscous compositions. The absence of the SiO_4^{4-} ion is notable. The SiO_4^{4-} ion is usually present in most oxide binary systems MO_x–SiO_2. However, in the case of the TiO_2–SiO_2 system, according to the experimental phase diagram, there is a wide region of immiscibility between TiO_2 and SiO_2. This indicates that TiO_2 does not participate in the destruction of the SiO_2 network, and does not use it together. In the model proposed in [49], liquid TiO_2 is described as $Ti^{4+} : O^{2-}$, where the addition of TiO_2 to SiO_2 does not destroy the oxygen bridge of SiO_2. Thus, there is a metastable miscibility gap between TiO_2 and SiO_2.

In [63], calculated data on the activity of SiO_2 in the TiO_2–SiO_2 system at 1527, 1627, and 2527 °C are also presented. Unfortunately, there is only one experimental point at 1627 °C for the $TiO_2 : SiO_2$ molar ratio of 1 : 1 [65]. A strong positive deviation from ideality and the inflection point of the liquidus arises due to the presence of liquid phase separation (Fig. 3).

The concepts of the nature of immiscibility in the TiO_2–SiO_2 system, opposite to those of [63], are given in [66]. Thermodynamic/dynamic modeling of liquid immiscibility in silicate systems is seriously hampered by the lack of *in situ* studies of the structural evolution of the melt. In work [51], the structural evolution at the atomic level of the TiO_2–SiO_2 system with a miscibility gap is studied by in situ high-energy X-ray diffraction. The authors suspended 10 mg fragments of sintered at 1000 °C ceramics in a stream of pure oxygen and melted with a CO_2-laser. Samples were overheated up to 2300 °C, then they were quenched to the target temperature, and the droplet was stabilized for 20–30 s and the diffractometric data were collected for 15 s. In the opinion of the authors, this was sufficient to avoid a strong drift of the composition due to the evaporation of SiO. For a composition of 30 mol. % TiO_2, a homogeneous liquid was assumed by the authors at a level of 2220 °C. At 1950 °C, according to their data for a composition of 30 mol. % TiO_2, a heterogeneous state was observed. At 1600 °C there was a metastable miscibility gap. Authors did not carry out measurements between these temperature levels. They chose the composition and temperature based on one of the versions of the phase diagram [46]. The authors, taking the work [46] as a basis, did not take into account other data [57, 58, 63], which can significantly affect the processing of their data and conclusions.

It was found that both the configuration of the [SiO] monomers and the polymerization between them are closely related to the incorporation and extraction of metal cations (Ti^{4+}). The [SiO] monomer undergoes oxygen-deficient polymerization and over-polymerization before liquid-liquid separation and self-healing after liquid-liquid separation, thus challenging the traditional concept of unchanged monomer [SiO_4].

Ti^{4+} cations with tetrahedral oxygen coordination first participate in the formation of the network before liquid separation. The four-fold Ti–O bond breaks during liquid separation, which can facilitate the movement of Ti^{4+} through the Si–O network to form TiO_2-rich nodules. The structural features of the nodules were also investigated and found to be very similar to those of the TiO_2 melt, suggesting parallel crystallization behavior in the two cases. The authors [66] hope that their results will allow one to see the structural evolution of immiscible liquid phases on

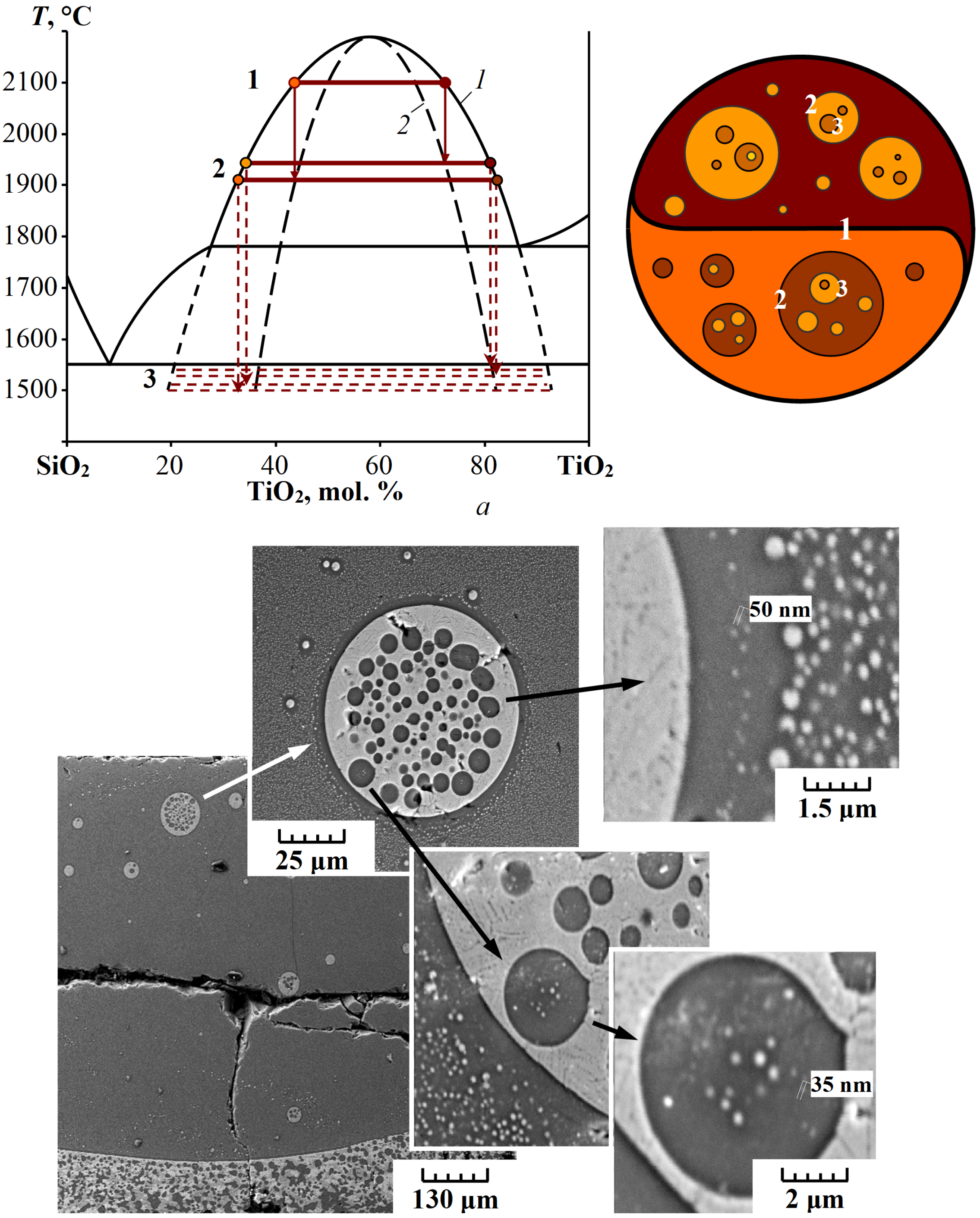

a

b

FIG. 2. Formation of a multilevel hierarchical microstructure in the process of spinodal decomposition of immiscible oxide liquids [58]: *a* – scheme of the phenomenon: *1* – binodal separation curve and *2* – spinodal decomposition curve; **1**, **2**, **3** – levels of the structural hierarchy, *b* – hierarchically organized microstructure in the TiO_2–SiO_2 system

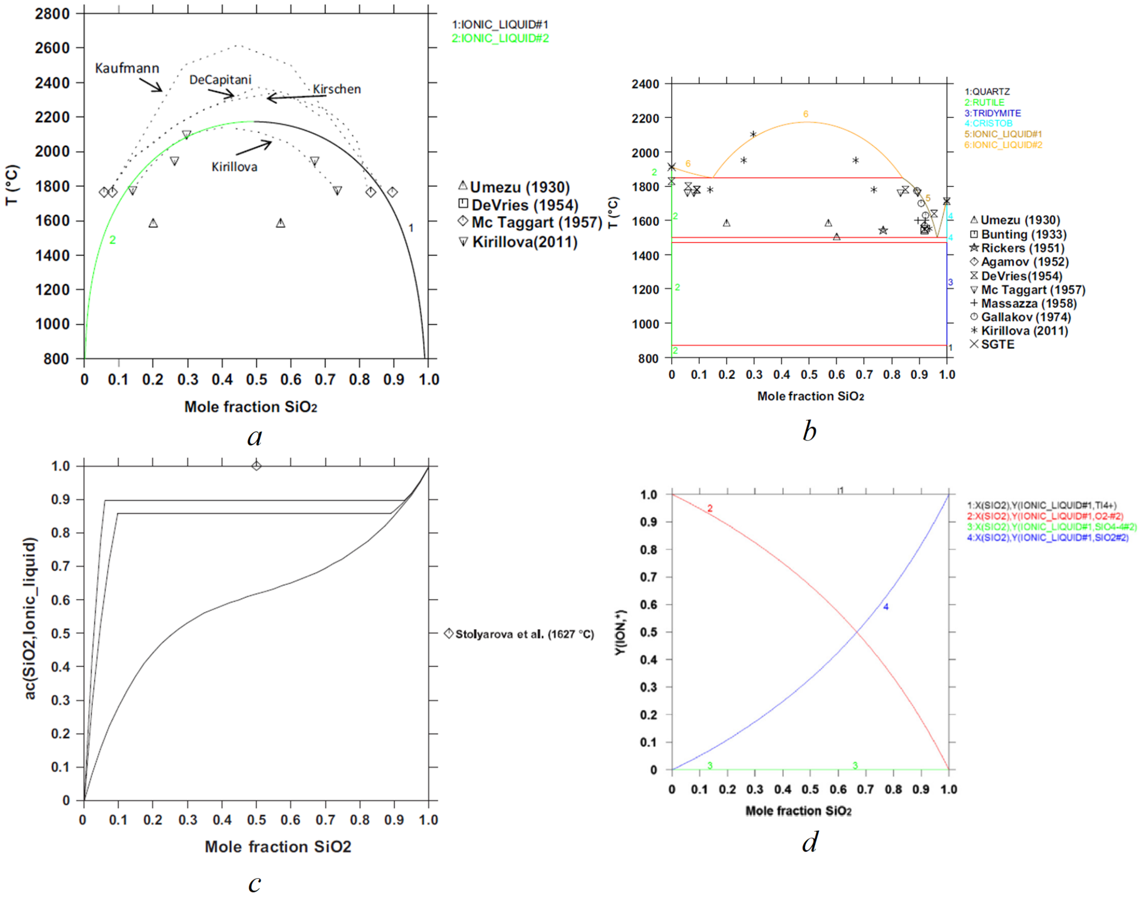

a *b* *c* *d*

FIG. 3. Immiscibility thermodynamic analysis in the TiO_2–SiO_2 system taken from [63]: *a* – calculated miscibility gap, experimental data and models; *b* – calculated miscibility gap, liquidus, terminal phases and experimental data; *c* – SiO_2 activity at 1527, 1627 and 2527 °C, experimental point at 1627 °C; *d* – Y_{ion} for SiO_2, SiO_4^{4-}, O^{2-} species at 2727 °C

an atomic scale, which will contribute to the construction of a complete thermodynamic/dynamic structure describing systems of silicate immiscibility in the liquid phase outside of existing models.

Thus, despite a large number of studies on phase equilibria in the TiO_2–SiO_2 system, there are a number of conflicting information on the position of the phase equilibrium lines that require additional analysis, experimental and calculated refinements.

3. TiO_2–ZrO_2 system

Phase formation in the TiO_2–ZrO_2 system was studied in a number of works [67–98], but only the high-temperature region of the phase diagram is described in detail, as a rule, above 1000–1200 °C. There are very few studies of the behavior of this system in the low-temperature region, as well as those taking into account the particle size of the components. At the same time, for the creation of new materials, including those based on TiO_2–ZrO_2 composites, nanosized compositions can be promising, the reactivity, behavior, structure and properties of which are determined to a large extent by the sizes of their constituent particles [99–105].

The data obtained in [104] show that the nucleation process limits chemical transformations in the low-temperature region in the system under study. The formation of a compound of variable composition $(Zr,Ti)_2O_4$ with a fluorite structure at low temperatures is caused by the formation of the hydroxocomplex $[Zr(OH)_2{\cdot}4H_2O]_4^{8+}(OH)_8^-$ in the structure of which Ti^{4+} ions are dissolved at the stage of precipitation. Moreover, the limiting substitution of Zr^{4+} ions for Ti^{4+} ions in the amorphous hydroxocomplex is significantly lower than 45 mol. %. Thus, the results obtained in this work confirm the promise of an approach to the control of solid-phase chemical transformations and phase transformations in nanostructured systems based on the formation of pre-nucleus clusters with a given structure (see, for example, [106, 107]).

It was noted in [105] that there are significant inconsistencies between the versions of the TiO_2–ZrO_2 phase diagrams regarding the structure and phase field of the existence of zirconium titanate, especially at low temperatures. As a result, a detailed study of the formation of zirconium titanate was carried out. $ZrTiO_4$ nanocrystals with a skrutinite structure (α-PbO_2) were obtained by coprecipitation followed by calcination in air. Phase formation was studied in the temperature range 25–1100 °C using simultaneous thermal analysis, high-temperature diffractometry, and scanning electron microscopy. It was found that crystallization of $ZrTiO_4$ occurs at temperatures above 700 °C after complete removal of water. Nanoceramics based on $ZrTiO_4$ were obtained by sintering the nanopowder at 1200 °C for 5 hours. The thermophysical characteristics of the obtained nanodispersed ceramics were measured using laser pulse analysis and thermomechanical analysis. The resulting ceramics exhibit improved thermal insulation properties (α = 0.138–0.187 mm^2/s, λ = 5.446–11.512 W/(m K)) and a low coefficient of thermal expansion (CTE = (3.45–7.38) $\times$ 10^{-6} K^{-1}) in the temperature range 25–800 °C. This makes the resulting nanoceramics promising as a material for creating thermal barrier coatings.

Fig. 4 shows the known experimental versions of the phase diagrams of the TiO_2–ZrO_2 system. It is easy to see that the data on phase equilibria are replete with discrepancies, both in the region of the solubility of the components in each other, and in the field of the formation of compounds, their nature and character.

It should be noted that in [67] the liquidus curve is shown with the eutectic in exact accordance with the historically first constructed phase diagram [70] (Fig. 4*a*, red lines). Compounds formation was not found in [68]. The phase diagram published in [69] shows the absence of compounds and eutectics at 45–50 mass. % TiO_2 and 1600 °C.

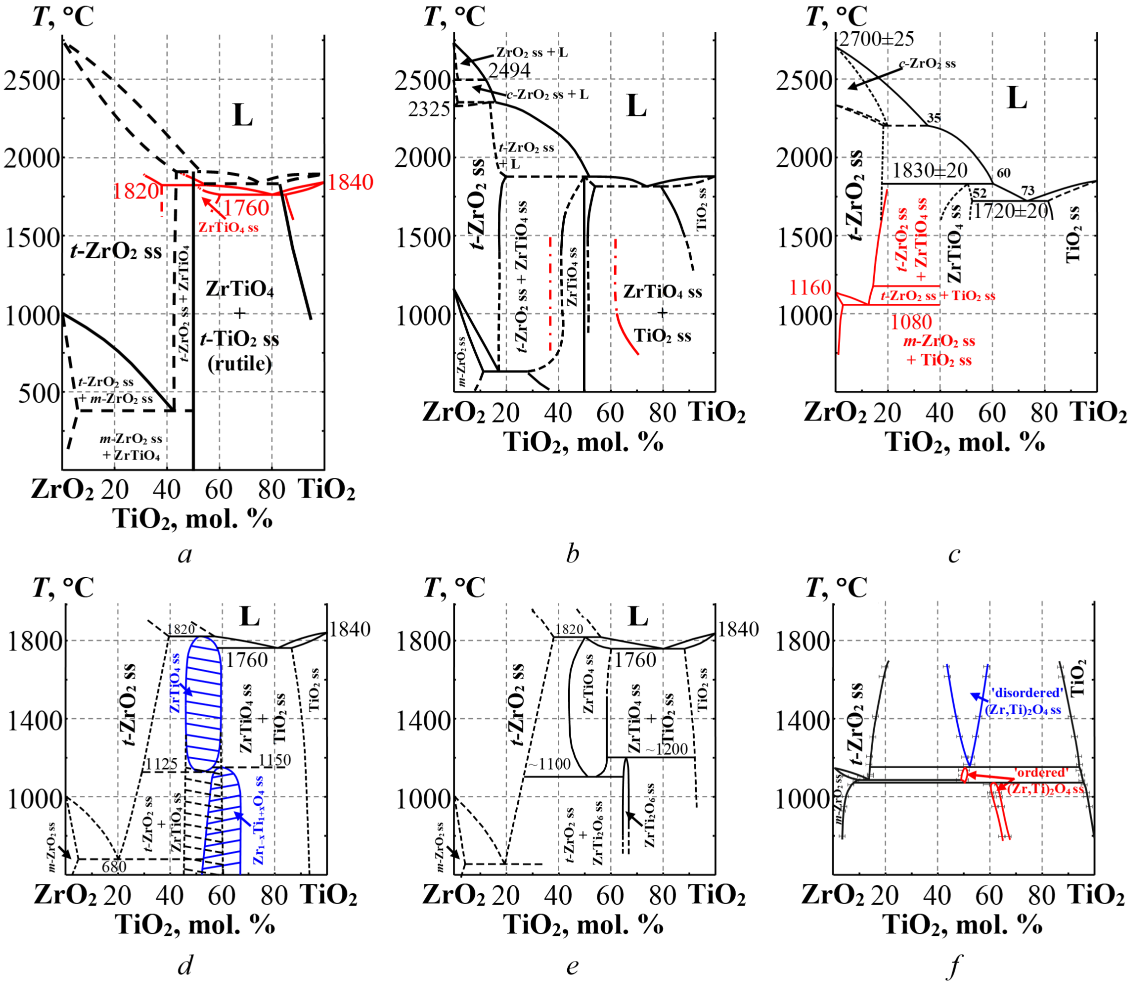

a *b* *c* *d* *e* *f*

FIG. 4. Phase diagram of the TiO_2–ZrO_2 system (experimental study): *a* – red line [70], black line [71], *b* – black line [72, 73, 75, 85], red line [88], *c* – red line [78], black line [79], *d* – [81, 82], *e* – [83], *f* – [96]; ss – solid solution, *m*-, *t*-, *c*- – monoclinic, tetragonal and cubic polymorph, respectively, L – liquid

In [71], fourteen compositions were prepared from zirconium dioxide with impurities less than 1 % and anatase. The samples were mixed, compressed into tablets and heated for two hours in an oxygen-acetylene oven with excess O_2 at 1760 °C. After that, they were heated in an electric resistance furnace at 1370 °C for 336 hours and at 980 °C for 1465 hours. The phases were determined using X-ray diffractometry. The plotted phase diagram (Fig. 4*a*, black lines) does not include the cubic form of the ZrO_2 solid solution or the $ZrTi_2O_6$ phase.

The system has been extensively researched and the phase diagram (Fig. 4*b*, black lines) reproduced the results of other studies [72, 73, 75, 85]. In [72], ZrO_2 (with 2 mass. % HfO_2 and without other spectrographically observed impurities of more than 0.05 %) and TiO_2 (with 1.5 mass. % SiO_2 and without other spectrographically observed impurities of more than 0.005 %) was used. They investigated the solid solution boundaries between ZrO_2 and $ZrTiO_4$, the effect of the TiO_2 solid solution on the monoclinic-tetragonal transition of ZrO_2, and the TiO_2 solid solution boundary. The following analytical methods were used: X-ray diffraction at elevated and room temperatures and electrical conductivity.

In [75, 85], using ZrO_2 with a purity of 99.8 %, including 1.8 mass. % HfO_2 and TiO_2 with a purity of 99.7 %, 18 liquidus points were determined from the solar heating and rapid cooling curves. The temperatures measured by the brightness pyrometer were considered with accuracy up to ±20 °C at 2700 °C and ±15 °C at 1700 °C. In addition, 25 compositions quenched in air from the melt, as well as from 1700 °C were studied by X-ray diffractometry. High temperature X-ray diffractometry was also used on the ZrO_2 rich side to determine the boundaries of the solid solution below 1200 °C. As for the maximum degree of a tetragonal solid solution, the data [75,85] agree with the data [72–74], but differ somewhat from other studies.

The agreement for the lowest transition temperature between monoclinic and tetragonal ZrO_2 is poor. In [75, 85], the dependence of the unit cell parameters on the composition for solid solutions based on ZrO_2, $ZrTiO_4$ and TiO_2 are presented. They also offer a fourth form of ZrO_2 that is stable above 2494 °C, but this is doubtful as it is based solely on small kinks in the rapid cooling curves.

Although other studies [72–75, 85] agree with the end terms of solid solutions and one solid solution based on an intermediate compound, some details of phase equilibria remain a big question.

In [70], the starting materials were dense ZrO_2 with a nominal purity of 99 % and highly purified TiO_2 with a purity of >99.9 %. Samples for 16 compositions were mixed with a binder and compressed into tablets, which were then annealed in air for 4 hours at 1200 °C on Pt foil. After cooling, the samples were crushed, pressed, and annealed for 4 h at 1350 °C in air. X-ray examination showed that the solid phase reactions were completely done. The tablets were then ground, mixed again with the binder, compressed into tablets, from which small four-sided pyramids were ground. These pyramid samples were heated in an oven with resistance heaters and thorium oxide lining with an oxidizing atmosphere to determine the solidus and liquidus temperatures. The rounding of the corners of the pyramids was taken as the temperature of the solidus, and the complete melting was taken as the liquidus. Cooled fused samples and others quenched at temperatures up to 1600 °C were studied petrographically and by X-ray diffraction. The X-ray diffraction pattern of $ZrTiO_4$ powder is indexed as a rhombic phase.

In Fig. 4 (*b*, red lines) show the phase diagram of the TiO_2–ZrO_2 system according to [88]. The precursors were prepared by the sol-gel method, heated to 800 °C, and held at that temperature for 10 h. The products were studied by X-ray diffraction and DTA. Metastable solid solution based on $ZrTiO_4$ is shown by dash-dotted lines. The main diagram is taken from [76] (Fig. 4*b*, black lines).

In [78], analytically pure ZrO_2 and TiO_2 were used as starting materials. The pressed powders were heated in an electric resistance oven for 168 hours. The samples were examined by DTA and X-ray diffractometry. It was found that the ZrO_2 tetragonal solid solution undergoes eutectoid decomposition at 1080 °C. The monoclinic to tetragonal transition of ZrO_2 occurs at 1160 °C and the tetragonal to cubic transition at 2300 °C. The data obtained are shown as a refinement on a fragment of the phase diagram (Fig. 4*c*, red lines).

Twenty-five compositions were prepared from ZrO_2 and TiO_2 of high-purity qualification, pressed into tablets, and heated in a gas (air) furnace at 1700 °C in corundum crucibles in [79]. Sintering and thermal analysis were carried out on air in a solar oven. DTA in a He atmosphere was used to determine the temperatures of formation of $ZrTiO_4$ and eutectic. The phases were studied by X-ray diffraction and microstructural analysis. At 1700 °C, there is a single-phase region of tetragonal zirconia up to about 17.5 mol. % TiO_2, a single-phase solid solution $ZrTiO_4$ from ∼40 to 52 mol. % and a rutile-based solid solution TiO_2 from about 82.5 mol. %. Cooling curves of pure ZrO_2 and ZrO_2-based solid solutions show that cubic ZrO_2 transfers to the tetragonal form at 2330±25 °C and the transition temperature is reduced to 2190 °C by adding TiO_2. The unit cell sizes of various solid solutions are reported. Phase diagrams are constructed (Fig. 4*c*, black lines).

The subsolidus region of the system has attracted and continues to attract close attention of researchers. In papers [81, 82], preliminary data on phase relations are given for the system. The experimental data also are focused around the $ZrTiO_4$ compound. Pure (unalloyed) powders were prepared using alkoxide precursors. It was found that $ZrTiO_4$

solid solutions undergo an order-disorder phase transition, and the phase below ∼1125–1150 °C is only metastable (Fig. 4*d*, dashed lines). The stable phase at temperatures below ∼1150 °C is the solid solution $Zr_{1-x}Ti_{1+x}O_4$. This phase has an incommensurate superstructure, and its structure based on $Zr_5Ti_7O_{24}$ was described in [84]. Evidence for a phase transition in $ZrTiO_4$ was included in [81, 82].

The phase relations in the TiO_2–ZrO_2 system in [83] were investigated near the $ZrTiO_4$ compound by means of an experimental study, including the characterization of both single-crystal and powder samples. Since $ZrTiO_4$ melted incongruently at 1820 °C, it could not be grown directly from the melt of its own composition. Therefore, growth methods using a flux were used [77]. Conventional ceramic powders with particle sizes several orders of magnitude larger than powdered alkoxide precipitates were obtained by solid-phase reaction of high-purity TiO_2 (anatase) and low-hafnium ZrO_2. Several cycles of prolonged thermal treatment at ∼1500 °C with grinding between heat treatments were necessary for the complete reaction to proceed until a homogeneous solid solution was obtained.

The total number of heat treatments varied from ∼3–7 for different compositions. In the case of some compositions, doping with 0.5 mol. % Y_2O_3 was carried out to accelerate the kinetics of phase transitions in order to achieve phase equilibrium in studies. Some compositions were prepared by coprecipitation of a mixed metal alkoxide solution using zirconium n-butoxide [$Zr(OC_4H_9)_4$] and titanium isopropoxide [$Ti(OC_3H_7)_4$] as starting materials and toluene as solvent. The sediment was X-ray amorphous. The average particle size of the agglomerates was from 1.0 to 0.05 μm, and the BET surface area was 350 m^2/g, corresponding to a particle size of 10.5 nm. These powders crystallized at temperatures above 450 °C to a metastable single-phase structure. To achieve true structural equilibrium, prolonged annealing (over 1 month) at temperatures from 500 to 1000 °C was required. Powder X-ray diffraction, neutron powder diffraction, and X-ray diffraction studies on a single-crystal precession chamber were used to characterize the structure of various solid solutions of zirconium titanate prepared and thermally-treated for research.

The presented unit cell parameters were obtained from the refinement of X-ray powder diffraction data using the least squares method [77], with additional refinement using multiple regression analysis to determine the disproportionate vector (intermediate degrees of the *a*-axis superstructure observed during a continuous phase transition from high to low temperature forms of zirconium titanate) when appropriate. The existence of the new compound $ZrTi_2O_6$ as a stable low-temperature phase was confirmed by the recently published discovery of the mineral srilankite [80], which has the same nominal composition and structure. The lattice parameters reported for the new mineral are in good agreement with the results of experiments on low-temperature crystallization at 650 °C using coprecipitated powders. The wide range of solid solution from 35 to 75 mol. % TiO_2 was the result of metastable crystallization at low temperature of the high-temperature disordered α-PbO_2 polytype, and the single-phase field was much wider than the equilibrium region at high temperatures. It was found that minor impurities play a large role in the kinetics of the order-disorder transition in zirconium titanate compositions. The addition of 0.5 % Y_2O_3 to compositions for high-temperature synthesis leads to the fact that the cell of tripled phase, leading to a phase with a Zr : Ti ratio of ∼5 : 7, is in equilibrium with cubic ZrO_2 and $Y_2Ti_2O_7$ pyrochlore. The authors revised the earlier phase diagram of the system represented on Fig. 4*d* to include this new information (Fig. 4*e*).

Fig. 4*f* shows the TiO_2–ZrO_2 phase diagram constructed from experimental data in the range from 800 to 1200 °C (1 atm) [96]. The data above 1200 °C correspond to the data of [92]. The temperature range under consideration was previously inaccessible for equilibrium experiments due to the kinetic features of crystallization of $(Zr,Ti)_2O_4$. The crystallization of the ordered phase from the oxides was facilitated by the addition of a flux (CuO or Li_2MoO_4/MoO_3), and seeds. Note that all phases (tetragonal and monoclinic ZrO_2, ordered and disordered $(Zr,Ti)_2O_4$, TiO_2) are solid solutions, and the phase fields are marked with a predominant end member of the corresponding series. No distinction is made between partially or fully ordered $(Zr,Ti)_2O_4$, and the “ordered” label includes both partially and fully ordered $(Zr,Ti)_2O_4$ in this study.

The method of synthesis at high pressures with flux and seeds, developed previously [93, 94], was successfully applied for synthesis at atmospheric pressure and effectively ensured phase equilibria in the ZrO_2–TiO_2 system at temperatures below 1200 °C. Thus, the phase diagram extended by 400 °C differs from previously published works in that the composition of ordered $(Zr,Ti)_2O_4$ depends more on temperature than is constant [83, 89]. Moreover, the authors of [96] did not find evidence of the previously proposed two-phase field of the coexistence of ordered and disordered $(Zr,Ti)_2O_4$ [97]. Rather, the onset of the ordered transition was marked by the stability of the $(Zr,Ti)_2O_4$ phase with a composition (x_{Ti} = 0.495), which differs both from the disordered $(Zr,Ti)_2O_4$ above 1160 °C and from the ordered $(Zr,Ti)_2O_4$ below 1060 °C. Thus, the two different ordered phases differ in composition. Nevertheless, it was noted in [96] that detailed studies are needed to determine their exact ordering [86].

Many attempts have been made at the thermodynamic optimization of the phase diagram of the TiO_2–ZrO_2 system (Fig. 5). But since there is a wide variety of experimental material, the calculated versions of the diagram also differ greatly.

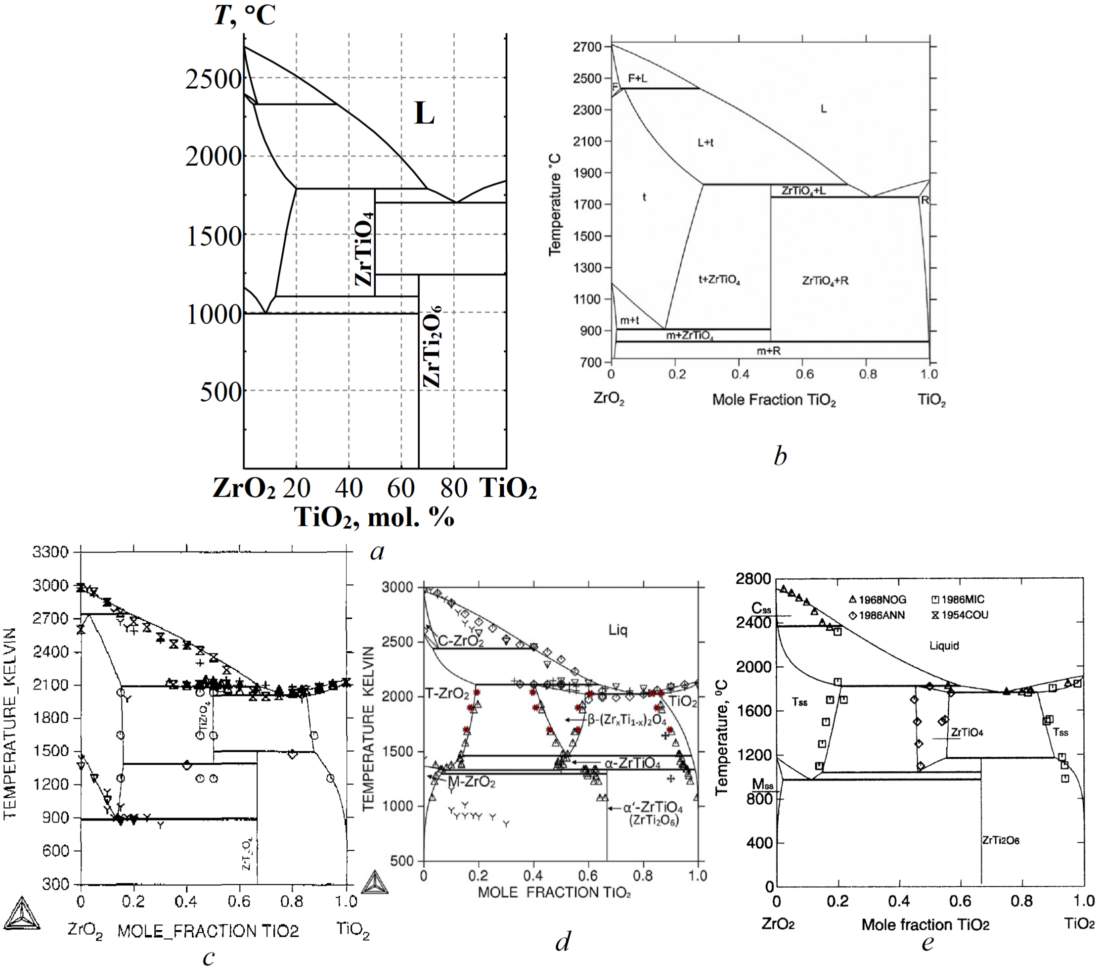

a *b* *c* *d* *e*

FIG. 5. Phase diagram of the TiO_2–ZrO_2 system (thermodynamic optimization): *a* – [85, 87], *b* – [97], *c* – [91], *d* – [98], *e* – [90]; ss – solid solution, *m*-, *t*-, *c*- – monoclinic, tetragonal and cubic polymorph, respectively, R – rutile, L – liquid

Fig. 5*a* shows a calculated version of the phase diagram based on data from [87]. The diagram was calculated using the known thermodynamic data for ZrO_2, various estimates for TiO_2 based on correlations between the interaction parameters and ionic radius [85], and other data. To model the mixing of components, a simple subregular model was adopted using only the ideal entropy of mixing and without taking into account any temperature dependence of the mixing parameter coefficients. The thermodynamic properties of the $ZrTiO_4$ and $ZrTi_2O_6$ compounds relative to hypothetical "cubic" TiO_2 have been determined to comply with the published experimental phase relationships.

Various interaction parameters were used for the crystalline and liquid phases, the solubility of ZrO_2 in TiO_2 was neglected. The parameter of interaction of the liquid phase was adjusted in such a way as to reproduce the peritectic melting of $ZrTiO_4$ at 1820 °C, as well as a temperature of 1760 °C and a composition of 80 mol. % TiO_2 corresponding to the eutectic point.

The thermodynamic optimization of the TiO_2–ZrO_2 phase diagram performed in [97] are in good agreement with the available experimental data (Fig. 5*b*). The presence of two-phase fields between pyrochlore and $ZrTiO_4$, as well as between pyrochlore and *t*-ZrO_2 at 1300 °C, which were not considered in earlier versions of the phase diagram, is essential. Two invariant transition-type reactions were found in calculations and then experimentally confirmed in the temperature range between 1300 and 1500 °C.

The phase diagram of the TiO_2–ZrO_2 system, calculated on the basis of the available experimental data [70–72, 74–76, 79, 83], based on the fact that $ZrTiO_4$ and $ZrTi_2O_6$ are taken as peritectically decomposing stoichiometric compounds, is shown in Fig. 5*c* according to the data of [91].

The phase diagram and thermodynamic data available for the TiO_2–ZrO_2 system were reviewed. An attempt was made to provide a consistent set of thermodynamic parameters describing the system by combining the CALPHAD method using Thermo-Calc software and a database system. The set of thermodynamic functions is intended for a simplified version of the TiO_2–ZrO_2 phase diagram, in which $ZrTiO_4$ and $ZrTi_2O_6$ are considered as stoichiometric compounds. Comprehensive comparisons are made with the available experimental data, and it is shown that the set can satisfactorily take into account most of the experimental data, with the exception of the data on the homogeneity of $ZrTiO_4$ and $ZrTi_2O_6$.

The thermodynamically optimized phase diagram of the TiO_2–ZrO_2 system according to experimental data [98] and data from other authors is shown in Fig. 5*d*.

The phase relationships in the TiO_2–ZrO_2 system were studied in the temperature range from 1000 to 1600 °C using X-ray diffractometry and scanning electron microscopy (SEM) with energy dispersive X-ray spectrometry (EDS). The temperature of peritectic reactions Liquid = β-$(Zr_xTi_{1-x})_2O_4$ + TiO_2 and Liquid + t-ZrO_2 = β-$(Zr_xTi_{1-x})_2O_4$ were determined to be 1756 and 1844 °C, respectively.

The compositions of the eutectic were determined by SEM/EDS as 83.2 ± 1.0 mol. % TiO_2. The temperature of the eutectic reaction Liquid = β-$(Zr_xTi_{1-x})_2O_4$ + TiO_2 determined in this work is in good agreement with other data. The eutectic composition measured in this work contains more TiO_2 compared to previous results. However, the results obtained are within the uncertainty of experimental methods. The enthalpy of formation of the β-$ZrTiO_4$ compound from oxides was measured to be -18.3 ± 5.3 kJ/mol using capillary calorimetry.

The molar heat capacities of the β-$(Zr_xTi_{1-x})_2O_4$ compound were measured in the range –38–950 °C. Experimental data were used for the thermodynamic values (i.e., the heat capacity and enthalpy of formation of the β-$ZrTiO_4$ compound) measured in this work. In order to optimize the description of the heat capacity of α-$ZrTiO_4$ and β-$(Zr_xTi_{1-x})_2O_4$, as well as the contribution of the enthalpy of formation of the β-$Zr_xTi_{1-x}O_4$ phase, respectively. Using the obtained experimental results together with the literature data, thermodynamic parameters were obtained in the TiO_2–ZrO_2 system.

In [90], a thermodynamic description of the TiO_2–ZrO_2 system based on a critical evaluation of limited experimental data from literature is obtained. Non-stoichiometric compound $ZrTiO_4$ is described as $(Ti,Zr)_1O_2$ while $ZrTi_2O_6$ is treated as a stoichiometric phase. Comparison shows that the calculated phase diagram agrees reasonably with the experimental set selected by authors (Fig. 5*e*).

So, in this system, there are many contradictions in both experimental and calculated data. In general, we can conclude that this system needs detailed revision, with independent experimental and calculation expertise.

4. SiO_2–ZrO_2 system

Interest in the phase relationships in the SiO_2–ZrO_2 system in connection with the need for these data for the technology of baddeleyite and zircon refractories has not weakened since [108]. The known variants of state diagrams are shown in Fig. 6.

The most complete version is presented in the experimental work [109] (Fig. 6*b*). Subsequent works are only clarifying on the temperature boundaries of the existence of zircon [110] (Fig. 6*b*), on the region of solid solutions [111] (Fig. 6*c*), and on the border of metastable miscibility gap and the critical point of the immiscible region [112] (Fig. 6*c*).

In [113] (Fig. 6*d*), the Gibbs energies of three solid polymorphic and liquid ZrO_2 were again optimized based on a critical assessment of all available experimental data. All data from the experimental phase diagram and thermodynamic properties of the solid and liquid phases in each binary system were simultaneously evaluated and optimized to obtain a set of model parameters. Certain discrepancies in the phase diagram and thermodynamic data in the literature were eliminated with this optimization. Any type of thermodynamic data and phase equilibria can be calculated using models with optimized parameters.

It can be concluded that this system has been studied in sufficient detail and no additional research is required on it. However, if we discuss the nanoscale state of the components of this system, then it is possible for the manifestation of features that appear to contradict the available data on phase equilibria, for example, the phenomenon of phase selection [114].

An example of phase selection, which is a consequence of the fact that for the formation of a critical nucleus, the condition of a minimum distance between nanoparticles of more than half the size of the critical nucleus must be met, can be the nature of the course of solid-phase processes in systems with different reagent particle sizes of. In particular, the study of the interaction between ZrO_2 and SiO_2 showed that the use of a mixture of ZrO_2 nanoparticles (15–20 nm) with amorphous SiO_2 nanoparticles (about 5 nm) as a reaction composition does not lead to the formation of $ZrSiO_4$, but crystallization of cristobalite occurs. At the same time, during thermal treatment of a mixture of ZrO_2 particles tens of micrometers in size with the same SiO_2 nanoparticles, $ZrSiO_4$ is formed in significant amounts. The explanation for this phenomenon, unusual for the kinetics of solid-phase reactions, when a decrease in the particle size of reagents causes a decrease in the rate of the chemical reaction, is that the size of the critical $ZrSiO_4$ nucleus is much

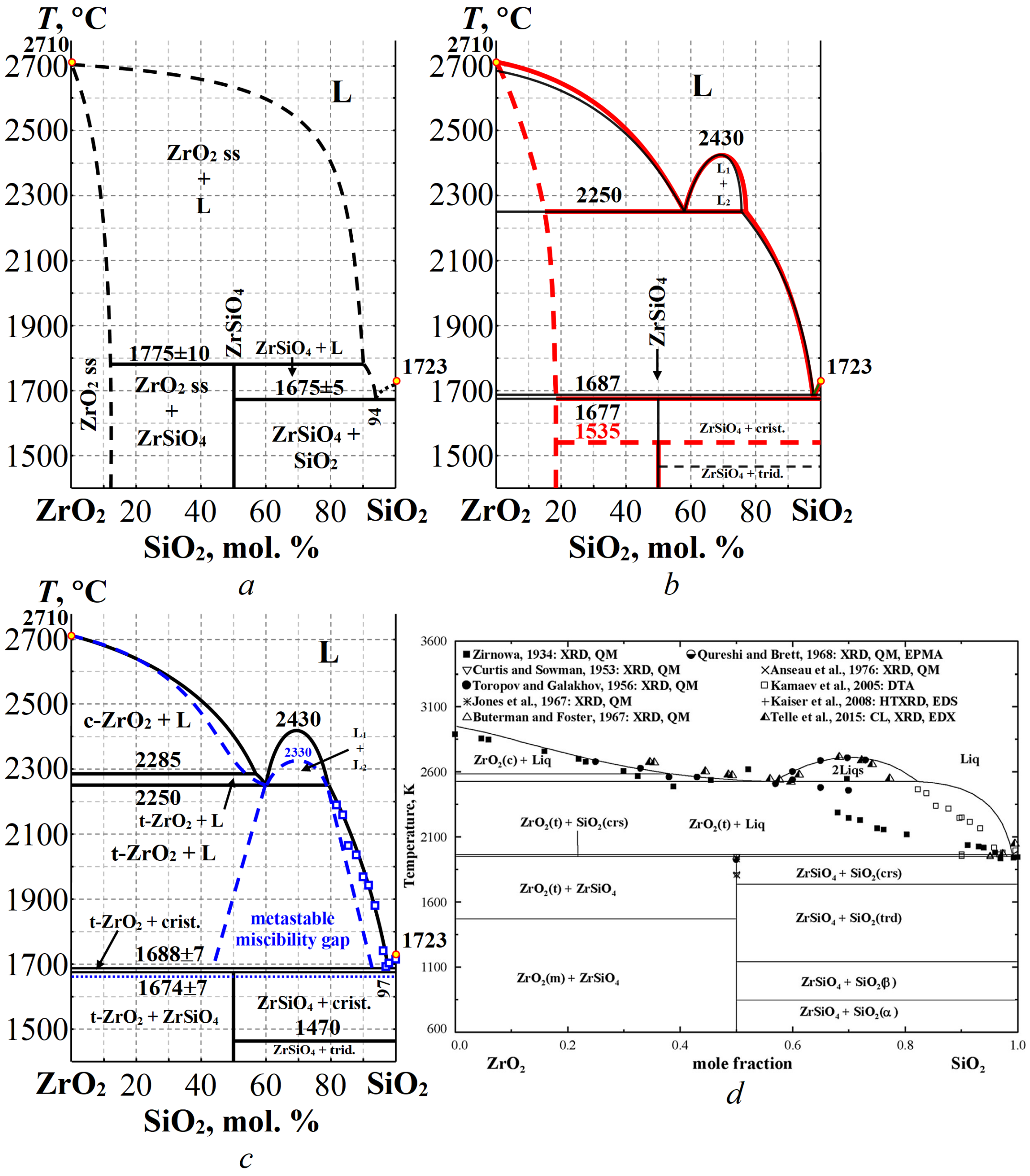

FIG. 6. Phase diagram of the SiO_2–ZrO_2 system: *a* – [108]; *b* – red line [109], black line [110]; *c* – black line [111], blue line and dots [112], *d* – [113]; ss – solid solution, *m*-, *t*-, *c* – monoclinic, tetragonal and cubic polymorph, respectively, trid. – tridymite, crist. – cristobalite, L – liquid

larger than the distance between ZrO_2 nanoparticles in the reaction composition of ZrO_2 and SiO_2 nanoparticles [114]. At the same time, crystallization of cristobalite in a composition of ZrO_2 and SiO_2 nanoparticles is possible, which is explained by the small size of the nuclei of this phase.

It should also be noted that isostructural $ZrSiO_4$ uranium silicate is not formed by high-temperature methods, but is easily synthesized under hydrothermal conditions at relatively low temperatures [115].

5. TiO_2–SiO_2–ZrO_2 system

There are only a few brief works on the study of the TiO_2–SiO_2–ZrO_2 ternary system [51, 116, 117]. In [116], a projection of the liquidus surface was constructed, on which the dashed line indicates the immiscibility area (Fig. 7*a*), as well as two isothermal sections at 1400 °C (Fig. 7*b*) and at 1500 °C (Fig. 7*c*).

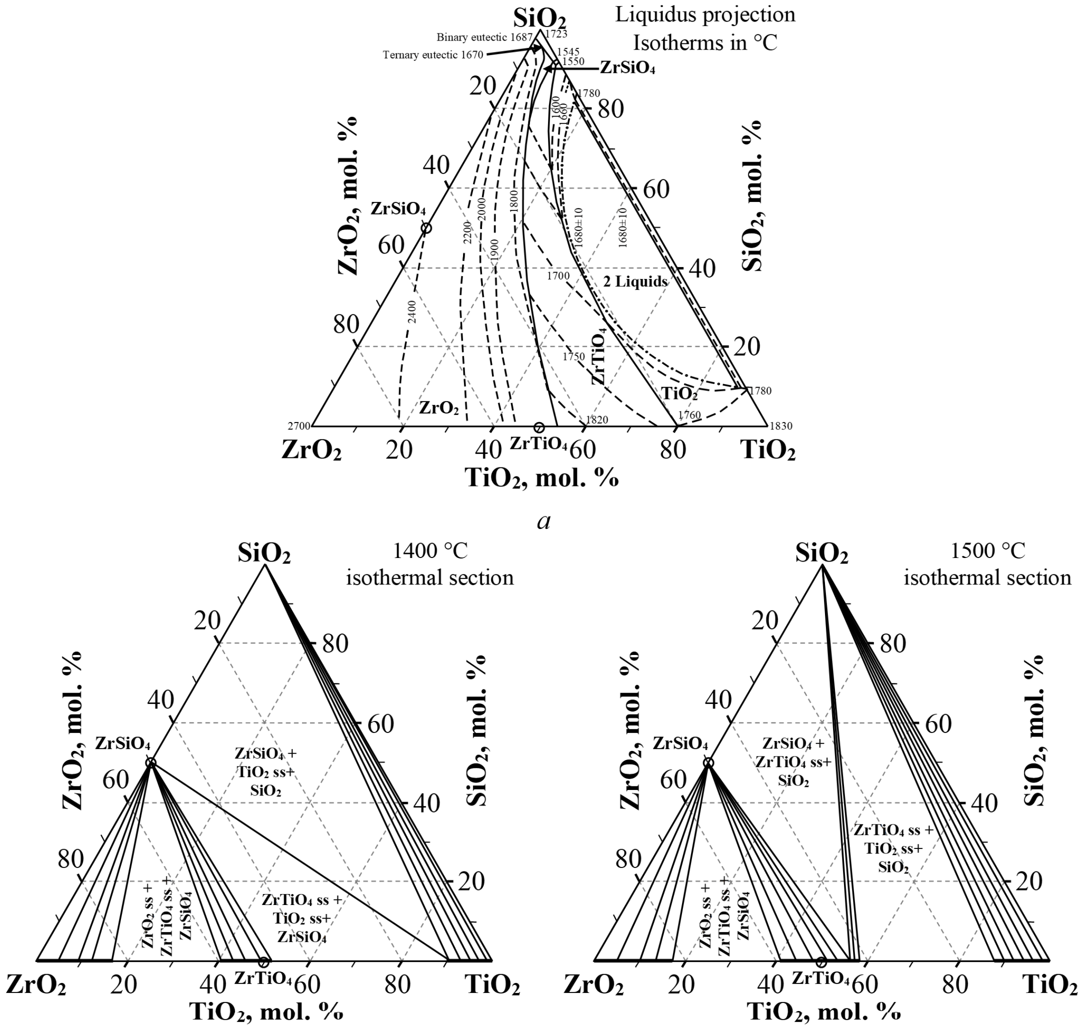

a

b *c*

FIG. 7. Phase diagram of the TiO_2–SiO_2–ZrO_2 system [116]: *a* – liquidus surface projection; *b* – 1400 °C isothermal section; *c* – 1500 °C isothermal section, ss – solid solution

Initial reagents are not described. The original compositions were taken according to previous studies [51, 117] to clarify the critical points. The exact compositions are not given, as are the instruments or research methods. However, most likely, the DTA method was used to obtain data of this type in this temperature range.

Fig. 7*a* is taken from [51] with modification according to the results of study [116] (Fig. 7*b*,*c*) present a summary of several experimental studies of the $ZrSiO_4$–TiO_2 system [117] and the TiO_2–ZrO_2 system [70]. Data are summarized as preliminary experimental results. Three peritectics and one eutectic were found. Only a eutectic at 1500 °C has been suggested by earlier studies in this system. The new critical points appear to be consistent with experimental observations of the cooling and crystallization behavior of the respective compositions, as shown in Fig. 7. Thus, the system needs further detailed research.

6. Conclusions

The incompleteness, contradictions of the available data and the arising problems in the interpretation of study results are demonstrated. As an example, the proposed in [116] topology of the liquidus surface in ternary system does not take into account the presence of a miscibility gap in the binary section of the SiO_2–ZrO_2 system, as well as the character of the liquidus line in the binary TiO_2–ZrO_2 system.

It should be noted that during the preparation of this review a perfect tool was actively used to search for information on phase diagrams – Phase Equilibria Diagrams Online Search System by NIST ACerS [118], which unfortunately has limited availability for free use. The development of such tools and databases makes it possible to significantly simplify the search for the necessary information [119] and reduce routine procedures to a possible minimum [120]. It would be beneficial to see more of these tools, not only commercial, but also freely available. This will undoubtedly contribute to progress in materials science and technology.

The analyzed information allows us to conclude that the design of new materials based on the TiO_2–SiO_2–ZrO_2 system with a given set of physicochemical, structural and dimensional parameters without using data on phase equilibria is almost impossible. It should be especially emphasized that the greatest contradictions in the data are observed in the synthesis and analysis of nanoscale substances and nanomaterials. This feature of the nanoscale state leads to the conclusion that, for completeness, it is necessary to add a dimension factor to the analysis of phase equilibria. At the same time, there are still few examples of such an approach [106]. This greatly complicates and constrains the possibilities of directed synthesis and analysis of nanoscale objects. Thus, a wide field for experiments opens in front of us – a new dimension and a new life of classical physicochemical analysis. By combining the acquisition of these data with the development of software tools that make it possible to work with them comfortably and efficiently, it is possible to bring the design of nanoscale substances and nanostructured materials to a brand-new level.

The question is in which field the new approach will be firstly applied. Of course, for a precedent to grab the attention of researchers, it must be a critically important task in a topical area.

Of great concern today is the energy crisis and the ways out of it. The emphasis is shifting towards nuclear energy as the main hope of overcoming energy and resource problems. But the fact is that at the dawn of the century of atomic energy a great leap forward was made. Many options have been tried, out of which a small number of solutions were preferred. At that date and level of knowledge these decisions seemed optimal. But, the experience of nuclear power development has shown that there are serious safety problems for the most popular solution which seemed ideal – for oxide nuclear fuel in a zirconium cladding.

The serious problem is the zirconium reaction with vapor. If this reaction occurs, then it launches a chain of negative events that aggravate each other. As a result, the probability is very high that a nuclear power plant have a severe accident, such as the Chernobyl and Fukushima-1 accidents, could occur. Thus, with the renaissance of nuclear energy for preventing the described problem, began the development new safer options for fuel assemblies – an advanced accident-tolerant fuel.

One of the solutions to improve fuel safety is the use of special coatings to protect the cladding from oxidation. In particular, a promising coating option are MAX-phases, that have a good compatibility with the cladding material, high ductility and, potentially, good resistance to high temperatures.

At the same time, these phases and their combinations with metallic and oxide materials have not practically been studied, and we need experimental and theoretical evidence of their effectiveness. The first and most important step on the way is the study of phase equilibria. In particular, it is necessary to know what happens with that coating under oxidizing conditions at high temperatures. This requires comprehensive physicochemical information not only about MAX-phases, but their oxidation products and possible interactions.

For that, a critical analysis was carried out for the synthetic possibilities, the conditions for high-temperature experiments, the assessment of nonequilibrium phase formation in binary systems and information about the TiO_2–SiO_2–ZrO_2 system which is the currently available. It will allow us to further take into account the features of phase formation and phase equilibria in the TiO_2–SiO_2–ZrO_2 system at high temperatures and in nanoscale to evaluate the stability limits of MAX-phases in conditions at severe accidents on nuclear power plants.

Successful implementation of this or another actual problem must demonstrate the effectiveness of the described approach. We are hope to see this.

Acknowledgement

The authors are grateful to Corresponding Member of the Russian Academy of Sciences Professor Victor V. Gusarov for fruitful discussions and advices on improving the quality of this review.

The reported study was funded by Russian Foundation for Basic Research and ROSATOM (project no. 20-21-00056).

References

[1] Retention of Molten Core Materials in Water-Cooled Reactors (RASPLAV and MASCA International Projects), Ed. by V.G. Asmolov, A.Yu. Rumyantsev, and V.F. Strizhov, Moscow, Rosenergoatom, 2018, 576 p. [in Russian].

[2] Gonzalez-Julian J. Processing of MAX phases: From synthesis to applications. *J. Am. Ceram. Soc.*, 2021, **104**(2), P. 659–690.

[3] Zhang Z., Duan X., Jia D., Zhou Y., van der Zwaag S. On the formation mechanisms and properties of MAX phases: A review. *J. Eur. Ceram. Soc.*, 2021, **41**(7), P. 3851–3878.

[4] Medvedeva N.I., Enyashin A.N., Ivanovskii A.L. Modeling of the electronic structure, chemical bonding, and properties of ternary silicon carbide Ti_3SiC_2. *J. Struct. Chem.*, 2011, **52**(4), P. 785–802.

[5] Arkundato A., Hasan M., Pramutadi A., Rivai A.K., Su'ud Z. Thermodynamics and Structural Properties of Ti_3SiC_2 in Liquid Lead Coolant. *J. Phys. Conf. Ser.*, 2020, **1493**, Article 012026.

[6] Tretyakov Yu.D. Self-organisation processes in the chemistry of materials. *Russ. Chem. Rev.*, 2003, **72**(8), P. 651–679.

[7] Gleiter H. Nanostructured materials: Basic concepts and microstructure. *Acta Mater.*, 2000, **48**(1), P. 1–29.

[8] Ozin G.A., Arsenault A.C., Cademartiri L. *Nanochemistry: A Chemical Approach to Nanomaterials*, 2nd ed. Cambridge: Royal Society of Chemistry, 2009, 820 p.

[9] Ivanov V.V., Talanov V.M. Principle of modular building of nanostructures: the information codes and the combinatorial design. *Nanosyst.: Phys. Chem. Math.*, 2010, **1**(1), P. 72–107 [in Russian].

[10] Galakhov F.Ya., Varshal B.G. On the causes of liquation in simple silicate systems. Proceedings of the First All-Union Symposium "Liquidation Phenomena in Glass", Leningrad, April 16–18, 1968, Leningrad: "Nauka", 1969, P. 6–11 [in Russian].

[11] Porai-Koshits E.A., Averyanov V.I. On the phenomena of primary and secondary immiscibility in glasses. Proceedings of the First All-Union Symposium "Liquidation Phenomena in Glass", Leningrad, April 16–18, 1968, Leningrad, Nauka, 1969, P. 26–30 [in Russian].

[12] Galakhov F.Ya. Microliquation and Its Image on the Binary System State Diagram. *Bull. Acad. Sci. USSR, Chem. Ser.*, 1964, **8**, P. 1377–1383 [in Russian].

[13] Andreev N.S., Mazurin O.V., Porai-Koshits E.A., Roslova G.P., Filippovich V.N. *Phenomena of liquation in glasses*. Ed. M.M. Schultz, Leningrad, Nauka, 1974, 217 p. [in Russian].

[14] Hudon P., Baker D.R. The nature of phase separation in binary oxide melts and glasses. I. Silicate systems. *J. Non-Cryst. Solids*, 2002, **303**(3), P. 299–345.

[15] Hudon P., Baker D.R. The nature of phase separation in binary oxide melts and glasses. II. Selective solution mechanism. *J. Non-Cryst. Solids*, 2002, **303**(3), P. 346–353.

[16] Hudon P., Baker D.R. The nature of phase separation in binary oxide melts and glasses. III. Borate and germanate systems. *J. Non-Cryst. Solids*, 2002, **303**(3), P. 354–371.

[17] Mriglod I.M., Patsagan O.V., Melnik R.S. Metastable liquation processes in multicomponent glass-forming systems: a review of experimental and theoretical results; phase diagrams with metastable segregation. Preprint IFCS NAS Ukraine, ICMP-03-15U, 2003, 22 p. [In Ukrainian].

[18] Kündig A.A., Ohnuma M., Ping D.H., Ohkubo T., Hono K. In situ formed two-phase metallic glass with surface fractal microstructure. *Acta Mater.*, 2004, **52**(8), P. 2441–2448.

[19] Chang H.J., Yook W., Park E.S., Kyeong J.S., Kim D.H. Synthesis of metallic glass composites using phase separation phenomena. *Acta Mater.*, 2010, **58**(7), P. 2483–2491.

[20] Delitsyn L.M. Liquid immiscibility phenomena in magmatic systems, Moscow, GEOS, 2010, 222 p.

[21] Blinova I.V., Gusarov V.V., Popov I.Yu. "Almost quasistationary" approximation for the problem of solidification front stability. *Z. Angew. Math. Phys.*, 2009, **60**(1), P. 178–188.

[22] Eliseev A.A., Lukashin A.V. Functional nanomaterials. Ed. Yu.D. Tretyakov. Moscow, FIZMATLIT, 2010, 456 p.

[23] Trusov L.A., Zaitsev D.D., Kazin P.E., Tret'yakov Yu.D., Jansen M. Preparation of Magnetic Composites through SrO–Fe_2O_3–Al_2O_3–B_2O_3 Glass Crystallization. *Inorg. Mater.*, 2009, **45**(6), P. 689–693.

[24] Kazin P.E., Trusov L.A., Zaitsev D.D., Tret'yakov Yu.D. Glass Crystallization Synthesis of Ultrafine Hexagonal M-Type Ferrites: Particle Morphology and Magnetic Characteristics. *Russ. J. Inorg. Chem.*, 2009, **54**(14), P. 2081–2090.

[25] Kazin P.E., Trusov L.A., Kushnir S.E., Yaroshinskaya N.V., Petrov N.A., Jansen M. Hexaferrite Submicron and Nanoparticles with Variable Size and Shape via Glass-Ceramic Route. *J. Phys. Conf. Ser.*, 2010, **200**(7), Article 072048.

[26] Khodakovskaya R.Ya. Chemistry of titanium-containing glasses and sitalls. Moscow, Khimiya, 1978, 288 p. [in Russian].

[27] von Olleschik-Elbheim L., el Baya A., Schmidt M.A., Zhu D.-M., Kosugi T. Thermal conductivity of GeO_2–SiO_2 and TiO_2–SiO_2 mixed glasses. *J. Non-Cryst. Solids*, 1996, **202**(1), P. 88–92.

[28] You H., Nogami M. Persistent spectral hole burning of Eu^{3+} ions in TiO_2–SiO_2 glass prepared by sol-gel method. *J. Alloys Compd.*, 2006, **408–412**, P. 796–799.

[29] Lebedeva G.A. Formation of a liquation structure in titanium-containing aluminosilicate glasses. *Glass and Ceramics*, 2008, **9**, P. 25–28 [in Russian].

[30] Scannell G., Koike A., Huang L. Structure and thermo-mechanical response of TiO_2–SiO_2 glasses to temperature. *J. Non-Cryst. Solids*, 2016, **447**, P. 238–247.

[31] Romy Dwipa Y. Away, Chika Takai-Yamashita, Takayuki Ban, Yutaka Ohya. Photocatalytic properties of TiO_2–SiO_2 sandwich multilayer films prepared by sol-gel dip-coating. *Thin Solid Films*, 2021, **720**, Article 138522.

[32] Yorov K.E., Kolesnik I.V., Romanova I.P., Mamaeva Yu.B., Lermontov S.A., Kopitsa G.P., Baranchikov A.E., Ivanov V.K. Engineering SiO_2–TiO_2 binary aerogels for sun protection and cosmetic applications. *J. Supercrit. Fluid.*, 2021, **169**, Article 105099.

[33] Sun S., Ding H., Wang J., Li W., Hao Q. Preparation of a microsphere SiO_2/TiO_2 composite pigment: The mechanism of improving pigment properties by SiO_2. *Ceram. Int.*, 2020, **46**(14), P. 22944–22953.

[34] Llamas S., Ponce Torres A., Liggieri L., Santini E., Ravera F. Surface properties of binary TiO_2–SiO_2 nanoparticle dispersions relevant for foams stabilization. *Colloids Surf. A Physicochem. Eng. Asp.*, 2019, **575**, P. 299–309.

[35] Ren Y., Li W., Cao Z., Jiao Y., Xu J., Liu P., Li S., Li X. Robust TiO_2 nanorods-SiO_2 core-shell coating with high-performance self-cleaning properties under visible light. *Appl. Surf. Sci.*, 2020, **509**, Article 145377.

[36] Wang T., Li Y., Wu W.-T., Zhang Y., Wu L., Chen H. Effect of chiral-arrangement on the solar adsorption of black TiO_2–SiO_2 mesoporous materials for photodegradation and photolysis. *Appl. Surf. Sci.*, 2021, **537**, Article 148025.

[37] Bao Y., Guo R., Gao M., Kang Q., Ma J. Morphology control of 3D hierarchical urchin-like hollow SiO_2@TiO_2 spheres for photocatalytic degradation: Influence of calcination temperature. *J. Alloys Compd.*, 2021, **853**, Article 157202.

[38] Shabanova N.A., Popov V.V., Sarkisov P.D. *Chemistry and technology of nanodispersed oxides*. Moscow, Akademkniga, 2006, 309 p. [in Russian].

[39] Ermilov P.I., Indeikin E.A., Tolmachev I.A. Pigments and pigmented paintwork materials. Leningrad, Khimiya, 1987, 200 p. [in Russian].

[40] *Titanium Dioxide (TiO_2) and Its Applications*. A volume in Metal Oxides. Edited by F. Parrino, L. Palmisano. Amsterdam, Elsevier, 2020, 702 p.

[41] Rieke R. Melting Influence of Titanic Acid on Silica, Alumina, and Kaolin. *Sprechsaal*, 1908, **41**, P. 405.

[42] Umezu S., Kakiuchi F. Investigations on Iron Blast. Furnace Slags Containing Titanium. *Nippon Kogyo Kwaishi*, 1930, **46**, P. 866–877.

[43] Bogatzkii D.P. Investigation of the system TiO_2–SiO_2. *Metallurgist*, 1938, **11**, P. 59–67 [in Russian].

[44] Bunting E.N. Phase equilibria in the systems. TiO_2, TiO_2–SiO_2, and TiO_2–Al_2O_3. *J. Res. Nat. Bur. Stand.*, 1933, **11**(5), P. 719–725.

[45] Ricker R.W., Hummel F.A. Reactions in the System TiO_2–SiO_2; Revision of the Phase Diagram. *J. Amer. Ceram. Soc.*, 1951, **34**(9), P. 271–279.

[46] DeVries R.C., Roy R., Osborn E.F. The System TiO_2–SiO_2. *Trans. Brit. Ceram. Soc.*, 1954, **53**(9), P. 525–540.

[47] Kaufman L. Calculation of multicomponent ceramic phase diagrams. *Physica B+C (Amsterdam)*, 1988, **150**(1–2), P. 99–114.

[48] Kubaschewski O., Alcock C.B. International Series on Materials Science and Technology, V. 24 (Metallurgical Thermochemistry), 5th ed. Oxford, United Kingdom: Pergamon Press, Elsevier Science Ltd., 1979, 449 p.

[49] DeCapitani C., Kirschen M. A generalized multicomponent excess function with application to immiscible liquids in the system CaO–SiO_2–TiO_2. *Geochim. Et Cosmochim. Acta*, 1998, **62**(23/24), P. 3753–3763.

[50] Kirschen M., DeCapitani C., Millot F., Rifflet J.-C., Coutures J.-P. Immiscible silicate liquids in the system SiO_2–TiO_2–Al_2O_3. *Eur. J. Mineral.*, 1999, **11**, P. 427–440.

[51] Don McTaggart G., Andrews A.I. Immiscibility Area in the System TiO_2–ZrO_2–SiO_2. *J. Am. Ceram. Soc.*, 1957, **40**(5), P. 167–170.

[52] Massazza F., Sirchia E. Il sistema MgO–SiO_2–TiO_2. *La Chimica e l'industria*, 1958, **XL**(5), P. 376–380.

[53] Galakhov F.Ya., Areshev M.P., Vavilonova V.T., Aver'yanov V.I. Determination of the boundaries of metastable liquation in the silica part of the TiO_2–SiO_2 system. *Izv. Akad. Nauk SSSR, Ser. Neorg. Mater.*, 1974, **10**(1), P. 179–180 [in Russian].

[54] Saunders N., Miodownik A.P. CALPHAD (calculation of phase diagrams): a comprehensive guide. Pergamon materials series. Vol. 1, 1998, 479 p.

[55] Kamaev D.N. High-temperature phase equilibria in TiO_2–SiO_2, ZrO_2–Al_2O_3, ZrO_2–SiO_2, FeO–ZrO_2–SiO_2, Fe–Zr–Si–O systems: dissertation ... candidate of chemical sciences: 02.00.04. Chelyabinsk, 2005, 168 p. [in Russian].

[56] Mikhailov G.G., Novolotskiy D.Ya. Thermodynamics of steel deoxidation. Moscow, Metallurgy, 1993, 114 p. [in Russian].

[57] Kirillova S.A., Al'myashev V.I., Gusarov V.V. Phase Relationships in the SiO_2–TiO_2 System. *Russ. J. Inorg. Chem.*, 2011, **56**(9), P. 1464–1471.

[58] Kirillova S.A., Almjashev V.I., Gusarov V.V. Spinodal decomposition in the SiO_2–TiO_2 system and hierarchically organized nanostructures formation. *Nanosyst.: Phys. Chem. Math.*, 2012, **3**(2), P. 100–115 [in Russian].

[59] Gurvich L.V., Iorish V.S., Chekhovskoi D.V., Yungman V.S. IVTANTHERMO – A Thermodynamical Database and Software System for the Personal Computer. User's Guide. CRC Press, Inc., Boca Raton, 1993.

[60] Hlaváč J. Melting temperatures of refractory oxides: Part I. *Pure & Appl. Chem.*, 1982, **54**(3), P. 681–688.

[61] Chase Jr., M.W. NIST-JANAF Thermochemical Tables (Journal of Physical and Chemical Reference Data Monographs), 4th ed., Monograph No. 9. American Institute of Physics, 1998–2000, 1952 p.

[62] Almjashev V.I., Gusarov V.V., Khabensky V.B., Bechta S.V., Granovsky V.S. Influence of the temperature difference at immiscibility liquids interface on their phase instability. OECD/NEA MASCA2 Seminar 2007, Cadarache, France, 11–12 October 2007, 2007, paper 3.3.

[63] Boulay E., Nakano J., Turner S., Idrissi H., Schryvers D., Godet S. Critical assessments and thermodynamic modeling of BaO–SiO_2 and SiO_2–TiO_2 systems and their extensions into liquid immiscibility in the BaO–SiO_2–TiO_2 system. *CALPHAD*, 2014, **47**, P. 68–82.

[64] Lu X., Jin Z. Thermodynamic assessment of the BaO–TiO_2 quasibinary system. *CALPHAD*, 2000, **24**(3), P. 319–338.

[65] Stolyarova V.L., Lopatin S.I. Mass-spectrometric study of the vaporization and thermodynamic properties of components in the BaO–TiO_2–SiO_2 system. *Glass Phys. Chem.*, 2005, **31**(2), P. 132–137.

[66] Zhang C., Ge X., Hu Q., Yang F., Lai P., Shi C., Lu W., Li J. Atomic scale structural analysis of liquid immiscibility in binary silicate melt: A case of SiO_2–TiO_2 system. *J. Mater. Sci. Technol.*, 2020, **53**, P. 53–60.

[67] Von Wartenberg H., Gurr W. Schmelzdiagramme höchstfeuerfester Oxyde. III. *Z. Anorg. Allg. Chem.*, 1931, **196**(1), P. 374–383.

[68] Büssem W., Schusterius C., Ungewiss A. X-Ray Investigations of the Binary Systems TiO_2–MgO, ZrO_2–MgO, and ZrO_2–TiO_2. *Ber. Dtsch. Keram. Ges.*, 1937, **18**(10), P. 433–443.

[69] Sowman H.G., Andrews A.I. A Study of the Phase Relations of ZrO_2–TiO_2 and ZrO_2–TiO_2–SiO_2. *J. Am. Ceram. Soc.*, 1951, **34**(10), P. 298–301.

[70] Coughanour L.W., Roth R.S., DeProsse V.A. Phase equilibrium relations in the systems lime-titania and zirconia-titania. *J. Res. Natl. Bur. Stand. (U. S.)*, 1954, **52**(1), P. 37–42.

[71] Brown Jr. F.H., Duwez P. The Zirconia-Titania System. *J. Am. Ceram. Soc.*, 1954, **37**(3), P. 129–132.

[72] Cocco A., Torriano G. Relations between the solid phases in the system ZrO_2–TiO_2. *Ann. Chim. (Rome)*, 1965, **55**(3), P. 153–163.

[73] Cocco A., Torriano G. *Ann. Chim. (Rome)*, 1958, **48**(8/9), P. 587–599.

[74] Webster A.H., MacDonald R.C., Bowman W.S. The System PbO–ZrO_2–TiO_2 at 1100 °C. *J. Can. Ceram. Soc.*, 1965, **34**, P. 97–102.

[75] Noguchi T., Mizuno M. Phase changes in solids measured in a solar furnace ZrO_2–TiO_2 system. *Sol. Energy*, 1967, **11**(1), P. 56–61.

[76] Noguchi T., Mizuno M. Phase changes in the ZrO_2–TiO_2 system. *Bull. Chem. Soc. Jpn.*, 1968, **41**(12), P. 2895–2899.

[77] Sugai T., Hasegawa S. Growth of zirconium titanate ($ZrTiO_4$) single crystals from molten salts. *J. Geram. Assoc. Japan*, 1968, **76**(12), P. 429–430.

[78] Ono A. Solid solutions in the system ZrO_2–TiO_2. *Mineral. J.*, 1972, **6**(6), P. 433–441.

[79] Shevchenko A.V., Lopato L.M., Maister I.M., Gorbunov O.S. The TiO_2–ZrO_2 system. *Russ. J. Inorg. Chem.*, 1980, **25**(9), P. 1379–1381.

[80] Willgallis A., Seigmann E., Hettiarachi T. Srilankite, a new Zr-Ti-oxide mineral. *Neues Jahrb. für Mineral. Monatshefte*, 1983, **4**, P. 151–157.

[81] Domingues L.P., McHale A.E., Negas T., Roth R.S. Processing and properties of $ZrTiO_4$-Based Ceramics; P. A21-A21 in International Conf. on the Science and Technology of Zirconia, Extended Abstract, 2nd, Stuttgart, Germany, June 21–23, 1983.

[82] McHale A.E., Roth R.S. Investigation of the Phase Transition in $ZrTiO_4$ and $ZrTiO_4$-SnO_2 Solid Solutions. *J. Am. Ceram. Soc.*, 1983, **66**(2), P. C18–C20.

[83] McHale A.E., Roth R.S. Low-Temperature Phase Relationships in the System ZrO_2–TiO_2. *J. Am. Ceram. Soc.*, 1986, **69**(11), P. 827–832.

[84] Bordet P., McHale A.E., Santoro A., Roth R.S. Powder neutron diffraction study of $ZrTiO_4$, $Zr_5Ti_7O_{24}$, and $FeNb_2O_6$. *J. Solid State Chem.*, 1986, **64**(1), P. 30–46.

[85] Kim D.-J. Lattice Parameters, Ionic Conductivities, and Solubility Limits in Fluorite-Structure MO_2 Oxide [M = Hf^{4+}, Zr^{4+}, Ce^{4+}, Th^{4+}, U^{4+}] Solid Solutions. *J. Am. Ceram. Soc.*, 1989, **72**(8), P. 1415–1421.

[86] Christoffersen R., Davies P.K. Structure of Commensurate and Incommensurate Ordered Phases in the System $ZrTiO_4$–$Zr_5Ti_7O_{24}$. *J. Am. Ceram. Soc.*, 1992, **75**(3), P. 563–569.

[87] Yokokawa H., Sakai N., Kawada T., Dokiya M. Phase Diagram Calculations for ZrO_2 Based Ceramics: Thermodynamic Regularities in Zirconate Formation and Solubilities of Transition Metal Oxides. P. 59–68 in Sci. Technol. Zirconia V, [Int. Conf.], 5th, Melbourne, Australia, August 16–21, 1992. Edited by S.P.S. Badwal, M.J. Bannister, and R.H.J. Hannink, Technomic Publishing Co., Inc., Lancaster, Pennsylvania, 1993.

[88] Kobayashi K., Kato K., Terabe K., Yamaguchi S., Iguchi Y. Metastable Phase Relationship in the ZrO_2–$YO_{1.5}$, ZrO_2–TiO_2 and $YO_{1.5}$–TiO_2 Systems. *J. Ceram. Soc. JAPAN*, 1998, **106**(1236), P. 782–786.

[89] Sham E.L., Aranda M.A.G., Farfan-Torres E.M., Gottifredi J.C., Martínez-Lara M., Bruque S. Zirconium titanate from sol–gel synthesis: thermal decomposition and quantitative phase analysis. *J. Solid State Chem.*, 1998, **139**(2), P. 225–232.

[90] Gong W., Jin Z., Du Y. Thermodynamic Assessment of the ZrO_2–TiO_2 Quasibinary System. *J. Min. Met.*, 2000, **36**(3–4)B, P. 123–132.

[91] Park J.-H., Liang P., Seifert H.J., Aldinger F., Koo B.-K., Kim H.-G. Thermodynamic Assessment of the ZrO_2–TiO_2 System. *J. Korean Ceram. Soc.*, 2001, **7**(1), P. 11–15.

[92] Troitzsch U., Ellis D.J. High-PT study of solid solutions in the system ZrO_2-TiO_2: The stability of srilankite. *Eur. J. Mineral.*, 2004, **16**(4), P. 577–584.

[93] Troitzsch U., Christy A.G., Ellis D.J. Synthesis of Ordered Zirconium Titanate $(Zr,Ti)_2O_4$ from the Oxides Using Fluxes. *J. Am. Ceram. Soc.*, 2004, **87**(11), P. 2058–2063.

[94] Troitzsch U., Ellis D.J., Christy, A.G. (2003–2006). Patent: Synthesis of Ceramic Crystals. Patent Application No. 2003906410 (Australian), PCT/AU2004/001615 WO 2005049497 (International).

[95] Troitzsch U., Christy A.G., Ellis D.J. The crystal structure of disordered $(Zr,Ti)O_2$ solid solution including srilankite: evolution towards tetragonal ZrO_2 with increasing Zr. *Phys. Chem. Miner.*, 2005, **32**(7), P. 504–514.

[96] Troitzsch U., Ellis D.J. The ZrO_2–TiO_2 phase diagram. *J. Mater. Sci.*, 2005, **40**(17), P. 4571–4577.

[97] Schaedler T.A., Fabrichnaya O., Levi C.G. Phase equilibria in the TiO_2–$YO_{1.5}$–ZrO_2 system. *J. Eur. Ceram. Soc.*, 2008, **28**(13), P. 2509–2520.

[98] Saenko I., Ilatovskaia M., Savinykh G., Fabrichnaya O. Experimental investigation of phase relations and thermodynamic properties in the ZrO_2–TiO_2 system. *J. Am. Ceram. Soc.*, 2018, **101**(1), P. 386–399.

[99] Andrievsky R.A., Ragulya A.V. *Nanostructured materials*. Moscow, Ed. Center “Academy”, 2005, 192 p. [in Russian].

[100] Bae D.-S., Han K.-S., Choi S.-H. Fabrication and microstructure of TiO_2–ZrO_2 composite membranes. *J. Mater. Sci. Lett.*, 1997, **16**(8), P. 658–660.

[101] Guo H., Zhao S., Wu X., Qi, H. Fabrication and characterization of TiO_2/ZrO_2 ceramic membranes for nanofiltration. *Microporous Mesoporous Mater.*, 2018, **260**, P. 125–131.

[102] Hwang D.-H., Lee B.-H. Synthesis and Formation Mechanism of $ZrTiO_4$ Gray Pigment. *J. Korean Ceram. Soc.*, 2012, **49**(1), P. 84–89.

[103] Wang C.L., Lee H.Y., Azough F., Freer R. The microstructure and microwave dielectric properties of zirconium titanate ceramics in the solid solution system $ZrTiO_4$–$Zr_5Ti_7O_{24}$. *J. Mater. Sci.*, 1997, **32**(7), P. 1693–1701.

[104] Vasilevskaya A.K., Almyasheva O.V. Features of phase formation in the ZrO_2–TiO_2 system under hydrothermal conditions. *Nanosyst.: Phys. Chem. Math.*, 2012, **3**(4), P. 75–81 [in Russian].

[105] Bachina A.K., Almjasheva O.V., Danilovich D.P., Popkov V.I. Synthesis, Crystal Structure, and Thermophysical Properties of $ZrTiO_4$ Nanoceramics. *Russ. J. Phys. Chem. A*, 2021, **95**(8), P. 1529–1536.

[106] Gusarov V.V. Rapid solid-phase chemical reactions. *Russ. J. Gen. Chem.*, 1997, **67**(12), P. 1959–1964 [in Russian].

[107] Almyasheva O.V. Hydrothermal synthesis, structure and properties of nanocrystals and nanocomposites in the ZrO_2–Al_2O_3–SiO_2 system: dissertation abstract ... candidate of chemical sciences: 02.00.04, St. Petersburg, 2007, 24 p. [in Russian].

[108] McMurdie H.F., Hall F.P. Phase diagrams for ceramists: Supplement No. 1. *J. Am. Ceram. Soc.*, 1949, **32**(s1), P. 154–164.

[109] Toropov N.A., Galakhov F.Ya. Liquid immiscibility in the ZrO_2–SiO_2 system. *Izv. Akad. Nauk SSSR, Otd. Khim. Nauk*, 1956, **2**, P. 157–162 [in Russian].

[110] Jones T.S., Kimura S., Muan A. Phase Relations in the System FeO-Fe_2O_3-ZrO_2-SiO_2. *J. Am. Ceram. Soc.*, 1967, **50**(3), P. 137–142.

[111] Butterman W.C., Foster W.R. Zircon stability and the ZrO_2–SiO_2 phase diagram. *Am. Mineral.*, 1967, **52**(5–6), P. 880–885.

[112] Kamaev D.N., Archugov S.A., Mikhailov G.G. Study and Thermodynamic Analysis of the ZrO_2–SiO_2 System. *Russ. J. Appl. Chem.*, 2005, **78**(2), P. 200–203.

[113] Kwon S.Y., Jung I.-H. Critical evaluation and thermodynamic optimization of the CaO-ZrO_2 and SiO_2-ZrO_2 systems. *J. Eur. Ceram. Soc.*, 2017, **37**(3), P. 1105–1116.

[114] Al’myasheva O.V., Gusarov V.V. Nucleation in media in which nanoparticles of another phase are distributed. *Dokl. Phys. Chem.*, 2009, **424**(2), P. 43–45.

[115] Almjashev V.I., Gusarov V.V., Khabensky V.B. $USiO_4$ stability analysis. *Technologies for ensuring the life cycle of nuclear power plants*, 2020, **2**(20), P. 80–97 [in Russian].

[116] Pena P., De Aza S. El Sistema ZrO_2–SiO_2–TiO_2. *Bol. Soc. Esp. Cerám. Vidr.*, 1976, **15**(2), P. 93–95.

[117] Sugai M., Fujimori K., Sahara R., Hirano S., Somiya S. Phase Relations in the system $ZrSiO_4$–TiO_2 at temperatures between 1500 and 1700 °C. *J. Ceram. Soc. JAPAN*, 1974, **82**(8), P. 447–453.

[118] Phase Equilibria Diagrams Online Search system by NIST ACerS. URL: https://phaseonline.ceramics.org/ped_figure_search (date of access: 01.03.21).

[119] Mazurin O.V., Gusarov V.V. The Future of Information Technologies in Materials Science. *Glass Phys. Chem.*, 2002, **28**(1), P. 50–58.

[120] Information-analytical system for phase diagrams and properties of refractory oxides. URL: http://chemdm.ru/index.php/PhDIAS (date of access: 01.03.21).

NANOSYSTEMS: PHYSICS, CHEMISTRY, MATHEMATICS, 2021, 12 (6), P. 728–748

Removal of metal ions using Chitosan based electro spun nanofibers: A review

Texin Joseph[1], Meera Jacob[1], Veena R. Nair[2], Jaya T. Varkey[3]
[1]Department of Chemistry, St. Pauls College, Kalamassery-683053, Kerala, India
[2]Department of Chemistry, The Cochin College, Kochi-682002, Kerala, India
[3]Department of Chemistry, St. Teresa's College. Ernakulam- 682035, Kerala, India
texin@stpauls.ac.in, meera@stpauls.ac.in, jayavarkey@yahoo.com, veenamk2004@gmail.com

DOI 10.17586/2220-8054-2021-12-6-728-748

Chitosan is a promising environmentally-friendly polymer with a wide range of applications in biological, medical and water treatment fields. Recent research in chitosan-based electro spun nanofibers has led to the very cost-effective and efficient removal of toxic metal ions from solutions that are extremely important in today's pollution-ridden world. Nanofiber fabrication of chitosan blends can easily be done by the novel electrospinning technique. Because of their high adsorption capability, metal chelation ability, nontoxicity, biocompatibility, biodegradability, hydrophilicity, and cost effectiveness, chitosan-based nanofibers have seen rapid growth in water treatment applications. This review outlines the ability of electrospinning produced chitosan-based nanofibers to remove toxic metals. The primary goal of this review is to provide current information on various chitosan blend nanofibers that may be useful in water purification, as well as to encourage further research in this area.

Keywords: Chitosan, electrospinning, nanofibers, toxic metal removal, water purification.

Received: 4 July 2021

Revised: 30 October 2021

1. Introduction

Chitosan is a novel biomolecule which is biodegradable and bio-compatible. This polysaccharide is obtained by the deacetylation of chitin which is the major constituent of the exoskeleton of water-borne crustaceans [1]. Chitosan is a versatile and promising biomaterial [2]. The cationic nature of this polymer has attracted interest for a number of purposes and is the only abundant aminated polysaccharides which are available [3–6]. Chitosan is the N-deacetylated derivative of chitin, but this N-deacetylation is never complete. A rigid nomenclature with regards to the degree of N-deacetylation has not been defined between chitin and chitosan. About 6.89 % of nitrogen is present in chitin and chitosan this is the reason why these materials are used as a chelating agent and have many commercial applications [7, 8]. Consequently, chitosan has attracted tremendous attention for the creation of novel functional materials and potentially important renewable agricultural resource, and has been widely applied in the fields of agriculture, medicine, pharmaceuticals, cosmetic, food industries, environmental protection, and biotechnology (see Fig. 1). Recently [9], the chitosan backbone has had an increased capacity of adsorption due to the presence of a large number of amine groups [10–12].

Several physical and chemical methods have been used to modify raw flaked chitosan [13, 14]. Physical modifications may increase the sorption properties; gel formation decreases the crystallinity of the sorbent and involves in an expansion of the porous network [15]. Chemical modifications also offer a wide spectrum of tools to enhance the sorption properties of chitosan for metals. Both hydroxyl and amine groups of chitosan can be chemically modified. They may increase the chemical stability of the sorbent in acidic media but decreases the solubility in most mineral and organic acids. They also increase its resistance to biochemical and microbiological degradation [13, 16]. The physical and mechanical properties can be improved by cross-linking with glutaraldehyde [17–19], sulfuric acid [20], epoxides [21] and di-aldehyde starch [22]. Glutaraldehyde has been frequently used to cross-link chitosan. To stabilize the crosslinking of the chitosan in acidic solutions, a Schiff's base reaction between aldehyde groups of glutaraldehyde and some amine groups of chitosan were commonly used. It has been noted that cross-linking may reduce the adsorption capacity; it enhances the resistance of chitosan against acid, alkali and chemicals. The chemically modified chitosan has a great future and its development is practically limitless.

1.1. Electrospinning

For the fabrication of submicron-sized polymer nanofibers ranging from 5 to 500 nm, electrospinning has been recognized as an effective technique. The nanofibers thus formed from the electrospinning process may be 100 times smaller than those prepared by traditional methods of solution or melt spinning [23]. The uniaxial stretching of a viscoelastic solution is used for the preparation of nanofibers through electrospinning. The principles of electrospinning and the different parameters that affect the processes have to be considered to understand and appreciate the

FIG. 1. Applications of chitosan

process which enables the formation of various nanofiber assemblies. For the solidification of the solution, electrospinning makes use of electrostatic forces [24]. An electric field is applied between the collector and the capillary end so that surface charge is induced on a polymeric fluid, deforming a spherical pendant droplet to a conical shape in an electrospinning process [25]. The charged fluid jet is ejected from the tip of the conical protrusion commonly referred to as Taylor cone. When the electric field surpasses a threshold value, the electrostatic repulsion forces of the surface charges overcome the surface tension and then the charge density on the jet interacts with the external field to produce instability. Large surface charge densities enhance a whipping mode rather than axisymmetric mode. Bending of the jet produces a highly stretched polymeric fiber with simultaneous rapid evaporation of the solvent. The main advantage of the electrospinning nano-manufacturing process is that it is cost effective compared to that of most bottom-up methods. The nanofibers prepared from an electrospinning process are often uniform and continuous and do not require expensive purification, unlike sub-micrometer diameter whiskers, inorganic nanorods, and composite material reinforcement [26].

1.2. Electrospinning arrangement

A high voltage supplier, a capillary tube with a needle and a collecting screen are the three main components of a typical electrospinning setup [27]. Fig. 2 shows a typical electrospinning setup. A 6 kV applied voltage is required for initiation of the electrospinning process. The collector and the syringe needle are kept at the proper distance one from the other. Metallic plates, aluminum foils and rotating drums can be used as target for the collection of nanofibers during the electrospinning process. The potential difference enables the surface tension to be overcome by the electrostatic forces of the polymeric solution ejected from the needle tip and the so called “Taylor cone” configuration [28]. This process shapes the polymeric solution into a jet of charged fluid that is electrostatically attracted by the collector. The solvent evaporates during this transit from the needle to the collector, allowing for the accumulation of dry fibers on it. It is possible to run the electrospinning process at a lower applied voltage when a grounded target is introduced nearer to the spinneret [29]. The widely used spinnerets included clip spinneret, tubeless spinneret, co-axial spinneret, and heating spinneret. Co-axial electrospinning can be used to produce materials having low spin ability [30] and by using multi jet spinneret, materials can be electro spun at low voltages [31].

1.3. Adverse effects of heavy metals

Ground water pollution originating from both natural and anthropogenic sources presents a serious threat to the environment. Natural pollution sources include mineral and metallic deposits in sedimentary rocks and the release by soil of various metal ions into the environment. Man-made activities like mining, plating, glass making, ceramics, and battery manufacturing also lead to a great increase in heavy metal contamination in water, causing an ongoing risk to the biosphere [32]. Metals such as arsenic, chromium, copper, iron, lead, mercury, nickel and zinc, which have high toxicities and non-biodegradable properties, pose problems to both the environment and living organisms [33, 34]. Heavy metals pollutants in water are always an issue, because they can cause serious ailments such as dehydration,

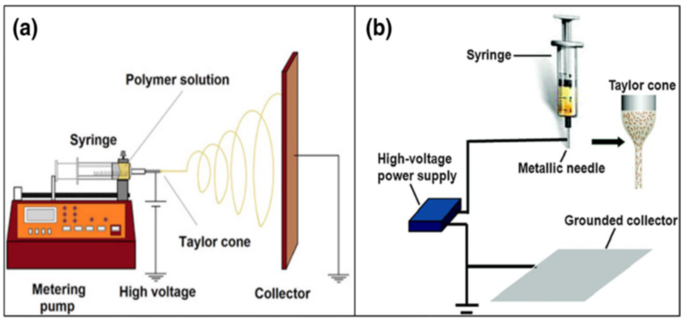

FIG. 2. Electrospinning arrangement (a) vertical; (b) horizontal [27]

stomach ache, nausea, and dizziness, lack of coordination in muscles, destruction of the nervous systems of young children, lung irritation, eye irritation, skin rashes, vomiting, lung insufficiency, and liver damage [35–37]. Many methods such as adsorption, electroplating, ion exchange, membrane separation, precipitation are being used to remove the ions of these metals from aqueous effluents [38–42]. Among these, adsorption is commonly regarded as an effective and economical method for wastewater treatment. Various types of adsorbents such as activated carbons [43–45], chitosan/ natural zeolites [46, 47], biosorbents [48–50], and chelating materials [51, 52] have been studied for the adsorption of metal ions from aqueous solutions. The adsorption properties of these adsorbents depend on the functional groups present on their surface. An adsorbent containing nitrogen-based ligands such as, amino, amidoxime, imidazole, and hydrazine groups was effective in forming complexes with metal ions [53–57].

In this work, the removal of metals like chromium, lead, copper, cadmium, thorium, uranium, mercury, nickel and arsenic from waste water by electro-spun nanofibers of chitosan, chitosan blends and modified chitosan were discussed.

2. Removal of metal ions

Heavy metal ions released into different water resources, are poisonous, carcinogenic, and pose a potential risk to human health and the atmosphere. Adsorption is one of the most effective techniques for removing heavy metal ions from aqueous solutions. Different kinds of adsorbents have been used to remove metal ions from various aqueous solutions, including activated charcoal, oxide crystals (ferric oxide, titanium oxide, cerium oxide, aluminium oxide, manganese oxide etc.), polymer fabrics, resins, and bio sorbents. In recent years, different natural fibers have drawn great interest as an adsorbent to remove heavy metal ions from wastewater due to their comparatively large exterior unique surface area. Metal ions in aqueous solutions can be transferred to the surface of the adsorbent by diffusion or convection, and then become bound to the surfaces due to various physical or chemical interactions between the metal ions and the adsorbent's surface functional groups. The formation of surface complexes, ion exchange, and chelation have all been proposed as effective adsorption mechanisms for heavy metal ions on various adsorbents. The amino group on an adsorbent, in particular, has been discovered to be one of the most important chelating groups for heavy metal ion adsorption. As a result, chitosan nanofibers produced via electrospinning with high adsorption potential for extracting heavy metal ions have piqued interest [58, 59].

Yunpeng Huang et al. analyzed the heavy metal removal by electro-spun fibrous membrane, its mechanism and adsorption kinetics. The efficiency can be improved by surface group functionalization incorporation of nanoparticles. Electro-spun fibrous membranes outperform conventional adsorbents in a variety of ways, including higher permeation flux, lower pressure drops, flexible component adjustment, and multi-target adsorption [60]. Lei Zhang, et al. examined the various factors such as pH, temperature, adsorbent dosage, contact time, and co-existing ions, which plays a key role in the metal removal. They also studied the adsorption kinetics, adsorption mechanism and furthermore, a response surface approach was used to optimize the process parameters of heavy metal adsorption by modified chitosan. Modified chitosan regeneration has received a lot of attention and several dynamic adsorption experiments have also been described [61]. Xin Rui, et al. investigated the role of electro-spun nanofibrous membranes in wastewater treatment. One of the primary issues associated is that the membrane with a nonwoven nanofibrous structure has very weak mechanical properties, which could limit its use in wastewater treatment. Different strategies and methodologies were investigated and discussed in this work, to improve the mechanical characteristics of nanofibrous membrane and ensuring the membrane's recyclability and reusability during the adsorption process [62]. Dhanush Gandavadi, et al. discussed in their work about bio-based nanofibers and their application in waste water treatment. They highlighted the use of biomaterials due to their ready availability, environmental friendliness aspects and resource efficiency. They also discussed various strategies like functionalization, incorporation of other natural and synthetic materials to improve the efficiency of nanofibers, which facilitates enhanced adsorption and the potential for removing heavy metal ions, dyes, and other contaminants polluting the environment [63].

2.1. Chromium

Chromium has been widely used in the pesticide industry, metallurgy, photography, corrosion control application, metal finishing, steel manufacture, paint formulations, leather industry, varnishes, dye industry, and textile industry, among others [64–66]. Chromium exists mainly in three oxidation states viz +2, +3 & +6 [67]. Among the different states, Cr[VI] is the most toxic one [68,69]. The presence of chromium in water is a serious threat to the human life and may cause severe health problems [70]. Different methods are used for the removal of chromium [VI] from aqueous solutions and these may include chemical precipitation, membrane filtration, ion exchange, and reverse osmosis [71, 72]. The production of large volumes of waste, requirement of high energy inputs, and high operating costs were some negative aspects of these methods [73, 74]. Among the various techniques, adsorption is a very effective one which offers high efficiency, low cost, operational simplicity, versatility and the availability of a wide range of chemically and thermally stable adsorbents [75, 76]. This method also has a broad applicability in water pollution control.

H. Behesthi et al. prepared, chitosan /multi-walled carbon nanotubes (MWCNT)/ Fe_3O_4 nanofiber for the effective removal of Cr(VI) from aqueous solutions. Chitosan powder is mixed with aqueous solution of 0.5 M acetic acid for 24 hours at 300 °C using a magnetic stirrer. The prepared MWCNT/Fe_3O_4 composite is stirred with the chitosan solution at room temperature for 6 hours. This composite solution is electro-spun to obtain a chitosan composite nanofiber. From the TEM image, it was clear that the nanofiber formed has a coaxial nanocable structure that had diameters of $\sim$10 – 15 nm. The adsorption capacity of this nanofiber depends on the concentration of MWCNT/Fe_3O_4, pH, temperature and time. The maximum adsorption of Cr[VI] ions has been occurred at a pH of 2, temperature 45 °C and at an equilibrium time of 30 minutes. Kinetic studies show that the reaction follows a pseudo second order model. One of the advantages that can be pointed out is that the chitosan/MWCNTs/ Fe_3O_4 nanofibers can be reused without any frequent loss in adsorption [77]. G. Kummer, et al. prepared novel nanofiber materials composed of chitosan/nylon 6 by the force spinning method using formic acid as the solvent and it was used for the effective removal of chromium [VI] ions from aqueous solutions. The maximum adsorption capacity was 23.9 mg/g. The kinetic studies shows that the reaction follows a pseudo second order model and the equilibrium isotherms best fit to the Langmuir model. The thermodynamic studies show that the adsorption was spontaneous, endothermic and favorable [78].

Liang Ma et al. developed core-shell-structured cellulose acetate-polycaprolactone/chitosan [CA–PCL/CS] nanofibers using coaxial electrospinning and reported an excellent removal performance of hexavalent chromium [Cr[VI]]. 10 g of chitosan was added to N, N-dimethylacetamide or acetone to obtain 10 % solution. 1 % cellulose acetate & 15 % poly caprolactone were dissolved in the formic acid or acetic acid by blending the solvent system to obtain polycaprolactone/cellulose acetatecomposite solution. The desired nanofiber cellulose acetate-polycaprolactone/chitosan as the shell components and chitosan as core were fabricated via coaxial electrospinning. It was noticed that the core shell structured fibers possess higher adsorption capability and good durability in acidic environment and also reported that CA–PCL/CS fibers with core-to-shell ratio of 0.442 have a maximum adsorption capability of 126 mg/g at room temperature. It is reported that it have a significant role in the adsorption of chromium [79].

Lei Li et al. reported the effective removal of chromium using chitosan nanofibers. Chitosan nanofibers were prepared using 90 % acetic acid as the solvent by electrospinning. The 75 nm diameter chitosan nanofibers were cross-linked by glutaraldehyde vapor to minimize the material's solubility in aqueous solutions, and thus, the formed cross-linked chitosan nanofibers were good adsorbents of hexavalent chromium directly from aqueous samples The results showed a maximum adsorption capacity of about 131.58 mg/g, which was more than double that of chitosan powder. It was also found that the adsorption is due to the presence of amino and the hydroxyl groups present in the chitosan [80].

Ehsan Bahmani et al. prepared the chitosan-grafted-poly [N-vinylcaprolactam][chitosan-g-PNVCL] nanofibers via electrospinning. ZIF-8 metal-organic frameworks nanoparticles were incorporated into the nanofibers for the adsorption of Cr[VI] from water. The scanning electron microscope (SEM) image indicated an average particle size of 65 nm was fabricated for ZIF-8 metal organic frame works. The SEM image of the prepared nanofiber with shows an average diameter of 235 nm. The effect of parameters on the Cr[VI] removal was studied. It is also found out that the synthesized nanofibers could be reused fora maximum of five sorption-desorption cycles.

The maximum experimental adsorption capacity of the chitosan-g-PNVCL/ZIF-8 nanofibers for Cr[VI] was 269.2 mg/g under ZIF-8 concentration of 3 wt. %, adsorbent dosage of 0.5 g/L, pH of 3, equilibrium times of 30 min, and temperature of 25 °C.

A pseudo first order and Langmuir adsorption model was used to match the kinetic and equilibrium data of chromium adsorption. The obtained results showed that the prepared nanofiber loaded with ZIF-8 had a high capacity for the removal of heavy metals [81].

Eryun Yan et al. synthesized the magnetic Fe_3O_4 containing polyvinyl alcohol/chitosan [Fe_3O_4@PVA/CS] composite nanofibers via the electrospinning method and characterized by scanning electron microscope [SEM], transmission electron microscope [TEM], vibrating sample magnetometer [VSM] and Fourier transform infrared [FT-IR]. The prepared composite nanofibers were used as a novel adsorbent for removing toxic chromium [VI] from the aqueous solution. The doping of Fe_3O_4 nanoparticles [NPs] into the fibers had made a good effect on the absorption for Cr(VI) ions under both neutral and acidic conditions, and the saturated adsorption reached the maximum when pH was 3.0. The kinetics of Cr(VI) removal by the prepared composite nanofibers follows the pseudo-first-order model [82]. The possible adsorption mechanism is shown in Fig. 3.

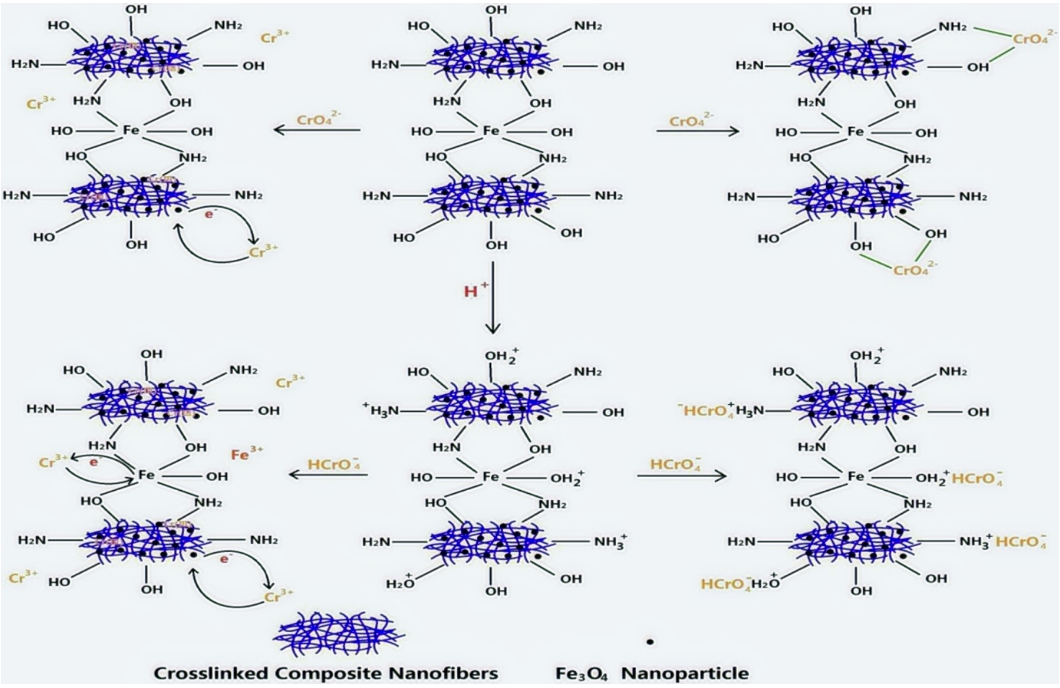

FIG. 3. The possible adsorption mechanism schematic diagram between Cr(VI) and the magnetic Fe_3O_4@PVA/CS composite nanofibers (Under neutral and acidic conditions) [82]

2.2. Lead

A major concern to the public health is the presence of heavy metal ions in water [83, 84]. The main source of lead is the waste water from battery manufacturing factories. The industrial waste water containing lead ions is always a threat to the ecosystem. Evidence has shown that excess lead ions can cause a harmful effect both on ecological environment and human health [85–87]. Exposure resulting in acute lead poisoning may cause severe damage to the kidneys, liver, brain, and nervous system, and in addition, may induce sterility, abortion, and neonatal death [88]. From the previous studies, it is proved that adsorption process, due to its low cost and high efficiency is the most popular method for the removal of heavy metal ions [89,90]. As the nanofibrous adsorbent prepared by electrospinning process have high surface area and porosity, they have been widely used in adsorption of lead [91–97].

Adib Razzaz et al. prepared the chitosan/TiO_2 nanofiber by two different techniques – coating method and entrapped method. The adsorbing capacity of the nanofibers for the removal of Pb [II] was found to be 526.5 mg/g for the entrapping method and 475.5 mg/g for the coating method. It was also studied to determine if the chitosan/TiO_2 nanofibers prepared by the entrapped method could be reused frequently without significant loss in adsorption performance after five adsorption/desorption cycles. Fig. 4 depicts the SEM images of chitosan/ TiO_2 SEM images. The kinetic and equilibrium studies had shown that it follows a pseudo first order kinetics and Redlich – Peterson isotherm model [98].

R. M. N Thumbi et al. proved that the Pb(II) removal by chitosan blend polyacrylamide nanofibers was accomplished without any additional synthetic modifications. They prepared the chitosan polyacrylamide blend solution

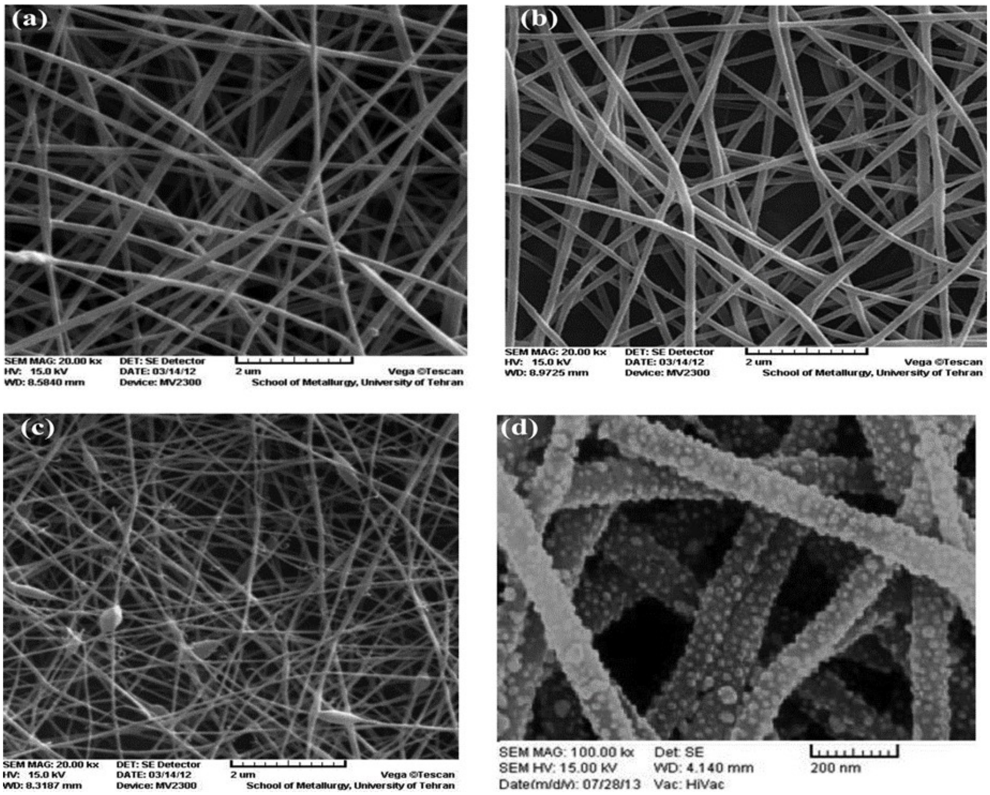

FIG. 4. SEM images of (a) chitosan; (b) chitosan/TiO_2 2 wt.%; (c) chitosan/TiO_2 4 wt.% and (d) TiO_2 coated chitosan nanofibers [98]

by electrospinning method. The synthes is used aqueous solution of 0.52 M acetic acid. The resultant nanofibers were crosslinked using glutaraldehyde as shown in Fig. 5. Parameters like different concentrations of acetic acid were taken for the optimization of the electrospinning parameters. The resulting solution is passed through the syringe to produce the electro-spun chitosan based nanofibers. The study reports show that the adsorption capacity for Pb was 56.54 mg/g. The Freundlich isotherms explain the theory better than Langmuir. The resultant nanofibers were applied in the purification of both contaminated pond water and pulp waste. It was noticed that nanofiber prepared have removal efficiency of 100 % in pond water; and 97.2 % in pulp wastewater. The regeneration efficiencies [recovery %] were 64 % and 72 % respectively [99].

Yan Li et al. prepared a novel and highly efficient lead ion-imprinted adsorbent of chitosan nanofiber mats. The electrospinning solution of chitosan with the lead chloride was prepared using trifluoroacetic acid (TFA)/CH_2Cl_2 as the solvent. The nanofiber formed was crosslinked with glutaraldehyde. The results shows that the maximum adsorption for Pb[II] ions was 577 mg/g, which is five times more than that of the common chitosan-based adsorbents. The kinetic study proves that the adsorption of Pb[II] ions follows a pseudo-second-order model [100].

Dong Wang et al. prepared a composite nanofibrous films using electrospinning technique and they modified the film by loading cellulose nanocrystals (CNC). The adsorption capacity of the films was studied by changing the CNC loading level, solution pH, and adsorption time. The results showed that the adsorption of lead ions by the films was the best with CNC loading level of 5 wt.%, pH of 6, and adsorption time of 4 h. The adsorption behavior of the films was agreed with the Freundlich model. The adsorption equation of metal ions could be described while using a pseudo-second order model. The maximum adsorption capacity of Pb[II] ions was estimated as 323.49 mg/g. The Pb[II] ion adsorption efficiency of the films after 4 adsorption-desorption cycles was 90.21 % [101].

Hossein Hadi et al. developed a novel electro-spun chitosan/graphene oxide [GO] nanofibrous adsorbent by electrospinning process. The adsorption behaviors of Pb^{2+} from aqueous solutions using chitosan/GO nanofibers were investigated. Kinetic and equilibrium studies showed that the experimental data of Pb^{2+} was best fitted with double-exponential model and Redlich – Peterson isotherm models. The maximum monolayer adsorption capacity of Pb^{2+} ions using chitosan/GO nanofibers was found to be 461.3 mg/g at an equilibrium time of 30 min and temperature of 45 °C. By the evaluation of the thermodynamic parameters, it was proved that the nature of the metal ions sorption by chitosan/GO nanofibers was endothermic and spontaneous. It is also noted that the chitosan/GO nanofibers could

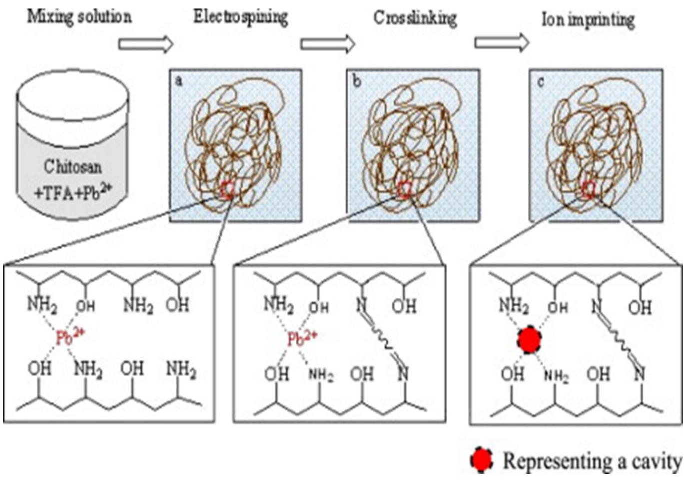

FIG. 5. Preparation of the lead-ion imprinted crosslinked electro-spun chitosan nanofiber mats [100]

be reused frequently without almost any significant loss in adsorption performance. This study provides a promising chitosan/GO nanofibrous adsorbent with a good adsorption property for heavy metal ions removal [102].

2.3. Copper

Water resources are extensively used in all stages of industrial production and consequently contaminated with heavy metal ions, which are often disposed into the environment. Heavy metal ions accumulate in living organisms as a result of their presence in drinking water, air, and soil, resulting in illnesses, poisoning, and mutations [103, 104]. Excess Cu^{2+} can cause some renal diseases, liver dysfunction, stroke, inflammation and cancer [105]. Therefore, environmental protection and remediation systems must be developed to eliminate pollution of this metal.

Natalia S. Surgutskaia et al. had prepared diethylenetriaminepentaaceticacid(DTPA)-modified chitosan [CS-DTPA] for the effective of Cu^{2+} ions by ethylcarbodiimidehydrochloride/N-hydroxy-succinimide crosslinking [106]. The preparation was done by mixing around 10 ml of 2 % chitosan solution of pH about 4.7 and 10 ml of DTPA solution which was activated with N-hydroxy-succinimide and ethylcarbodiimide hydrochloride at pH 4.7. Nanofibre formation is clearly in Fig. 6. This modified chitosan nanofiber showed better adsorption of Cu^{2+} from aqueous solutions as shown in Fig. 7. The maximum adsorption shown by this nanofiber was 177 mg/g for Cu^{2+} ions [107].

Ichrak Lakhdar et al. reported the removal of copper from aqueous solutions using modified chitosan nanofibers with polyethylene oxide. The solution was prepared by mixing 4 % wt chitosan in 50 % acetic acid and 4 % polyethylene oxide in 50 % acetic acid for 18 – 24 hours of ambient temperature and the 4 % weight electro-spun chitosan nanofibers were produced using a horizontal electrospinning technique. The results show an adsorption of 94.7 % of copper from the aqueous solutions. Kinetic studies have showed that the adsorption of copper ions on CS/PEO nanofibers follows a chemisorption by chelation mechanism. From the equilibrium studies, it was noted that the adsorbed copper forms a monolayer with equal distribution of the energy on the homogeneous surface of the adsorbent as seen in Fig. 8 [108].

Cardenas Bates et al. developed electro-spun chitosan-polyethylene oxide nanofiber mats using a new collector design. Continuous flawless nanofibers of 151 ± 36 nm in diameter were achieved by this method. Adsorption capacity of the mats for copper ions in aqueous solutions was investigated. The results showed that sorption equilibrium was achieved within 2.5 hours with a homogenous distribution of copper ions within the nanofiber mats. Kinetic studies show that pseudo-second order kinetic model is best fitted the experimental data. The sorption processes are best described with the Langmuir isotherm with a maximum adsorption capacity of 124 mg/g for trial temperatures ranging from 25 to 60 °C. Thermodynamic parameters [$\Delta G\ ^\circ$, $\Delta H\ ^\circ$ and $\Delta S\ ^\circ$] proved that the adsorption was feasible, endothermic and spontaneous. The results of desorption studies revealed that the electro-spun chitosan mats can be desorbed and reused up to 5 cycles without significant loss in adsorption performance [109].

Sajjad Haider et al. prepared chitosan nanofiber mat for the removal of copper from waste water. 3 wt % chitosan solutions were prepared in TFA and the nanofiber is prepared by electrospinning at 20 kV voltage. The dried nanofiber mat was neutralized using potassium carbonate solution [M], and the mat was taken out from the aqueous solution, washed repeatedly with the deionized water until the pH of the solution become 7 and dried at about 600 °C for about 24 hours under vacuum. The freeze dried chitosan nanofiber mats prepared shows a high adsorption value for the metal ions and good erosion stability in water. Fig. 9 depicts the SEM images of nanofibres during the various stages.

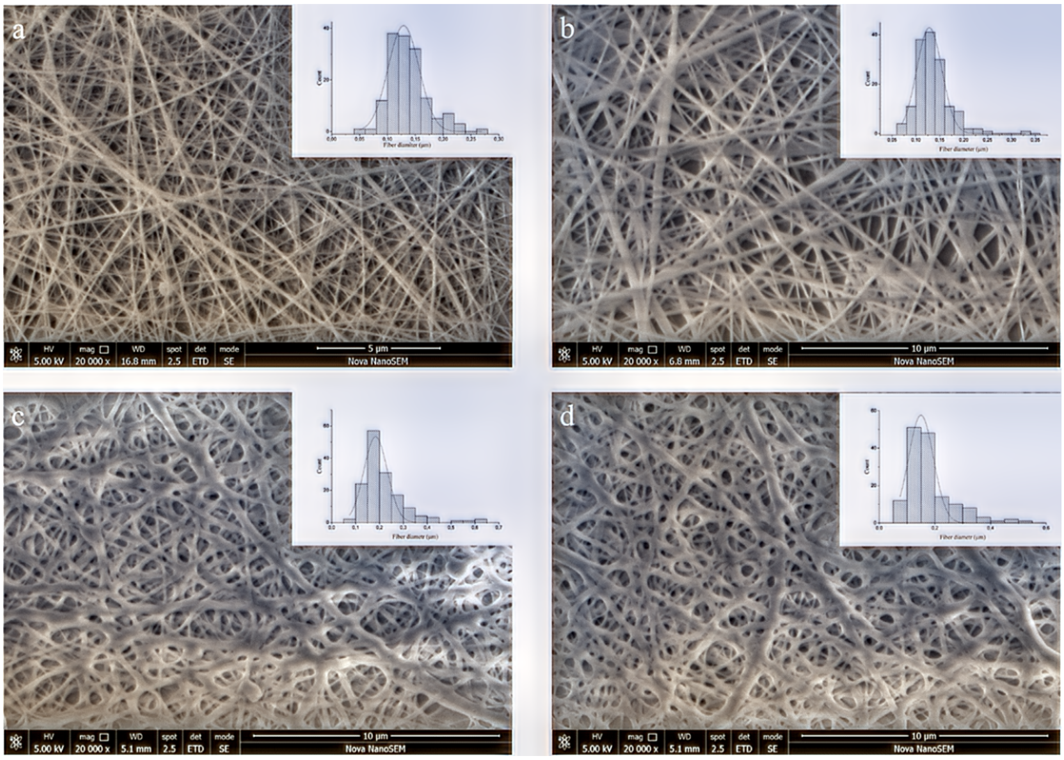

FIG. 6. SEM images and size distribution of pre- and post-stabilized CS/PEO (a,c) and CS-DTPA/PEO (b,d) nanofibers [107]

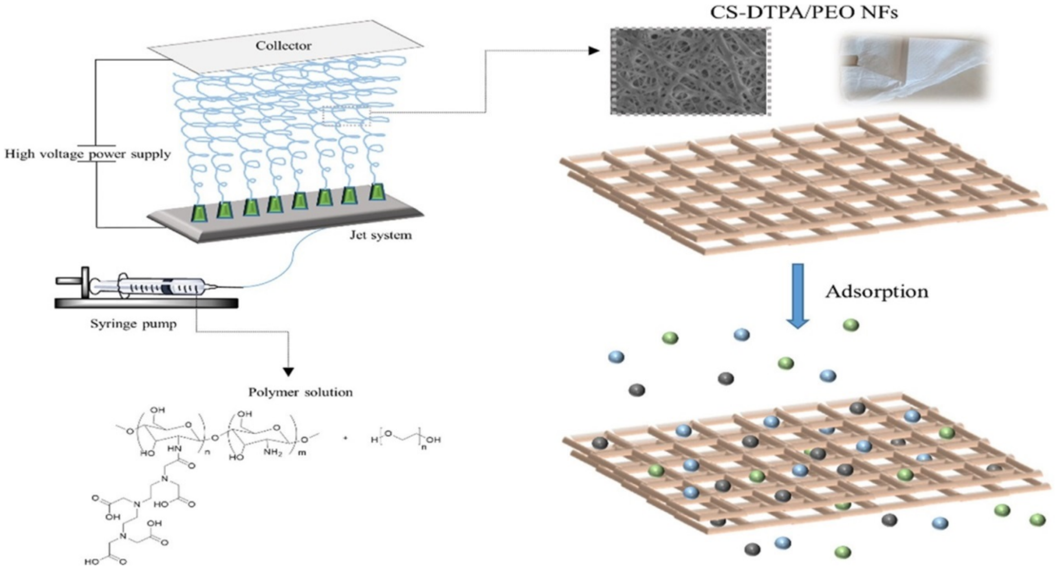

FIG. 7. Schematic illustration of preparation and adsorption properties of CS-DTPA/PEO NFs [107]

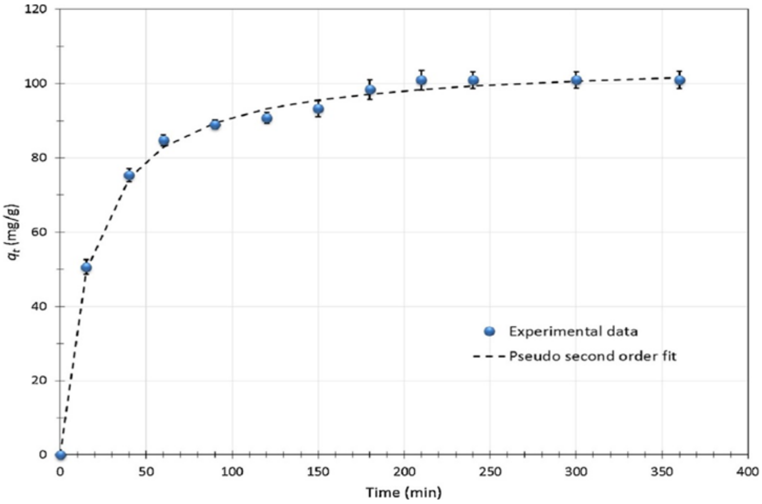

FIG. 8. Adsorption kinetic of copper ions by chitosan electro-spun nanofibers [108]

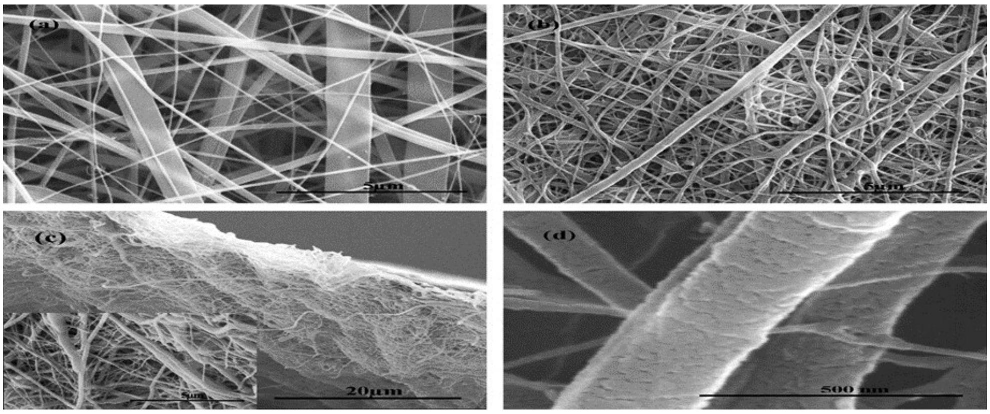

FIG. 9. FE-SEM micrographs of the chitosan nanofibers: (a) as-spun; (b) neutralized and (c) neutralized freeze-dried surfaces, and (d) enlarged nanofibers [110]

The results had showed that the equilibrium adsorption capacities for Cu[II] were 485.44 mg/g. It is reported that the Cu[II] adsorption capacity of this fiber is 6 higher than any other methods. This high adsorption capacity was explained based on the high surface area per unit mass of nanofiber [110].

Dongxue Yang et al. studied how to improve the adsorption ability of chitosan [CS] for heavy metal ions. They prepared rich amino-functionalized CS electro-spun membranes. During the efficient synthesis, polyglycidyl methacrylate [PGMA] and polyethylenimine [PEI] were orderly grafted on the surface of CS electro-spun membrane. X-ray diffractometer [XRD] analysis confirm the introduction of amino-group on the chitosan. The maximum adsorption capacity of Cu^{2+} by CS-PGMA-PEI was 69.27 mg/g. It was noted that the adsorption equilibrium of the heavy metal ion solutions was rapidly established in 60 min. The kinetics analysis revealed that the adsorption process of CS-PGMA-PEI followed a pseudo-second-order and can be described by Langmuir model. The prepared CS-PGMA-PEI membrane also exhibited a good reproducibility and stability [111].

Josó Ortiz C et al. studied about how nanofibrous mats based on chitosan can be used for removal of copper [II] ions in aqueous solutions. They fabricated different nanofibers based on chitosan-electro-spun CS-PEO nanofibers, PVA nanofibers coated with chitosan, and PVA: PAA nanofibers coated with chitosan to compare their effectiveness in the adsorption of Cu^{2+} in aqueous solutions. Among the different types of nanofibers prepared, PVA: PAA nanofibers had the best shape and thickness in comparison with CS-PEO nanofibers and PVA nanofibers. Beads were present in all the electro-spun nanofibers but they were reduced with the control of viscosity and surface tension parameters. The maximum average percentage of adsorption for the different nanofibers is as follows – CS-PEO nanofibers were of 32 %. For CS-PVA Nanofibers, this value was 16 %, and finally, for CS-PVA: PAA nanofibers, the figure was 98 %. In conclusion, CS-PVA: PAA nanofibers had the best percentage of adsorption [112].

Qasim Zia et al. prepared porous poly L-lactic acid [PLLA] nanofibrous membrane with the high surface area by electrospinning method and post acetone treatment was used as a substrate for the deposition of chitosan. The porous PLLA/chitosan structure provided the chitosan with a high surface framework to fully and effectively adsorb heavy metal ions from water and showed higher and faster ion adsorption. The composite membrane was used to eliminate the copper ions from the aqueous solutions. Chitosan acts as an adsorbent due to the presence of the amino and hydroxide groups which are complexation sites for the capture of copper ions. The maximum adsorption capacity of copper ions was 111.66 ± 3.22 mg/g at pH 7 at an interaction time of 10 min and temperature about 25 °C. The adsorption kinetics of copper ions and was well agreed with the second-order model and adsorption studies follow Langmuir isotherm. From the thermodynamic studies it was found that the adsorption system was exoergic and spontaneous. From this study chitosan modified porous PLLA nanofiber can be proved as a green adsorbent for purification of aqueous solutions containing metal ions such as copper [113].

2.4. Cadmium

Nowadays, the removal of heavy metal pollutants such as cadmium from the wastewater is a serious issue because of their serious and detrimental effects both to the environment and human health [114, 115]. Cd[II] ions are non-biodegradable and poisonous. The main source of the cadmium metal are organic chemicals, cadmium-nickel battery, mining, pigments, stabilizers and other industries leading to the release of pollutants to the natural environment by long-range transport diffusion [116]. A number of technologies were applied to eliminate heavy metal ions from water streams containing solvent extraction precipitation, membrane, flotation, coagulation,ion exchange, and adsorption etc. Among these methods, adsorption is the most effective and cheapest one.

Alharbi H.F. et al. prepared nanofiber of PAN (Poly Acrylo Nitrile) doped with metal oxide and chitosan by electrospinning for the removal of cadmium. The work investigated the role of pH, initial concentration, adsorption time were studied and established the influence of metal oxide doping [ZnO]/TiO_2. Introduction of chitosan to functionalized PAN enhances the adsorption of cadmium by four-fold. Kinetic studies review the pseudo-second order and Langmuir isotherm equation. The maximum adsorption capacity was found to be 160 mg/g for cadmium ion [117].

Ricardo Brandes et al., in their research for the removal of Cd[II] ions from aqueous solution, developed a new nanofibrous electro-spun nonwoven sorbent made from chitosan [CS] and phosphorylated nanocellulose [PNC]. SEM, EDX, AFM and FTIR were used for characterizing the adsorbent material. The results show that adsorption capacity reached 62.3 mg/g at pH 5.5 and 25 °C. The Cd[II] adsorption occurs at a rapid speed and achieved equilibrium within 120 minutes. Kinetic studies showed that the reaction fits a pseudo-second order kinetic model and the sorption isotherm was best described by the Langmuir adsorption isotherm. The maximum adsorption capacity of Langmuir was 232.55 mg/g at 25 °C, and increased with temperature, which can be explained by the high affinity of amine and phosphate groups with cadmium on the surface of the nanofibrous mats. The thermodynamic study showed that the adsorption follows a spontaneous endothermic reaction. This work also confirmed that an electro-spun nanofibrous mats based on CS and PNC can be used as an alternative material for the removal of cadmium ions, contributing to water sustainability [118].

Mohammad Rezaul Karim et al. synthesized nanofibers membranes which were fabricated by polyvinyl alcohol/chitosan [PVA/Chi] using an electrospinning technique for selective and high adsorption of cadmium Cd[II] ions based on the solution acidity. The adsorption capacity of this fiber was investigated against the parameters such as initial metal ions concentration, interaction time, adsorbent dosage and solution pH also were evaluated. The adsorption data fit towards the pseudo-second-order model for Cd[II] ions and the equilibrium data were well fitted with the Langmuir adsorption isotherms model. The maximum adsorption capacity was 148.79 mg/g for Cd[II] ions. The Cd[II] ions adsorptions were also measured to know the selectivity with simulated environmental solution, and the data shows the high selectivity for Cd[II] ions at the optimum conditions. Thus, the PVA/Chi NFs are considered to be an effective and promising material for the removal of Cd[II] ions from wastewaters with high efficiency [119].

Sana Jamshidifarda et al. prepared PAN/chitosan/UiO-66-NH_2 nanofibers for adsorption and membrane filtration of Cd[II] ions from aqueous solutions. UiO-66-NH_2 MOF content [0 – 15 wt. %], pH [2 – 7], contact time [5 – 90 min], initial metal ion concentration [20 – 1000 mg/L] and temperature [25 – 45 °C] have a marked influence on the adsorption capacity of the nanofiber. Kinetic studies follows a pseudo-second-order kinetic and Redlich – Peterson isotherm model accurately described the experimental sorption data. At optimum conditions, UiO-66-NH_2 the nanofibrous adsorbent for Cd[II] ions sorption was found to be 415.6 mg/g. It wasalso noted that an increase in the active layer thickness from 10 to 70 μm and increased the MOF content in the membrane matrix from 0 to 10 wt % as well as initial concentration of metal ions from 5 to 50 mg/L resulted in increasing metal ions removal and decrease in the water flux. When the temperature was increased from 25 to 45 °C it resulted in increasing the water flux and a slight decrease in the metal ion removal [120].

Merin S. Thomas et al., in their work, explained the fabrication of polylactic acid [PLA]/Nano chitosan [nCHS] composite fibers by electrospinning method for Cd^{2+} metal ion adsorption from water. Here, nCHS was synthesized by a method known as ionic gelation method. The scanning electron microscopic analysis revealed that the addition 0.1 wt % nCHS has decreased the fiber diameter as well as the secondary pore size and hence imparted unique properties to electro-spun composite fibers. The composite nanofibers have higher stability, reduced crystallinity, higher hydrophilicity and high surface area compared to individual material. The basic character of the composites has intensified with the increase in nCHS addition was proved by inverse gas chromatography. 70 % Cd^{2+} removal efficiency was achieved by this method [121].

2.5. Mercury

Mercury [II] is a highly reactive ion which binds to the amino acid cysteine in proteins. It is considered to be a carcinogen causing embryocidal, cytochemical, and histopathological events [122]. On converting into methylmercury, mercury and its compounds can affect the human beings even at very low concentrations [123, 124]. The main sources for contamination of water by mercury are wastewater discharges from industries like chlor-alkali, paper and pulp, oil refining, paint, pharmaceuticals and batteries. Various methods have been reported for removal of Hg[II], including chemical precipitation, ion exchange, membrane filtration, electrochemical separation, reverse osmosis, solvent extraction and adsorption [125–128].

Reena Sharma et al. prepared various combinations of Ce-PVA-CHT composite by electrospinning technique. From their experiments it has been noticed that from the various combinations, 7:3 ratio of PVA and CHT forms the bead free nanofibers. Homogenous solutions of 4 wt % CHT powder in 2 % [v/v] formic acid and 8 wt % PVA in 2 % [v/v] acetic acid were prepared at room temperature. A desirable viscous solution of 7:3 ratio was prepared and mixed with cerium [III] nitrate hexahydrate [0.5 – 5.0 w/w %]and was electro-spun at 20 kV to form Ce-PVA-CHT composite nanofiber. Nanofibers were cured at $\sim$ 110 °C for 5 hours prior to its use for Hg[II] adsorption studies. The main advantage of this polymer is that they are bio degradable, non-toxic and are of low cost. The results shows that the adsorption of PVA-CHT by Ce is around 31.44 mg/g and effective removal of Hg[II] occurs at low to moderate concentrations. The adsorption of Hg[II] on composite nanofibers may be due to the small ionic radii, high electric charge and high potential energy. Best results were observed at a pH range of 5.3 – 6.0. The kinetics studies showed that the adsorption process follows a pseudo second order and the Langmuir isotherm shows monolayer adsorption [129].

2.6. Thorium

Thorium [IV] is a radioactive fissionable metal ion, and the embodiment of its radioactive isotopes in living body over a period of time could cause several health hazards like neurotoxicity and other noxious diseases [130].

Prakash Macchindra Gore et al. prepared the chitosan/RTIL homogenous solution by dissolving 3 % chitosan in 5 % acetic acid and integrating to the 8 % PVA solution and stirred for 2 h using a magnetic stirrer for about 2 hrs. Solutions of 0.5, 1, 2, 3, 4, 5, 10 wt % 1-butyl-3-methylimidazolium tetrafluoroborate [BMIM-BF4] are added to the chitosan to prepare Chitosan/RTIL mixture and the mixture is stirred for an hour. The precursor solution for electrospinning is prepared by adding 0.01 wt % of thorium nitrate to get the ion-imprinted solution. A 1000 ppm solution of $Th[NO_3]_4$ in deionized water is used as the stock solution for the experiment. The influence of pH, temperature, adsorption and time were studied for the effective removal of thorium by chitosan/RTIL fibers. The possible mechanism of thorium adsorption is shown in Fig. 11. The maximum adsorption efficiency was reported as 90 % at a neutral pH of 7, temperature of 298 K within 2 hours [131].

2.7. Uranium

Uranium is a naturally occurring, primordial and ubiquitous heavy metal. The main sources of uranium pollution are nuclear fuel industry, nuclear weapons, exploitation of ore deposits for the extraction, have increased the presence of U in the environment. The element uranium can exhibit variable valences such as $+2$, $+3$, $+4$, $+5$ and $+6$ in nature; among these, the most common and stable form of uranium is U^{6+}, which is soluble in water [132, 133]. Recently, uranium has become a serious concern because of its chemical toxicity and radioactivity, and thus, the removal and recovery of uranium from contaminated sites and aqueous systems is of particular interest. Several methods were used for this and some of the methods were chemical precipitation, solvent extraction, membrane separation, and adsorption. Among these, the adsorption is considered as the best method for the removal and recovery of uranium because of its efficiency, low-cost and easy operation of the adsorption-based technologies [134, 135].

Christos Christoua et al. prepared PVP/chitosan blended nanofibers as adsorbent material for the removal of hexavalent uranium, U[VI] from aqueous solutions. By using batch type experiments, the nanofibers have been characterized prior to and after U[VI] adsorption by SEM and FTIR measurements, and the effect of various parameters

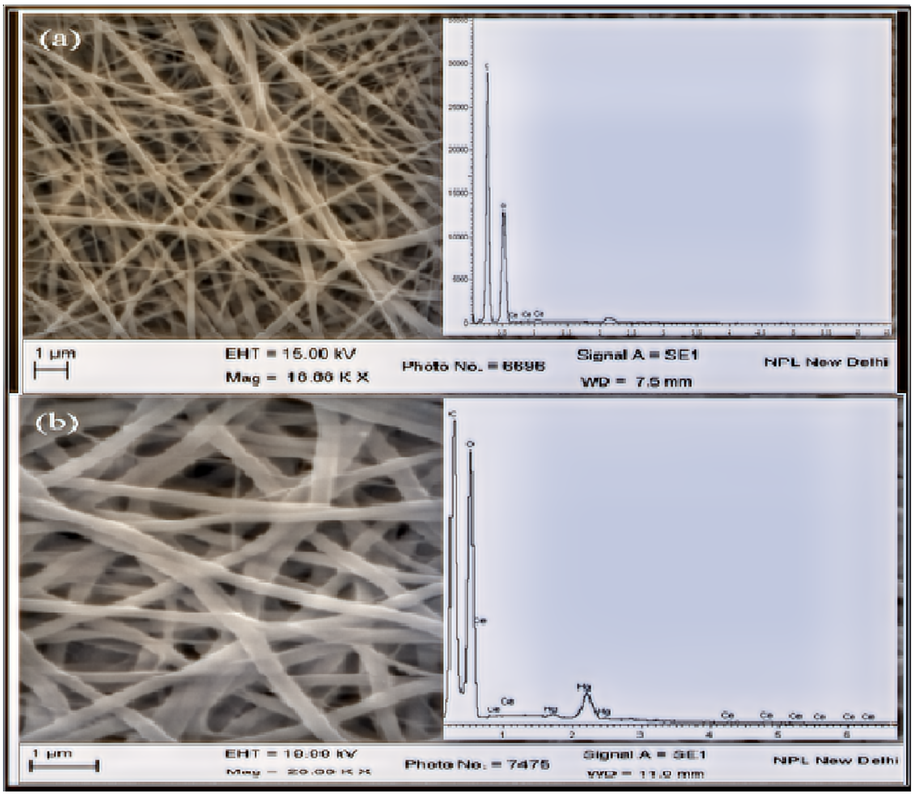

FIG. 10. SEM and EDAX of Ce-PVA-CHT composites nanofibers (a) Before adsorption, (b) After adsorption of Hg(II) [129]

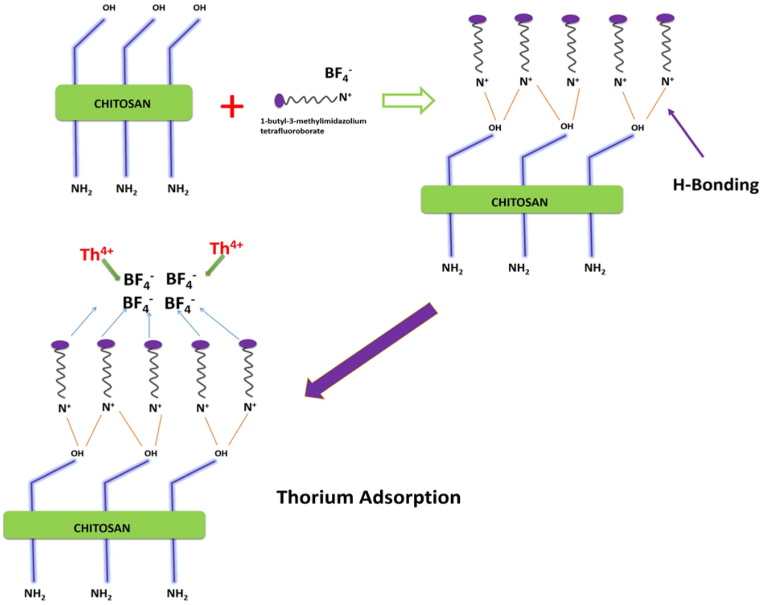

FIG. 11. Interaction between chitosan and RTIL [131]

such as metal-ion concentration, temperature and contact time on the adsorption efficiency were also investigated. The increased sorption capacity of this nanofiber can be explained by the presence of polar carbonyl group on the fiber, formation of the inner sphere complex between uranium and the fiber. The thermodynamic and kinetic studies revealed a relatively fast kinetics with a rate constant of $k_1 = 0.01$ min^{-1} and an entropy-driven process. From the recycling experiments, it was proved that the material can be reused used up to four cycles with 10 % efficiency loss [136].

Ali Reza Keshtkar et al. prepared Polyvinyl alcohol/tetraethyl orthosilicate/aminopropyltriethoxysilane (PVA/TEOS/APTES) nanofiber membrane by electrospinning method for the adsorption of uranium from aqueous solutions. From SEM, TEM and FTIR and BET analysis the surface area of electro-spun membranes obtained was 153 m^2/g. Experiments were carried out to find out the influence of different sorption parameters like pH, contact time, initial concentration and temperature. The maximum adsorption of uranium ions takes place at a pH 4.5 and at a high temperature of 45 °C. Langmuir, Freundlich and Dubinin – Radushkevich isotherm models were used to describe the equilibrium data of uranium to the prepared membrane at different temperatures (25 – 45 °C) and the kinetic data were analyzed by pseudo-first-order. The maximum adsorption capacity of uranium ions onto the PVA/TEOS/ APTES hybrid nanofiber membrane was found to be 168.1 mg/g. Thermodynamic parameters showed that the adsorption of uranium onto the electro-spun membrane was feasible, spontaneous and endothermic [137].

2.8. Nickel

The discharge of waste water into the rivers and surface waters from the industries may lead to the presence of heavy metals, and organic materials in the water sources which may cause various problems in vital organs of humans and animals [138–140]. Therefore, it should be removed before their diffusion into the ground waters [139]. Nickel has numerous applications in the field of medicine, automobiles, electricals and jewelry. Continuous exposure to nickel and heavy dosage can lead to allergy, cardiovascular and kidney diseases, lung fibrosis, lung and nasal cancer [141].

Alireza Karamipour et al. prepared CS nanofibers coated with Fe_3O_4 by weighing a defined amount of chitosan and dissolving it in 3 % acetic acid solvent with continuous stirring for 6 hours to obtain the polymeric solution. The electro-spun nanofibers were coated with Fe_3O_4 by immersing in NPs suspensions at room temperature to about 6 – 24 hrs. The results had shown that the maximum adsorption capacity of Ni[II] using Fe_3O_4-coated was 163.3 mg/g at pH 5, an adsorbent dosage of 0.4 g/L, at a contact time of 5 h, and 25 °C. Kinetic studies had proved that the reaction follows a pseudo second order kinetics and Redlich – Peterson isotherm model, respectively. This modified polymer sample can be used for more than 5 cycles of adsorption [142].

Mehran Bozorgi et al. removed Ni(II) from aqueous solution by using PVA/chitosan/ZnO/APTES nanofiber. Initially, 0.2 g of chitosan powder in acetic acid and 1 g of PVA in deionized water is mixed together using a magnetic stirrer for 4 hours. The ZnO nanoparticles synthesized were modified with APTES. PVA-chitosan composite solution is sonicated with modified ZnO nanoparticles and was electro-spun to obtain the desired nanofiber. The properties of nanofibers vary with ZnO-NH_2 loading. The TGA analysis showed that PVA/Chitosan/ZnO-NH_2 has higher thermal stability in comparison with PVA/Chitosan adsorbent. From the SEM analysis, it was found that the average diameter of the nanofiber was 98.5 nm. The optimum content of ZnO-NH_2 was 10 wt % for the maximum adsorption. The maximum adsorption for Ni^{2+} by the nanofiber is 0.851 mmol/g at 45 °C, which is double the value of the cast. The equilibrium data is well fitted with the Langmuir model. It follows a double exponential kinetic model [143].

Umma Habiba et al. synthesized chitosan/polyvinyl alcohol [PVA]/zeolite nanofibrous composite membrane via electrospinning. The characterization of the resulting nanofiber was done by electron microscopy, X-Ray diffraction, Fourier transform infrared spectroscopy, swelling test, and adsorption test. The nanofiber obtained was bead free. The resulting membrane was stable in distilled water, acidic, and basic media. Kinetic study showed that adsorption rate was high. Adsorption of Ni(II) on nanofibrous membrane follows pseudo second order kinetics and can be best explained by Langmuir adsorption isotherm. The adsorption rate decreases at high concentrations. The adsorption capacity of nanofiber was still retained after five recycling runs; this indicates the reusability of chitosan/PVA/zeolite nanofibrous membrane [144].

Mahtab Jafarnejad et al. described a multi-functionalized polyether sulfone [PES]/chitosan [CS]/Fe_3O_4-NH_2-SH nanofiber was prepared and applied for single and simultaneous removal of Ni[II] ions from the water systems. Fe_3O_4 nanoparticles were synthesized by co-precipitation method and were loaded with Fe_3O_4-NH_2-SH content. The authors have studied the simultaneous effects of solution pH, adsorbent dosage and Fe_3O_4-NH_2-SH. The composite nanofiber PES/CS/Fe_3O_4-NH_2-SH was prepared via electrospinning technique. The adsorption of nickel ion optimized with the parameters, pH, adsorbent dosage, Fe_3O_4-NH_2-SH load, the contact time and temperature. Kinetic data suited to the double-exponential model and a monolayer adsorption indicates the Langmuir adsorption model. The maximum adsorption capacity of CS/PES/Fe_3O_4-NH_2-SH was 95.3 mg/g. The main advantage of this nanofiber was their adsorption capacity was retained for 4 desorption steps. In a binary system of ions, the adsorption capacity decreased with the increase of competitive ion concentration [145].

2.9. Arsenic

Arsenic is a commonly distributed element in the natural environment, particularly in the ground water. Water contaminated with arsenic may lead to many health problems such as bladder cancer, skin lesions etc. As many technologies have been developed to remove arsenic from water, adsorption is the best method among them.

L-L. Min et al. synthesized chitosan based membrane [CS-ENM] by electrospinning process using acetic acid as solvent for the removal of arsenate from water. The resulting chitosan based fibrous membrane was highly porous, with a large specific surface area. Due to these factors, the adsorption capacity was higher than the most reported chitosan adsorbents and the value is about 30.8 mg/g. It was also noted that the pH value has shown a marked influence on the adsorption of As[V]. The result shows that the adsorption will be maximum at a lower pH [146].

Ping Tan et al. showed that the effective removal of arsenate from water at neutral pH can be done by using immobilizing chitosan nanofiber with lanthanum. An homogeneous solution of 4 % w/v chitosan and 4 % w/v PEO are prepared in acetic acid solvent and is loaded with lanthanum. The solution is electro-spun to obtain CS/PEO nanofiber doped with La. Lanthanum loading has marked influence on the adsorption of arsenate ion. The adsorption of arsenate ion using this lanthanum-doped chitosan nanofiber was about 83.6 mg/g, which is more than that of any other chitosan based nanofiber. This method was effective at wide range of pH values. The effect of doping of metal oxide Fe, Zr, Cu, Fe/Zr, and Fe/Cu with the nanofiber was also evaluated. The use of Fe-oxide impregnated mat give maximum adsorption of arsenate compared to other oxides. This could be explained on the basis of the formation of inner sphere complexes with Fe oxide [147].

L-L. Min et al. reported that a novel iron doped chitosan electro-spun nanofiber can be used for the effective removal arsenate from water at neutral pH, proving a vital role in the removal of arsenate. Fig. 12 indicates the formation of Fe doped chitosan nanofibres. Many works reported arsenate removal at acidic and basic conditions. This work proved that Fe doped chitosan fibers will remove arsenate ions from water over a wide range of pH values, even at neutral pH. The maximum adsorption capacity was noticed at 36.1 mg/g. When the adsorbent dosage increased above 0.3 g/L, more than 90 % removal efficiency was shown by the fiber. The XPS analysis suggested that the amino groups on chitosan backbone results in the adsorption of As[III] from the water samples [148].

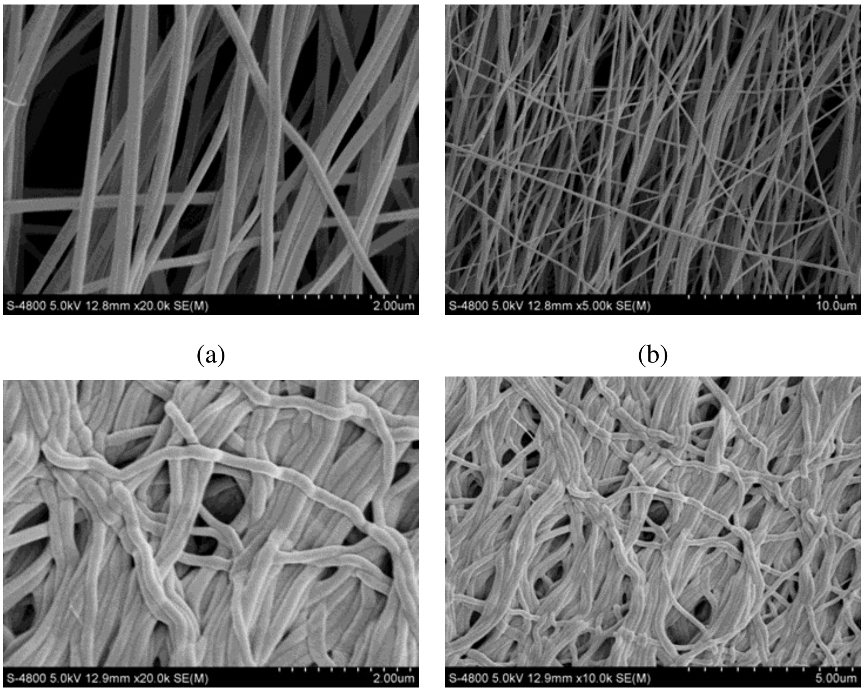

(a) (b)

(c) (d)

FIG. 12. SEM images of Fe doped chitosan fibers [148]

Reena Sharma et al. synthesized a Ce-CHT/PVA composite nanofiber through an electrospinning technique by mixing 4 wt % of CHT in 2 % v/v of formic acid and PVA in 2 % acetic acid in the ratio of 7:3 under constant stirring for about 4 – 5 hrs. The solution was electro-spun to obtain the desired nanofiber. Ce-CHT/PVA composite nanofiber showed greater efficiency in the removal of As[III] than CHT/PVA. A high adsorption of As[III] compared to the other adsorbents was due to the high surface area and presence of more active sites. The kinetic studies revealed that in the first 10 minutes, over 80 % of As[III] was removed and the adsorption capacity was about 18 mg/g, which was confirmed from the Langmuir adsorption isotherm [149].

The work of Ling-Li-Min, et al. reported the removal of As[V] using that Iron functionalized chitosan/PEO electro-spun nanofiber [ICS-PEO-ENF]. This can be synthesized by electrospinning a mixture of chitosan, PEO, and Fe^{3+} followed by crosslinking with the ammonia vapor. The experimental results has shown that the As[V] adsorption was decreased with the increased ionic strength, and this was due to the outer sphere complexion of As[V] on the nanofiber. Variation of pH also influences the adsorption. The adsorption isotherm was well described by Freundlich model and the maximum adsorption capacity was found to be up to 11.2 mg/g at pH 7.2 [150].

3. Conclusion

Chitosan is a remarkable green polymer with numerous applications in a variety of fields due to its biocompatibility and biodegradability, and also a renewable resource that can be found in abundance in nature. Nanofibers have a large surface area, which confers additional properties, giving them an advantage over conventional fibers. Bringing the two ideas together, chitosan and nanofibers could result in amazing materials of research interest. This is not, however, an easy mission. Natural polymers seem to be difficult substrates for electrospinning techniques due to their high molecular weights. Several methods were used to solve this challenge. The selection of a suitable solvent facilitates nanofiber fabrication. The use of chitosan blends with other synthetic or natural polymers, as well as chemical modifications, was another technique for creating smooth nanofibers. Chitosan based electro-spun nanofibers have proven capacity in the removal of heavy metals from water due to their properties like high adsorption capacity, non-toxicity, hydrophilicity, fast kinetics, and reusability. The disadvantages of these polymers include their low stability and poor mechanical characteristics. The mechanical properties, especially the porosity of chitosan-based electro-spun nanofibers, are influenced by the production methods and their blending and modifications, which enhances the removal efficiency. This review provides a comparison of adsorption of different heavy metals by electro-spun nanofibers of different chitosan blends. From the literature, it was understood that, temperature, pH, contact time, concentration were the process parameters which exert influences upon the fibers' adsorption capacities. Electrospinning parameters like voltage distance between tip and collector, flow rate also affects the properties of fiber. Blending with other polymers and doping with nanometals and metal oxides are the two significant factors that enhance metal removal by the chitosan fibers. The blending ratio, nature of dopant, and doping load have a favorable impact on the fiber characteristics. It was evident from the works; the metal adsorption by nanofibers follows pseudo second order kinetics in most cases. Currently the world is dealing with a serious problem of heavy metal contamination in water, which is detrimental to the entire ecosystem. Water purification systems can be better understood and developed in the future by simulating purification processes. This article may spur the development of more chitosan-based nanofibers for heavy metal removal as well as to contribute to water treatment industry. In addition to the nanofibers discussed here, many electro-spun chitosan nanofibers and its composites can be employed for the effective removal of metals which is shown in Table 1.

Abbreviations

MWCNT – Multi Walled Carbon Nanotubes
CA – Cellulose Acetate
PCL – Polycaprolactone
CS – Chitosan
PNVCL – Poly-N-Vinyl Caprolactam
ZIF-8 – Zeolitic Imidazolate Framework
PVA – Poly Vinyl Alcohol
TFA – Trifuoroacetic Acid
CNC – Cellulose Nanocrystals
GO – Graphene Oxide
DTPA – Diethylenetriaminepentaaceticacid
CS – Chitosan
PEO – Polyethylene Oxide
PEI – Polyethylenimine
XRD – X-Ray Diffraction Pattern
PGMA – Poly Glycidyl Methacrylate
NPs – Nanoparticles
APTES – (3-Aminopropyl)Triethoxysilane

TABLE 1. Comparative adsorption of different metal ions by chitosan blends

Nanofiber	**Metal ion**	**Maximum adsorption mg/g**	**Adsorption Model**	**Ref**
Chitosan – Graphene oxide	Cu[II]	423.8	Redlich – Peterson isotherm model	[102]
Chitosan – Graphene oxide	Cr[VI]	310.4	Redlich – Peterson isotherm model	[102]
Chitosan-Polyethylene oxide	Cu[II]	120.6	Dubinin – Daskovich model	[107]
Chitosan-Polyethylene oxide	Ni[II]	35.24	Dubinin – Daskovich model	[107]
Chitosan-diethylene triamine pentaacetate- polyethylene oxide	Pb[II]	144.7	Dubinin – Daskovich model	[107]
Chitosan-diethylene triamine pentaacetate- polyethylene oxide	Ni[II]	46.95	Dubinin – Daskovich model	[107]
TiO_2 coated chitosan	Pb[II]	475.5	Redlich – Peterson isotherm model	[110]
TiO_2 entrapped chitosan	Pb[II]	579.1	Redlich – Peterson isotherm model	[110]
chitosan/sulfydryl-functionalized graphene oxide composite	Pb[II]	447	Freundlich	[153]
Polyaniline grafted Chitosan	Pb[II]	13.23	Freundlich	[154]
Chitosan/Epichlorohydrin	Pb[II]	34.13		[155]
Chitosan/cellulose [CS/CL] nanofibers	Pb[II]	112.6		[156]
chitosan/TiO_2 composite Nano fibrous adsorbents	Cu [II]	579.1		[98]
Chitosan Stacking Membranes	Cu [II]	276.2	Multilayer adsorption	[157]
Chitosan electro spun on polyester	Cr[VI]	16.5	Adams Bohart Model	[151]
chitosan [CA–PCL/CS] nanofibers	Cr[VI]	126	Freundlich	[79]
Chitosan/cellulose [CS/CL] nanofibers	As[V]	39.4		[156]
Chitosan/Alumina	As[V]	96.46		[158]
Chitosan based electro spun nano fiber membrane	As[V]	30.8	Langmuir	[146]
electro spun DTPA-modified chitosan/polyethylene oxide nanofibers	Ni[II]	56	Freundlich, Langmuir, Temkin and Dubinin – Radushkevich isotherm models	[107]
Magnetic Chitosan	Ni[II]	22.07		[159]
	Pb[II]	27.95		
	Hg[II]	23.03		
	Cd[II]	27.83		
	Cu[II]	216.6		[160]
Chitosan/Diethylenetriamine	U[VI]	177.9		[161]
Chitosan/ polyethylene oxide/ carbonated nanofibers	Cu[II]	195.3		[162]
Chitosan PVC	Cu[II]	161.3		[163]

PAA – Peraceticacid
PLLA – Poly L-Lactic Acid
PNC – Phosphorylated Nano Cellulose
MOF – Metal Oxide Frame Works
nCHS – Nano Chitosan
CHT – Chitosan
RTIL – Room Temperature Ionic Liquid
BMIM-BF4 – 1-Butyl-3-Methylimidazolium Tetrafluoroborate
PES – Poly Ether Sulfone
SH – Thiol
ICS-ENF – Iron Functionalized Chitosan Electro Spun Nano Fiber
CL – Cellulose

References

[1] Allan G.G., Altman L.C., et al. Biomedical applications of chitin and chitosan. In: *Chitin, chitosan and related enzymes*. Zikakis J.P. ed., Academic Press, Inc., 1984, P. 119–133.

[2] Dutta P.K., Dutta J., Tripathi V.S. Chitin and chitosan: Chemistry, properties and applications. *J. of Scientific and Industrial Research*, 2004, **60**, P. 20–31.

[3] Muzzarelli R.A.A. *Chitin Enzymology*. Alda Tecnografica, Ancona, Italy, 1993.

[4] Muzzarelli, R. In vivo biochemical significance of chitin-based medical items. In: Dumitriu, S. Ed., *Polymeric Biomaterials*. Marcel Dekker, Inc, New York, 1994, P. 179–197.

[5] Muzzarelli R.A.A. *Chitin enzymology*. Atec Edizioni, Ancona, Italy, 1996.

[6] Muzzarelli R.A.A. *Chitin. The Polymeric Materials Encyclopedia*. Ed. Salamone J.C. CRC Press, Inc., BocaRaton, USA, 1996.

[7] Muzzarelli R.A.A. *Natural chelating polymers*. Pergamon Press, New York, 1973, 83 p.

[8] Zikakis J.P. *Chitin, chitosan and related enzymes*. Academic Press, Orlando, 1984.

[9] Kurita K. Chemistry and application of chitin and chitosan. *Polymer Degradation and Stability*, 1998, **59** (2), P. 117–120.

[10] Evans J.R., Davids W.G., MacRae J.D., Amirbahman A. Kinetics of cadmium uptake by chitosan-based crab shells. *Water Research*, 2002, **36**, P. 3219–3226.

[11] Lu G., Yao X., Wu X., Zhan T. Determination of the total iron by chitosan-modified glassy carbon electrode. *Microchemical Journal*, 2001, **69**, P. 81–87.

[12] Wu F., Tseng R., Juang R. Comparative adsorption of metal and dye on flake- and bead-types of chitosans prepared from fishery wastes. *J. of Hazardous Materials B*, 2000, **73**, P. 63–75.

[13] Guibal E., Dambies L., Milot C., Roussy, J. Influence of polymer structural parameters and experimental conditions on metal anion sorption by chitosan. *Polymer International*, 1999, **48**, P. 671–680.

[14] Yang Z., Zhuang L., Tan, G. Preparation and adsorption behavior for metal of chitosan crosslinked by dihydroxy azacrown ether. *J. of Applied Polymer Science*, 2002, **85**, P. 530–535.

[15] Onsoyen E., Skaugrud O. Metal recovery using chitosan. *J. of Chemical Technolnology and Biotechnology*, 1990, **49**, P. 395–404.

[16] Yang Z., Yuan Y. Studies on the synthesis and properties of hydroxyl azacrown ether-grafted chitosan. *J. of Applied Polymer Science*, 2001, **82**, P. 1838–1843.

[17] Goissis G., Junior E.M., et al. Biocompatibility studies of anionic collagen membranes with different degree of glutaraldehyde cross-linking. *Biomaterials*, 1999, **20**, P. 27–34.

[18] Guibal E., Milot C., Tobin J.M. Metal-anion sorption by chitosan beads: Equilibrium and kinetic studies. *Industrial and Engineering Chemistry Research*, 1998, **37**, P. 1454–1463.

[19] Hsien T.-Y., Rorrer G.L. Heterogenous cross linking of chistosan beads: Kinetics, modeling and influence on cadmium ion adsorption capacity. *Industrial and Engineering Chemistry Research*, 1997, **36**, P. 3631–3638.

[20] Huang R.Y.M., Pal R., Moon G.Y. Crosslinked chitosan composite membrane for the pervaporation dehydration of alcohol mixtures and enhancement of structural stability of chitosan/polysulfone composite membranes. *J. of Membrane Science*, 1999, **160**, 17.

[21] Wei Y.C., Hudson S.M., Mayer J.M., Kaplan D.L. Crosslinking of chitosan fibers. *J. of Polymer Science Part A: Polymer Chemistry*, 1992, **30**, P. 2187–2193.

[22] Schmidt C.E., Baier J.M. Cellular vascular tissues: Natural biomaterials for tissue repair and tissue engineering. *Biomaterials*, 2000, **21**, P. 2215–2231.

[23] Dietzel J.M., Kleinmeyer J.D., Hirvonen J.K., Tan N.C.B. Controlled deposition of electrospun poly (ethylene oxide) fibers. *Polymer*, 2001, **42** (19), P. 8163–8170.

[24] Teo W.E., Ramakrishna S. A review on electrospinning design and nanofibre assemblies. *Nanotechnology*, 2006, **17** (14), R89–R106.

[25] Geng X., Kwon O.H, Jang J. Electrospinning of chitosan dissolved in concentrated acetic acid solution. *Biomaterials*, 2005, **26** (27), P. 5427–5432.

[26] Shin Y.M., Hohman M.M, Brenner M.P., Rutledge G.C. Experimental characterization of electrospinning: The electrically forced jet and instabilities. *Polymer*, 2001, **42**, P. 9955–9967.

[27] Jaeger R., Schönherr H., Vancso G. Chain packing in electro-spun poly [ethylene oxide] visualized by atomic force microscopy. *Macromolecules*, 1996, **29** (23), P. 7634–7636.

[28] Taylor G. Disintegration of water drops in an electric field. *Proceedings of the Royal Society of London A*, 1964, **280** (1382), P. 383–397.

[29] Lai X., Wu D., Sun D. Electro spinning under sub critical voltage. *5th IEEE international conference on nano/micro engineered and molecular systems (NEMS)*, 2010, P. 1170–1173.

[30] Electrospinning set up. Mechanics Electronics Computer Corporation. URL: http://www.bioeng.nus.edu.sg/nanobio/ESmachines/MECC.pdf. Accessed on 8th September 2014.

[31] Multi jet spinneret. Mechanics Electronics Computer Corporation. URL: http://www.mecc.co.jp/en/html/nanon/spinneret/multijet.html. Accessed on 8th September 2014.

[32] Horzum N., Boyaci E., et al. Sorption efficiency of chitosan nanofibers toward metal ions at low concentrations. *Biomacromolecules*, 2010, **11** (12), P. 3301–3308.

[33] Mahmoud M.E., Osman M.M., Hafez O.F., Elmelegy E. Removal and preconcentration of lead (II), copper (II), chromium (III) and iron (III) from wastewaters by surface developed alumina adsorbents with immobilized 1-nitroso-2-naphthol. *J. of Hazardous Materials*, 2010, **173**, P. 349–357.

[34] Shukla S.R., Pai R.S., Shendarkar A.D. Adsorption of Ni(II), Zn(II) and Fe(II) on modified coir fibres. *Separation and Purification Technology*, 2006, **47**, P. 141–147.

[35] Jain C.K., Singhal D.C., Sharma M.K. Adsorption of zinc on bed sediment of River Hindon: adsorption models and kinetics. *J. of Hazardous Materials*, 2004, **114**, P. 231–239.

[36] Sekar M., Sakthi V., Rengaraj S. Kinetics and equilibrium adsorption study of lead[II] onto activated carbon prepared from coconut shell. *J. of Colloid and Interface Science*, 2004, **79**, P. 307–313.

[37] Iqbal M., Saeed A., Zafar S.I. Hybrid biosorbent: An innovative matrix to enhance the biosorption of Cd[II] from aqueous solution. *J. of Hazardous Materials*, 2007, **148**, P. 47–55.

[38] Navarro R.R., Wada S., Tatsumi K. Heavy metal precipitation by polycation-polyanion complex of PEI and its phosphonomethylated derivative. *J. of Hazardous Materials*, 2005, **123**, P. 203–209.

[39] Panayotova T., Dimova-Todorova M., Dobrevsky I. Equilibrium and kinetic modelling of iron adsorption by eggshells in a batch system: Effect of temperature. *Desalination*, 2007, **206**, P. 135–140.

[40] Dabrowski A., Hubicki Z., Podkoscielny P., Robens E. Selective removal of the heavy metal ions from waters and industrial wastewaters by ion-exchange method. *Chemosphere*, 2004, **56**, P. 91–106.

[41] Mbareck C., Nguyen Q.T., Alaoui O.T., Barillier D. Elaboration, characterization and application of polysulfone and polyacrylic acid blends as ultrafiltration membranes for removal of some heavy metals from water. *J. of Hazardous Materials*, 2009, **171**, P. 93–101.

[42] O'Connell D.W., Birkinshaw C., O'Dwyer T.F. Heavy metal adsorbents prepared from the modification of cellulose: A review. *Bioresource Technology*, 2008, **99**, P. 6709–6724.

[43] Zhu S., Yang N., Zhang D. Poly(N,N-dimethylaminoethyl methacrylate) modification of activated carbon for copper ions removal. *Material Chemistry and Physics*, 2009, **113**, P. 784–789.

[44] Zhang S., Li X., Chen J.P. Preparation and evaluation of a magnetite-doped activated carbon fiber for enhanced arsenic removal. *Carbon*, 2010, **48**, P. 60–67.

[45] Mishra P.C., Patel R.K. Removal of lead and zinc ions from water by low cost adsorbents. *J. of Hazardous Materials*, 2009, **168** (1), P. 319–325.

[46] Dragan E.S., Dinu M.V., Timpu D. Preparation and characterization of novel composites based on chitosan and clinoptilolite with enhanced adsorption properties for Cu^{2+}. *Bioresource Technology*, 2010, **101**, P. 812–817.

[47] Wang X., Zheng Y., Wang A. Fast removal of copper ions from aqueous solution by chitosan-g-poly(acrylic acid)/attapulgite composites. *J. of Hazardous Materials*, 2009, **168**, P. 970–977.

[48] Shen W., Chen S., et al. Adsorption of Cu(II) and Pb(II) onto diethylenetriamine-bacterial cellulose. *Carbohydrate Polymers*, 2009, **75**, P. 110–114.

[49] Jiang Y., Pang H., Liao B. Removal of copper(II) ions from aqueous solution by modified bagasse. *J. of Hazardous Materials*, 2009, **164**, P. 1–9.

[50] Zhang G., Qu R., et al. Adsorption for metal ions of chitosan coated cotton fiber. *J. of Applied Polymer Science*, 2008, **110**, P. 2321–2327.

[51] Sun S., Wang A. Adsorption properties of N-succinyl-chitosan and cross-linked N-succinyl-chitosan resin with Pb(II) as template ions. *Separation and Purification Technology*, 2006, **51**, P. 409–415.

[52] Kavakli P.A., Güven O. Removal of concentrated heavy metal ions from aqueous solutions using polymers with enriched amidoxime groups. *J. of Applied Polymer Science*, 2004, **93**, P. 1705–1710.

[53] Bilba N., Bilba D., Moroi G. Synthesis of a polyacrylamidoxime chelating fiber and its efficiency in the retention of palladium ions. *J. of Applied Polymer Science*, 2004, **92**, P. 3730–3735.

[54] Gong B. Synthesis of polyacrylaminoimidazole chelating fiber and properties of concentration and separation of trace Au, Hg and Pd from samples. *Talanta*, 2002, **57**, P. 89–95.

[55] Chang X., Su Q., et al. Efficiency and application of poly(acryldinitrophenylamidrazone-dinitroacrylphenylhydrazine) chelating fiber for preconcentrating and separating trace Au(III), Ru(III), In(III), Bi(III), Zr(IV), V(V), Ga(III) and Ti(IV) from solution samples. *Talanta*, 2002, **57**, P. 253–261.

[56] Deng S., Bai R. Removal of trivalent and hexavalent chromium with aminated polyacrylonitrile fibers: performance and mechanisms. *Water Research*, 2004, **38**, P. 2424–2432.

[57] Deng S., Bai R., Chen J.P. Aminated polyacrylonitrile fibers for lead and copper removal. *Langmuir*, 2003, **19**, P. 5058–5064.

[58] Ma N., Yang Y., Chen S., Zhang Q. Preparation of amine group-containing chelating fiber for thorough removal of mercury ions. *J. of Hazardous Materials*, 2009, **171**, P. 288–293.

[59] Ko Y.G., Choi U.S., Park Y.S., Woo J.W. Fourier transform infrared spectroscopy study of the effect of pH on anion and cation adsorption onto poly(acrylo-amidino diethylenediamine). *J. of Polymer Science Part A: Polymer Chemistry*, 2004, **42**, P. 2010–2018.

[60] Huang Y., Miao Y-E., Liu T. Electrospun fibrous membranes for efficient heavy metal removal. *J. of Applied Polymer Science*, 2014, **131** (19), 40864.

[61] Zhang L., Zeng Y.X., Cheng Z.J. Removal of heavy metal ions using chitosan and modified chitosan: A review. *J. of Molecular Liquids*, 2016, **214**, P. 175–191.

[62] Rui X., Hongyang M.A., Venkateswaran S., Benjamin S. Electrospun nanofibrous adsorption membranes for wastewater treatment: Mechanical strength enhancement. *Chemical Research in Chinese Universities*, 2021, **37** (3), P. 355–365.

[63] Gandavadi D., Sundarrajan S., Ramakrishna S. Bio-Based Nanofibers involved in wastewater treatment. *Macromolecular Materials and Engineering*, 2019, **304**, 1900345.

[64] Dehghani M.H., Sanaei D., Ali I., Bhatnagar A. Removal of chromium(VI) from aqueous solution using treated waste newspaper as a low-cost adsorbent: Kinetic modeling and isotherm studies. *J. of Molecular Liquids*, 2016, **215**, 671.

[65] Yang J., Yu M., Chen W. Adsorption of hexavalent chromium from aqueous solution by activated carbon prepared from longan seed: Kinetics, equilibrium and thermodynamics. *J. of Industrial and Engineering Chemistry*, 2015, **21**, 414.

[66] Chen L., Chen Z., Chen D., Xiong W. Removal of hexavalent chromium from contaminated waters by ultrasound-assisted aqueous solution ball milling. *J. of Environmental Sciences*, 2017, **52**, 27.

[67] Yuan P., Liu D., et al. Removal of hexavalent chromium [Cr[VI]] from aqueous solutions by the diatomite supported/unsupported magnetite nanoparticles. *J. of Hazardous Materials*, 2010, **173**, P. 614–621.

[68] Sun L., Zhang L., et al. Chitosan modified FeO nanowires in porous anodic alumina and their application for the removal of hexavalent chromium from water. *J. of Material Chemistry*, 2011, **21**, P. 5877–5880.

[69] Hu J., Chen C., Zhu X., Wang X. Removal of chromium from aqueous solution by using oxidized multiwalled carbon nanotubes. *J. of Hazardous Materials*, 2009, **162**, P. 1542–1550.

[70] Amalraj A., Selvi M.K., et al. Efficient removal of toxic hexavalent chromium from aqueous solution using threonine doped polypyrrole nanocomposite. *J. of Water Process Engineering*, 2016, **13**, 88.

[71] Harijan D.K.L, Chandra V. Polyaniline functionalized graphene sheets for treatment of toxic hexavalent chromium. *J. of Environmental Chemical Engineering*, 2016, **4**, 3006.

[72] Bhaumik M., Setshedi K., Maity A., Onyango M.S. Chromium(VI) removal from water using fixed bed column of polypyrrole/Fe_3O_4 nanocomposite. *Separation and Purification Technology*, 2013, **110**, 11.

[73] Won S.W., Kotte P., et al. Biosorbents for recovery of precious metals. *Bioresource Technology*, 2014, **160**, 203.

[74] Zhou J., Wang Y., et al. Effective removal of hexavalent chromium from aqueous solutions by adsorption on mesoporous carbon microspheres. *J. of Colloid and Interface Science*, 2016, **462**, 200.

[75] Mishra S., Verma N. Carbon bead-supported hollow carbon nanofibers synthesized via templating method for the removal of hexavalent chromium. *J. of Industrial and Engineering Chemistry*, 2016, **36**, 346.

[76] Gupta V.K., Ali I. *Environmental water: Advances in treatment, remediation and recycling*. Elsevier, Netherlands, 2012.

[77] Beheshti H., Irani M., et al. Removal of Cr[VI] fromaqueous solutions using chitosan/MWCNT/Fe_3O_4 composite nanofibers-batch and column studies. *Chemical Engineering Journal*, 2015, **284** (15), P. 557–564.

[78] Kummer G., Schonhart C., et al. Development of nanofibers composed of chitosan/nylon 6 and tannin/nylon 6 for effective adsorption of Cr[VI]. *J. of Polymers and the Environment*, 2018, **26**, P. 4073–4084.

[79] Ma L., Shi X., et al. Electrospun cellulose acetate polycaprolactone/chitosan core–shell nanofibers for the removal of Cr[VI]. *Physica Status Solidi (A) Applications and Materials*, 2019, **216** (22), 1900379.

[80] Li L., Li Y., Cao L., Yang C. Enhanced chromium [VI] adsorption using nanosized chitosan fibers tailored by electrospinning. *Carbohydrate Polymers*, 2015, **125**, P. 206–213.

[81] Bahmani E., Koushkbaghi S., et al. Fabrication of novel chitosan-g-PNVCL/ZIF-8 composite nanofibers for adsorption of Cr[VI], As[V] and phenol in a single and ternary systems. *Carbohydrate Polymers*, 2019, **224**, 115148.

[82] Yan E., Cao M., et al. A novel adsorbent based on magnetic Fe_3O_4 contained polyvinyl alcohol/chitosan composite nanofibers for chromium [VI] removal. *Solid State Sciences*, 2017, **72**, P. 94–102.

[83] Nooney R.I., Kalyanaraman M., Kennedy G., Maginn E.J. Heavy metal remediation using functionalized mesoporous silicas with controlled macrostructure. *Langmuir*, 2000, **17**, P. 528–533.

[84] Nourbakhsh M., Illhan S., Ozdag H. Biosorption of Cr^{6+}, Pb^{2+} and Cu^{2+} ions in industrial waste water on Bacillus sp. *Chemical Engineering Journal*, 2002, **85**, P. 351–355.

[85] Sokol R.Z., Berman N. The effect of age of exposure on lead-induced testicular toxicity. *Toxicology*, 1991, **69** (3), P. 269–278.

[86] Ahamed M., Siddiqui M.K.J. Environmental lead toxicity and nutritional factors. *Clinical Nutrition*, 2007, **26** (4), P. 400–408.

[87] Jarosińska D., Peddada S., Rogan W.J. Assessment of lead exposure and associated risk factors in urban children in Silesia, Poland. *Environmental Research*, 2004, **95** (2), P. 133–142.

[88] Gercel O., Gercel H.F. Adsorption of lead[II] ions from aqueous solutions by activated carbon prepared from biomass plant material of Euphorbia rigida. *Chemical Engineering Journal*, 2007, **132** (1–3) P. 289–297.

[89] Irani M., Amjadi M., Mousavian M.A. Comparative study of lead sorption on to natural perlite, dolomite and diatomite. *Chemical Engineering Journal*, 2011, **178**, P. 317–323.

[90] Shi T., Jia S., et al. Adsorption of Pb[II], Cr[II], Cu[II], Cd[II] and Ni[II] on to a vanadium mine tailing from aqueous solution. *J. of Hazardous Materials*, 2009, **169**, P. 838–846.

[91] Dastbaz A., Keshtkar A.R. Adsorption of Th^{4+}, U^{6+}, Cd^{2+}, and Ni^{2+} from aqueous solution by a novel modified polyacrylonitrile composite nanofiber adsorbent prepared by electrospinning. *Applied Surface Science*, 2014, **293**, P. 336–44.

[92] Lu Y., Wu Z., et al. Hydrophilic PVA-co PE nanofiber membrane functionalized with iminodiacetic acid by solid-phase synthesis for heavy metal ions removal. *Reactive and Functional Polymers*, 2014, **82**, P. 98–102.

[93] Rad L.R., Momeni A., et al. Removal of Ni2+ and Cd2+ ions from aqueous solutions using electrospun PVA/zeolite nanofibrous adsorbent. *Chemical Engineering Journal*, 2014, **256**, P. 119–127.

[94] Li X., Zhang C., et al. Efficient adsorption of gold ions from aqueous systems with thioamide-group chelating nanofiber membranes. *Chemical Engineering Journal*, 2013, **229**, P. 420–448.

[95] Irani M., Keshtkar A.R., Moosavian M.A. Removal of cadmium from aqueous solution using mesoporous PVA/TEOS/APTES composite nanofiber prepared by solgel/electrospinning. *Chemical Engineering Journal*, 2012, **200**, P. 192–201.

[96] Najafabadi H.H., Irani M., et al. Removal of Cu^{2+}, Pb^{2+} and Cr^{6+} from aqueous solutions using chitosan/grapheme oxide composite nanofibrous adsorbent. *RSC Advances*, 2015, **5**, P. 16532–16539.

[97] Wu S., Li F., et al. Effects of poly[vinylalcohol] [PVA] content on preparation of novel thiol-functionalized mesoporous PVA/SiO_2 composite nanofiber membranes and their application for adsorption of heavy metal ions from aqueous solution. *Polymer*, 2010, **51**, P. 6203–6211.

[98] Razzaz A., Ghorban S., et al. Chitosan nanofibers functionalized by TiO_2 nanoparticles for the removal of heavy metal ions. *J. of the Taiwan Institute of Chemical Engineers*, 2016, **58**, P. 333–343.

[99] Richard M., Nthumbi J., et al. Method development for flow adsorption and removal of lead and copper in contaminated water using electrospun nanofibers of chitosan blend. *Analytical Letters*, 2011, **44** (11), P. 1937–1955.

[100] Li Y., Qiu T., Xu X. Preparation of lead-ion imprinted crosslinked electro-spun chitosan nanofiber mats and application in lead ions removal from aqueous solutions. *European Polymer Journal*, 2013, **49** (6), P. 1487–1494.

[101] Wang D., Cheng W., et al. Electrospun cellulose nanocrystals/chitosan/polyvinyl alcohol nanofibrous films and their exploration to metal ions adsorption. *Polymers*, 2018, **10**, 1046.

[102] Hossein Hadi Najafabadi, Mohammad Irani, et al. Removal of Cu^{2+}, Pb^{2+} and Cr^{6+} from aqueous solutions using a chitosan/graphene oxide composite nanofibrous adsorbent. *RSC Adv.*, 2015, **5**, 16532.

[103] Karri V., Schuhmacher M., Kumar V. Heavy metals [Pb, Cd, As and Me Hg] as risk factors for cognitive dysfunction: A general review of metal mixture mechanism in brain. *Environmental Toxicology and Pharmacology*, 2016, **48**, P. 203–213.

[104] Chen L., Zhou S., et al. Heavy metals in food crops, soil, and water in the Lihe River Watershed of the Taihu Region and their potential health risks when ingested. *Science of the Total Environment*, 2018, **615**, P. 141–149.

[105] Sobhanardakani S., Tayebi L., Hosseini S.V. Health risk assessment of arsenic and heavy metals [Cd, Cu Co, Pb, and Sn] through consumption of caviar of Acipenser persicus from Southern Caspian Sea. *Environmental Science and Pollution Research*, 2018, **25**, P. 2664–2671.

[106] Darras V., Nelea M., Winnik F.M., Buschmann M.D. Chitosan modified with gadolinium diethylenetriaminepentaacetic acid for magnetic resonance imaging ofDNA/chitosan nanoparticles. *Carbohydrate Polymers*, 2010, **80**, P. 1137–1146.

[107] Surgutskaia N.S., Martino A.D., et al. Efficient Cu^{2+}, Pb^{2+} and Ni^{2+} ion removal from wastewater using electrospun DTPA-modified chitosan/polyethylene oxide nanofibers. *Separation and Purification Technology*, 2020, **247** (4), 116914.

[108] Lakhdhar I., Mangin P., Chabot B. Copper [II] ions adsorption from aqueous solutions using electrospunchitosan/peo nanofibres: Effects of process variables and process optimization. *J. of Water Process Engineering*, 2015, **7**, P. 295–305.

[109] Bates I.I.C., Loranger É., Chabot B. Chitosan-PEO nanofiber mats for copper removal in aqueous solution using a new versatile electrospinning collector. *SN Applied Sciences*, 2020, **2**, 1540.

[110] Haider S., Park S-Y. Preparation of the electrospun chitosan nanofibers and their applications to the adsorption of Cu[II] and Pb[II] ions from an aqueous solution. *J. of Membrane Science*, 2009, **328** (1–2), P. 90–96.

[111] Yang D., Li L., Chen B., Shi S., Nie J., Ma Get al. Functionalized chitosan electrospun nanofiber membranes for heavy-metal removal. *Polymer*, 2019, **163**, P. 74–85.

[112] Castillo J.E.O., Chabot B. Electrospun nanofibers for the removal of heavy metals from aqueous solutions. 2016, Technical Report, Universite du Quebec a Trois-Rivieres. DOI:10.13140/RG.2.2.29893.14569.

[113] Zia Q., Tabassum M., et al. Porous poly[L–lactic acid]/chitosan nanofibres for copper ion adsorption. *Carbohydrate Polymers*, 2019, **227** (1–2), 115343.

[114] Kokkinos E., Soukakos K., Kostoglou M., Mitrakas M. Cadmium, mercury, and nickel adsorption by tetravalent manganese feroxyhyte: selectivity, kinetic modeling, and thermodynamic study. *Environmental Science and Pollution Research*, 2018, **25** (13), P. 12263–12273.

[115] Mahmoud M.E., El Zokm G.M., Farag A.E., Abdelwahab M.S. Assessment of heat-inactivated marine Aspergillus flavus as a novel biosorbent for removal of Cd[II], Hg[II], and Pb[II] from water. *Environmental Science and Pollution Research*, 2017, **24**, P. 18218–18228.

[116] Petrella A., Spasiano D., et al. Heavy metals retention [Pb[II], Cd[II], Ni[II]] from single and multimetal solutions by natural biosorbents from the olive oil milling operations. *Process Safety and Environmental Protection*, 2018, **114**, P. 79–90.

[117] Alharbi H.F., Haddad M.Y., et al. Electrospun bilayer pan/chitosan nanofiber membranes incorporated with metal oxide nanoparticles for heavy metal ion adsorption. *Coatings*, 2020, **10** (3), 285.

[118] Brandes R., Belosinschi D., Brouillette F., Chabot B. A new electrospun chitosan/phosphorylated nanocellulose biosorbent for the removal of cadmium ions from aqueous solutions. *J. of Environmental Chemical Engineering*, 2019, **7** (6), 103477.

[119] Karim M.R., Aijaz M.O., et al. Composite nanofibers membranes of poly[vinyl alcohol]/chitosan forselective lead[II] and cadmium[II] ions removal from wastewater. *Ecotoxicology and Environmental Safety*, 2019, **169**, P. 479–486.

[120] Jamshidifard S., Koushkbaghi S., et al. Incorporation of UiO-66-NH_2 MOF into the PAN/chitosan nanofibers for adsorption and membrane filtration of Pb(II), Cd(II) and Cr(VI) ions from aqueous solutions. *J. of Hazardous Materials*, 2019, **15** (368), P. 10–20.

[121] Thomas M.S., S. Pillai P.K.S., et al. Polylactic acid/nano chitosan composite fibers and their morphological, physical characterization for the removal of cadmium[II] from water. *J. of Applied Polymer Science*, 2020, **137** (34), 48993.

[122] Miretzky P., Cirelli A.F. Hg(II) removal from water by chitosan and chitosan derivatives: A review. *J. of hazardous materials*, 2009, **167** (1–3), P. 10–23.

[123] Dorea J.G., Donangelo C.M. Exposure to mercury and aluminum in early life: Developmental vulnerability as a modifying factor in neurologic and immunologic effects. *Clinical nutrition*, 2006, **25**, P. 369–376.

[124] Nolan E.M., Lippard S.J. Tools and tactics for the optical detection of mercuric ion. *Chemical reviews*, 2008, **108**, P. 3443–3480.

[125] Nam K.H., Gomez-Salazar S., Tavlarides L.L. Mercury(II) adsorption from wastewaters using a thiol functional adsorbent. *Industrial & engineering chemistry research*, 2003, **42**, P. 1955–1964.

[126] Monier M., Ayad D., Wei Y., Sarhan A. Preparation and characterization of magnetic chelating resin based on chitosan for adsorption of Cu(II), Co(II), and Ni(II) ions. *Reactive and Functional Polymers*, 2010, **70** (4), P. 257–266.

[127] Wu F.C., Tseng R.L., Juang R.S. Kinetic modeling of liquid-phase adsorption of reactive dyes and metal ions on chitosan. *Water Research*, 2001, **35** (3), P. 613–618.

[128] Pérez-García F., Galán-Vidal C.A., et al. Selective liquid-liquid extraction of mercury(ii) from aqueous solution by N-alkyldithiophosphate compounds $CH_3(CH_2)_nS_2P(OC_6H_4)_2$ (n = 0 to 4). *Separation Science and Technology*, 2013, **48**, P. 736–740.

[129] Sharma R., Singh N., et al. Cerium functionalized PVA-Chitosan composite nanofibers for effective remediation of ultra-low concentrations of Hg [II] in water. *RSC Advances*, 2015, **5**, P. 16622–16630.

[130] Findeiß M.J., Schäffer A. Fate and environmental impact ofthorium residues during rare earth processing. *J. of Sustainable Metallurgy*, 2017, **3** (2), P. 179–189.

[131] Gore P.M., Khurana L., et al. Ion-imprinted electrospun nanofibers of chitosan/1-butyl-3-methylimidazolium tetrafluoroborate for the dynamic expulsion of thorium (IV) ions from mimicked effluents. *Environmental Science and Pollution Research*, 2018, **25**, P. 3320–3334.

[132] Martins M., Faleiro M.L., et al. Anaerobic bio-removal of uranium (VI) and chromium (VI): comparison of microbial community structure. *J. of Hazardous Materials*, 2010, **176** (1–3), P. 1065–1072.

[133] Villalobos-Rodriguez R., Montero-Cabrera M.E., et al. Uranium removal from water using cellulose triacetate membranes added with activated carbon. *Applied Radiation and Isotopes*, 2012, **70** (5), P. 872–881.

[134] Aly M.M., Hamza M.F. A review: Studies on uranium removal using differenttechniques. Overview. *J. of Dispersion Science and Technology*, 2013, **34** (2), P. 182–213.

[135] Bhalara P.D., Punetha D., Balasubramanian K. A review of potential remediation techniques for uranium[VI] ionretrieval from contaminated aqueous environment. *J. of Environmental Chemical Engineering*, 2014, **2**, P. 1621–1634.

[136] Christou C., Philippou K., Krasia-Christoforou T., Pashalidis I. Uranium adsorption by polyvinylpyrrolidone/chitosan blended nanofibers. *Carbohydarte polymers*, 2019, **219**, P. 298–305.

[137] Keshtkar A.R., Irani M., Moosavian M.A. Removal of uranium (VI) from aqueous solutions by adsorption using a novel electrospun PVA/TEOS/APTES hybrid nanofiber membrane: comparison with casting PVA/TEOS/APTES hybrid membrane. *J. of Radioanalytical and Nuclear Chemistry*, 2013, **295**, P. 563–5571.

[138] Rastmanesh F., Safaie S., Zarasvandi A.R., Edraki M. Heavy metal enrichment and ecological risk assessment of surface sediments in Khorramabad River, West Iran. *Environmental Monitoring and Assessment*, 2018, **190** (5), 273.

[139] Biglari H., Saeidi M.,et al. Review on hydrochemical and health effects of it in Sistan and Baluchistan groundwaters Iran. *Int. J. of Pharmacy and Technology*, 2016, **8** (3), P. 17900–17920.

[140] Goel P.K. *Water pollution: Causes, effects and control*. New Age International, New Delhi, 2006.

[141] Genchi G., Carocci A., et al. Nickel: Human Health and Environmental Toxicology. *Int. J. of Environmental Research and Public Health*, 2020, **17**, 679.

[142] Karamipour A., Khadiv-Parsi P., et al. Using Fe_3O_4-coated nanofibers based on cellulose acetate/chitosan for adsorption of Cr[VI], Ni[II] and phenol from aqueous solutions. *Int. J. of Biological Macromolecules*, 2019, **154**, P. 1132–1139.

[143] Bozorgi M., Abbasizadeh S., Samani F., Mousavi S.E. Performance of synthesized cast and electrospun PVA/chitosan/ZnO-NH_2 nano-adsorbents in single and simultaneous adsorption of cadmium and nickel ions from wastewater. *Environmental Science and Pollution Research*, 2018, **25**, P. 17457–17472.

[144] Habiba U., Afifi A.M., Salleh A., Ang B.C. Chitosan/[polyvinyl alcohol]/zeolite electrospun composite nanofibrous membrane for adsorption of Cr^{6+}, Fe^{3+} and Ni^{2+}. *J. of Hazardous Materials*, 2016, **322**, P. 182–194.

[145] Jafarnejad M., Asli M.D., Taromi F.A., Manoochehri M. Synthesis of multi-functionalized Fe_3O_4-NH_2-SH nanofiber based on chitosan for single and simultaneous adsorption of Pb[II] and Ni[II] from aqueous system. *Int. J. of Biological Macromolecules*, 2020, **148**, P. 201–217.

[146] Min L-L., Yuan Z-H., et al. Preparation of chitosan based electro spun nanofiber membrane and its adsorptive removal of arsenate from aqueous solution. *Chemical Engineering Journal*, 2014, **267**, P. 132–141.

[147] Tan P., Zheng Y., Hub Y. Efficient removal of arsenate from water by lanthanum immobilized electrospun chitosan nanofiber. *Colloids and Surfaces A: Physicochemical and Engineering Aspects*, 2020, **589**, 124417.

[148] Min L-L., Yang L-M., et al. Enhanced adsorption of arsenite from aqueous solution by an iron-doped electro spun chitosan nanofiber mat: Preparation, characterization and performance. *J. of Colloid and Interface Science*, 2019, **535**, P. 255–264.

[149] Sharma R., Singh N., et al. Electro spun chitosan-polyvinyl alcohol composite nanofibers loaded with cerium for efficient removal of arsenic from contaminated water. *J. of Material Chemistry A*, 2014, **2**, P. 16669–16677.

[150] Min L-L., Zhong L-B., et al. Functionalized chitosan electro spun nanofiber for effective removal of trace arsenate from water. *Scientific Reports*, 2016, **6**, 32480.

[151] Li L., Li Y., Yang C. Chemical filtration of Cr (VI) with electrospun chitosan nanofiber membranes. *Carbohydrate Polymers*, 2016, **140**, P. 299–307.

[152] Aliabadi M., Irani M., et al. Electrospun nanofiber membrane of PEO/Chitosan for the adsorption of nickel, cadmium, lead and copper ions from aqueous solution. *Chemical Engineering Journal*, 2013, **220**, P. 237–243.

[153] Li X., Zhou H., et al. Studies of heavy metal ion adsorption on chitosan/sulfydryl-functionalized graphene oxide composites. *J. of Colloid and Interface Science*, 2015, **448**, P. 389–397.

[154] Karthik R., Meenakshi S. Removal of Pb(II) and Cd(II) ions from aqueous solution using polyaniline grafted chitosan. *Chemical Engineering Journal*, 2015, **263**, P. 168–177.

[155] Chen A.H., Liu S.C., Chen C.Y., Chen C.Y. Comparative adsorption of Cu[II], Zn[II], and Pb[II] ions in aqueous solution on the crosslinked chitosan with epichlorohydrin. *J. of Hazardous materials*, 2008, **154** (1), P. 184–191.

[156] Phan D-N., Lee H., et al. Fabrication of electrospun chitosan/cellulose nanofibers having adsorption property with enhanced mechanical property. *Cellulose*, 2019, **26**, P. 1781–1793.

[157] Zhang X., Shi X., et al. Preparation of chitosan stacking membranes for adsorption of copper ions. *Polymers*, 2019, **11**, 1463.

[158] Boddu V.M., Abburi K., et al. Removal of arsenic [III] and arsenic [V] from aqueous medium using chitosan-coated biosorbent. *Water Research*, 2008, **42** (3), P. 633–642.

[159] Guo X., Du B., et al. Synthesis of amino functionalized magnetic graphenes composite material and its application to remove Cr(VI), Pb(II), Hg(II), Cd(II) and Ni(II) from contaminated water. *J. of Hazardous Materials*, 2014, **278**, P. 211–220.

[160] Li J., Jiang B., et al. Preparation and adsorption properties of magnetic chitosan composite adsorbent for Cu^{2+} removal. *J. of Cleaner Production*, 2017, **158**, P. 51–58.

[161] Mahfouz M.G., Galhoum A.A., et al. Uranium extraction using magnetic nano-based particles of diethylenetriamine-functionalized chitosan: Equilibrium and kinetic studies. *Chemical Engineering Journal*, 2015, **262**, P. 198–209.

[162] Shariful M.I., Sepehr T., et al. Adsorption capability of heavy metals by chitosan/poly (ethylene oxide)/activated carbon electrospun nanofibrous membrane. *J. of Applied Polymer Science*, 2017, **135**, 45851.

[163] Min M., Shen L., et al. Micro-nano structure poly(ether sulfones)/poly(ethyleneimine) nanofibrous affinity membranes for adsorption of anionic dyes and heavy metal ions in aqueous solution. *Chemical Engineering Journal*, 2012, **197**, P. 88–100.

NANOSYSTEMS: PHYSICS, CHEMISTRY, MATHEMATICS, 2021, 12 (6), P. 749–762

Novel gold nanoparticle-protein-semiconductor quantum dot hybrid system: synthesis, characterization and application in cancer cell imaging

Runjun Sarma[1,*], Monoj KumarDas[2], Lakshi Saikia[3], Ratul Saikia[4]

[1]Department of Physics, Mehr Chand Mahajan DAV College for Women, Sector-36, Chandigarh, India

[2]Cancer Genetics and Chemoprevention Research Group, Department of Molecular Biology and Biotechnology, Tezpur University, Assam-784028, India

[3]Advanced Materials Group, Material Science and Technology Division, CSIR-North East Institute of Science and Technology, Jorhat, Assam-785006, India

[4]Biological Science and Technology Division, CSIR-North East Institute of Science and Technology, Jorhat, Assam-785006, India

*runjun2018chd@gmail.com

DOI 10.17586/2220-8054-2021-12-6-749-762

Formation of a hybrid system by metallic nanoparticle, protein (or peptide), and a semiconductor QD can be a new and alternate material which may be used for biological applications including cancer cell detection and treatment. Herein, we report on the colloidal synthesis of metal-protein-QD hybrid system considering Au NPs, CdSe QDs, BSA and Lysozyme protein. We demonstrate the structural, optical and vibrational properties of Au-CdSe, Au-BSA-CdSe and Au-Lysozyme-CdSe hybrid systems following their use as cancer cell markers. The study of photoluminescence spectra reveals the predominance fluorescence resonance energy transfer (FRET) between CdSe QDs and Au NPs, Au-BSA and Au-Lysozyme complex. The energy transfer efficiency between QDs donor and the Au NPs, Au-BSA, Au-Lysozyme acceptors are estimated to be 46%, 94% and 64%; respectively. Fluorescence imaging results represent high biocompatibility and fluorescent behavior of the QDs and its hybrid system in the MDA-MB-231 breast cancer cells. The calculation of corrected total counts of fluorescence (CTCF) predicts the higher uptake of CdSe QDs as compared to the Au-QDs, Au-BSA-QDs, Au-Lysozyme-QDs by the cells. The significantly varied zeta potential values of the hybrid systems influence the cellular uptake processes. The fabrication of biocompatible (water soluble, biologically stable, having bioconjugation capability, low cytotoxic to the normal cells, fluorescent in biological environment) Au-CdSe, Au-protein-CdSe hybrid systems would open up an alternative strategy in nanobiotechnology, due to their special physical, optical as well as chemical properties.

Keywords: Semiconductor QDs, Metallic Nanoparticles, Nanoparticle-QDs hybrid system, Protein, Cancer Cell imaging.

Received: 22 September 2021

Revised: 9 November 2021

1. Introduction

Cancer is becoming one of the leading causes of death and the number of cancer cases worldwide is expected to reach 22 million in the next two decades [1]. Although different treatment options are available, including, surgery, chemotherapy, radiation etc., they cannot be considered as completely effective because of lack of high sensitivity and toxicity response to the non-cancerous normal tissue [2]. However, these treatments result in slow progression of the disease and hence increasing the duration for the survival of the patient. In this regard, the use of nanotechnology-based cancer therapies have received considerable attention in recent years because of: early detection with high sensitivity and efficacy, target specific drug delivery, high *in vivo* imaging resolution etc. [3,4]. In recent years, metallic nanoparticles in general, and gold nanoparticles (Au-NPs) in particular have attracted considerable interest in nanotherapeutic cancer cell treatment as targeting ligands, contrast agents for cancer imaging, therapeutic drugs etc. [5–8].This is due to their unique optical properties, chemical stability, easy synthesis and functionalization, potential biocompatibility, size and surface-dependent properties etc. [9, 10]. Moreover, Au NPs do not show cytotoxic effect or severe damage on normal cells even when administered orally for a specific period of time [11].

Semiconductor nanocrystals, or quantum dots (QDs) on the other hand, have been considered as efficient luminescent probes and labels for numerous biological applications including target specific cancer therapy owing to their special optoelectronic properties, such as, size-tunable light emission, high signal brightness, long term photostability and narrow emission line width [12, 13]. Amongst quantum dots (QD), cadmium selenide (CdSe), is remarkable, because of its various advantages, including band gap tunability and bright emission behavior [14]. Again, the cytotoxicity of ionic cadmium (Cd^{2+}) in nanosized CdSe and CdTe has been reported to be appreciably less as compared to elemental cadmium [15]. In addition, cytotoxicity in the cellular studies is mainly contributed from the surface modifier rather than CdSe or CdTe core [16]. Consequently, there exist plentiful scope for safe use of nanoscale CdSe in biological systems [17–19] without causing severe damage to normal cells.

Metallic NPs-semiconductor QDs, on the other hand, formed as a result of interaction of quantum confined electrons (excitons) in the QDs and dielectric confined electromagnetic modes (localized surface plasmon resonance (LSPR)) of metallic NPs, opens up their utilization in various novel technological applications in recent years [20]. This is due to their extraordinary optical properties which includes plasmon-induced fluorescence enhancement and quenching [21], plasmon-assisted Forster energy transfer [22], induced exciton-plasmon photon conversion [23] generation of a single plasmons and so on. The study of energy transfer mechanism in metal-QDs systems has great potential in the areas of luminescence tagging, imaging, medical diagnostics, multiplexing, biosensors etc. Until recently, according to various reports, among various semiconductor QDs, CdSe-QDs were proven to act as an effective donor in a fluorescence resonance energy transfer (FRET) mechanism [24].

Biocompatibility is the property of a material that describes its compatibility with the biological particles such as, protein, cells tissue etc. The prerequisites of a NP or a QD to be biocompatible are water solubility, biological environment stability (low aggregation), bioconjugation capability (biological affinity), low cytotoxicity for the normal cells, etc. Biocompatible water soluble, stable NPs/QDs can be achieved through surface modification and functionalization. The different surface modification processes to make biocompatible NPs/QDs are: i) Use of different polymer [25,26], surfactant [27] ii) Capping of the NPs by suitable ligand molecule [28,29] etc. iii) Surface silanization [30] etc. The high adsorption capacity of nanoparticle in biological environment signifies an increased bioconjugation capability and thus biocompatibility of the nanoparticles. Nanoparticles (NPs) have significant adsorption capacities due to their relatively larger surface area. Thus, they are able to bind or carry other molecules such as drugs, probes and proteins attached to their surface by covalent bonds or by adsorption. By attaching specific chemical compounds, peptides or proteins to the surface, the physicochemical properties including charge, hydrophobicity etc. of the NPs can be altered. With the exposure of Au NPs to biological fluid environments, proteins are easily adsorbed onto the surface. This results in a significant variation of the surface property of the Au NPs as well as physiological functions of the adsorbed proteins [31–33]. Similarly, conjugation of QDs, such as CdSe with different biological molecules, including proteins can create a system with desirable luminescent and bio-compatible properties [34,35]. A protein-conjugated NP or QD, results in various special properties of the protein - NP (or QD) system which is based on the characteristics of the conjugated proteins [36,37]. Bovine Serum Albumin (BSA) is the most abundant protein (molecular mass $\sim$66.5 kDa, consisting of $\sim$583 amino acid) in cow-based plasma. It is extensively used in various bio-nanotechnology applications including sensing, imaging etc [38]. Moreover, BSA-conjugated NPs are more stable against flocculation, show better quantum yield and low toxicity. Similarly, Lysozyme proteins (molecular mass $\sim$14 kDa, consisting of $\sim$129 amino acids) that are found in cow/human milk, saliva, serum, tears, hen egg whites have various biomedical applications due to their special antibacterial, anti-inflammatory and anti-cancer properties [39].

In the present work, we describe simple colloidal routes for the synthesis of polyvinyl pyrrolidone (PVP) and sodium dodecyl sulfate (SDS) capped Au NPs and highly fluorescent CdSe QDs; respectively. We report also here the formation of a Au NPs-CdSe QDs hybrid system. The structural, optical, vibrational properties and zeta potential measurement of the Au, CdSe, Au-CdSe hybrid systems are studied. The influence of protein molecules on the aforementioned properties was investigated by inclusion of BSA and Lysozyme proteins to the Au-CdSe. In addition, we have highlighted the energy transfer behavior of the CdSeQDs to Au NPs, Au-BSA, Au-Lysozyme by considering FRET. Finally, a critical evaluation on the cellular uptake of the CdSe QDs, Au-CdSe s, Au-BSA-CdSe, Au-Lysozyme-CdSe hybrid systems by MDA-MB-231 breast cancer cells lines are highlighted through studies of fluorescence imaging and cytotoxicity.

Forming a biocompatible hybrid system with metallic nanoparticle, protein (or peptide), and a semiconductor quantum dot can be a new and alternate material which may be used for biological applications including cancer cell detection and treatment [39].

2. Experimental Details

2.1. Synthesis of Au Nanoparticles

Polyvinylpyrrolidone (PVP) is used for the surface modification of the Au NPs to allow their stabilization in the dispersion media. The polymers cause steric repulsion and prevent aggregation of the colloid particles, making them good stabilizer. PVP is widely accepted as a biocompatible polymeric material and it can effectively bind to BSA and Lysozyme proteins [40]. Moreover, PVP can be safely used, as it is nontoxic for normal cells [41].

For the synthesis of PVP surface modified Au NPs, at first, a 1% PVP solution was prepared by dissolving 0.1 g of PVP in 10 mL distilled water with stirring for 30 min. Then, 3.39 g of gold salt (chloroauric acid, $HAuCl_4$) was dissolved in 10 mL distilled water to prepare 1 mM stock solution. From the stock solution a 0.2 mM solution was prepared and added to the PVP solution. After 10 minutes of stirring, freshly prepared 1 mL of 0.2 mM sodium borohydride ($NaBH_4$) in ice cold water was added to the above mixture drop wise. With the addition of $NaBH_4$, the color of the solution spontaneously changes from the light yellow to reddish indicating the formation of the Au NPs by reduction of $HAuCl_4$ by $NaBH_4$.

2.2. Synthesis of CdSe-SDS QDs

SDS surfactant-modified CdSe QDs has been found to be less cytotoxic to the normal cells as compared to other surfactants [19]. Here, SDS-capped CdSe QDs (CdSe-SDS) were prepared and washed by reported method [17]. Briefly, a suitable amount of cadmium nitrate-tetrahydrate $[Cd(NO_3)_2{\cdot}4H_2O]$ and SDS were dissolved in deionized Millipore water followed by stirring at ∼40°C for 20 min. At high pH, the selenium precursor, selenium dioxide (SeO_2) was reduced by sodium borohydride ($NaBH_4$) and mixed with the above solution and stirred for 1 h at 80°C to get CdSe-SDS QDs.

The synthesized PVP-capped Au NPs, SDS-functionalized CdSe QDs, were found to be water soluble and stable in the biological environment. The bio-conjugation capability of the synthesized Au NPs and CdSe QDs were studied by conjugating the nanoparticle/QDs with BSA and Lysozyme proteins as well as by studying their (Au-CdSe, Au-BSA-CdS, Au-Lysozyme-CdSe systems) fluorescent behavior in the cancer cell environment. Prior to bioconjugation, Au NPs, CdSe QDs, the colloidal solutions were subjected to centrifugation (∼7000 rpm) separately followed by several rinses with deionized water.

2.3. Synthesis Au-CdSe, Au-BSA-CdSe, Au-Lysozyme-CdSe hybrid system

For the preparation of Au-CdSe complex, 20 mL Au NPs solution was mixed with 2 mL CdSe QDs solution and stirred for 1 h. 5 mL Au-BSA (or Au-Lysozyme) were prepared by mixing BSA (or Lysozyme) protein (each protein concentration 20 μg/mL)to Au NPs in two separate beakers. This is followed by mild stirring and incubation of the mixtures at 37°C for 1 h. The CdSe QDs were conjugated to Au-BSA (or Au-Lysozyme) by stirring for 1 h at 500 rpm to get Au-BSA-CdSe and Au-Lysozyme-CdSe hybrid system.

The pyrrolidone side group of PVP in Au-PVP NPs may interact with the anionic SDS surfactant coated CdSe QDs. This results the formation of the Au-CdSe hybrid system [42]. Inserting BSA (or Lysozyme) protein in the Au-CdSe complex, there is a possibility of interaction of H_3N^+ of group of BSA (or Lysozyme) to the anionic SDS in one side and in the other side COO- part of BSA to the positively charged PVP molecule resulting Au-BSA-CdSe and Au-Lysozyme-CdSe hybrid [43, 44]. Fig. 1 shows the schematic figure of possible formation of Au-CdSe (Fig. 1A), Au-BSA-CdSe and Au-Lysozyme-CdSe (Fig. 1B).

2.4. Cell culture, fluorescent and cytotoxicity study

Breast cancer cell line MDA-MB-231 was purchased from the National Centre for Cell Science (NCCS), Pune, India. MDA-MB-231 cells were cultured in L-15 medium (Leibovitz) (HiMedia, Mumbai, India) containing 10% fetal bovine serum, 100 U/mL penicillin and 100 mg/mL streptomycin. The cells were washed with phosphate buffer solution (PBS) and harvested with 0.25% trypsin–EDTA solution and seeded at densities of $2{\times}10^4$ cells/well onto cover glasses placed inside a 6-well tissue culture plate. Cells were treated with 25 μg/mL QDs, Au-QD and Au-protein-QD complexes separately for 24 h. After this treatment, the cells were washed twice with 1X PBS to remove the unattached cells and then 10 μL of cell suspension were taken into slides and observed in a fluorescence microscope. The CdSe QDs and its different complexes were used as cancer cell probes by using fluorescent a microscope (Model: LeicaDM300, USA) equipped with a cooled color CCD camera (Model DP71) with 40× objectives. QD fluorescence was detected using band-pass (BP) excitation and emission filters.

In vitro cytotoxicity of QDs, Au-protein-QD complexes was assessed using a standard MTT (3-(4,5-dimethyl-2-thiazolyl)-2,5- diphenyl-2-H-tetrazoliumbromide) assay with cell lines (MDA-MB231 cells) $2{\times}10^3$ cells were seeded in a 96-well plate and treated with increasing concentrations 5, 10 and 25 μg/mL of QDs, Au-protein-QD complexes for 24 h at 37°C, 5% CO_2 Cytotoxicity was determined by adding 10 μL of MTT (0.5 mg/mL in PBS) to each well and incubated for 4 h. The medium was removed and 200 μl DMSO was added to each well and after 10 min of mechanical shaking, the optical density was measured at 570 nm in plate reader. The viability was determined in relation to control cells cultured in drug-free media. All experiments were repeated at least three times. SEM values were less than 10%.

2.5. Characterization Techniques

The structural characterizations of the Au NPs, CdSe QDs and Au-CdSe systems were performed by a high-resolution transmission electron microscopy (HRTEM), (Model: JEM-2100) at NEHU working at an accelerating voltage of 200 kV. The optical absorption study was performed by the UV–Visible absorption spectroscopy (Model:

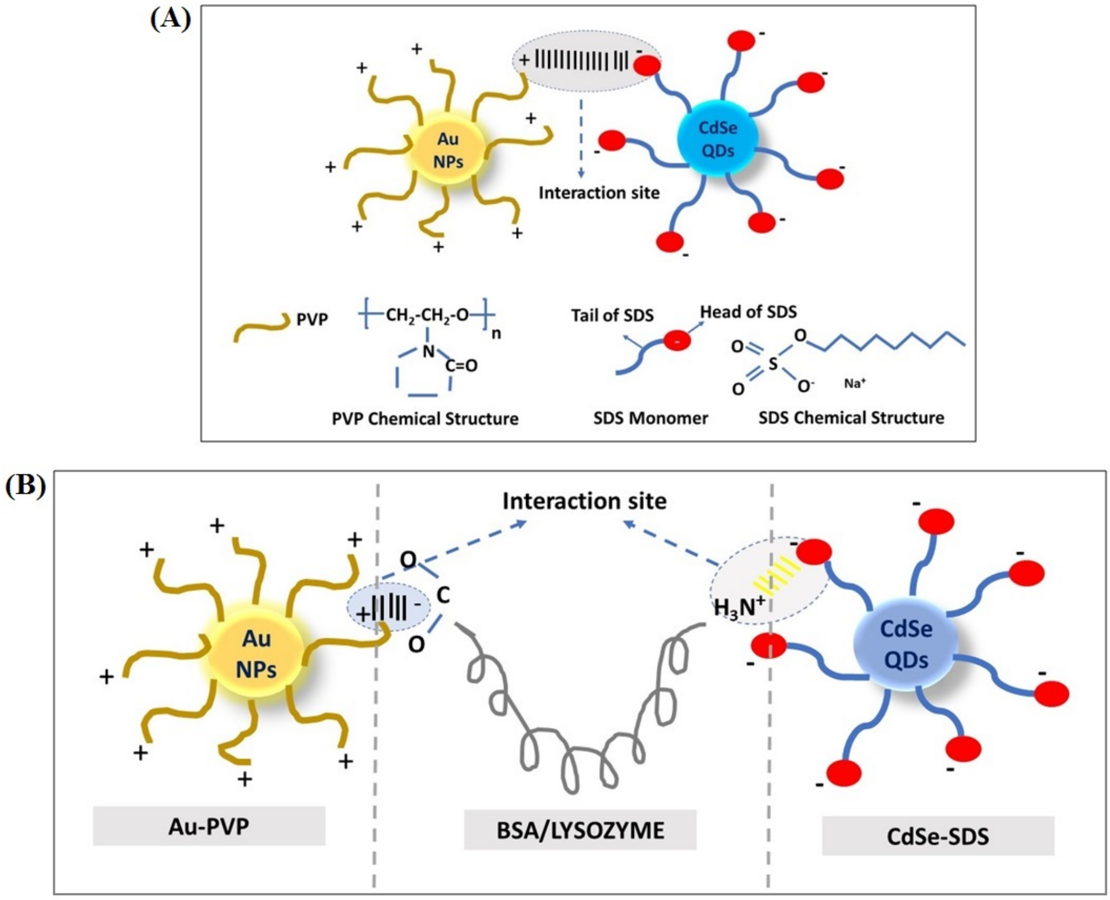

FIG. 1. Schematic diagram of formation of (A) PVA capped Au NP and SDS coated CdSe QD complex (B) Au-BSA-CdSe (or Au-Lysozyme-CdSe) hybrid system

MS-11-UV-1800, Shimadzu Corporation), whereas photoluminescence (PL) spectra were obtained by using a spectrofluorometer (FluoroMax-4CL, HORIBA Scientific). The zeta potential was measured using a Malvern Zetasizer (Model: Nano ZS). Furthermore, IR-active vibrational features were assessed through Fourier transform infrared (FT-IR) (Model: NicoletImpact-410) studies. The QDs were used as cancer cell probe by using fluorescent microscope (Model: Leica DM300, USA).

3. Results and Discussions

We discuss below the analysis of PVP-capped Au NPs, SDS-coated CdSeQD, Au-CdSe, Au-Protein-CdSe complexes characterized by different techniques.

3.1. Morphological analysis through transmission electron microscopy studies

The HRTEM images of the as-synthesized PVP capped Au NPs, CdSe-SDS QDs, and Au-CdSe metallic semiconductor hybrid system are shown in Fig. 2A, 2B and 2C respectively. The Au NPs are found to be fairly hexagonal in shape and each particle are isolated from each other (Fig. 2A(i)). The magnified image of a Au NP is shown in the inset of Fig. 2A(i). Whereas, the obtained CdSe-QDs (Fig. 2B(i)) and Au–CdSe (Fig. 2C(i)) NP-QD systems were nearly spherical in shape. The average size (D) of the Au NPs, CdSe-QDs and Au-CdSe were predicted to be $\sim$2 nm, $\sim$4.68 nm and 3.8 nm; respectively as obtained from the size distribution histogram (Insets Fig. 2A(i), 2B(i), 2C(i)). The SAED patterns revealed the polycrystalline nature of Au NPs (Fig. 2A,(ii)) [45], CdSe QDs (Fig. 2B,(ii)) [46] and Au-CdSe (Fig. 2C,(ii)) complex. The SAED pattern of Au NPs clearly indicates the growth of lattice planes along (111), (200) and (220) directions with interplanar distance of $\sim$0.23, $\sim$0.20, $\sim$0.14 nm; respectively. The *fast Fourier transform* (FFT) of a selected part was taken to measure the lattice plane distances with increased accuracy. Consequently, it signified the lattice plane distance of 0.23 nm having growth along the (111) direction (upper left inset of Fig. 2A, (ii)). The value of d_i of Au NPs resembled the value for the bulk Au system. A magnified, well- resolved

TABLE 1. Values of Zeta potentials

Sample	Zeta potential (mV)
Au NPs	-13.2
CdSe-SDS QDs	-54
Au NPs-CdSe QDs	-16.9
Au NPs-BSA-CdSe QDs	-16.7
Au NPs-Lysozyme-CdSe QDs	-9.7

lattice planes of a single Au-NP has been shown as in lower right corner of the Figure. In the case of an isolated CdSe-SDS QD, the FFT image (upper left inset of Fig. 2B, (ii))) highlight the distinct diffraction spot corresponding to (101) plane with an inter-planar spacing (d_i) of ∼0.35 nm. For the composite Au-QD system, the SAED pattern (Fig.2C(ii)) was found to be different from that of pure Au or pure CdSe QDs system. This indicates that particles are not the pure Au NPs or pure CdSe QDs. The first diffraction ring of the SAED pattern was predicted to be from (111) plane of pure Au NPs, while the second is due to the diffraction from (112) plane of CdSe QDs. We have taken FFT image and produced the intensity plot profile (IPF)[https://imagej.nih.gov/ij/docs/examples/tem/] of the inverse FFT image considering different sections of the TEM image of a single particle to more clear visualization of interplanar spacing in this complex. It is to be noted that the corresponding FFT and IPF of the section A (shown in Fig. 2C,(iii)) clearly indicates the d_i of 0.20 nm of (111) crystallographic orientation of Au NP. Whereas, the section B specifies the presence of CdSe QDs with lattice plane direction along (102) with d_i of 0.26 nm. As TEM images are 2D images, the spatial locations of the QDs in the Au NPs are impossible to identify. However, their presence as attached part in the outer side can easily be identified. The increase of average diameter of Au NPs from ∼2 nm to ∼3.8 nm supports this fact. Similar behavior has been observed for $\mathrm{CdS}_x\mathrm{Se}_{1-x}$/ZnS QDs in Au NPs [47].

3.2. Measurement of zeta potential

The magnitude of the zeta potential gives an indication of the potential electrostatic stability of the colloidal system. As the zeta (ξ) potential increases (negative or positive), the repulsion between the constituent particles gets enhanced, resulting in a more stable colloidal dispersion [48]. However, a colloidal solution with nanoparticles having zeta potential values varying in the range of -30 to ± 30 mV is generally considered to be stable [49]. In nano-drug delivery systems, the zeta potential not only affects the stability of the colloidal system, but also it dramatically changes their circulation in the blood stream and absorption of the NPs into the cellular membranes [50]. It is to be noted that particles with negative zeta potential values are less cytotoxic as compared to the positive counterparts. This is because of their rapid opsonization and hence clearance by the reticuloendothelial system (RES) in the blood stream [50]. The positively charged NPs, on the other hand, can be cytotoxic due to their cationic charge density and the molecular weight etc.

While studying the zeta potential (Table 1) behavior of the as synthesized NPs, it was observed that all the systems showed negative zeta potential values (Table 1), indicating a good colloidal stability. By conjugating Au NPs with CdSe QDs, the zeta potential values of the Au NPs were improved to -16.9 mV from -13.2 mV. A zeta potential value of ~ -15 mV for PVP capped Au NPs has been reported previously [51].

While conjugating BSA protein, the zeta potential of Au-CdSe complex slightly changes to -16.7 mV. On the other hand, significant variation of Zeta potential of Au-CdSe complex occurs to -9.7 mV from -16.9 mV while forming the Au-Lysozyme-CdSe complex. The change of the zeta potential values for Au-CdSe system with the inclusion of BSA and Lysozyme protein, signify the efficient conjugation of the respective proteins to the NP-QD complex. Moreover, the reduction of zeta potential value of the parent Au NPs with formation of Au-CdSe, Au-BSA-CdSe, Au-Lysozyme-CdSe complexes signifies the enhancement of the stability of the Au NPs system.

3.3. Molecular vibrations in Au NPs, Au-CdSe NPs-QDs, and Au-BSA-CdSe, Au-Lysozyme-CdSe complex

The FTIR spectra of Au NPs, CdSe-QDs, Au-CdSe, Au-BSA-CdSe, Au-Lysozyme-CdSe complexes are shown in Fig. 3. The common bands observed around 3411 cm^{-1} and 1630 cm^{-1} in all the spectra, reveal O-H stretching and an O-H bending vibration of water respectively. Whereas, in the case of PVP-capped Au NPs (Fig. 3, curve, (i)), the sharp band observed at 2122 cm^{-1} may correspond to the C-H bonding band of Au-PVP NPs which is red shifted from original peak at 2900 cm^{-1} of pure PVP [52]. The FTIR band due to the C=O stretching band of PVP has been observed at ∼1650 cm^{-1}. This band is red shifted from original band at 1667 cm^{-1} contained in the pure PVP. This indicates a charge transfer interaction of PVP molecules with Au surface via O-atom of pyrrolidone ring [53]. Similarly, CH_2 twisting (1,230 cm^{-1}) vibrations in the pyrrolidone ring of PVP molecules have been observed at

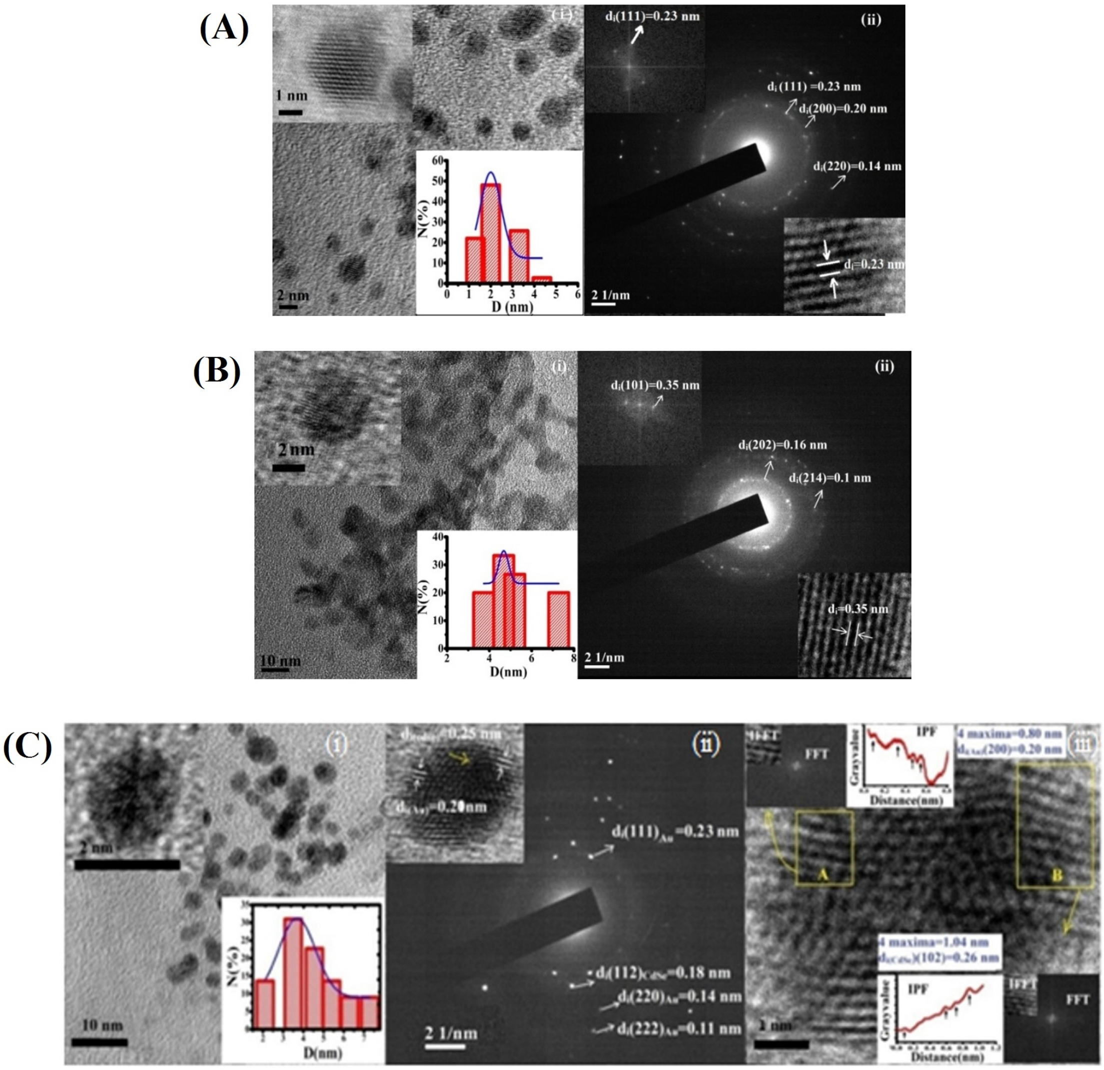

FIG. 2. HR-TEM image of (A) Au NPs (B) CdSe-SDS QDs (C) Au-CdSe NPs-QDs. Particle size distribution histogram are shown in lower right corners and single magnified particle in the upper left corner of the Fig. 1A(i), B(i), C(i). The SAED patterns with of the NPs systems are shown in (ii). The FFT pattern of the Fig. 1A(ii), B(ii) are shown in the upper left corner. Figure 1C(iii) shows the FFT patterns with IPF of different parts of a Au-CdSe complex indicating fromation of CdSe shell on the outer part of Au NPs

1192 cm^{-1} in PVP-capped Au NPs. Fig. 3, curve (ii) shows the FTIR spectra of SDS capped CdSe QDs. It can be observed that, with SDS coating, the peak due to the asymmetric -CH_2 stretching (ν_{asym}(-CH_2)) of the SDS surfactant can be witnessed at ~2919 cm^{-1}. However, the band at ~1524 cm^{-1} is assigned to the scissoring mode of the SDS surfactant, which is slightly shifted to a higher wave number position wrt 1559 cm^{-1} of pure SDS molecules. The spectral region located in 1300–1400 cm^{-1} in SDS is characteristic of the -CH_2 wagging modes. This region contains features which are related to gauche conformations. Thus, the band observed at ~1356 cm^{-1} of the CdSe-SDS QDs can be assigned to the CH_2 wagging mode. Whereas, the band corresponding to ν_{sym} (–SO_3^-) stretching mode of the SO_3^{2-} group is located at ~1207 cm^{-1}. The observed shifting of the ν_{sym}(–SO_3^-) mode from a value of 1084 cm^{-1} (pure SDS) to a value of ~1207 cm^{-1} (for CdSe-SDS QDs), is presumably due to an improved interaction of the headgroups with plentiful Na^+ counterions. The band observed at ~632 cm^{-1} is assigned to an effaceable bending of the Cd-Se itself. It can be anticipated that, the enhancement of interaction of the headgroups, as observed in case of SDS-capped QDs may create a stable dispersion of the QDs in the aqueous medium, thereby resulting in the formation of smaller sized QDs with good surface passivation [17,54].

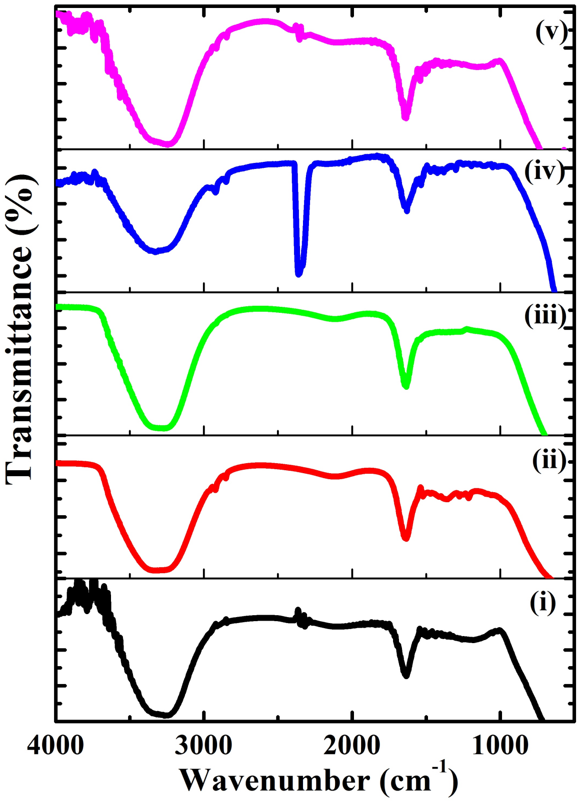

FIG. 3. FTIR spectra of (i) Au NPs (ii) CdSe-QDs (iii) Au-CdSe (iv) Au-BSA-CdSe and (v) Au-Lysozyme-CdSe hybrid system

The FTIR spectrum of Au-CdSe hybrid system can be depicted from Fig. 3, curve (iii). In this case, the band arises due to C-H bonding of PVP in Au-PVP NPs is slightly blue shifted to ∼2360 cm^{-1} from the original 2122 cm^{-1} of the parent Au NPs. The band corresponding to the ν_{sym} (–SO_3^-) stretching mode of the SO_3^{2-} group of SDS molecule was observed at 1268 cm^{-1} in this case.

Fig. 3,(iv), (v) shows the FTIR spectra Au-BSA-CdSe, Au-Lysozyme-CdSe complex; respectively. In this, the band raised due to C-H bonding of PVP can be observed at 2103 cm^{-1}. Whereas, the band at 1654 cm^{-1} is due to the C=O stretching vibration of peptide bond, while the bands at 1535 cm^{-1} and 1240 cm^{-1} are due to C-N stretching vibration/N-H bending vibration which are called the amide II band and amide III band, respectively. The band due to the asymmetric -CH_2 stretching (ν_{asym}(-CH_2)) of the SDS surfactant can be witnessed at ∼2842 cm^{-1}. While conjugating Lysozyme proteins to Au-CdSe NPs-QDs system, the bond due to amide I and amide II appears with lower intensity along with the appearance of C-H bond vibration of PVP and CH_2 stretching (ν_{asym}(-CH_2)) related to SDS. Note that the amide I band has a correlation with the secondary structure of the protein, whereas the amide II is indicative of the amount of protein adsorbed on surfaces. Thus, the arisen of FTIR peaks for amine groups of BSA in addition to the band due to PVP and SDS predicts the conjugation/absorption of BSA and Lysozyme protein to the Au-CdSe metal-semiconductor system [55].

3.4. UV-Vis spectra of Au NPs, Au-CdSe NPs-QDs, and Au-BSA-CdSe, Au-Lysozyme-CdSe hybrid system

Fig. 4 depicts the UV-Vis absorption spectra of Au NPs, CdSe QDs, Au-CdSe NPs-QDs and different protein conjugated systems. As can be found, Au NPs shows SPR band at ∼539 nm arising from the collective oscillation of free conduction electrons induced by an interacting electromagnetic field. Whereas, a prominent absorption band at ∼300 nm (4.13 eV), has been observed for CdSe-SDS QDs with a blue shifting of ∼2.39 eV from the bulk value of 1.74 eV. This shows effective quantum confinement of charge carriers in the SDS capped CdSe QDs. In the Au-CdSe hybrid system NPs, the SPR band assigned to Au NPs is observed at ∼545 nm with a red shifting of ∼5 nm from the parent Au NPs system. Moreover, this peak is found to be broadened than the original peak in Au NPs. On the other hand, a slight red shifting to ∼303 nm has been observed for CdSe-QDs peak in the hybrid metal semiconductor NPs system. This broadening of the SPR peak may be due to multipolar excitations and radiative damping in hybrid system [56]. While, the red shifting of plasmonic bands due to the conjugation to QDs suggests a strong interaction between the Au NPs and the CdSe QDs [57]. The covering of Au (RI:0.20) NPs core with CdSe (RI:2.5) QDs having larger refractive index (RI) may cause the observed red-shifting of the excitonic feature [58].

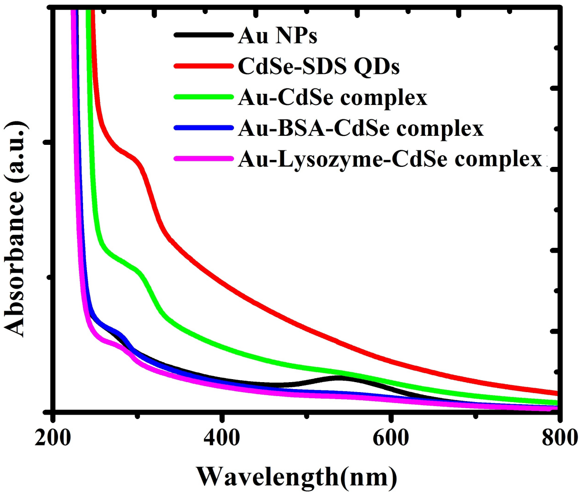

FIG. 4. UV-Vis spectra of Au NPs, CdSe-QDs, Au-CdSe NPs-QDs and their different protein conjugated hybrid systems

Note that, with conjugation of BSA protein, the absorption spectrum shows excitonic features at wavelengths of 277 nm and 545 nm. The absorption peak at ~277 nm is attributed to absorption feature of tryptophan molecule of BSA. Similarly, the Lysozyme protein conjugation results in absorption maxima at ~279 nm and at ~544 nm. The appearance of hump at ~277 and 279 nm in case of Au-BSA-CdSe and Au-Lysozyme-CdSe complex can be related to the interaction between serum albumin and AuNPs through a ground state complex formation, caused by the partial adsorption of BSA/Lysozyme proteins on the surface of NPs. Such an adsorption leads to a partial unfolding of the proteins due to the breaking of disulfide thus causing conformational changes [59].

3.5. PL spectra of Au-CdSe hybrid NPs/QDs, and Au-BSA-CdSe, Au-Lysozyme-CdSe complex

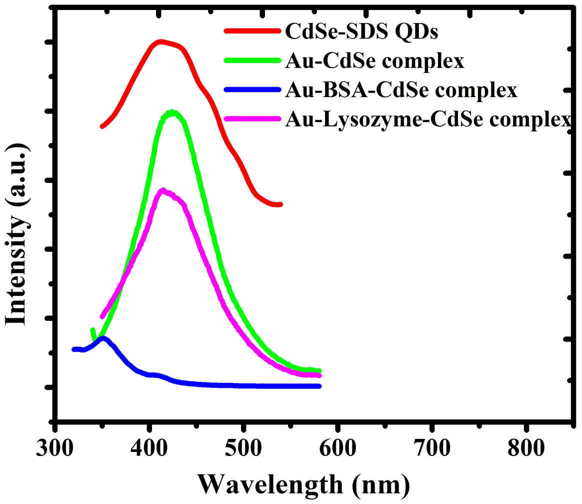

FIG. 5. PL spectra of CdSe-QDs, Au-CdSe NPs-QDs and their different protein conjugated hybrid systems

The PL spectra of Au NPs, CdSe QDs, Au-CdSe NPs-QDs and different protein conjugated systems are shown in Fig. 5 (excitation wavelengths, $\lambda_{ex} = 300$ for all the samples). When Au NPs form a hybrid system with CdSe-QDs, the emission maxima intensity of the QDs showed a quenching of intensity by 20%. Similar behavior has been observed with the formation of Au-Lysozyme-CdSe NP- protein-QD system. In this case, the intensity has been reduced to 57% as compared to bare CdSe-SDS QDs. On the other hand, while replacing Lysozyme with BSA protein, a sharp decrease of PL intensity of the QDs (up to ∼15%) has been observed. In addition, a significant blue shifting of the peak from ∼416 nm for the CdSe QDs to ∼344 nm has been observed in this system (Au-BSA-CdSe). In this case, the blue shifting of the emission peak in Au-BSA-CdSe hybrid system may signify a change in the tertiary structure of the BSA molecule with flexible conformation on the QDs surface by the SDS surfactant [60]. However, no blue shifting and hence, no effect of SDS surfactant on the modification of secondary has been observed for Lysozyme protein case. This is may be due to the highly stable behavior of the Lysozyme proteins [61].

While forming Au NPs-CdSe QDs system, a strong interaction between the plasmons of the metallic NPs and the excitons of the semiconductor QDs can be predicted to occur from the observed luminescence quenching of the QDs [57]. The conjugations of protein(s) with the Au NPs-CdSe QDs system(s) significantly influence the quenching phenomena by absorption of photons with their tryptophan moieties. The quenching of fluorescence intensity of the CdSe-QDs with conjugation of Au NPs and BSA or Lysozyme protein is due to the nonradiative energy transfer from QDs to metallic-semiconductor Au NPs and protein conjugated Au NPs [62].

The energy transfer efficiency can be measured experimentally by using the following equation [63]:

$$E = 1 - \frac{F_{DA}}{F_D}, \tag{1}$$

where F_{DA} is the integrated fluorescence intensity of the donor (CdSe-SDS QDs) in presence of the acceptor (Au NPs/ Au-BSA/ Au-Lysozyme NPs-protein complex) and F_D is the integrated fluorescence intensity of the donor alone. In the present case, the energy transfer efficiency of the CdSe-SDS QDs to the Au NPs was 46%. The corresponding value for the Lysozyme-conjugated Au NPs (Au-Lysozyme) was found to be 60%, whereas, for the BSA conjugated Au NPs (Au-BSA), the transfer efficiency was 94%.

In the classical Förster energy transfer mechanism, there should be significant overlapping between acceptor absorption spectra and donor emission spectra. In the present case(s), the overlapping can be possible by coupling of dipole of the QDs with the dipole of the LSPR field created by the Au NPs (or Au-protein complexes) [64]. As the LSPR is highly sensitive to the small changes in the surface environment, the coupling of CdSe QDs with the Au NPs and Au-BSA/Lysozyme significantly regulates the QDs fluorescent emission behavior.

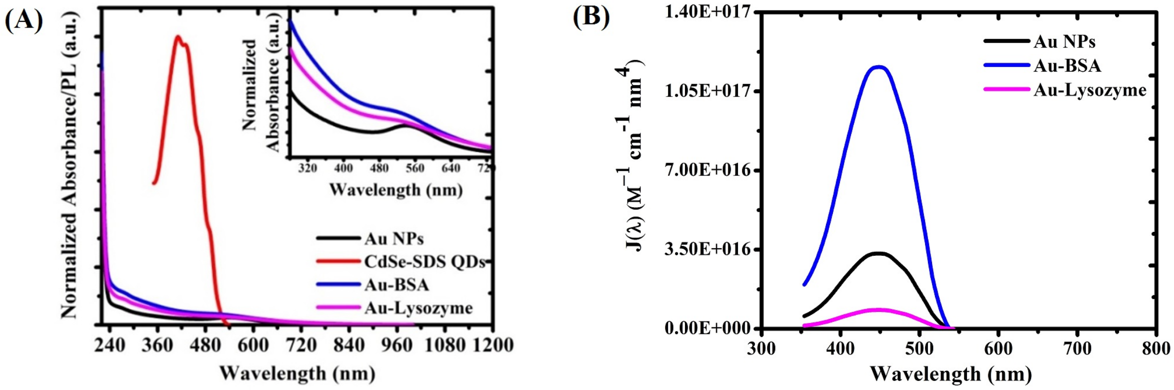

FIG. 6. (A) overlapping behavior (B) overlapping integral spectra between the normalized absorption spectra of Au NPs/ Au-BSA/ Au-Lysozyme complex and emission spectra of CdSe-SDS QDs

Fig. 6(A) shows the overlapping feature of the normalized absorption spectra of Au NPs/Au-BSA/Au-Lysozyme system and emission spectra of CdSe-SDS QDs. The corresponding overlapping integral spectra are shown in Fig. 6(B). The expression for overlapping integral is given by:

$$J(\lambda) = \frac{\int_0^\infty F_D(\lambda)\varepsilon_A(\lambda)\lambda^4 d\lambda}{\int_0^\infty F_D(\lambda) d\lambda} \tag{2}$$

Here, $F_D(\lambda)$ is the integrated fluorescence intensity of the donor, ε_A is the molar extinction coefficient of the acceptor, and λ is the wavelength in nanometers. The required values of the ε_A of the acceptors were calculated by using power-law expressions for the dependence of the maximum extinction coefficient on particle diameter [65]. Whereas, the diameter of acceptors, Au NPs, Au-BSA and Au-Lysozyme complex were obtained by using the Haiss equation [66].

The theoretically calculated values of size of the acceptors are depicted in the Table 2. The size of Au NPs (∼1.63 nm) is found to be comparable with the average size obtained from HRTEM (∼2 nm). The calculated values of $J(\lambda)$ are obtained as 3.45×10^{16}, 8.5×10^{15}, 1.19×10^{17} $M^{-1}cm^{-1}nm^4$ for independent Au-CdSe, Au-BSA-CdSe

TABLE 2. Parameters calculated for FRET

Sample	$D_{(theoretical)}$, (nm)	ε_A	$J(\lambda)$	E	d_0 (Å), FRET
Au	1.63	23.56×10^4	3.45×10^{16}	46	73.5
Au-Lysozyme	1.07	5.87×10^4	8.5×10^{15}	60	58
Au-BSA	2.38	82×10^4	1.19×10^{17}	94	90

and Au-Lysozyme-CdSe donor acceptor-pairs respectively. Thus, the overlap integral between the emission spectrum of the QD and the extinction spectrum of the Au NPs increases as the gold particle size increases. The overlapping integrals as well as the transfer efficiency are found to be highest in case of Au-BSA-CdSe FRET pair due to increased spectral overlap of the plasmonic band with the luminescence band of QDs. The coupling behavior of the QDs and the Au NPs (or Au-Protein) could be changed not only by the overlapping of the absorption spectra of Au NPs (or Au-Protein) and emission spectra of the QDs, it is also affected by the distance between absorber (Au, Au-BSA, Au-Lysozyme) and the emitter (CdSe QDs) [67].

To verify further the mechanism of energy transfer from the QDs to the Au NPs, we have examined the separation distance (d_0) at which the energy transfer efficiency is 50%

For FRET, d_0 can be expressed as:

$$d_0 = 0.211(k^2 J(\lambda) n^{-4} Q_D)^{1/6}. \tag{3}$$

Here, k^2 is the dipole orientation factor and its value is 2/3 for randomly oriented dipole, n∼1.33 is the RI of the solvent, while Q_D is the quantum yield of the donor. The calculated d_0 values for Au NPs, Au-BSA complex and Au-Lysozyme complexes are calculated to be 73.5, 90, 58 Å; respectively. Here, it is important to mention that for an ideal FRET pair, the typical Forster distance is in the range of 20–100 Å [67]. Hence, FRET can be likely to occur in all the systems.

3.6. CdSe QDs, Au-CdSe Au-BSA-CdSe, Au-Lysozyme-CdSe systems as cancer cell probe

Fig. 7A shows a series of imaging snap-shots of MDA-MB231 cancer cell treated with QDs and its different complex. The snapshots represent high biocompatibility and fluorescent behavior of the QDs and its complex in the cancer cellular environment.

Using image J-1.46r software, the quantitative analysis of the fluorescent counts can be predicted presuming complete localization of the QDs inside the cell. Fig. 7B highlights the areas of interest and selected background area of fluorescent images, marked with encircled regions. The corrected total counts of fluorescence (CTCF) intensity value can be calculated using the relation given by:

$$\text{CTCF= Integrated density} - (\text{Area} \times \text{ mean fluorescent of background setting}). \tag{4}$$

Here, the integrated density (Int.Den.) of a fluorescent image is the sum of the values of the pixels in the selected regions. As shown in Fig. 7B(a-d), different selected fluorescent areas are labeled as A, B, C, D.... etc. and different selected background regions (region without fluorescence) are represented as bk1, bk2, bk3.........etc. Fig. 7C signifies a comparative view on representative histograms of the average CTCF and average Int.Den. obtained for different QDs system. These predict the biocompatibility and fluorescent behavior of the QDs with the treatment of cancer cell. Moreover, the fluorescence intensity indicates the level of the internalization of QDs by cells.

Note that, the fluorescence efficiency (CTCF) of semiconductor QDs(Q) in the cancer cellular medium is dramatically quenched while conjugating (AQ) with metallic Au NPs (by factor of ∼31.4). Further reduction of the intensity of the QDs has been observed with formation of Au-Lysozyme-CdSe (AQL, by factor of ∼74) and Au-BSA-CdSe (AQB, by factor of 400), complex. The reduction of flourescence in the cancer cell environment is strongly resembled with the photoluminiscence quenching behavior as described above. Thus, the cellular uptake and bioimaging aspects are significantly affected by the metallic-semiconductor system and its bio complex. The significantly varied zeta potential values of the complex systems over the QDs (Table 1) is largely responsible for altering the cellular uptake processes [68, 69]. Although the fluorescent intensity of the hybrid metal NPs-protein-QDs are found to be reduced as compared to a CdSe-SDS QD, the former will be more favorable than the latter ones. This is because of the higher cytotoxicity of the protein conjugated Au-CdSe systems against cancer cells relative to normal cells [70]. In presence of protein, there is elevation of reactive oxygen species (ROS) levels in cancer cells in the hybrid NP-protein-QDs [71–73]. At low levels, ROS may play an important role in molecular signaling, regulating fundamental biological processes such as cell viability, proliferation, migration, and differentiation. Increase of ROS levels may result in interference with basic cellular functions, leading to DNA damage and finally cell death. By using proteins in different concentrations and exposure times, the ROS elevation and hence the cancer cell death can precisely

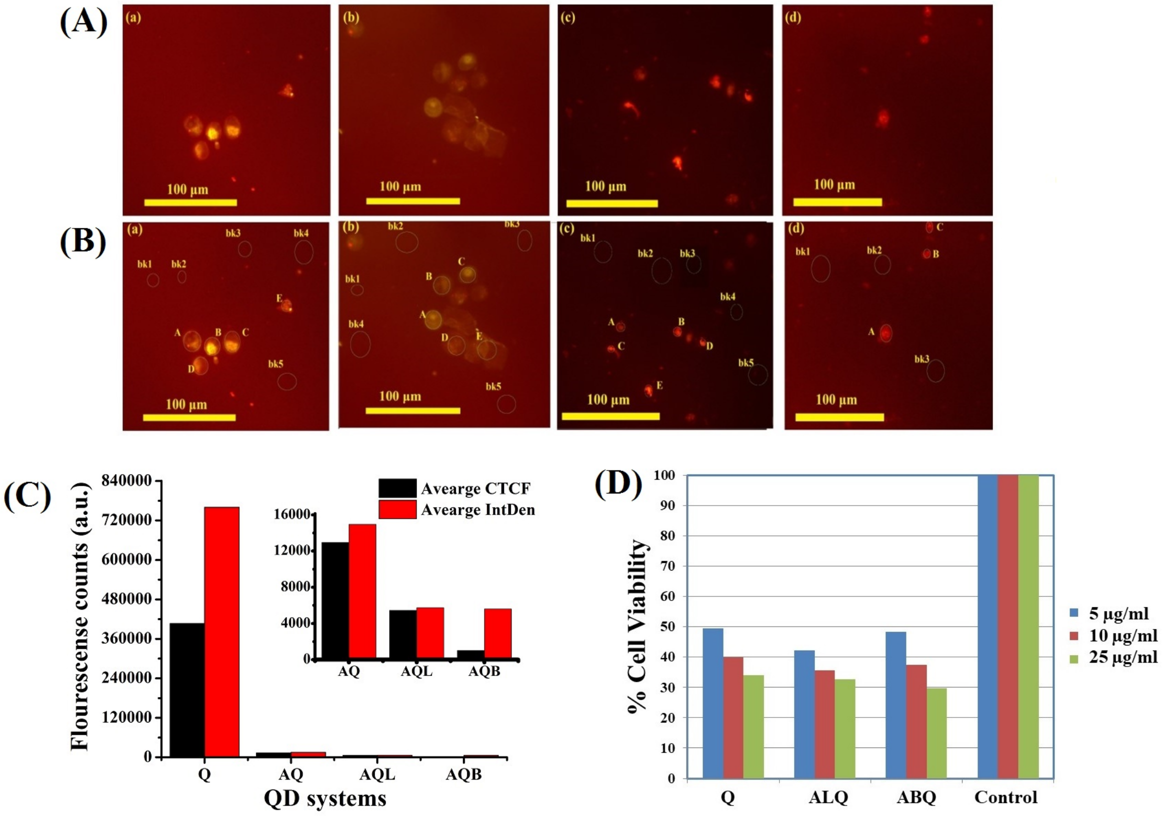

FIG. 7. Fluorescent imaging (using violate filter) of cancer cells with A(a) CdSe-SDS QDs (b) Au-CdSe QDs (c) Au-Lysozyme-CdSe QDs(d) Au-BSA-CdSe QDs. The lower panel B shows selected fluorescent and background areas of fluorescent images respectively. Histograms representing the average value of Int.Den. and CTCF of different types QD systems is shown in C(D) cell viability study of cancer cellswith the treatment of CdSe-SDS QDs (sample Q), Au-BSA-CdSe (sample ABQ) and Au-Lysozyme-CdSe (ALQ) hybrid system

controlled [72]. While studying cell viability of the MDA-MB231 cancer cells (Figure 7D) with the treatment of CdSe-SDS QDs (sample Q), Au-BSA-CdSe (sample ABQ) and Au-Lysozyme-CdSe (ALQ) hybrid system, it was observed that cell viability decreases with the inclusion of BSA or Lysozyme proteins into protein unconjugated CdSe QDs. For 5 μg/mL QDs, the cell viability obtained as 50%. Whereas, in the same concentration, the cell viabilities are decreased to 42% and 48% for Lysozyme and BSA conjugated Au-QDs samples; respectively. Similarly, with increase of concentration up to 10 μg/mL of Au-Lysozyme-QDs and Au-BSA-QDs, the cell viability decreased by the factor of $\sim$1.12 and $\sim$1.07 as compared to protein unconjugated QDs. These factors are $\sim$1.04 and 1.14; respectively for the concentration of 25μg/mL. Thus, it signifies the higher efficiency of cancer cell death by inclusion proteins in the Au-CdSe system.

4. Conclusions

A simple colloidal route has been followed for the synthesis of Au NPs, CdSe QDs and their hybrid system (Au-CdSe). A special emphasis was given to the conjugation of BSA and Lysozyme proteins to this metal-semiconductor complex. HR-TEM data revealed the enhancement of average diameter of Au NPs while conjugating with CdSe QDs from 2 nm to $\sim$3.8 nm. Moreover, considering different sections and their corresponding FFT and IPF of HRTEM image of Au-CdSe hybrid, the presence of CdSe QDs as outer shell of Au NPs can be predicted. The zeta potential measurement signifies the enhancement of stability of Au NPs while forming Au-CdSe, Au-BSA-CdSeandAu-Lysozyme-CdSe hybrid system. Multipolar excitations and radiative damping along with strong interaction between plasmons of Au NPs and excitons of CdSe QDs in hybrid Au-CdSe system may cause the appearance of red shifted and broadened absorption peaks at ∼545 nm and ∼303 nm as compared to parent Au and CdSe QDs. Photoluminescence study shows significant reduction of peak maxima intensity of CdSe QDs while conjugating with Au NPs and Au-BSA or Au-Lysozyme complex. There is expected to occur high probability of FRET phenomenon in between the donor CdSE-SDS QDs and acceptor(s) Au-PVP NPs (or Au-BSA, Au-Lysozyme). The energy transfer efficiency from acceptor to donor was found to be as high as 94% for the FRET pair CdSe and Au-BSA. From the fluorescence microscopy imaging data, it can be observed that, the synthesized QDs and its complex with Au NPs and Au-BSA/Lysozyme are highly biocompatible with a high fluorescent contrast in cancer cell environment. The significantly varied zeta potential values of the complex systems over the QDs influenced the cellular uptake processes.

Acknowledgement

The author R Sarma thanks DBT-New Delhi for financial support under DBT-RA scheme, Material Science Division, CSIR-NEIST, Jorhat for providing me nanoparticle synthetic lab facility and UV-Vis, Zeta potential measurement. The authors gratefully acknowledge Analytical Chemistry Group, CSIR-NEIST for FTIR data, SAIF, NEHU, Shillong for HR-TEM measurements, Department of Physics-IIT Guwahati for PL study and Dr. Manash Jyoti Kashyap for providing important inputs in restructuring and editing the manuscript extensively.

5. Conflict of interest

On behalf of all authors, the corresponding author states that there is no conflict of interest.

References

[1] Wild C.P. *Cancer control: a reminder of the need for a balanced approach between prevention and treatment*, 2014.

[2] Yang C., et al. Gold nanoparticle mediated combined cancer therapy. *Cancer Nanotechnology*, 2018, **9**(1), P. 4.

[3] Hartshorn C.M., et al. Nanotechnology Strategies To Advance Outcomes in Clinical Cancer Care. *ACS Nano*, 2018, **12**(1), P. 24–43.

[4] Grodzinski P., et al. Integrating Nanotechnology into Cancer Care. *ACS Nano*, 2019, **13**(7), P. 7370–7376.

[5] Vines J.B., et al. Gold Nanoparticles for Photothermal Cancer Therapy. *Frontiers in Chemistry*, 2019, 7(167).

[6] Singh P., et al. Gold Nanoparticles in Diagnostics and Therapeutics for Human Cancer. *International journal of molecular sciences*, 2018, **19**(7), P. 1979.

[7] Riley R.S., Day E.S. Gold nanoparticle-mediated photothermal therapy: applications and opportunities for multimodal cancer treatment. Wiley interdisciplinary reviews. *Nanomedicine and nanobiotechnology*, 2017, **9**(4), P. 10.

[8] Xiao W., et al. Normalizing Tumor Vessels To Increase the Enzyme-Induced Retention and Targeting of Gold Nanoparticle for Breast Cancer Imaging and Treatment. *Molecular Pharmaceutics*, 2017, 14(10), P. 34890–3498.

[9] Lara-Cruz C., et al. Gold nanoparticle uptake is enhanced by estradiol in MCF-7 breast cancer cells. *International journal of nanomedicine*, 2019, **14**, P. 2705–2718.

[10] Hoshyar R., et al. A novel green one-step synthesis of gold nanoparticles using crocin and their anti-cancer activities. *Journal of Photochemistry and Photobiology B: Biology*, 2016, **159**, P. 237–242.

[11] Connor E.E., et al. Gold nanoparticles are taken up by human cells but do not cause acute cytotoxicity. *Small*, 2005, **1**(3), P. 325–327.

[12] Dimitri A., et al. Semiconductor nanostructures in biological applications. *Journal of Physics: Condensed Matter*, 2005, **17**(26), P. R637.

[13] Sarma R., et al. Physical and biophysical assessment of highly fluorescent, magnetic quantum dots of a wurtzite-phase manganese selenide system. *Nanotechnology*, 2014, **25**(27), P. 275101.

[14] Chu M., et al. The therapeutic efficacy of CdTe and CdSe quantum dots for photothermal cancer therapy. *Biomaterials*, 2012, **33**(29), P. 7071–7083.

[15] Zayed J., Philippe S. Acute oral and inhalation toxicities in rats with cadmium telluride. *International journal of toxicology*, 2009, **28**(4), P. 259–265.

[16] Hardman R. A toxicologic review of quantum dots: toxicity depends on physicochemical and environmental factors. *Environmental health perspectives*, 2006, **114**(2), P. 165–172.

[17] Sarma R., Mohanta D. Luminescence and bio-imaging response of thio-glycolic acid (TGA) and sodium dodecyl sulfate (SDS)-coated fluorescent cadmium selenide quantum dots. *Journal of Luminescence*, 2015, **161**, P. 395–402.

[18] Chen F., Gerion D. Fluorescent CdSe/ZnS Nanocrystal-Peptide Conjugates for Long-term, Nontoxic Imaging and Nuclear Targeting in Living Cells. *Nano Letters*, 2004, **4**(10), P. 1827–1832.

[19] Guo G., et al. Probing the cytotoxicity of CdSe quantum dots with surface modification. *Materials Letters*, 2007, **61**(8), P. 1641–1644.

[20] Achermann M. Exciton-Plasmon Interactions in Metal-Semiconductor Nanostructures. *The Journal of Physical Chemistry Letters*, 2010, **1**(19), P. 2837–2843.

[21] Feng A.L., et al. Distance-dependent plasmon-enhanced fluorescence of upconversion nanoparticles using polyelectrolyte multilayers as tunable spacers. *Scientific reports*, 2015, 5.

[22] Govorov A.O., Lee J., and Kotov N.A. Theory of plasmon-enhanced Förster energy transfer in optically excited semiconductor and metal nanoparticles. *Physical Review B*, 2007, **76**(12), P. 125308.

[23] Fedutik Y., et al. Exciton-plasmon-photon conversion in plasmonic nanostructures. *Physical review letters*, 2007, **99**(13), P. 136802.

[24] Medintz I.L., et al. Proteolytic activity monitored by fluorescence resonance energy transfer through quantum-dot–peptide conjugates. *Nature materials*, 2006, **5**(7), P. 581–589.

[25] Fuller M.A. and Köper I. Biomedical applications of polyelectrolyte coated spherical gold nanoparticles. *Nano Convergence*, 2019, **6**(1), P. 11.

[26] Hezinger A., Teßmar J., and Göpferich A. Polymer coating of quantum dots–a powerful tool toward diagnostics and sensorics. *European Journal of Pharmaceutics and Biopharmaceutics*, 2008, **68**(1), P. 138–152.

[27] Hamouda R.A., Abd El-Mongy M., and Eid K.F. Comparative study between two red algae for biosynthesis silver nanoparticles capping by SDS: Insights of characterization and antibacterial activity. *Microbial pathogenesis*, 2019, **129**, P. 224–232.

[28] Rajh T., Micic O.I., and Nozik A.J. Synthesis and characterization of surface-modified colloidal cadmium telluride quantum dots. *The Journal of Physical Chemistry*, 1993, **97**(46), P. 11999–12003.

[29] Zhang Y. and Clapp A. Overview of stabilizing ligands for biocompatible quantum dot nanocrystals. *Sensors*, 2011, **11**(12), P. 11036–11055.

[30] Gerion D., et al. Synthesis and properties of biocompatible water-soluble silica-coated CdSe/ZnS semiconductor quantum dots. *The Journal of Physical Chemistry B*, 2001, **105**(37), P. 8861–8871.

[31] Wang P., et al. Interaction of gold nanoparticles with proteins and cells. *Science and technology of advanced materials*, 2015, **16**(3), P. 034610–034610.

[32] Casals E., et al. Hardening of the Nanoparticle-Protein Corona in Metal (Au, Ag) and Oxide (Fe_3O_4, CoO, and CeO_2) Nanoparticles. *Small* (Weinheim an der Bergstrasse, Germany), 2011, **7**, P. 3479–86.

[33] Malek M., et al. Charged and Neutral Au Nanoparticles Interact Differently with Langmuir Film-Based Synthetic Membranes: Implications for Nanoparticle Uptake and Membrane Protein Activity. *ACS Applied Nano Materials*, 2020, **3**(9), P. 9276–9284.

[34] Clapp A.R., Goldman E.R., and Mattoussi H. Capping of CdSe–ZnS quantum dots with DHLA and subsequent conjugation with proteins. *Nature Protocols*, 2006, **1**(3), P. 1258–1266.

[35] Foubert A., et al. Bioconjugation of quantum dots: Review and impact on future application. *TrAC Trends in Analytical Chemistry*, 2016, **83**, P. 31–48.

[36] Ding S., et al. Protein-based nanomaterials and nanosystems for biomedical applications: A review. *Materials Today*, 2021, **43**, P. 166–184.

[37] Spicer C.D., et al. Peptide and protein nanoparticle conjugates: versatile platforms for biomedical applications. *Chemical Society reviews*, 2018, **47**(10), P. 3574–3620.

[38] Xie J., Lee J.Y., and Wang D.I.C. Synthesis of Single-Crystalline Gold Nanoplates in Aqueous Solutions through Biomineralization by Serum Albumin Protein. *The Journal of Physical Chemistry C*, 2007, **111**(28), P. 10226–10232.

[39] Sarkar S., et al. Protein nanocomposites: Special inferences to Lysozyme based nanomaterials. *International Journal of Biological Macromolecules*, 2020, **151**, P. 467–482.

[40] Das T., et al. Functionalisation of Polyvinylpyrrolidone on Gold Nanoparticles Enhances Its Anti-Amyloidogenic Propensity towards Hen Egg White Lysozyme. *Biomedicines*, 2017, **5**(2), P. 19.

[41] Damjanovic V. and Thomas D. The use of polyvinylpyrrolidone as a cryoprotectant in the freezing of human lymphocytes. *Cryobiology*, 1974, 11(4), P. 312–316.

[42] Prasad M., Palepu R., and Moulik S.P. Interaction between sodium dodecyl sulfate (SDS) and polyvinylpyrrolidone (PVP) investigated with forward and reverse component addition protocols employing tensiometric, conductometric, microcalorimetric, electrokinetic, and DLS techniques. *Colloid and Polymer Science*, 2006, **284**(8), P. 871–878.

[43] Romani A., Gehlen M., and Itri R. Surfactant-Polymer Aggregates Formed by Sodium Dodecyl Sulfate, Poly(N -vinyl-2-pyrrolidone), and Poly(ethylene glycol). *Langmuir: the ACS journal of surfaces and colloids*, 2005, **21**, P. 127–33.

[44] Kavlak S. and Guner A. Intermolecular interactions between bovine serum albumin and certain water-soluble polymers at various temperatures. *Journal of applied polymer science*, 2006, **100**(2), P. 1554–1560.

[45] Jette E.R. and Foote F. Precision determination of lattice constants. *The Journal of Chemical Physics*, 1935, **3**(10), P. 605–616.

[46] Freeman D., Mair S., and Barnea Z. The structure and Bijvoet ratios of cadmium selenide. *Acta Crystallographica Section A: Crystal Physics, Diffraction, Theoretical and General Crystallography*, 1977, **33**(3), P. 355–359.

[47] Li Y. and Chopra N. Gold nanoparticle integrated with nanostructured carbon and quantum dots: synthesis and optical properties. *Gold Bulletin*, 2015, **48**(1), P. 73–83.

[48] Paolino D., et al. *Drug delivery systems. Encyclopedia of medical devices and instrumentation*, 2006.

[49] Joseph E. and Singhvi G., Chapter 4 – Multifunctional nanocrystals for cancer therapy: a potential nanocarrier, in Nanomaterials for Drug Delivery and Therapy, A.M. Grumezescu, Editor. 2019, William Andrew Publishing, P. 91–116.

[50] Honary S. and Zahir F. Effect of Zeta Potential on the Properties of Nano-Drug Delivery Systems – A Review (Part 1). *Tropical Journal of Pharmaceutical Research*, 2013, **12**.

[51] Behera M. and Ram S. Inquiring the mechanism of formation, encapsulation, and stabilization of gold nanoparticles by poly(vinyl pyrrolidone) molecules in 1-butanol. *Applied Nanoscience*, 2013, **4**.

[52] Borodko Y., et al. Probing the interaction of poly (vinylpyrrolidone) with platinum nanocrystals by UV-Raman and FTIR. The *Journal of Physical Chemistry B*, 2006, **110**(46), P. 23052–23059.

[53] Behera M. and Ram S. Inquiring the mechanism of formation, encapsulation, and stabilization of gold nanoparticles by poly (vinyl pyrrolidone) molecules in 1-butanol. *Applied Nanoscience*, 2014, **4**(2), P. 247–254.

[54] Viana R.B., da Silva A.B.F., and Pimentel A.S. Infrared Spectroscopy of Anionic, Cationic, and Zwitterionic Surfactants. *Advances in Physical Chemistry*, 2012, **2012**, P. 14.

[55] Chaudhary A., et al. Morphological effect of gold nanoparticles on the adsorption of bovine serum albumin. *Physical Chemistry Chemical Physics*, 2014, **16**(38), P. 20471–20482.

[56] Kvítek O., et al. Noble metal nanostructures influence of structure and environment on their optical properties. *Journal of Nanomaterials*, 2013, **2013**, P. 111.

[57] Haldar K.K., et al. Photophysical properties of Au-CdTe hybrid nanostructures of varying sizes and shapes. *ChemPhysChem*, 2012, **13**(17), P. 3989–3996.

[58] Templeton A.C., et al. Solvent refractive index and core charge influences on the surface plasmon absorbance of alkanethiolate monolayer-protected gold clusters. *The Journal of Physical Chemistry B*, 2000, **104**(3), P. 564–570.

[59] Singh S., et al. Conjugation of nano and quantum materials with bovine serum albumin (BSA) to study their biological potential. *Journal of Luminescence*, 2013, **141**, P. 53–59.

[60] Vaishanav S.K., et al. Adsorption Kinetics and Binding Studies of Protein Quantum Dots Interaction: A Spectroscopic Approach. *Journal of Fluorescence*, 2016, **26**(3), P. 855–865.

[61] Blout E.R. and L. Visser, Elastase. II. Optical properties and the effects of sodium dodecyl sulfate. *Biochemistry*, 1971, **10**(5), P. 743–752.

[62] Xia Y., Song L., and Zhu C. Turn-On and Near-Infrared Fluorescent Sensing for 2,4,6-Trinitrotoluene Based on Hybrid (Gold Nanorod)–(Quantum Dots) *Assembly. Analytical Chemistry*, 2011, **83**(4), P. 1401–1407.

[63] Clapp A.R., et al. Fluorescence resonance energy transfer between quantum dot donors and dye-labeled protein acceptors. *Journal of the American Chemical Society*, 2004, **126**(1), P. 301–310.

[64] Li M., et al. Size-Dependent Energy Transfer between CdSe/ZnS Quantum Dots and Gold Nanoparticles. *The Journal of Physical Chemistry Letters*, 2011, **2**(17), P. 2125–2129.

[65] Navarro J.R. and Werts M.H. Resonant light scattering spectroscopy of gold, silver and gold–silver alloy nanoparticles and optical detection in microfluidic channels. *Analyst*, 2013, **138**(2), P. 583–592.

[66] Haiss W., et al. Determination of size and concentration of gold nanoparticles from UV-vis spectra. *Analytical chemistry*, 2007, **79**(11), P. 4215–4221.

[67] Li X., et al. Plasmon-Emitter Hybrid Nanostructures of Gold Nanorod-Quantum Dots with Regulated Energy Transfer as a Universal Nano-Sensor for One-step Biomarker Detection. *Nanomaterials* (Basel, Switzerland), 2020, **10**(3), P. 444.

[68] Patil S., et al. Protein adsorption and cellular uptake of cerium oxide nanoparticles as a function of zeta potential. *Biomaterials*, 2007, **28**(31), P. 4600–4607.

[69] Zhao M.-X. and Zeng E.-Z. Application of functional quantum dot nanoparticles as fluorescence probes in cell labeling and tumor diagnostic imaging. *Nanoscale Research Letters*, 2015, **10**(1), P. 1-9.

[70] Azizi M., et al. Anti-cancerous effect of albumin coated silver nanoparticles on MDA-MB 231 human breast cancer cell line. *Scientific Reports*, 2017, **7**(1), P. 5178.

[71] Matulionyte M., et al. Photoluminescent Gold Nanoclusters in Cancer Cells: Cellular Uptake, Toxicity, and Generation of Reactive Oxygen Species. *International journal of molecular sciences*, 2017, **18**(2), P. 378.

[72] Dong L., et al. Cytotoxicity of BSA-Stabilized Gold Nanoclusters: In Vitro and In Vivo Study. *Small*, 2015, **11**.

[73] Poderys V., et al. Protein-stabilized gold nanoclusters for PDT: ROS and singlet oxygen generation. *Journal of Photochemistry and Photobiology B: Biology*, 2020, **204**, P. 111802.

NANOSYSTEMS: PHYSICS, CHEMISTRY, MATHEMATICS, 2021, 12 (6), P. 763–772

Dispersibility of freeze-drying unmodified and modified TEMPO-oxidized cellulose nanofibrils in organic solvents

A. A. Luginina[1], S. V. Kuznetsov[1], V. K. Ivanov[2], V. V. Voronov[1], A. D. Yapryntsev[2], D. I. Petukhov[3],
S. Yu. Kottsov[2], E. V. Chernova[1], P. P. Fedorov[1]*

[1]Prokhorov General Physics Institute of the Russian Academy of Sciences,
38 Vavilov Street, Moscow 119991, Russia
[2]Kurnakov Institute of General and Inorganic Chemistry of the Russian Academy of Sciences,
31 Leninsky Prospect, Moscow 119991, Russia
[3]Lomonosov Moscow State University, Chemical department, 1-3 Leninskie Gory, Moscow, 119991, Russia
*ppfedorov@yandex.ru

DOI 10.17586/2220-8054-2021-12-6-763-772

Cellulose nanofibrils (TOCNF) with a width of 20 ± 6 nm and a length of 809 ± 98 nm were prepared using 2,2,6,6-tetramethylpiperidinyl-1-oxyl (TEMPO)-mediated oxidation. Two modifying agents were used to functionalize the TOCNF surface in aqueous media: alkyl ketene dimer (AKD) and 3-aminopropyltriethoxysilane (APS). The hydrophilic aerogel L-TOCNF, hydrophobic aerogels L-TOCNF-AKD and L-TOCNF-APS with water contact angles of 0, 139 ± 2, and 133 ± 2 °, respectively, were prepared by freeze-drying of the aqueous dispersions. The elemental composition, morphology, sizes and crystal structure were determined by EDX analysis, scanning electron microscopy and X-ray diffraction, respectively. The process of redispersion of lyophilized samples in water and four organic solvents was investigated. The effect of TOCNF modification and solvent polarity on the redispersibility of lyophilized samples was revealed: the dispersibility of hydrophobic L-TOCNF-AKD and L-TOCNF-APS in organic solvents was significantly improved.

Keywords: TEMPO-oxidized cellulose nanofibrils, hydrophobic modification, freeze-drying, redispersibility.

Received: 25 October 2021

1. Introduction

Nanocellulose is one of the most promising environmentally friendly materials for a number of reasons, including: abundance of renewable sources for its production, biodegradability, biocompatibility, and non-toxicity [1]. Cellulosic nanomaterials have received increased attention in recent years due to their exceptional properties and potential for a variety of applications, including biomedical, energy storage, electronic devices, packaging, and composite materials [2–7], as well as the development of economical and green manufacturing methods. One such environmentally friendly method is TEMPO-mediated oxidation of cellulose pulp followed by mild mechanical disintegration treatment. This method allowed effective individualization of cellulose fibrils because of the formation of TEMPO-oxidized cellulose nanofibrils (TOCNFs), which have uniform width and high aspect ratio (about 3 – 10 nm width and about 1 μm length) with minimal energy consumption [8, 9]. Single TOCNF elements have high mechanical strength (about 3 GPa tensile strength and about 140 GPa Young's modulus), low density of about 1.6 g/cm^3 and increased chemical reactivity, that are crucial for the development of new functional materials [10–12]. The hydrophilic nature of TOCNF requires its production as an aqueous dispersion. This creates serious transportation problems that can be avoided by drying. Drying also inhibits the growth of bacteria and fungi in nanocellulose [13]. TOCNFs, initially nanodispersed in water, form large agglomerates when aqueous dispersions are dried by natural evaporation, which leads to a loss of aforementioned TOCNF inherent functional properties [10]. Potential applications of TOCNF include their use as nanofillers in polymer composites. Most synthetic polymers are hydrophobic and, therefore, it is difficult to reinforce them with hydrophilic TOCNFs without aggregation the latter. As a result, preparation of the polymer composites requires mixing TOCNFs with polymer solutions in organic solvents.

One of the ways to obtain organic sols is the solvent gradual replacement. Isogai et al. [14] demonstrated the dispersibility of TOCNF in the various polar organic solvents such as dimethyl sulfoxide (DMSO), N,N-dimethylformamide (DMF), 1,3-dimethyl-2-imidazolidinone, N,N-dimethylacetamide (DMA) and 1-methyl-2-pyrrolidinone (NMP) by replacing -COONa groups with -COOH groups in TOCNF and subsequent solvent exchange. It was noted that the sodium salt form of TOCNFs could be dispersed only in DMSO. To solve the problem of dispersing TOCNF in the other organic solvents, various methods of surface modification, followed by solvent replacement, have been studied:

- poly(ethylene glycol) (PEG)-grafted TOCNF-COO were individually dispersed in chloroform, toluene, dichloromethane, 1,4-dioxane, DMA [15–17];
- n-dodecylamine-modified TOCNF-COO were dispersed at the level of individual nanofibrils in isopropyl alcohol [18];
- cetyltrimethylammonium bromide-modified TOCNFs demonstrated increased hydrophobicity and improved redispersibility in DMF [19];
- TOCNFs, modified with tannic acid and hexadecylamine, were dispersed in toluene, ethanol, acetone [20];
- TOCNF-COO with amphiphilic diblock copolymer-modified surface exhibited an increased dispersibility in such organic solvents as DMSO, DMF, ethanol, and methanol [21].

It should be noted that the aforementioned solvent exchange process is quite laborious because of the use of intermediate solvents and multiple centrifugation cycles.

An alternative method to improve the redispersion of TOCNF includes the use of freeze-drying. Numerous studies were devoted to redispersion of modified and unmodified nanocrystals (CNC) and nanofibrils (CNF) of cellulose after the freeze-drying [22–30]. It is worth mentioning that TOCNFs have a large number of sodium carboxylate groups on nanofibril surfaces and much higher aspect ratios than CNC, so TOCNF cannot be redispersed in organic solvents using protocols previously developed for CNC.

Despite the urgency of the aforementioned problem, a relatively small number of papers have been devoted to the redispersion of lyophilized TOCNF in organic solvents. Jiang et al. [31] investigated the redispersion of lyophilized TOCNF as function of the medium composition and/or freezing conditions and found that TOCNFs, lyophilized from an aqueous dispersion, were redispersed only in water, while TOCNFs, lyophilized from tert-butanol/water mixtures, were readily dispersed in both water and DMF. Isogai [10, 11] confirmed that TOCNFs, lyophilized from tert-butanol/water mixtures, were readily dispersed in DMF. Indarti et al. [32] redispersed TOCNFs, thoroughly dried by freeze-drying, in chloroform. It is necessary to note the very low concentration of redispersed TOCNF (0.5 mg in 10 ml of chloroform) and the short-term stability of the obtained dispersions (15 min) [32]. Araki et al. [33] showed that lyophilized PEG-grafted TOCNFs can be redispersed in water as well as in the non-polar solvent chloroform (0.2 %) by sonication. Johnson et al. [34] investigated the effect of hydrophobization of TOCNF by surface modification with octadecylamine on dispersion in organic solvents with a wide range of polarities and found that lyophilized hydrophobic TOCNFs could be dispersed by ultrasonic treatment in both polar and non-polar organic solvents (isopropyl alcohol, tetrahydrofuran and toluene). Chu et al. [35] revealed that the modification of TOCNFs and imparting hydrophobic properties to them were an effective way to improve the dispersion of TOCNF in organic solvents.

In this work, two modifying agents – alkyl ketene dimer (AKD) and 3-aminopropyltriethoxysilane (APS) were utilized in order to increase the hydrophobicity of TOCNF. This study evaluated the effect of the TOCNF modification and lyophilization on the redispersion ability in polar and non-polar solvents (DMSO, DMF, chloroform, hexane) as factors for increase in TOCNF redispersibility.

2. Experimental section

2.1. Chemicals

Ash free filter paper (FP) "Blue Ribbon" ($I\beta$ crystal structure, crystallinity index 68.7, degree of polymerization 1112, particle width 25 – 50 μm, particle length 200 – 1500 μm [36]); TEMPO (99 %) (NIOCH SB RAS, Russia); 3-aminopropyltriethoxysilane (97 %) (PENTA-91 company, Russia); water emulsion of alkyl ketene dimer (mixture of stearic and palmitic acids, 60 – 40 % by weight), (AKD) Flouise-200 brand containing 19 % AKD and 3 % anionic starch (Skiff Special Chemicals, Russia); 19 wt. % sodium hypochlorite solution; sodium bromide; sodium hydroxide; acetic acid and hydrochloric acid (analytical grade); bidistilled water; and regenerated cellulose dialysis tube 12 – 14 kDa molecular weight cut-off by Orange Scientific (Belgium) were used as starting materials. The solvents dimethyl sulfoxide (DMSO), dimethylformamide (DMF), chloroform, and hexane, chemically pure, (Chimmed, Russia) were used as received without additional purification.

2.2. Preparation of the aqueous dispersion of TOCNF

TOCNF was prepared by hydrolysis of FP with a 5.5 M solution HCl at 80 °C, using the TEMPO/NaBr/NaClO system in water at pH 10.0 – 10.5, followed by ultrasonic treatment by the previously reported technique [37]. TOCNF yield was about 70 %. TOCNF dispersion was stored at 4 °C. TOCNF content in the dispersion was determined gravimetrically.

2.3. Freeze-drying of the aqueous dispersion of TOCNF

Aqueous TOCNF (1 wt.%) dispersions (100 mL) in polypropylene containers were quickly frozen by immersing in liquid nitrogen (-196 °C) for 10 min, then lyophilized (-5 °C, $15 \div 20$ Pa) for 48 h in a freeze-drier LS-1000 (Russia), followed by a rise in temperature up to 35 °C for 22 hours. The prepared sample was designated as L-TOCNF.

2.4. Preparation of freeze-dried modified TOCNF with AKD or APS

The modification protocol of TOCNF with AKD is based on our previous research [38]. A certain amount (0.1364 g) of AKD aqueous emulsion was added to 1.00 wt.% TOCNF dispersion (100 g) and sonicated for 5 min in an ice bath to obtain a sample loaded with 30 mg dry AKD per gram dried TOCNF. After sonication, aqueous TOCNF-AKD mixtures were freeze-dried as described for aqueous dispersion of TOCNF.

The modification protocol of TOCNF with APS is based on our previous research [37]. The pH of bidistilled water was adjusted to 4.0 by dropping glacial acetic acid. APS aqueous solution (3.0 wt.%) were prepared by adding 1.1068 g APS to 35.7865 g bidistilled water with pH = 4.0 under vigorous stirring in fluoroplastic beaker for 10 min while maintaining pH value at pH = 4.0. Then, 100 g of TOCNF dispersion (1.38 wt.%) were added dropwise to APS solution and stirred with magnetic stirrer at room temperature for 30 min, while maintaining a pH of 4.0. The pH value was adjusted using glacial acetic acid. The APS loading was 5 mmol per gram dried TOCNF in the obtained sample. After stirring, aqueous TOCNF-APS mixtures were freeze-dried as described for aqueous dispersion of TOCNF.

The prepared samples were designated as L-TOCNF-AKD and L-TOCNF-APS. Freeze-dried samples were stored in a desiccator over phosphorus pentoxide.

2.5. Redispersion of the L-TOCNF, L-TOCNF-AKD and L-TOCNF-APS in various solvents

Water or an organic solvent (DMSO, DMF, chloroform or hexane) was added to the freeze-dried product of L-TOCNF, L-TOCNF-AKD or L-TOCNF-APS to prepare 0.2 % (w/v) of nanofibrils. A weight of the freeze-dried sample (M) was taken with an accuracy of 0.0002 g. After the freeze-dried samples were transferred to the solvent, the mixture was sonicated for 7 min (ultrasonic homogenizer with a 7 mm probe-tip diameter UZG13-01/22, 110 W, VNIITVCH, Russia) under ice bath cooling while maintaining a constant solvent volume. The concentration of each homogenized dispersion was maintained at 0.2 % (w/v).

The colloidal stability of the dispersions both after 1 hour and after 5 days was assessed visually according to the sedimentation and clarification of the dispersion. The dispersing degree (Dr) was calculated from the dry weight of the lyophilized product present in the supernatan and was used as a criteria for redispersibility. Dr was determined after ultrasonic treatment of the suspensions and their centrifugation at 11000 rpm for 10 min. Centrifugation was used to separate individualized nanofibrils from aggregates of nanofibrils. The precipitate and transparent supernatant were separated by pipetting. Solvents such as chloroform and hexane were removed from the supernatant by air drying at 35 – 40 °C. Solvents (DMSO and DMF) were removed from the supernatant by drying in vacuum at 50 °C for 2 h. The dried fraction of the lyophilized product present in the supernatant (m_s, g) was weighed. Dr (%) was determined as:

$$Dr = \frac{m_s \times 100}{M}, \tag{1}$$

where M (g) is the total dry weight of redispersed nanocellulose.

2.6. Characterization

X-ray diffraction patterns were recorded with Bruker D8 Advance diffractometer (Bruker AXS GmbH, Karlsruhe, Germany; CuKα-radiation; 8 – 60 ° 2θ range, 0.02 ° 2θ step). The 22.7 ° 2θ diffraction peak was used for TOCNF crystallinity index (IC, %) calculation by Segal's method [7]. X-ray diffraction data were obtained in reflection geometry, in which the incident radiation is most intensively scattered by crystallites whose reflecting planes are parallel to the axis of the fibrils, which makes it possible to determine their thickness. The transverse size of crystallites (D[200], nm) was estimated using the Scherrer equation [36].

The degree of polymerization (DP) was assessed by viscosity measurements using diluted solutions of dry TOCNF films in Cadoxen (cadmium ethylenediamine) [29]. DP was determined as an average of two independent measurements.

The carboxylate content (mmol/g) in TOCNF was determined by a conductometric titration technique according to the protocol described elsewhere [39]. The conductivity values were recorded at room temperature using an Expert-002 conductometer as the mean value of three measurements.

TABLE 1. Characteristics of TOCNF

Particle size (SEM), nm		Particle width (AFM), nm	DP	ζ-potential, mV	Carboxyl group content, mmol/g	IC, %	D[200], nm
width	length						
20 ± 6	809 ± 98	16 ± 6	123 ± 3	-50 ± 2	1.20 ± 0.05	78.2	2.9

Zeta potential (ζ-potential) values of the dispersions were measured by an electrophoretic light scattering technique using the phase analysis light scattering (PALS) on the Photocor Compact-Z analyzer at room temperature. The resulting ζ-potential values are mean values in five consecutive measurements.

The morphology of the freeze-dried samples and the distribution of the elements on the surface were analyzed by simultaneous use of scanning electron microscopy (SEM) (NVision 40 microscope, Carl Zeiss NTS GmbH, Germany) and energy-dispersive X-ray spectroscopy (EDX), (X-Max detector, Oxford Instruments, UK). The size, and shape of nanofibrils were also analyzed by SEM. A drop of dilute aqueous dispersion of 0.01 wt.% TOCNF was applied onto a single crystal silicon substrate and air-dried for the SEM farther analysis.The size of nanofibrils, and pore size were revealed by the ImageJ software as a mean value in 25 independent measurements.

The surface morphology of TOCNF film was investigated using NTEGRA Prima atomic force microscope (NT-MDT Spectrum Instruments, Russia) in a tapping mode. All experiments were carried out under controlled conditions maintained by a TRACKPORE ROOM-05 measuring complex (purity class 5 ISO (100), the accuracy of maintaining air temperature in the range of 23 ± 5 K is ± 0.05 K, the relative air humidity is 55 ± 1 %).

The value of the specific surface area (S_{BET}) of the samples was measured by low-temperature adsorption of nitrogen using an ATKh-06 analyzer (KATAKON, Russia) with preliminary degassed stage for 1 h at 90 °C under vacuum. The specific surface area was calculated using the Brunauer–Emmett–Teller model (BET) and the five points method within the partial pressure range 0.05 – 0.25.

The water contact angle (WCA) was measured on a FTA1000 Drop Shape Instrument B Frame System. The test sample was placed on a horizontal holder. The water droplet volume 100 μl was applied onto the surface of the test sample by a special microdosing syringe. The images were recorded 1 s after application of the droplets using a 640×480 pixel CCD detector. The measurements were performed at room temperature (24 ± 2 °C) and repeated for 5 times on various fresh surfaces.

3. Results and discussion

3.1. Characterization of TOCNF

The characteristics of the TOCNF are summarized in Table 1. SEM images of the TOCNF samples show entangled nanofibrils with width (20 ± 6 nm), and length (809 ± 98 nm), Fig. 1(a). The fibril width according to AFM data is slightly lower, 16 ± 6 nm, Fig. 1(b). HCl hydrolysis followed by TEMPO oxidation significantly reduced the particle size (by three orders of magnitude) while also lowering the TOCNF degree of polymerization down to 123 ± 3 compared to the original FP cellulose (one order of magnitude), Table 1 [36].

The aqueous dispersions of TOCNF are stable for a long time (up to 6 months) due to the electrostatic repulsion of the carboxyl groups with content of 1.20 ± 0.05 mmol/g TOCNF (Table 1. The ζ-potential value of TOCNF aqueous dispersions was -50 ± 2 mV).

X-ray diffraction pattern of TOCNF film (Fig. 2(a)) shows diffraction peak at $2\theta = 22.5$ ° and double peak in the range $2\theta = 14.8 - 16.8$ ° corresponding to the crystallographic planes (200), $(1\bar{1}0)$ and (110) of monoclinic $I\beta$ cellulose [39]. The crystallinity (78.2 %) and a crystallite size (2.9 nm in the crystallographic plane [200]) are presented in Table 1.

3.2. Morphology and physical properties of L-TOCNF, L-TOCNF-AKD, L-TOCNF-APS

Freeze-drying yielded aerogels whose volume corresponded to the volume of the dispersion, Fig. 3(a–c). L-TOCNF-APS aerogel has a pale yellow tint. For the samples after lyophilization, the X-ray diffraction pattern retains initial structure of $I\beta$ cellulose (Fig. 2(b–d)), but the intensity of diffuse halo increases. The crystallinity index from TOCNF film (78.2 %) to 69.1 % for L-TOCNF (Fig. 3d) was decreased.

The crystallinities of the modified L-TOCNF-AKD and L-TOCNF-APS were slightly decreased compared to L-TOCNF, due to the introduction of amorphous AKD or APS on the surface of the cellulose nanofibrils, Fig. 3(d). However, the crystallite size D[200] in the L-TOCNF-AKD and L-TOCNF-APS samples no showed obvious changes after modification (Fig. 3(d)). This occurred due to the modification that occurred only on the surface of the cellulose

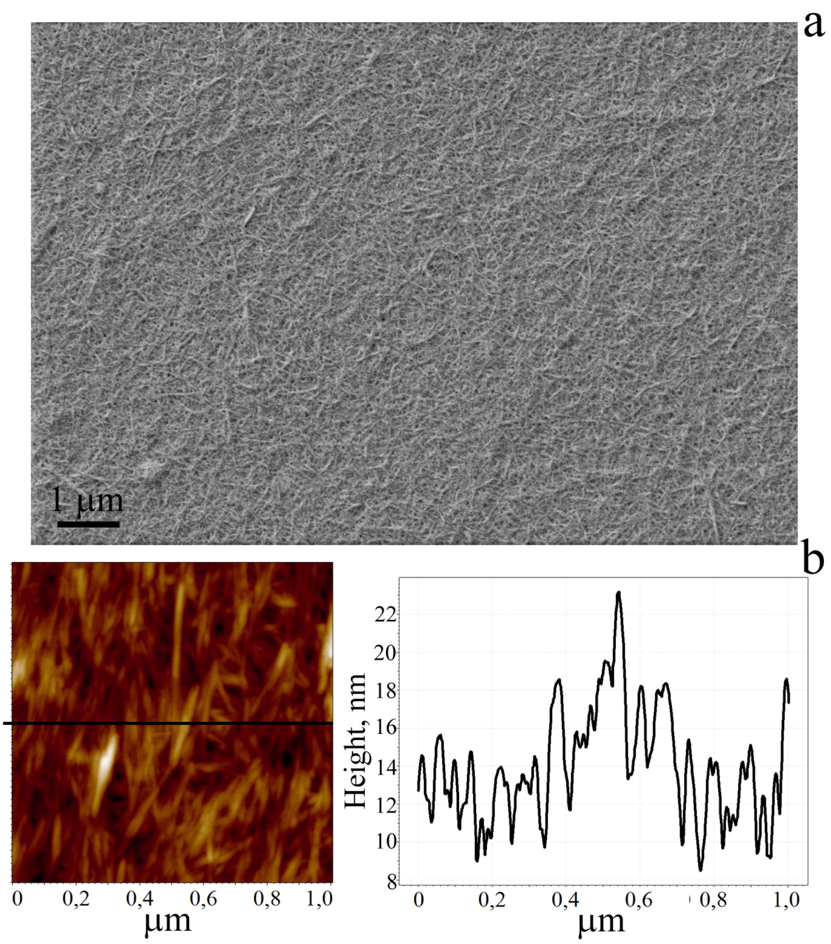

FIG. 1. SEM images of diluted dispersions of TOCNF 0.01 wt.%, dried on a single-crystal silicon substrate (a), AFM images of TOCNF film and height profile along the black line (b)

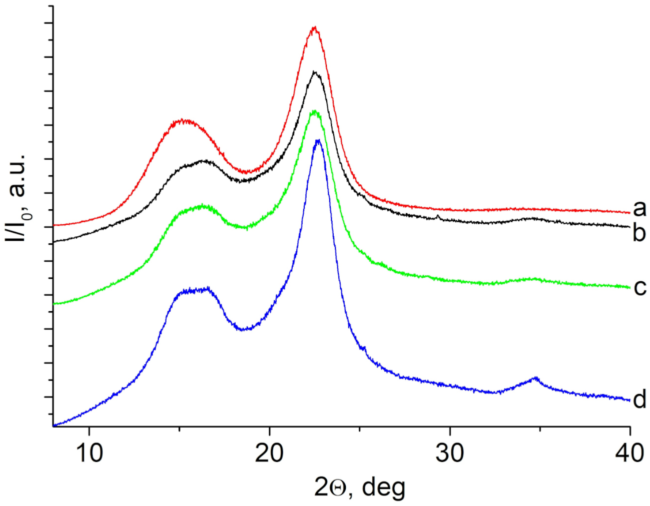

FIG. 2. XRD patterns of the samples: TOCNF (a), L-TOCNF (b), L-TOCNF-AKD (c), L-TOCNF-APS (d)

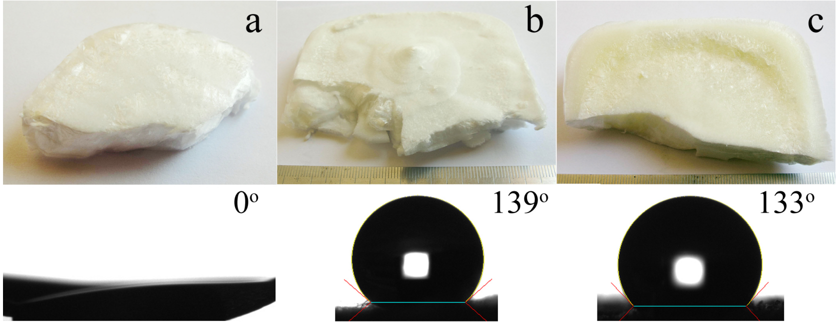

Sample	L-TOCNF	L-TOCNF-AKD	L-TOCNF-APS
IC, %	69.1	63.7	63.8
D [200], nm	2.9	2.8	2.8
S_{BET}, m^2/g	18.7	18.3	20.7

d

FIG. 3. Photographic images of aerogels and water drops (WCA) on the surface L-TOCNF (a), L-TOCNF-AKD (b), L-TOCNF-APS(c), and their physical properties (d)

nanofibrils with the simultaneous increase of the proportion of the amorphous phase, and retained the crystalline structure of the cellulose. The BET specific surface areas were in the range of 18.7 – 20.7 m^2/g for all aerogels (Fig. 3(d)).

The morphology of the lyophilized samples is characterized by scanning electron microscopy. TOCNFs form layered porous aerogels with ribbon-like film structures (Fig. 4(a)) which are the result of the lateral agglomeration of cellulose nanofibrils. Similar morphology was observed by Han et al. and Du et al. [25, 40], which explained by mean of lateral aggregation due to hydrogen bonding.

After lyophilization of L-TOCNF-AKD and L-TOCNF-APS hydrosols, porous plate-like materials were obtained (Fig. 4(b,c)). Aerogels contain heterogeneously shaped pores with a wide range of sizes from four to several tens micrometers. The thickness of the L-TOCNF, L-TOCNF-AKD, and L-TOCNF-APS layers were estimated from SEM photographs as 15 – 30, 30 – 60, and 45 – 80 nm, respectively. The increase in the thickness of the L-TOCNF-AKD and L-TOCNF-APS layers is apparently associated with surface modification [37, 38]. EDX results showed an increased C content and a lower O content in L-TOCNF-AKD sample compared to the L-TOCNF sample, which confirms the presence of aliphatic chains of fatty acids (stearic and palmitic) on the surface of L-TOCNF-AKD (Fig. 4(d,e)). The hydrophobic nature of AKD-modified TOCNFs is due to the adsorption through electrostatic interaction of AKD with dissociated carboxyl groups of TOCNF, as well as the formation of β-ketoester bonds between AKD and TOCNF [38]. EDX analysis indicated the presence of $N = 5.7 \pm 0.4$ at.% and $Si = 5.6 \pm 0.4$ at.% in L-TOCNF-APS sample due to the coating of its surface with aminopolysiloxane networks, Fig. 4(f), as shown in our previous study [37].

Unmodified L-TOCNF exhibited hydrophilic properties as the aerogel immediately absorbed a drop of water (WCA = 0 °). In contrast, the modified L-TOCNF-AKD (WCA 139 ± 2 °) and L-TOCNF-APS (WCA 133 ± 2 °) were highly hydrophobic (Fig. 3(a-c)).

3.3. Redispersing of lyophilized L-TOCNF, L-TOCNF-AKD and L-TOCNF-APS

The main purpose of hydrophobizing TOCNFs is to improve their dispersibility in organic solvents. Solvents are usually classified according to their dissolving ability as polar and nonpolar. However, the polarity of a solvent cannot be expressed in a specific physical quantity. Dielectric constant (ε) and dipole moment (μ) are often used to quantify the polarity of a solvent [41]. Hexane ($\varepsilon = 1.9$, $\mu = 0$), chloroform ($\varepsilon = 4.7$, $\mu = 1.15$), DMF ($\varepsilon = 36.7$, $\mu = 3.2$) and DMSO ($\varepsilon = 46.7$, $\mu = 4.0$) were selected as nonpolar organic solvent, low and medium polarity solvents, respectively. For comparison, all lyophilized samples were redispersed in high polarity solvent – water ($\varepsilon = 78.5$, $\mu = 1.8$).

Suspensions of the lyophilized samples were sonicated to disrupt aggregation between nanofibers after freeze-drying. The lyophilized unmodified and modified TOCNFs were redispersed in various solvents, presented in Fig. 5. The fact that sonication is effective for homogenizing dispersions has been also demonstrated in previous studies [42, 43]. The need for sonication indicates the endothermic nature of the redispersion. Both after 1 hour and after 5 days aging, the sedimentation and clarification of the suspension were checked. L-TOCNF showed excellent redispersibility to transparent dispersions in water and dispersion stability after both 1 hour and 5 days (Fig. 5(a,b)). The resulting clear stable dispersion and high dispersing degree ($Dr = 98$ %) of L-TOCNF indicate successful nanofibrillation of lyophilized TOCNF in water. L-TOCNF was also redispersed in DMSO with formation of a translucent dispersion

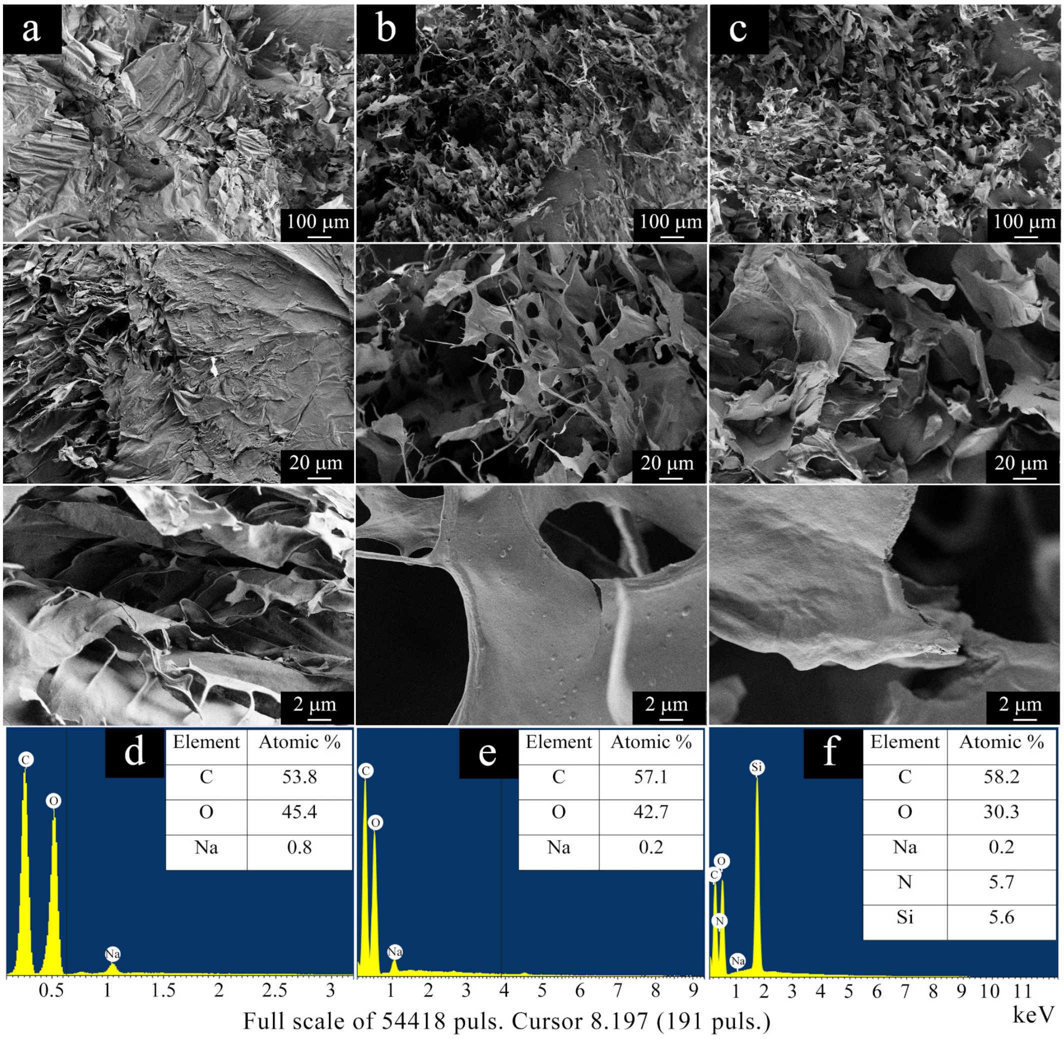

Element	Atomic %
C	53.8
O	45.4
Na	0.8

Element	Atomic %
C	57.1
O	42.7
Na	0.2

Element	Atomic %
C	58.2
O	30.3
Na	0.2
N	5.7
Si	5.6

FIG. 4. SEM images and EDX of the samples: L-TOCNF (a, d), L-TOCNF-AKD (b, e), L-TOCNF-APS (c, f)

after 1 hour and little sedimentation after 5 days (Fig. 5(a,b)) and $Dr = 67$ %, (Fig. 6). L-TOCNF did not disperse in DMF with opaque dispersion (Fig. 5(a)) formation and sedimentation after 5 days (Fig. 5(b)) ($Dr = 5$ %). L-TOCNF did not disperse in chloroform and hexane due to their very low dielectric constant (Figs. 5, 6).

The hydrophobic L-TOCNF-AKD and L-TOCNF-APS has not shown sign of redispersability in water, as the particles started immediately separating after sonication. Even flotation was observed for L-TOCNF-AKD, due to the presence of long aliphatic chains fatty acid (stearic and palmitic) on the TOCNF surface (Fig. 5). On the contrary, sedimentation of L-TOCNF-APS in aqueous suspensions occurred despite its high wetting angle (WCA 133 ± 2 °) due to the presence of polar NH_2 groups in the grafted polyaminopropylsiloxane (Fig. 5). L-TOCNF-AKD and L-TOCNF-APS showed good redispersibility in medium polarity solvents such as DMSO, DMF, which is confirmed by translucent dispersions after 1 hour (Fig. 5(a)) and slight sedimentation after 5 days (Fig. 5(b)) and high Dr (Fig. 6). It should be noted that L-TOCNF-AKD ($Dr = 97$ %) is more readily redispersible in a less polar solvent (e.g., DMF) than L-TOCNF-APS ($Dr = 75$ %). The dispersion of L-TOCNF-AKD no showed signs of sedimentation for 5 days (Fig. 5(b)). This effect can be attributed to the hydrophobic aliphatic chains of AKD, which prevent the formation of TOCNF intermolecular hydrogen bonds due to steric hindrance. L-TOCNF-AKD and L-TOCNF-APS was demonstrated partial redispersibility in the low-polarity solvent chloroform (Fig. 5), $Dr = 34$ % and $Dr = 11$ % respectively (Fig. 6). In this case, the same pattern is observed as in the case of redispersibility in DMF. However, neither L-TOCNF-AKD nor L-TOCNF-APS can be redispersed in the non-polar solvent hexane (Figs. 5, 6). Finally, the redispersibility of lyophilized modified TOCNFs in organic solvents decreases with decreasing solvent polarity up to the complete absence of redispersibility in a nonpolar solvent hexane.

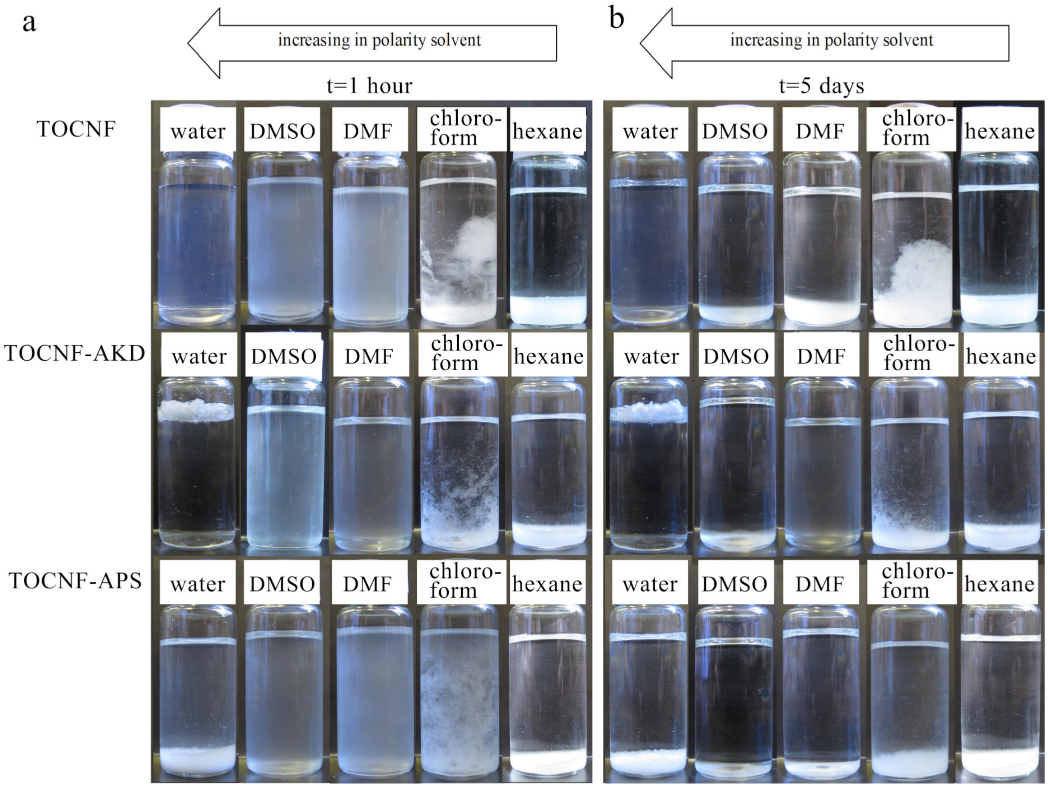

FIG. 5. Photograph of L-TOCNF, L-TOCNF-AKD, L-TOCNF-APS dispersed in different solvents (0.2 % w/v) after 1 hour (a) and 5 days (b)

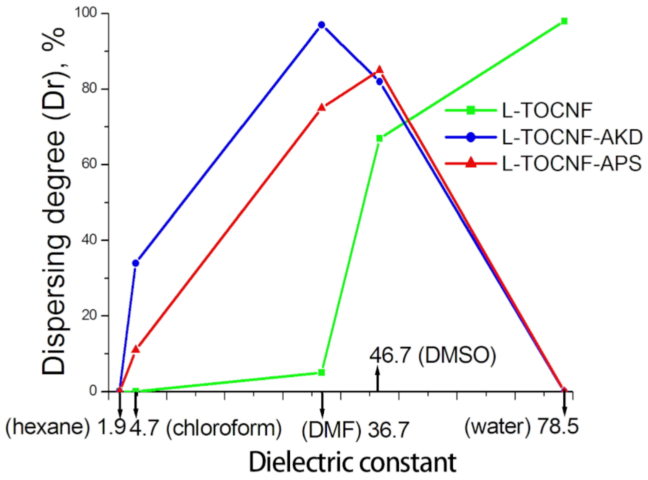

FIG. 6. Correlation between the dispersion degree in organic solvents L-TOCNF, L-TOCNF-AKD, L-TOCNF-APS and ε solvent

4. Conclusions

The hydrophobic aerogels L-TOCNF-AKD (WCA $139\pm2\ ^\circ$) and L-TOCNF-APS (WCA $133\pm2\ ^\circ$) were prepared by freeze-drying. The redispersion of lyophilized samples of unmodified and modified TOCNFs in organic solvents was studied by the method of visualization and assessment of the dispersing degree. It was shown that hydrophilic L-TOCNF samples are redispersed in water and in the polar solvent DMSO, but not in less polar and nonpolar organic solvents. The redispersibility of hydrophobic L-TOCNF-AKD and L-TOCNF-APS in organic solvents has been significantly improved. This may be due to the significantly reduced polarity of the modified chain on the surface. Transparent supernatant dispersions containing individualized nanofibrils were observed in DMSO and DMF. Partial redispersibility was noted in the low-polarity solvent (chloroform). None of the samples can be redispersed in a non-polar solvent such as hexane. L-TOCNF-AKD redispersed better in less polar solvents such as DMF and chloroform than L-TOCNF-APS due to hydrophobic aliphatic AKD chains on the surface of TOCNF. The developed approach can be applied to improve of redispersibility of lyophilized modified TOCNFs in organic solvents without using laborious solvent replacing technique.

Acknowledgements

This work was supported by the Ministry of Science and Higher Education within the State assignment to Prokhorov General Physics Institute of the Russian Academy of Sciences. Authors express their sincere gratitude to Dr. Arthur I. Popov for his most kind assistance in the preparation of the present manuscript, Dr. Radmir V. Gainutdinov for the study of Atomic Force Microscopy, Dr. Khursand Yorov for freeze-drying and Dr. Vladimir N. Kuryakov for zeta potential measurements.

References

[1] De France K., Zeng Z., Wu T., Nyström G. Functional Materials from Nanocellulose: Utilizing Structure-Property Relationships in Bottom-Up Fabrication. *Advanced Materials*, 2021, **33** (28), P. 2000657.

[2] De Amorim J.D.P., de Souza K.C., et al. Plant and bacterial nanocellulose: production, properties and applications in medicine, food, cosmetics, electronics and engineering. A review. *Environ. Chem. Lett.*, 2020, **18**, P. 851–869.

[3] Liu Z., Zhang S., He B. et al. Synthesis of cellulose aerogels as promising carriers for drug delivery: a review. *Cellulose*, 2021, **28**, P. 2697–2714.

[4] Ahankari S.S., Subhedar A.R., Bhadauria S.S., Dufresne A. Nanocellulose in food packaging: a review. *Carbohyd. Polym.*, 2020, **255**, P. 117479.

[5] Dias O.A.T., Konar S., et al. Current State of Applications of Nanocellulose in Flexible Energy and Electronic Devices. *Front. Chem.*, 2020, **8**, P. 420.

[6] Nie S., Hao N., et al. Cellulose nanofibrils-based thermally conductive composites for flexible electronics: a mini review. *Cellulose*, 2020, **27**, P. 4173–4187.

[7] Luginina A.A., Kuznetsov S.V., et al. Hydrophobization of up-conversion luminescent films based on nanocellulose/MF_2:Ho particles (M = Sr, Ca) by acrylic resin. *Nanosystems: Phys. Chem. Math.*, 2019, **10** (5), P. 585–598.

[8] Saito T., Kimura S., Nishiyama Y., Isogai A. Cellulose nanofibers prepared by TEMPO-mediated oxidation of native cellulose. *Biomacromolecules*, 2007, **8** (8), P. 2485–2491.

[9] Isogai A., Saito T., Fukuzumi H. TEMPO-oxidized cellulose nanofibers. *Nanoscale*, 2011, **3** (1), P. 71–85.

[10] Isogai A. Development of completely dispersed cellulose nanofibers. *Proceedings of the Japan Academy, Series B*, 2018, **94** (4), P. 161–179.

[11] Isogai A. Emerging Nanocellulose Technologies: Recent Developments. *Advanced Materials*, 2020, **53**, P. 2000630.

[12] Forti E.S., El AwadAzrak S.M., et al. Mechanical enhancement of cellulose nanofibril (CNF) films through the addition of water-soluble polymers. *Cellulose*, 2021, **28** (10), P. 6449–6465.

[13] Beck S., Bouchard J., Berry R. Dispersibility in Water of Dried Nanocrystalline Cellulose. *Biomacromolecules*, 2012, **13** (5), P. 1486–1494.

[14] Okita Y., Fujisawa S., Saito T., Isogai A. TEMPO-Oxidized Cellulose Nanofibrils Dispersed in Organic Solvents. *Biomacromolecules*, 2011, **12**, P. 518–522.

[15] Fujisawa S., Saito T., et al. Surface Engineering of Ultrafine Cellulose Nanofibrils toward Polymer Nanocomposite Materials. *Biomacromolecules*, 2013, **14** (5), P. 1541–1546.

[16] Fujisawa S., Saito T., et al. Comparison of mechanical reinforcement effects of surface-modified cellulose nanofibrils and carbon nanotubes in PLLA composites. *Composites Science and Technology*, 2014, **90**, P. 96–101.

[17] Soeta H., Fujisawa S., Saito T., Isogai A. Controlling Miscibility of the Interphase in Polymer-Grafted Nanocellulose/Cellulose Triacetate Nanocomposites. *ACS Omega*, 2020, **5** (37), P. 23755–23761.

[18] Fujisawa S., Saito T., Isogai A. Nano-dispersion of TEMPO-oxidized cellulose/aliphatic amine salts in isopropyl alcohol. *Cellulose*, 2012, **19**, P. 459–466.

[19] Qu J., Yuan Z., et al. Enhancing the redispersibility of TEMPO-mediated oxidized cellulose nanofibrils in N,N-dimethylformamide by modification with cetyltrimethylammonium bromide. *Cellulose*, 2019, **26**, P. 7769–7780.

[20] Shrestha S., Chowdhury R.A., et al. Surface hydrophobization of TEMPO-oxidized cellulose nanofibrils (CNFs) using a facile, aqueous modification process and its effect on properties of epoxy nanocomposites. *Cellulose*, 2019, **26**, P. 9631–9643.

[21] Dong H., Napadensky E., et al. Cellulose Nanofibrils and Diblock Copolymer Complex: Micelle Formation and Enhanced Dispersibility. *ACS Sustain. Chem. Eng.*, 2016, **5** (2), P. 1264–1271.

[22] Viet D., Beck-Candanedo S., Gray D.G. Dispersion of cellulose nanocrystals in polar organic solvents. *Cellulose*, 2007, **14**, P. 109–113.

[23] Heux L., Chauve G., Bonini C. Nonflocculating and Chiral-Nematic Self-ordering of Cellulose Microcrystals Suspensions in Nonpolar Solvents. *Langmuir*, 2000, **16** (21), P. 8210–8212.

[24] Peng S.X., Chang H., et al. A comparative guide to controlled hydrophobization of cellulose nanocrystals via surface esterification. *Cellulose*, 2016, **23** (3), P. 1825–1846.

[25] Han J., Zhou C., et al. Self-assembling behavior of cellulose nanoparticles during freeze-drying: effect of suspension concentration, particle size, crystal structure, and surface charge. *Biomacromolecules*, 2013, **14**, P. 1529–1540.

[26] Kaboorani A., Riedl B., Surface modification of cellulose nanocrystals (CNC) by a cationic surfactant. *Ind. Crops Prod.*, 2015, **65**, P. 45–55.

[27] Samir M.A.S.A., Alloin F., et al. Preparation of Cellulose Whiskers Reinforced Nanocomposites from an Organic Medium Suspension. *Macromolecules*, 2004, **37** (4), P. 1386–1393.

[28] Tang L.M., Weder C. Cellulose Whisker/Epoxy Resin Nanocomposites. *ACS Appl. Mater. Interfaces*, 2010, **2** (4), P. 1073–1080.

[29] Voronova M.I., Surov O.V., et al. Dispersibility of Nanocrystalline Cellulose in Organic Solvents. *Russian Journal of Bioorganic Chemistry*, 2020, **46** (7), P. 1295–1303.

[30] Hu Z., Berry R.M., Pelton R., Cranston E.D. One-Pot Water-Based Hydrophobic Surface Modification of Cellulose Nanocrystals Using Plant Polyphenols. *ACS Sustain. Chem. Eng.*, 2017, **5**, P. 5018–5026.

[31] Jiang F., Hsieh Y.L. Assembling and redispersibility of rice straw nanocellulose: effect of tert-butanol. *ACS Appl. Mater. Interfaces*, 2014, **6**, P. 20075–20084.

[32] Indarti E., Marwan, Wanrosli W.D. Dispersion Stability of Nanocellulose in Nonpolar Solvent: Chloroform. *Materials Science Forum*, 2020, **998**, P. 170–175.

[33] Araki J., Wada M., Kuga S. Steric Stabilization of a Cellulose Microcrystal Suspension by Poly(ethylene glycol) Grafting. *Langmuir*, 2001,**17** (1), P. 21–27.

[34] Johnson R.K., Zink-Sharp A., Glasser W.G. Preparation and characterization of hydrophobic derivatives of TEMPO-oxidized nanocelluloses. *Cellulose*, 2011, **18**, P. 1599–1609.

[35] Chu Y., Sun Y., Wu W., Xiao H. Dispersion Properties of Nanocellulose: A Review. *Carbohyd. Polym.*, 2020, **250**. P. 116892.

[36] Fedorov P.P., Luginina A.A., et al. Composite up-conversion luminescent ?lms containing a nanocellulose and $\mathrm{SrF_2}$:Ho particle. *Cellulose*, 2019, **26** (4), P. 2403–2423.

[37] Luginina A.A., Kuznetsov S.V., et al. Laser damage threshold of hydrophobic up-conversion carboxylated nanocellulose/$\mathrm{SrF_2}$:Ho composite films functionalized with 3-aminopropyltriethoxysilane. *Cellulose*, 2021, **28**, P. 10841–10862.

[38] Fedorov P.P., Luginina A.A., et al. Hydrophobic up-conversion carboxylated nanocellulose/fluoride phosphor composite films modified with alkyl ketene dimer. *Carbohyd. Polym.*, 2020, **250**, P. 116866.

[39] Jiang F., Han S., Hsieh Y.L. Controlled defibrillation of rice straw cellulose and selfassembly of cellulose nanofibrils into highly crystalline fibrous materials. *RSC Advances*, 2013, **3** (30), P. 12366–12375.

[40] Du L., Yu Z., Wang J., et al. Analyzing the film formation mechanism of cellulose nanoparticles (CNPs) based on the fast freeze-drying morphology. *Cellulose*, 2020, **27**, P. 6921–6933.

[41] Reichardt C. *Solvents and Solvent Effects in Organic Chemistry*. Second ed., Mir Publishers, Moscow, 1991, 763 p.

[42] Kasuga T., Isobe N., et al. Clearly transparent nanopaper from highly concentrated cellulose nanofiber dispersion using dilution and sonication. *Nanomaterials*, 2018, **8** (2), P. 104.

[43] Sharma A., Mandal T., Goswami S. Dispersibility and Stability Studies of Cellulose Nanofibers: Implications for Nanocomposite Preparation. *J. Polym. Environ.*, 2021, **29**, P. 1516–1525.

NANOSYSTEMS: PHYSICS, CHEMISTRY, MATHEMATICS, 2021, 12 (6), P. 773–782

Photocatalytic degradation of Rose Bengal dye over mechanochemically synthesized zinc oxide under visible light irradiation

Y. D. Kaldante[1,3], R. N. Shirsat[3], M. G. Chaskar[1,2]

[1]Department of Chemistry, PDEA's Baburaoji Gholap College, Sangvi, Pune, Maharashtra – 411027, India
[2]Department of Chemistry, PDEA's Prof. Ramkrishna More College, Akurdi, Maharashtra – 411044, India
[3]Department of Chemistry, PDEA's Annasaheb Waghire College, Otur, Tal. Junnar, Dist. Pune, Maharashtra – 412409, India

ydkaldante@gmail.com, manohar_c@hotmail.com

DOI 10.17586/2220-8054-2021-12-6-773-782

Present work summarized efficient synthesis of ZnO by mechanochemical method via zinc oxalate dihydrate precursor for studies of the photocatalytic degradation of Rose Bengal dye. The process of conversion of zinc oxalate dihydrate to ZnO was studied by TGA-DTG analysis and FT-IR Spectroscopy, XRD data obtained clearly revealed the hexagonal wurtzite crystallite structures of ZnO. FE-SEM images confirmed nanocrystalline morphology of ZnO with an approximately uniform particle size distribution. The purity of ZnO was confirmed by EDX study. The optical band gap of ZnO was determined from UV-Visible spectroscopy. The photocatalytic activity of ZnO was investigated with degradation of Rose Bengal dye. The colorimetric absorbance measurement was used to estimate degradation efficiency. The catalytic activity was studied with reference to the condition of dye concentration, photocatalyst loading capacity, pH of dye solution, irradiation time, etc. Photocatalytic degradation of Rose Bengal dye over mechanochemically synthesized ZnO under visible light irradiation was successfully studied.

Keywords: zinc oxide, Rose Bengal, degradation efficiency, photocatalysis.

Received: 7 August 2021

Revised: 30 October 2021

1. Introduction

Water scarcity is one of the most serious problems presently we are facing all over the world. Prolonged shortages in the water supply have a substantial impact not only on the ecosystem and agriculture [1] but also harm local economies [2]. Consequently, water shortages create environmental, economic and social problems. The lack of water for prolong period of time results in a drought. Some common consequences of drought includes reduced crop growth or yield productions [1], soil erosion, desertification [3] and dust storms [4], habitat damage, affecting both terrestrial [5] and aquatic wildlife [6], hunger, malnutrition, dehydration and related diseases, mass migration [7], reduced hydroelectric power production, shortages of water for industrial uses [4], social unrest [8], wildfires [3], accumulation of cyanotoxin within food chains and water supply can cause cancer with low exposure over the long term [9]. Increased demands of clean intake water and water for sterilization are the major present problems of our society [10]. To deal with the problems of water scarcity, drought situations as well as to fulfill the demands of society, water treatment or detoxification and rain water harvesting are the best initiatives which need to be executed.

The process of removal of undesirable chemicals, biological contaminants, suspended solids and gases from water is called as water purification. It is necessary to produce pure water suitable for specific purposes such as drinking, pharmacological, medical, chemical and industrial applications. The clarification or purification of water can be achieved by physical methods like filtration, distillation and sedimentation; biological methods like slow sand filtration, biologically activated carbon filtration; chemical methods such as chlorination, flocculation and the use of ultraviolet light. All these are the conventional methods of water treatment and purification which are not always suitable for treating moderate to high concentration waste waters.

The execution of solar light driven advanced oxidation processes (AOPs) has been an auspicious alternative for the detoxification of industrial effluents [11–14], and thus, for environmental protection [14]. The coloring agent dyes are the organic substances mainly used in textile, paper, printing, leather and plastics industries are most common and are one of the major contaminant responsible for water pollution. The photocatalysis is one of the most efficient and economical method among AOPs employed for the total mineralization of organic contaminants to CO_2, H_2O and inorganic salts [15–18]. Metal oxides like TiO_2, ZnO, SnO_2, NiO, Cu_2O, Fe_3O_4, etc. have been effectively utilized as a heterogeneous photocatalyst for dye degradation. These are nontoxic, stable, highly photosensitive, wide band gap materials. An activated semiconductor metal oxide usually promotes the photodegradation of dyes under solar light [19]. In this method, a semiconductor metal oxide catalyst is illuminated with solar light or a suitable light source, electron-hole pairs are generated in the oxide material. Due to intensive reduction potential of the holes present in the valence band, it gives in situ generation of hydroxyl radicals. Due to the high redox potential (2.8 V) of hydroxyl radicals, they are capable of complete non-selective breakdown of the dye molecules [20]. Among the various metal oxides, ZnO was found to be the most suitable candidate for the visible light mediated photocatalysis, so, for the present study, ZnO was selected. Also, due to its simple, economic and environmentally friendly nature, the mechanochemical method was selected for the present study.

One of the extensively used classes of dyes is xanthene dyes containing xanthene nucleus with aromatic groups as the chromophore. These dyes are widely used as colorants in the textile, printing and dyeing industries. These dyes are reported to be genotoxic, mutagenic, cytotoxic and cytostatic [21–25]. Rose Bengal is one of the widely used anionic water-soluble and important xanthene dyes in textile, dyeing and photochemical industries. Therefore, for the present study, Rose Bengal is taken as a model dye for the photocatalytic degradation over ZnO photocatalyst. The chemical structure of the dye molecule is shown in Fig. 1.

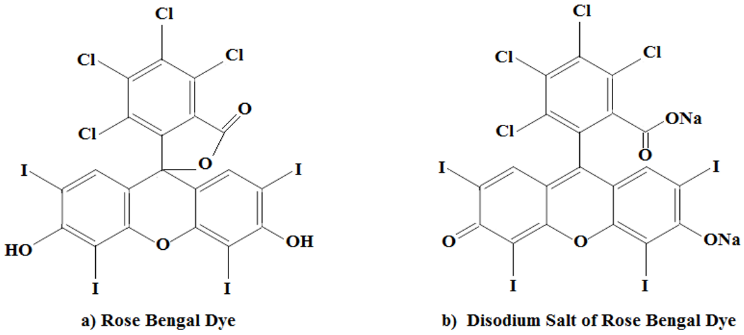

a) Rose Bengal Dye

b) Disodium Salt of Rose Bengal Dye

FIG. 1. Chemical structure of the Rose Bengal dye molecule

In this study, an attempt was made to synthesize the ZnO by efficient, solution free mechanochemical method and study the photocatalytic degradation of Rose Bengal dye over this ZnO in presence of artificial light (visible). The various operational parameters such as dye concentration, photocatalyst loading capacity, pH of dye solution, irradiation time, etc. were studied in detail. Further exploration of this work is particularly beneficial for the water treatment by photocatalysts in those areas of the world where solar light is not abundantly available.

2. Experimental

2.1. Materials

Zinc acetate dihydrate (assay 99.5 %), oxalic acid dihydrate (assay 99.0 %), Rose Bengal disodium salt (assay 99.5 %) and other essential chemicals used during this work were AR grade reagents obtained from S. D. Fine Chemicals, India and used without further purification. All the experimental solutions were prepared in distilled water. The pH of these solutions was adjusted to the desired values with aqueous NaOH (0.1 N) and H_2SO_4 (0.1 N) wherever necessary.

2.2. Synthesis of photocatalyst

Powdered zinc oxide (ZnO) catalyst was prepared by a two-step method. In the first step zinc oxalate dihydrate precursor was obtained simply by mechanical hand grinding of a mixture of 10.975 g of zinc acetate dihydrate with 6.93 g of oxalic acid dihydrate in an agate mortar for 20 – 30 minutes at room temperature. In second step the zinc oxalate dihydrate precursor was subjected to thermal disintegration by calcination at 450 °C leads to the formation of ZnO [26].

$$\mathrm{Zn(CH_3COO)_2\cdot 2H_2O + H_2C_2O_4\cdot 2H_2O \longrightarrow ZnC_2O_4\cdot 2H_2O + 2CH_3COOH + 2H_2O,} \tag{1}$$

$$\mathrm{ZnC_2O_4\cdot 2H_2O \longrightarrow ZnO + CO_2 + CO + 2H_2O.} \tag{2}$$

2.3. Equipment

The temperature of the transformation of zinc oxalate dihydrate precursor to the zinc oxide was obtained by thermogravimetric analysis machine (Shimadzu, TG-DTG-60H) and FT-IR (*PerkinElmer* UATR Spectra Two) spectrometer. For ZnO crystallite, the X-ray diffraction (XRD) pattern was obtained with X-ray Diffractometer (*Rikagu*

Miniflex-600) using CuKα radiation ($\lambda\alpha = 1.5418$ Å) and the average crystallite size (D) of the particles was determine from the Debye–Scherer equation [27]: $D = \dfrac{0.90 \times \lambda}{\beta \times \cos\theta}$ where, λ is the wavelength (CuKα), β is the full width at the half maximum (FWHM) of the most intense peak (101) in the XRD pattern of ZnO and θ is the diffraction angle [27]. The morphological characterization of powder was performed by using FE-SEM (JEOL JSM-6360A). The elemental composition of the ZnO was studied with energy dispersive X-ray (EDX) spectra. The optical band gap of ZnO was estimated from UV-Visible spectra obtained with UV-Visible Spectrophotometer (*PerkinElmer* Lambda 365). The photocatalytic reactions were carried out at room temperature in batch reactor under adequately constant intensity visible light irradiation source (400W MH-TBT-E40) providing nearly 0.4 – 0.6 kW/m^2 radiation intensity at 15 cm distance. Colorimetric absorbance measurement with digital colorimeter (EQUIP-TRONICS EQ-353) was utilized to determine the degradation efficiency. The preliminary pH of suspension was adjusted with the help of pH meter (LABTRONICS LT-11). A Lux meter HTC LX-100 was used to measure the light intensity.

2.4. Photocatalytic degradation experiments

For optimization of photocatalytic parameters and photocatalytic degradation studies, Rose Bengal dye solutions with variable initial concentration were prepared using double distilled water. All experiments are conducted in a batch photoreactor with glass cool trap and magnetic stirrer. Rose Bengal (100 mL) dye solution having known preliminary concentration at suitable pH and at room temperature was taken with known extent of zinc oxide powder in a photoreactor with 5 cm diameter. Mixture was then subjected to ultrasonic agitation for 5 minutes to obtain a uniform suspension. Container was then fixed on magnetic stirrer kept under adequately constant intensity visible light irradiation source (400W MH-TBT-E40) at a distance of 15 cm. At specified time intervals supernatant solution (5.0 ml) was collected and centrifuged to settle down ZnO particles. Then absorbance was recorded at predetermined $\lambda_{\max}$ (500 nm) value of Rose Bengal dye solution using a digital colorimeter. The degradation efficiency was estimated from the colorimetric absorbance measurement as percent (%) Degradation: $\%D = \dfrac{100 \times [A_0 - A_t]}{[A_0]}$, where $\%D$ – percent degradation, A_0 – initial absorbance, A_t – absorbance at time t.

3. Result and discussion

3.1. Characterization of zinc oxide

The process of conversion of zinc oxalate dihydrate to Zinc Oxide (ZnO) was studied by TGA-DTG analysis and FT-IR Spectroscopy. The ZnO thus obtained was further characterized by X-ray diffraction, FE-SEM and EDX study. The optical band gap of ZnO was determined from UV-Visible spectroscopy.

3.1.1. Thermal gravimetric analysis. Fig. 2 shows the TGA-DTG plots for zinc oxalate dihydrate precursor. From the DTG plot it is clear that, the thermal disintegration of zinc oxalate dihydrate precursor occurred with three endothermal steps from 30 to 450 °C to give ZnO. The 1.40 % weight loss from 30 to 105 °C is due to the removal of residual acetic acid. The 17.71 % weight loss from 105 to 165 °C is due to removal of adsorbed water, residual water and residual acetic acid (Boiling Point 118 °C). The 37.35 % weight loss from 335 to 455 °C in TG curve is recognized to the decomposition of oxalate moiety from zinc oxalate. From this, the conversion temperature for zinc oxalate dihydrate to zinc oxide is 455 °C.

3.1.2. FT-IR spectroscopic study. Fig. 3 shows changes in the FT-IR spectra during the transformation of zinc acetate dihydrate to zinc oxide through zinc oxalate precursor. The replacement of acetate ions in the zinc acetate dihydrate by oxalate ions to yield zinc oxalate precursor during mechanical grinding with oxalic acid is clearly understood with the help of diminishing of bands corresponding to various symmetric and asymmetric stretching and bending vibrations in the acetate group (621, 686, 952, 1016, 1426, 1542, 1664, 3073 cm^{-1}) and enhancement of the bands corresponding to various symmetric and asymmetric stretching and bending vibrations in the oxalate group (547, 720, 1116, 1608, 3412 cm^{-1}). Zinc oxalate precursor shows well defined bands (493, 588, 723, 822, 1122, 1245, 1319, 1364, 1626, 1888 and 3390 cm^{-1}). Diminishing of all bands other than that centered at 450 cm^{-1} upon calcination of zinc oxalate precursor at 500 °C confirms the formation of spherical shape ZnO and same also confirmed by XRD study.

3.1.3. X-Ray diffraction (XRD) study. The XRD peak position and intensity data for synthesized ZnO was procured over the appropriate (20 – 80 °) 2θ range with CuKα radiation ($\lambda = 1.5418$ Å). The data contained (Fig. 4) a series of peaks centered at $2\theta = 31.74$, 34.38, 36.22, 47.50, 56.58, 62.82, 66.36, 67.90, 69.08, 72.62, 76.86 ° belonging to the (100), (002), (101), (102), (110), (103), (200), (112), (201), (004) and (202) planes respectively, which are in very fine agreement with the JCPDS card for the standard hexagonal wurtzite structure of pure ZnO [26,28].

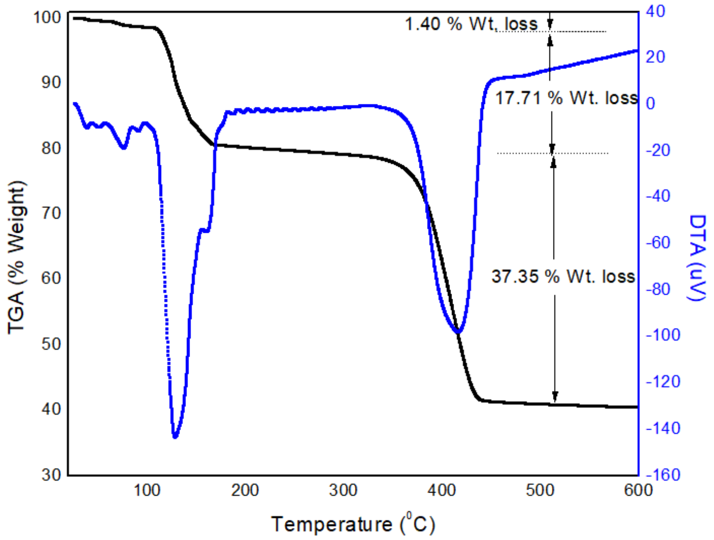

FIG. 2. TG-DTA plots for Zinc Oxalates Dihydrate

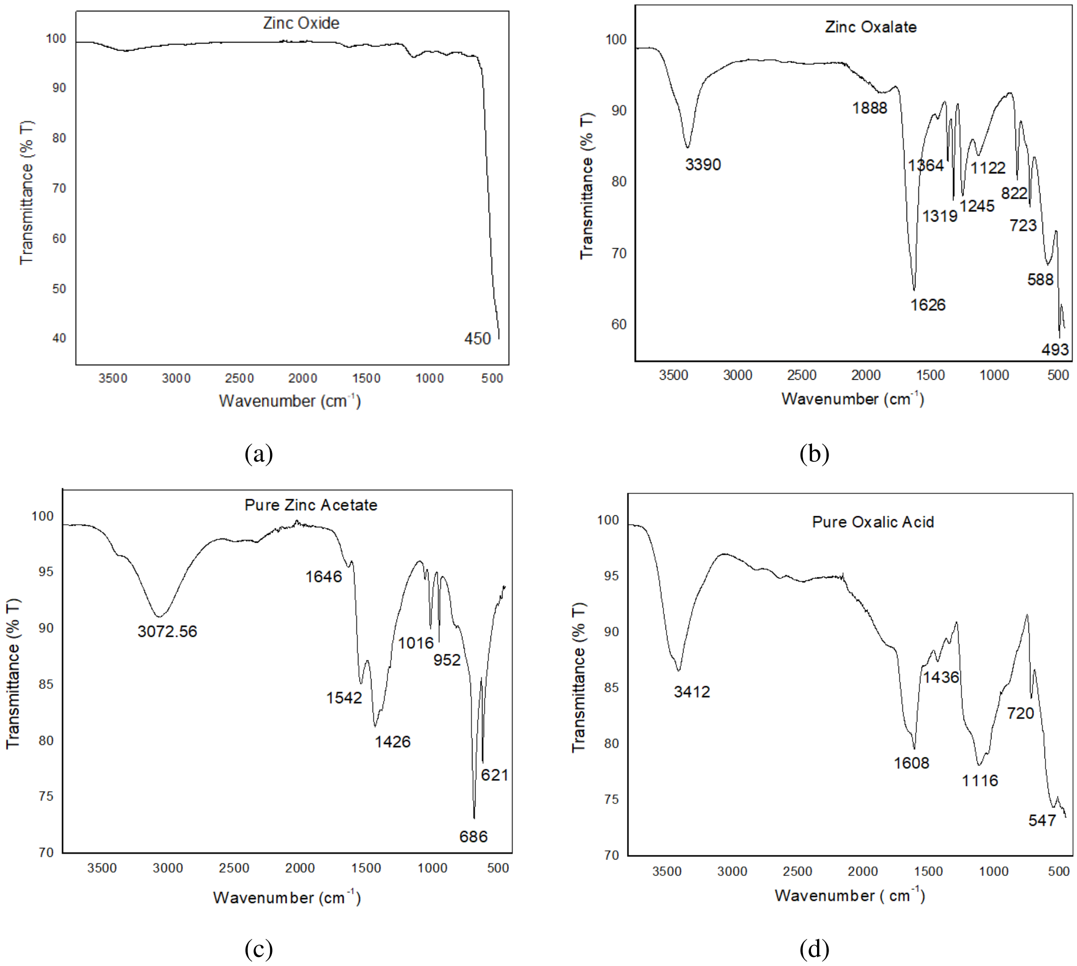

(a) (b)

(c) (d)

FIG. 3. Changes in FT-IR spectra during the transformation of $ZnC_2O_4 \cdot 2H_2O$ to ZnO

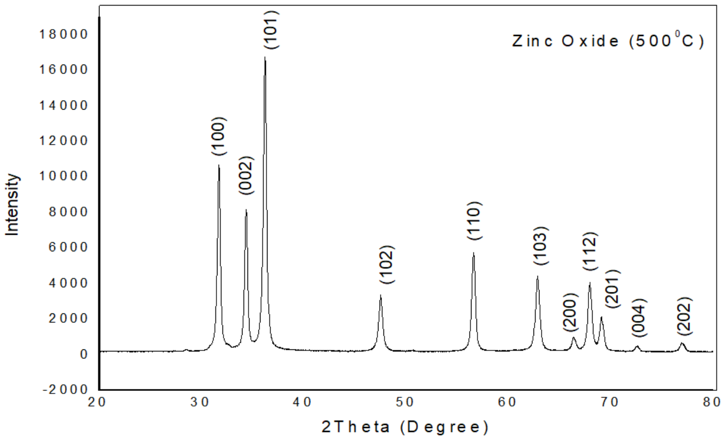

FIG. 4. XRD pattern of Zinc Oxide

The mean crystallite size of ZnO was calculated from data of most intense peak corresponding (101) crystal plane using Debye Scherer's formula [27] and was found to be 18.67 nm, corresponding to the mean FWHM = 0.4237 also the lattice strain calculated by using tangent formula [29] was found to be 0.324. Also, the specific surface area was determined by using Sauter Formula [30] and was found to be 57.33 m^2/g.

3.1.4. FE-SEM study. The morphological characterization of ZnO was studied by using field emission scanning electron microscopy (FESEM). Fig. 5 indicates the FESEM image ZnO powder. Formation of nearly homogeneous phase having non-agglomerated, dense particles of hexagonal morphology is clearly seen from the FE-SEM image. Nearly uniform particle size distribution is also found. The mean particle size is found be around 31.62 nm.

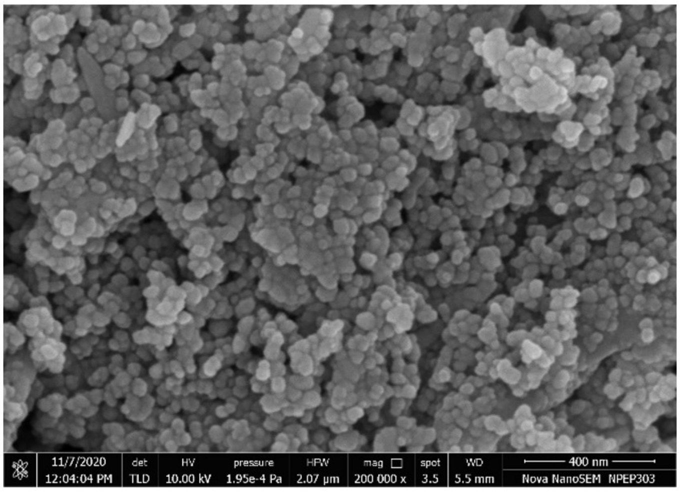

FIG. 5. FE-SEM image of Zinc Oxide

3.1.5. EDX analysis. Energy Dispersive X-ray (EDX) spectra of ZnO is shown in Fig. 6(a), which shows peaks corresponding to Zn and O only in significance with purity of the zinc oxide. Also elemental mapping showing distribution of Zn and O is shown in the Fig. 6(b).

3.1.6. UV-Visible spectra. Fig. 7 represents UV-visible Spectra of ZnO which shows evidently situated optical extinction bands in the range of 370 to 415 nm. The calculated band gap energy of ZnO was found to be 3.14 eV.

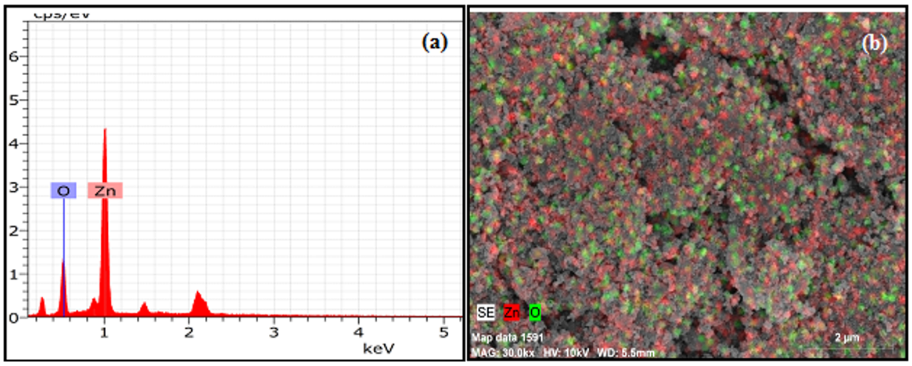

FIG. 6. Zinc Oxide's EDX Spectra Figure (a) and Elemental Mapping Figure (b)

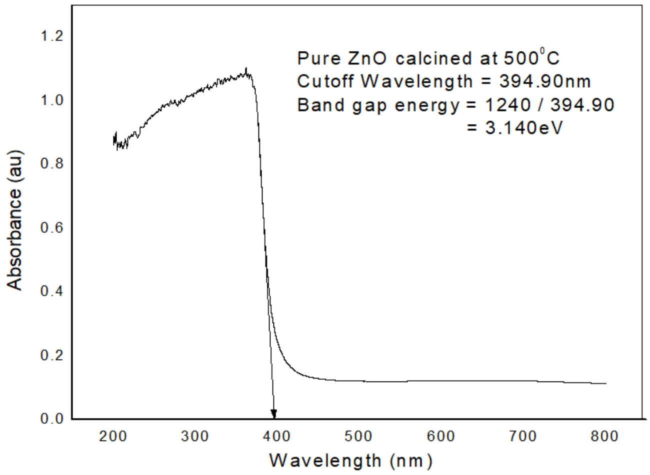

FIG. 7. UV-visible Spectra of ZnO

3.2. Optimization of photocatalytic operational parameters for degradation of Rose Bengal over ZnO catalyst

3.2.1. Mechanism of Rose Bengal dye degradation. An advanced oxidation process is involved in the photocatalytic degradation of Rose Bengal dye [19]. Upon absorption of photons by photosensitive Rose Bengal dye, the molecule forms an excited singlet state (RB_1), which is then converted to excited triplet state (RB_2) by means of inter system crossing (ISC). Zinc oxide (ZnO), upon irradiation, excites the electron from valence band to conduction band and a hole left behind on the valence band. This hole adsorbs an electron from water or hydroxide ion to produce ·OH radical. The radicals oxidize the Rose Bengal dye to its colorless leuco form and finally to harmless compounds [19].

The most feasible mechanism is as follows [19]:

$$\mathrm{RB}_0 + h\nu \longrightarrow \mathrm{RB}_1, \tag{3}$$

$$\mathrm{RB}_1 \xrightarrow{(ISC)} \mathrm{RB}_2, \tag{4}$$

$$\mathrm{ZnO} + h\nu \longrightarrow h^+(\mathrm{VB}) + e^-(\mathrm{CB}), \tag{5}$$

$$\mathrm{H}_2\mathrm{O} + h^+ \longrightarrow \cdot\mathrm{OH} + \mathrm{H}^+, \tag{6}$$

$$\mathrm{O}_2 + e^- \longrightarrow \cdot\mathrm{O}_{2-}, \tag{7}$$

$$\cdot\mathrm{O}_{2-} + \mathrm{H}^+ \longrightarrow \cdot\mathrm{HO}_{2-}, \tag{8}$$

$$\mathrm{RB}_2 + \cdot\mathrm{OH} \longrightarrow \text{Leuco RB}, \tag{9}$$

$$\text{Leuco RB} \longrightarrow \text{Products}. \tag{10}$$

Optimization of the photocatalytic degradation of Rose Bengal over ZnO surface was explored by varying the operational parameters, e.g.: the initial pH of the suspension (6 – 10), ZnO loading quantity (50 – 150 mg/ 100 ml), initial dye concentration (50 – 150 ppm), illumination time (0 – 6 hours) under adequately constant intensity visible light irradiation source. The degradation efficiency was estimated from the colorimetric absorbance measurement as percent (%) Degradation: $\%D = \dfrac{100 \times [A_0 - A_t]}{[A_0]}$, where $\%D$ – percent degradation, A_0 – initial absorbance, A_t – absorbance at time t. The results encountered are detailed as follows.

3.2.2. Effect of the initial pH of Rose Bengal dye solution. The effect of initial pH of the Rose Bengal dye solution over the pH range 6 – 10 was studied with arbitrary chosen 50 ppm dye solution and 100 mg ZnO/ 100 ml loading with 4 hours of irradiation time. The pH of the dye solutions was adjusted only at initial stage and not controlled during the course of reaction. The other parameters were kept constant. The results gained are indicated in Fig. 8. The slight solubility of ZnO in acidic medium (pH 6) may be reflected in the decreased degradation of Rose Bengal in acidic medium [31]. Also up to pH 6 to 8 the dye molecule remains in its protonated form and also ZnO catalyst is somewhat positively charged due to adsorption of protons, hence, the dye molecules and ZnO repel each other. which results in a low degradation efficiency. The percent degradation was found to be maximum (100 %) at pH 8, where the repulsion between dye molecule and ZnO catalyst is at its lowest. Beyond pH 8, the rate of degradation decreases with increase in initial pH from 9 to 10, this is due to negative charge produce on the ZnO due to adsorption of hydroxyl ions and hence anionic dye molecule again face intermolecular repulsion [19]. The pH value of 8 is thus optimum for the photocatalytic degradation of Rose Bengal dye.

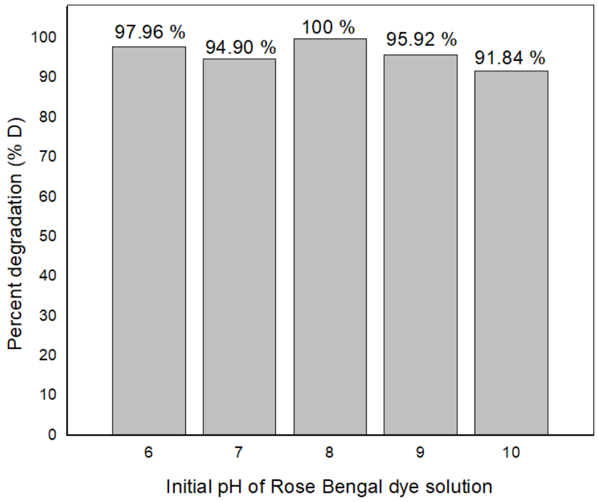

FIG. 8. Variation of percent (%) degradation of Rose Bengal dye with initial pH of dye solution

3.2.3. Effect of the photocatalyst (ZnO) quantity. The blank experiments were carried out in absence of ZnO to know the extent to which Rose Bengal dye photolyzed. In absence of ZnO, Rose Bengal dye photolyzed to the extent of only 20 – 23 %. When aqueous solution of Rose Bengal dye containing ZnO was irradiated with light PCD of Rose Bengal was observed to a greater extent. The amount of catalyst used for dye degradation has a profound impact on the rate of degradation [32]. The optimum amount of ZnO required for thorough mineralization of 100 ml, 50 ppm Rose Bengal dye at an optimum pH 8 to CO_2 and H_2O and inorganic ions was inspected by changing the amount of ZnO from 25 to 150 mg/100 ml and upon 3.5 hours of irradiation. From the Fig. 9, it is depicted that the percent of dye degraded increases with an increased amount of ZnO loading from 25 to 150 mg/100 ml. As the amount of ZnO increases, the surface area of catalyst increases, hence adsorption of dye molecules over the surface of ZnO increases, which increases the percent degradation. Also, increasing amount of photocatalyst increases the number of active sites on its surface, which promotes an increased number of photogenerated electron-hole pair, hence the number of hydroxyl radicals responsible for dye degradation.

From the above data, one can see 100 % dye degradation is observed for in each case of catalytic loading 125 mg ZnO/ 100 ml dye solution and 150 mg ZnO/ 100 ml dye solution. The 100 mg ZnO/ 100 ml dye solution is selected as optimum catalyst loading for the present study; doing so circumvents the formation of a turbid solution and thus avoids the shadowing and screening effect for the light photons due to scattering of light, which negatively impacts photodegradation [33, 34].

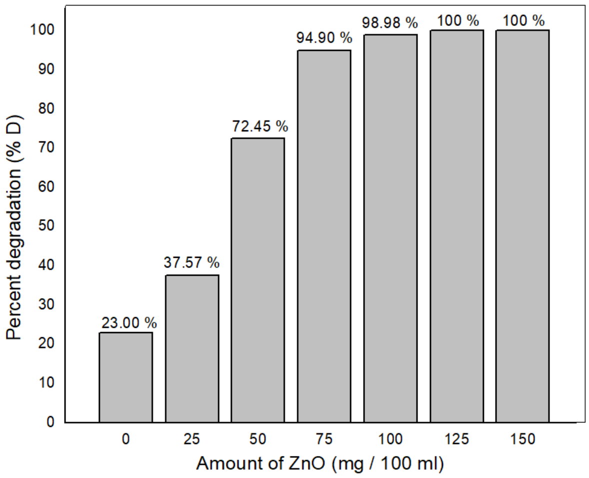

FIG. 9. Variation of percent (%) degradation of Rose Bengal dye with catalyst (ZnO) quantity

3.2.4. Effect of the initial concentration of Rose Bengal dye solution. The degradation of Rose Bengal dye was studied at different initial concentrations ranging from 25 to 150 ppm with respect to 4 hours of illumination time under the optimum conditions (Catalytic loading 100 mg ZnO/ 100 ml of dye solution at pH 8). The results gained are indicated in Fig. 10. As expected the increased initial concentration of the dye solution has a negative impact on percent degradation due to the fact that, under constant conditions of catalytic amount and irradiation time the same number of reactive radicals were generated on the surface of ZnO, but more and more dye molecules were adsorbed on its surface [34]. Therefore, the number of dye molecules adsorbed over the surface of ZnO catalyst is relatively more in comparison with number of reactive radicals available for attack. Hence, photodegradation decreases [34,35]. Also,the increased concentration of dye solution interrupts the photons before reaching to the ZnO surface which in terms decreases the absorption of photons and consequently reduces the photodegradation of dye [34]. Hence 100 ml 50 ppm Rose Bengal dye solution was completely degraded by 100 mg of ZnO at pH 8 on 4 hours of illumination under the aforesaid light source.

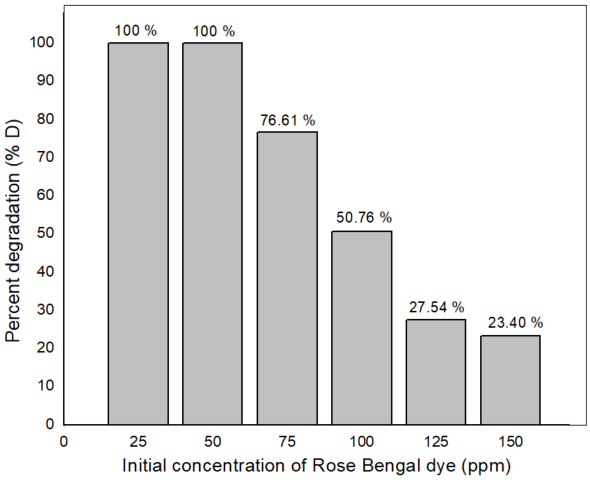

FIG. 10. Variation of percent (%) degradation of Rose Bengal dye over ZnO with initial dye concentration

3.2.5. Effect of the irradiation time. The PCD of 75 ppm Rose Bengal dye under the optimum conditions (Catalytic loading 100 mg ZnO/ 100 ml of dye solution at pH 8) in artificial light was found to increase with increase in irradiation time and within 8 hours there was 100 % degradation (Fig. 11). When 75 ppm Rose Bengal dye solution along with ZnO is magnetically stirred for 8 hours in the absence of light (dark), negligible (6 – 7 %) photodegradation was observed. For reference it is considered as zero hour irradiation. It is observed that with increase in irradiation time, the absorbance of Rose Bengal dye decreases and after 8 h irradiation of sunlight it becomes zero.

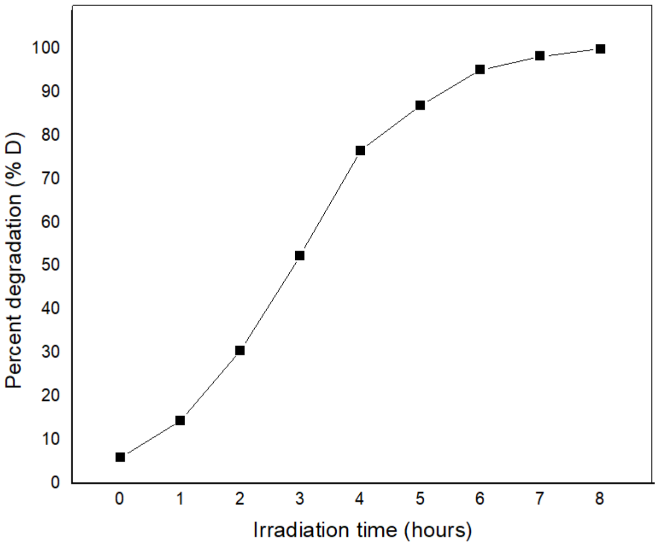

FIG. 11. Variation of percent (%) degradation of Rose Bengal dye over ZnO with irradiation time

3.2.6. Reusability of ZnO catalyst. The stability of ZnO nanoparticle catalyst was also studied. The ZnO materials were recovered from reaction mixture by centrifugation followed by filtration and were reused for 3 times under identical experimental conditions. It is found that even reused ZnO nanoparticles were efficient for the degradation of Rose Bengal and there was negligible change in its photocatalytic activity.

4. Conclusion

In the present research work,

1. Zinc Oxide (ZnO) was successfully synthesized by an efficient mechanochemical method via zinc oxalate dihydrate precursor.
2. Photocatalytic operational parameters for the Rose Bengal dye degradation over ZnO under artificial light illumination were satisfactorily studied and optimized.
3. ZnO was found to be an efficient photocatalyst for degradation of Rose Bengal dye.
4. In dark conditions, ZnO is found to be inactive.
5. Rose Bengal solutions of lower concentration were completely mineralized by photo-degradation on the surface of ZnO.

Acknowledgements

Authors specifically wish to thank PDEA's Annasaheb Waghire College, Otur and Baburaoji Gholap College, Sangvi for offering their continuous and valuable support, in terms of facilities like laboratories for all experimental work, instrumental facilities for the characterization of materials and libraries for the literature review.

References

[1] Mancosu N., Snyder R.L., Kyriakakis G., Spano D. Water Scarcity and Future Challenges for Food Production. *Water*, 2015, 7, P. 975–992.

[2] Ding, Y., Hayes M.J., Widhalm M. Measuring economic impacts of drought: a review and discussion. *Disaster Prevention and Management*, 2011, 20 (4), P. 434–446.

[3] Van Leeuwen C.C.E., Cammeraat E.L.H., de Vente J., Boix-Fayos C. The evolution of soil conservation policies targeting land abandonment and soil erosion in Spain: A review. *Land use policy*, 2019, 83, P. 174–186.

[4] Velayatzadeh M. Introducing the causes, origins and effects of dust in Iran. *J. of Air Pollution and Health*, 2020, 5 (1), P. 63–70.

[5] He B., Cui X., Wang H., Chen A. Drought: The most important physical stress of terrestrial ecosystems. *Acta Ecologica Sinica*, 2014, 34 (4), P. 179–183.

[6] Humphries P., Baldwin D.S. Drought and aquatic ecosystems: an introduction. *Freshwater biology*, 2003, 48 (7), P. 1141–1146.

[7] Bifulco M., Ranieri R. Impact of drought on human health. *European J. of internal medicine*, 2017, 46, e9–e10.

[8] Bellemare M.F. Rising food prices, food price volatility, and social unrest. *American J. of agricultural economics*, 2015, 97 (1), P. 1–21.

[9] Ibelings Bas W., Chorus I. Accumulation of cyanobacterial toxins in freshwater "seafood" and its consequences for public health: a review. *Environmental pollution*, 2007, 150 (1), P. 177–192.

[10] Braun A., Augustynski J., et. al. Photocatalysis for energy and environmental sustainability. *J. Mater. Res.*, 2010, 25 (1), P. 1–2.

[11] Legrini O., Oliveros E., Braun A.M. Photochemical processes for water treatment. *Chemical reviews*, 1993, 93 (2), P. 671–698.

[12] Barka N., Qourzal S., Assabbane A., Ait-Ichou Y. Solar photocatalytic degradation of textile dyes on dynamic pilot plant using supported TiO_2. *Arabian J. for Science and Engineering*, 2010, 35 (2A), 131.

[13] Parsons S., ed. *Advanced oxidation processes for water and wastewater treatment*, IWA publishing, 2004.

[14] Munoz I., Rieradevall J., et al. Environmental assessment of different solar driven advanced oxidation processes. *Solar Energy*, 2005, 79 (4), P. 369–375.

[15] Yu Z., H. Keppner, et al. Photocatalytic discoloration of Methyl Orange on innovative parylene–TiO_2 flexible thin films under simulated sunlight. *Applied Catalysis B: Environmental*, 2008, 79 (1), P. 63–71.

[16] Chan, Samuel Hong Shen, et al. Recent developments of metal oxide semiconductors as photocatalysts in advanced oxidation processes (AOPs) for treatment of dye waste-water. *J. of Chemical Technology & Biotechnology*, 2011, 86 (9), P. 1130–1158.

[17] Mills A., Davies R.H., Worsley D. Water purification by semiconductor photocatalysis. *Chemical Society Reviews*, 1993, 22 (6), P. 417–425.

[18] Rajeshwar K., Osugi M.E., et al. Heterogeneous photocatalytic treatment of organic dyes in air and aqueous media. *J. of photochemistry and photobiology C: photochemistry reviews*, 2008, 9 (4), P. 171–192.

[19] Vidya C., Chandra Prabha M.N., Antony Raj M.A.L. Green mediated synthesis of zinc oxide nanoparticles for the photocatalytic degradation of Rose Bengal dye. *Environmental Nanotechnology, Monitoring & Management*, 2016, 6, P. 134–138.

[20] Mills A., Le Hunte S. An overview of semiconductor photocatalysis. *J. of photochemistry and photobiology A: Chemistry*, 1997, 108 (1), P. 1–35.

[21] Drumond Chequer, Farah M., et al. Genotoxic and mutagenic effects of erythrosine B, a xanthene food dye, on HepG2 cells. *Food and chemical toxicology*, 2012, 50 (10), 3447.

[22] Zhang Huanqiu, Jun Peng, et al. Hybrid microtubes of polyoxometalate and fluorescence dye with tunable photoluminescence. *Chemical communications*, 2012, 48 (37), P. 4462–4464.

[23] Seo, Hyung-Kee, and Hyung-Shik Shin. ”Study on photocatalytic activity of ZnO nanodisks for the degradation of Rhodamine B dye.” Materials Letters 159 (2015): P. 265–268.

[24] Mpountoukas P., Pantazaki A., et al. Cytogenetic evaluation and DNA interaction studies of the food colorants amaranth, erythrosine and tartrazine. *Food and Chemical Toxicology*, 2010, 48 (10), P. 2934–2944.

[25] Ritchie E.E., Princz J.I., Robidoux P.J., Scroggins R.P. Ecotoxicity of xanthene dyes and a non-chlorinated bisphenol in soil. *Chemosphere*, 2013, 90 (7), P. 2129–2135.

[26] Pardeshi S.K., Patil A.B. Effect of morphology and crystallite size on solar photocatalytic activity of zinc oxide synthesized by solution free mechanochemical method. *J. of Molecular Catalysis A: Chemical*, 2009, 308 (1–2), P. 32–40.

[27] Wu L., Yu J.C., Fu X. Characterization and photocatalytic mechanism of nanosized CdS coupled TiO_2 nanocrystals under visible light irradiation. *J. of Molecular Catalysis A: Chemical*, 2006, 244 (1–2), P. 25–32.

[28] JCPDS Card No. 36-1451.

[29] Nafees M., Liaqut W., Ali S., Shafique M.A. Synthesis of ZnO/Al: ZnO nanomaterial: structural and band gap variation in ZnO nanomaterial by Al doping. *Applied Nanoscience*, 2013, 3 (1), P. 49–55.

[30] Aparna P.U., Divya N.K., Pradyumnan P.P. Structural and dielectric studies of Gd doped ZnO nanocrystals at room temperature. *J. of Materials Science and Chemical Engineering*, 2016, 4 (2), P. 79–88.

[31] Behnajady M.A., Modirshahla N., Hamzavi R. Kinetic study on photocatalytic degradation of CI Acid Yellow 23 by ZnO photocatalyst. *J. of hazardous materials*, 2006, 133 (1–3), P. 226–232.

[32] Xia Juan, Anqi Wang, Xiang Liu, Zhongxing Su. Preparation and characterization of bifunctional, Fe_3O_4/ZnO nanocomposites and their use as photocatalysts. *Applied Surface Science*, 2011, 257 (23), P. 9724–9732.

[33] Anandan S., Vinu A., et al. Photocatalytic activity of ZnO impregnated Hß and mechanical mix of ZnO/Hß in the degradation of monocrotophos in aqueous solution. *J. of Molecular Catalysis A: Chemical*, 2006, 256 (1–2), P. 312–320.

[34] Pardeshi S.K., Patil A.B. Solar photocatalytic degradation of resorcinol a model endocrine disrupter in water using zinc oxide. *J. of hazardous materials*, 2009, 163 (1), P. 403–409.

[35] Kaur Japinder, Sonal Singhal. Heterogeneous photocatalytic degradation of rose bengal: effect of operational parameters. *Physica B: Condensed Matter*, 2014, 450, P. 49–53.

NANOSYSTEMS: PHYSICS, CHEMISTRY, MATHEMATICS, 2021, 12 (6), P. 783–791

Study of the resistive switching and electrode degradation in Al/TiO$_2$/FTO thin films upon thermal treatment in reducing atmosphere

G. A. Illarionov[1], D. S. Kolchanov[1], V. V. Chrishtop[1], I. A. Kasatkin[2], A. V. Vinogradov[1], M. I. Morozov[1]

[1]ITMO University, Kronverkskiy prosp., 49, St. Petersburg, 197101, Russia

[2]Saint Petersburg State University, Universitetskaya nab. 7-9, St. Petersburg, 199034, Russia

morozov@scamt-itmo.ru

PACS 81.40.Rs, 73.50.-h **DOI 10.17586/2220-8054-2021-12-6-783-791**

Application of sol-gel derived titania nanoparticles in memristive thin film devices has been a subject of several studies. The reported data on the functional properties and stability of such devices scatter considerably. Meanwhile, the role of post-fabrication treatment, such as annealing in reducing atmosphere, is still poorly investigated for this class of devices. In this study, the effects of thermal annealing in a reducing atmosphere on the resistive switching behavior and the morphological changes of the top electrode during the electroforming process have been systematically addressed for the samples of Al/TiO$_2$/FTO thin film memristors prepared using sol-gel derived titania. Manifestations of several phenomena affecting the functional stability of these thin films, such as electrode delamination and collapse due to formation of gas bubbles, appearance of electrochemical patterns at the electrode surface, and morphological changes induced by the electroforming process have been systematically established in relation with the various conditions of thermal treatment in a reducing atmosphere.

Keywords: TiO$_2$, memristors, electrode degradation.

Received: 25 November 2021

1. Introduction

The field of memristive electronics is one of the promising areas of rapidly developing technologies covering novel types of memory devices and bioinspired computers [1–4]. Memristor is a passive two-terminal element of electric circuit, whose resistance dynamically depends on of the electric current amplitude [5]. This key feature has been proposed for application in the information storage [6,7] or emulation of similar electrical processes in biological synapses [8–10]. The memristive effect occurs in many organic and inorganic nanomaterials including simple oxides of transition metals.

Titanium dioxide has been one of the first and most widely used materials in resistive switching applications. Since the first conceptual implementation of memristive effect in TiO$_2$ thin films [3], this material has been extensively studied regarding both the underlying mechanism of the resistive switching, various applications, as well as technological approaches towards design and fabrication of final devices [11–13]. The frontier research and application of TiO$_2$ memristors concern random-access memory [13–16], neuromorphic computing [3, 17–19], biohybrid interfaces [20–23], and sensors [24–27]. The key advantages of TiO$_2$ thin film memristors include a relatively high resistive switching ratio R$_{OFF}$/R$_{ON}$ (typically, much above 10^2), low threshold voltage (typically, 1-3 volts), and technological versatility of the fabrication methods [12, 13]. Meanwhile, TiO$_2$ memristors are rather inferior to other transition oxide counterparts with respect to the functional endurance that in most reported cases has not exceeded a few hundred cycles [13], though in some episodic studies some higher values above 10^4-10^6 have been reported [28–31]. However, this range is still far below compared to the TaO$_x$ counterparts with endurance typically exceeding 10^9–10^{10} cycles [32, 33]. Another obvious disadvantage of TiO$_2$ based memristor is apparently low reproducibility that manifested itself in an extremely large scattering of the functional properties reported for the films fabricated by similar to each other technological methods and synthesis routes [12, 13].

Recently, several studies have addressed the solution chemistry approaches to synthesize TiO$_2$ nanoparticles along with appropriate deposition methods to fabricate thin film memristors, including spin-coating [34, 35], dip coating [36–38], drop casting [39], or inkjet printing [40, 41]. In contrast to memristive devices produced by the physical deposition techniques, an extremely high scattering of the key memristive properties such as the resistive switching ratio, endurance and retention time have been reported for the devices fabricated using TiO$_2$ nanoparticles obtained by the solution chemistry routes [12]. In these studies, different electrode materials and post-treatment annealing regimes have been used, while the effect of thermal annealing at a reduced oxygen partial pressure on the resistive and resistive switching properties of TiO$_2$ thin film has not been systematically addressed yet. Another critical issue rarely addressed for the memristive devices fabricated using TiO$_2$ nanoparticles is the degradation of the top electrode as the result of electrochemical interaction with the TiO$_2$ adjacent layer under applied external voltage. This includes formation and collapse of oxygen bubbles under the metal layer [42–44] and damages produced by the morphological changes resulting from the electroforming process [45–47].

In this study, we investigate the effect of thermal annealing at various temperatures in Ar atmosphere on the resistive switching manifestation of an Al/TiO_2/FTO thin film memristor fabricated using sol-gel derived TiO_2 nanoparticles deposited onto FTO glass by spin-coating and covered by top Al electrodes using thermal evaporation. Additionally, we address the effect of top electrode degradation as the result of electrochemical interactions occurring during the switching upon various stages of thermal annealing in oxygen reducing atmosphere.

2. Materials and Methods

2.1. Chemicals

Titanium(IV) isopropoxide (97%, Sigma-Aldrich), nitric acid (65%, Sigma-Aldrich), deionized water ($<5\ \mu S\cdot cm^{-1}$), isopropanol ($\geq$99.9%, Vekton), methanol ($\geq$99,8%, Fisher Scientific).

2.2. TiO_2 synthesis

TiO_2 sol was synthesized via sol-gel procedure. Two solutions were prepared. For the first solution 16 mL of titanium isopropoxide and 12 mL of 2-propanol were mixed. For the second solution 0.7 mL of nitric acid was added to 100 mL of water and heated up to 70 °C. After that, the first solution was slowly added to the second one under constant stirring. The resulting mixture was maintained for 1 h at 80 °C then hermetically covered by a film and kept for 5 days under stirring at room temperature.

2.3. TiO_2 ink preparation

The synthesized sol was dried in a vacuum evaporator to form TiO_2 xerogel. Then, TiO_2 ink was obtained by mixing aqueous solution of TiO_2 xerogel (20%) with methanol in a ratio of 1:3.

2.4. Thin film fabrication

Fluorine-doped tin oxide (FTO) glass substrates ($25\times25\times2$ mm, $<10\ \Omega\cdot cm^{-2}$, FTO thickness 950 nm) were treated in an ultrasonic bath for 5 minutes sequentially in 5 solutions: NaOCl, $NaHCO_3$, deionized water, isopropyl alcohol, and acetone, then dried with N_2 flow. The surface hydrophilization was performed in air plasma for 10 minutes using a Femto Low Pressure Plasma System (Diener Electronic GmbH, Germany). After that, one layer of prepared TiO_2 ink was spin coated onto the precleaned and hydrophilized FTO using a spin coater APT Spin – 150i NPP (SPS Europe, France). The coating was performed as one-step procedure with the following parameters: spin speed 2500 rpm, acceleration 350 rpm, time 45 sec. The top Al electrodes were deposited by thermal evaporation in a vacuum chamber.

2.5. Top electrode deposition

Aluminum layer with a thickness of 50 nm was deposited onto TiO_2 layer by thermal evaporation in a vacuum chamber using a mask with circular holes. The surface area of each Al electrode was set to be 5.85 mm^2. The resulting array of the sandwiched TiO_2 layer memristors with the common bottom FTO electrode is illustrated in Fig. 1a. The thickness of the functional TiO_2 layer was evaluated by atomic force microscopy (AFM) using a Solver Next microscope (NT-MDT, Russia). As illustrated in Fig. 1b, the thickness of the TiO_2 layer was estimated to be ca. 60 nm.

2.6. Thermal treatment

After each electrical and microscopical examination, the sample was annealed in Ar for at least 12 h at 250, 350 and 500 °C using a tube furnace LOIP LF-50/500-1200. The ramp rate was set to 3 °C/min.

2.7. Material characterization

Images of the electrode surface were taken using a LOMO Biolam M-1 microscope equipped with a Micrometrics 519CU CMOS 5.0 camera. Scanning electron microscopy (SEM) images were obtained using an electron microscope Tescan Vega 3. Energy dispersive X-ray spectroscopy (EDX) mapping was performed using an X-act Silicon Drift Detector from Oxford Instruments. Phase composition at the film surface was analyzed by the X-ray diffraction (XRD) using a Bruker D8 Discover X-ray diffractometer with filtered parallel beam CuK_α radiation in grazing incidence regime. The current – voltage dependencies were measured using a SubFemtoamp SourceMeter Keithley 6430 controlled by KickStart Instrument Control Software Version 2.0.6 (Tektronix). Voltage was applied with a wire tip connected to the Al top electrode, while another wire was connected to the bottom FTO electrode.

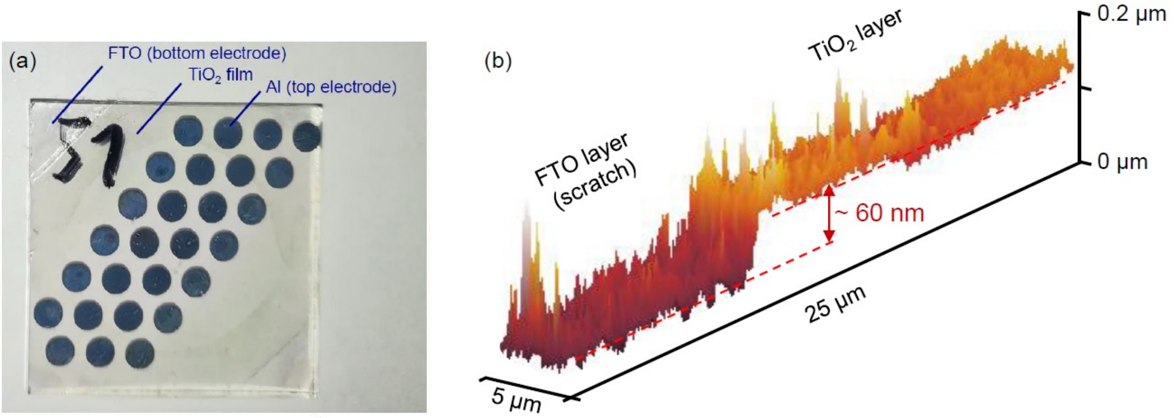

FIG. 1. (a) Experimental sample of Al/TiO$_2$/FTO memristors; (b) AFM characterization of TiO$_2$ layer thickness

3. Results and discussion

In this section we present and discuss the results of electrical characterization of Al/TiO$_2$/FTO thin film memristors along with morphological changes of the top electrode surface before and after several stages of annealing in Ar at 250, 350, and 500 °C, correspondingly.

3.1. Unannealed film

The positive and negative voltage-current curves obtained for an unannealed Al/TiO$_2$/FTO thin film are shown in Fig. 2. The insets depict images of the top electrode surfaces taken after each 20 negative and positive cycles. At negative polarity, no visible degradation was observed for the top Al electrode, while no notable resistive switching has been observed. At positive polarity, the current amplitude has been gradually descending during the cycling, which corresponds to the formation of gas bubbles resulting in partial delamination of the aluminum layer thus reducing the contact area. Similar formation of the gas bubbles was documented in several studies including the cases of SrTiO$_3$ single crystal with Au electrode [42] and Pt-TiO$_2$-Pt thin films fabricated with the sandwiched [43] and planar [44] configurations. The mechanism of the gas bubble formation under the anode was studied in detail [43] and rationalized by the drift of O$_2$- anions towards the positively biased top electrode followed by the discharging with the subsequent formation of O$_2$ gas between TiO$_2$ and the top electrode. Consequently, the drift of oxygen vacancies occurs in the opposite direction [6]. Despite this evidence of the ionic drift manifestation, no filamentary resistive switching was observed in the unannealed thin film.

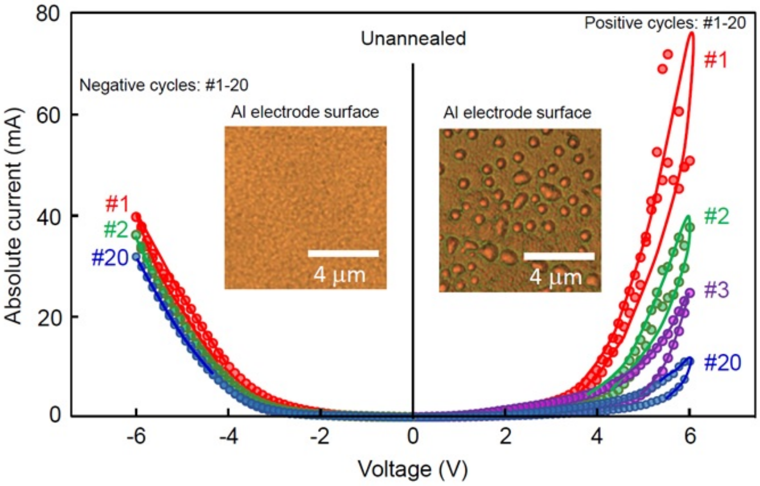

FIG. 2. Positive and negative I-V curves for Al/TiO$_2$/FTO thin film and the effect of positive and negative cycles on the top Al electrode

3.2. Characterization upon annealing at 250 °C in Ar

Fig. 3a depicts the positive and negative voltage - current curves obtained for a sample of Al/TiO_2/FTO thin film annealed in Ar at 250 °C. An appreciably high resistive switching ratio R_{OFF}/R_{ON} above 10^4 was obtained in the sub-switching characterization regime, as illustrated in Fig. 3b.

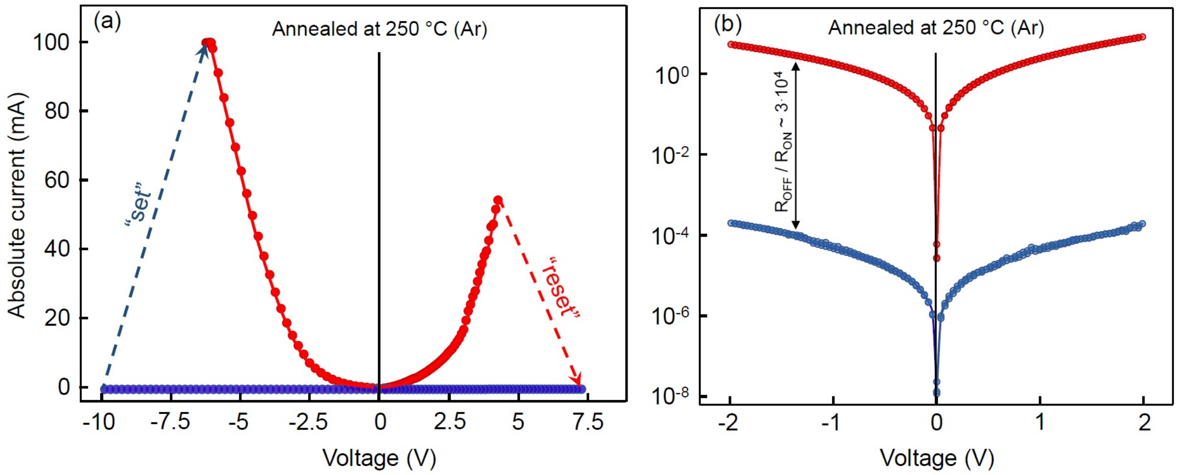

FIG. 3. I-V characterization of Al/TiO_2/FTO thin film annealed in Ar at 250 °C: (a) negative and positive switching curves; (b) sub-switching curves in the "OFF" and "ON" states

The activation of the resistive switching to the "ON" state has been investigated in detail by application of elongated voltage pulses with stepwise changing amplitude, as illustrated in Fig. 4. The primary switching event was observed at voltage pulse amplitude of -6 V (Fig. 4a) upon nearly a minute since the pulse had been applied (Fig. 4b). This observation is in line with a model of the resistive switching mechanism based on filament formation [6, 48, 49]. In contrast, the reverse processes observed upon changing the polarity have demonstrated rather slow dynamics of current relaxation, as shown by the U-I curves 11–13 in Fig. 4b.

Upon several bipolar cycles, the resistive switching in Al/TiO_2/FTO thin film annealed in Ar at 250 °C became unstable. As exemplified in Fig. 5, several set-reset switching fails have been observed at relatively low voltage.

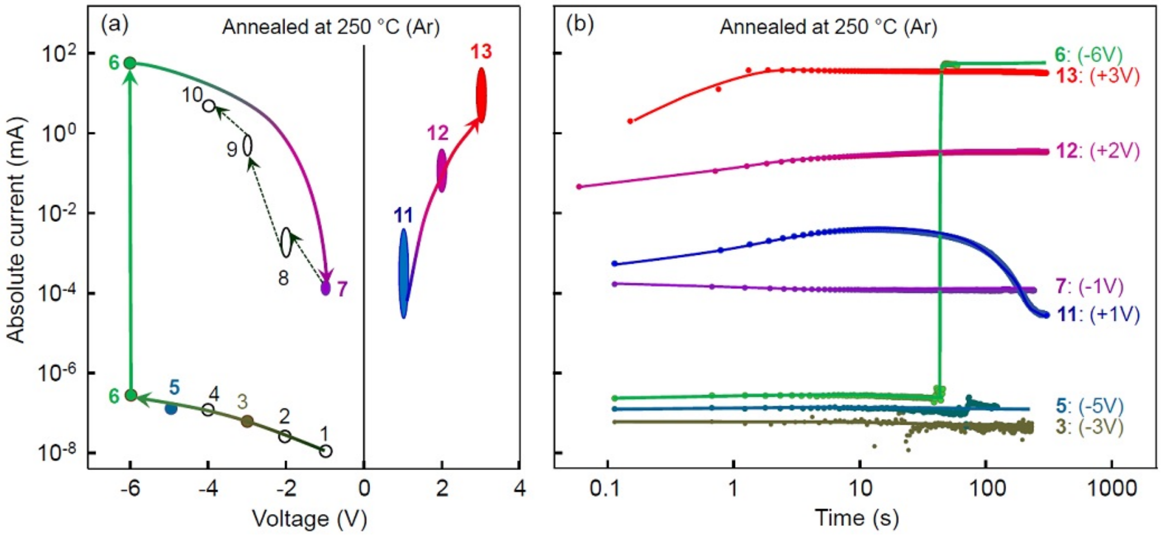

FIG. 4. Electrical switching cycle in Al/TiO_2/FTO thin film annealed in Ar at 250 °C: (a) the resistive switching process measured with elongated voltage pulses; (b) the corresponding current curves as a function of time for the stepwise varying voltage measured for the selected points shown in (a)

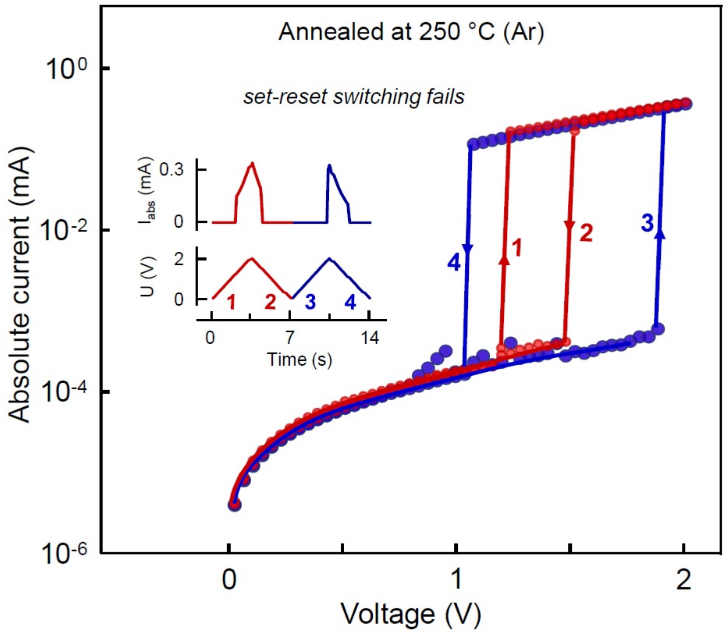

FIG. 5. Instability of resistive switching in Al/TiO$_2$/FTO thin film annealed in Ar at 250 °C. The inset illustrates the corresponding applied voltage pulses and the current response as functions of time

Inferior functional endurance and retention of the resistive switching memory devices based on TiO$_2$ have been reported in several studies, especially those addressing solution chemistry approaches to the synthesis of the primary nanoparticles [12, 13, 50]. The reasons for this phenomenon are still poorly understood. However, one of the known factors affecting the stability of resistive switching is degradation and morphological changes in the electrodes induced by electroforming and switching [51, 52]. The state of the electrode surface in a sample of Al/TiO$_2$/FTO thin film annealed in Ar at 250 °C and subjected to several resistive switching cycles have been observed using optical and scanning electron microscopy with EDX analysis. The results are shown in Fig. 6. The optical microscopy (Fig. 6a) revealed traces of electrochemical patterns that are typical for the aluminum electropolishing process [53, 54]. This suggests that the thermal treatment at 250 °C was not sufficient for complete removal of the acidic substances used for the synthesis of TiO$_2$ nanoparticles. Furthermore, some local delaminated spots of the Al electrode with circular profile evidenced on the SEM microphotograph (Fig. 6b) and EDX aluminum map (Fig. 6c) indicate the formation of gas bubbles with their consequent outbreak through the Al electrode. Thus, the examined thermal treatment was also not sufficient to achieve the concentration of oxygen vacancies in the TiO$_2$ layer at a level required for the resistive switching. For these reasons, further examination was conducted upon thermal treatment in Ar at 350 °C.

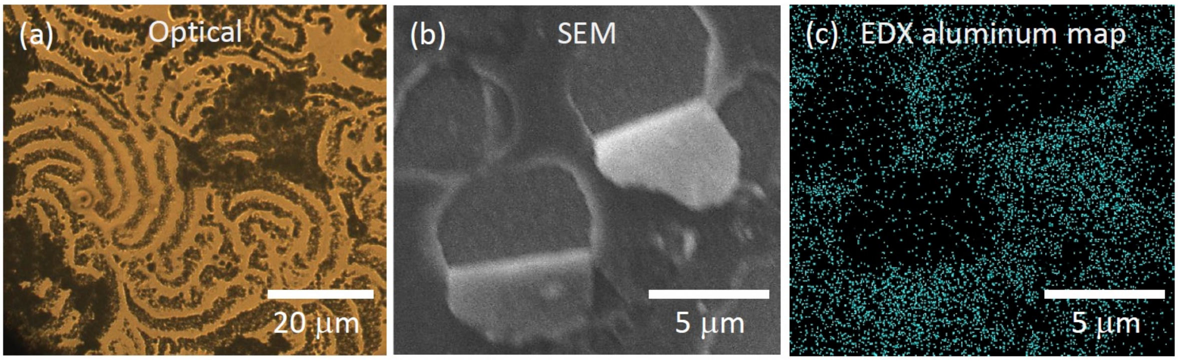

FIG. 6. (a) Optical microscopy, (b) SEM, and (c) EDX (Al mapping) images taken from the top aluminum electrode of the Al/TiO$_2$/FTO thin film sample annealed in Ar at 250 °C and subjected to several bipolar resistive switching cycles

3.3. Characterization upon annealing at 350 °C in Ar

Fig. 7a shows the first three bipolar switching cycles measured in response to the applied voltage pulses with stepwise increasing amplitude for the sample of Al/TiO_2/FTO thin film annealed in Ar at 350 °C. The observed resistive switching ratio R_{OFF}/R_{ON} in this case remained above 10^4, as exemplified in Fig. 7b. However, the instability of the set-reset resistive switching voltage persisted (Fig. 7b). A magnified image of the top electrode surface (Fig. 8) indicates the presence of minor traces of electrochemical pattern, which is in contrast to the case of the sample annealed in Ar at 250 °C. Furthermore, no traces of collapsed gas bubbles were observed. However, the morphological changes induced by the electroforming process persisted in this sample as well. Similar observations were reported in literature for other configurations of TiO_2 memristor, including the cases with Pt electrodes [51,52]. At the next stage, an examination of an Al/TiO_2/FTO thin film was carried out upon thermal annealing in Ar at 500 °C.

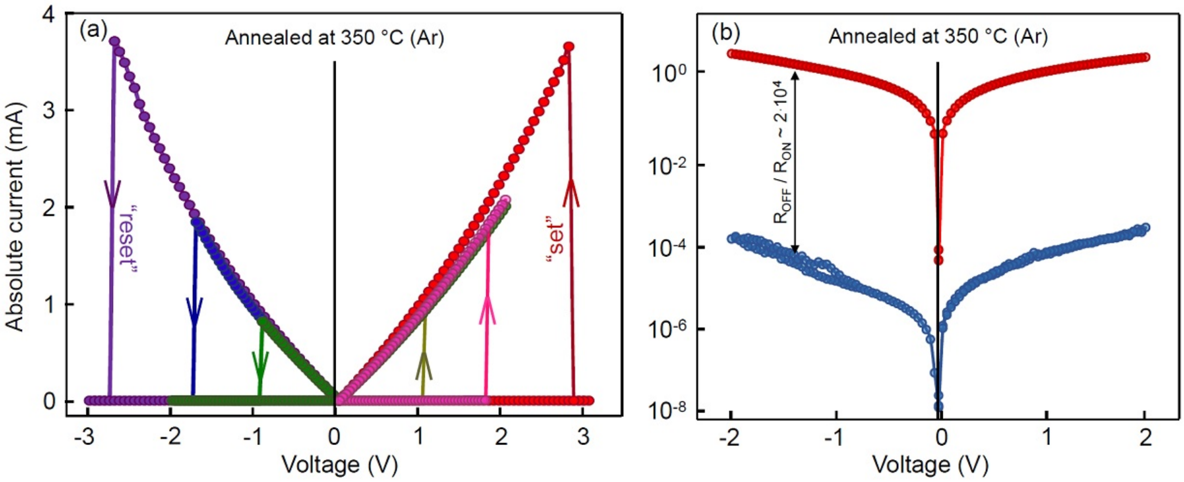

FIG. 7. I-V characterization of Al/TiO_2/FTO memristive film annealed in Ar at 350 °C: (a) The first three bipolar switching cycles measured at stepwise increasing amplitude of the applied voltage pulses; (b) sub-switching curves in the "OFF" and "ON" states

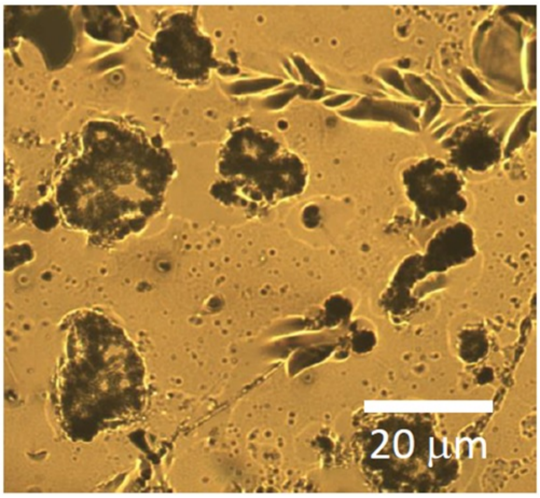

FIG. 8. Optical microphotograph of the top aluminum electrode surface in the Al/TiO_2/FTO thin film sample annealed in Ar at 350 °C

3.4. Characterization upon annealing at 500 °C in Ar

Samples of Al/TiO_2/FTO thin film annealed in Ar at 500 °C have been characterized at various voltage regimes. They showed no reversible switching of the electrical resistance. As exemplified in Fig. 9a, a slow non-filamentary current increase was observed at a rectangular voltage pulses with 4V amplitude, however this process was unstable and followed by a rapid decay (curve # 4). Further increase in the applied voltage have resulted in a similar behavior: a gradual increase in the current response followed by a rapid drop, as illustrated in Fig. 9b.

A microphotograph of the top electrode surface is shown in Fig. 10a. It appears to be rough and porous. An XRD analysis performed at the grazing incidence geometry for the sample of Al/TiO$_2$/FTO thin film annealed in Ar at 500 °C has revealed the formation of a secondary phase, as marked by asterisks in Fig. 10b. This suggests that the applied annealing conditions likely induced an irreversible chemical interaction resulting in the formation of a secondary phase, which seemingly suppresses the resistive switching of the thin film.

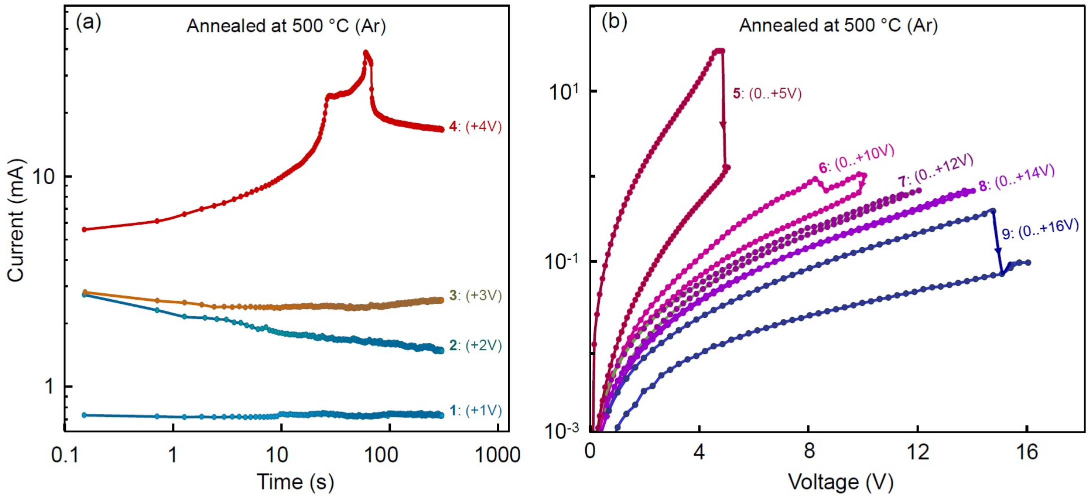

FIG. 9. I-V characterization of Al/TiO$_2$/FTO thin film annealed in Ar at 500 °C. The first nine unipolar cycles with stepwise increasing amplitude of the applied voltage: (a) the first four cycles as a function of time; (b) the next five cycles as I-V hystereses

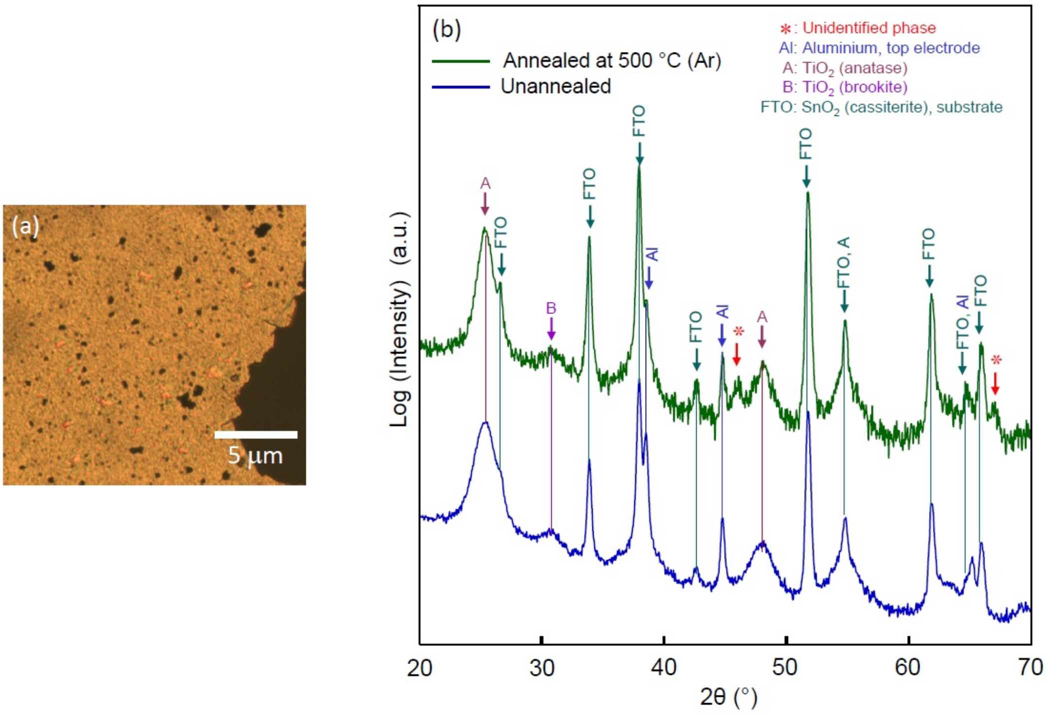

FIG. 10. (a) Optical microphotograph of the top aluminum electrode surface in the Al/TiO$_2$/FTO thin film sample annealed in Ar at 500 °C and (b) XRD spectra taken in the grazing incidence geometry from the same surface and the surface of an unannealed sample

4. Conclusion

In this study, the effect of thermal annealing in a reducing atmosphere on the resistive switching behavior and the morphological changes of the top electrode during the electroforming process have been systematically addressed for samples of Al/TiO_2/FTO thin film memristors prepared using sol-gel derived titania. Manifestations of several phenomena affecting the functional stability of these thin films, such as electrode delamination and collapse due to formation of gas bubbles, appearance of electrochemical patterns on the electrode surface, and morphological changes induced by the electroforming process have been established in relation with the various conditions of thermal treatment in a reducing atmosphere. The temperature limit for the post-fabrication treatment has also been established. Thermal treatment at 500 °C or above was shown to induce irreversible phase transformation due to chemical interaction, despite the treatment being performed in an inert atmosphere.

Acknowledgement

The research has been carried out with financial support from the Russian Science Foundation (Grant No. 19-19-00433).

References

[1] Yang J.J. Strukov D.B., Stewart D.R. Memristive devices for computing. *Nat. Nanotechnol*, 2012, **8**, P. 13–24.

[2] Zidan M.A. The future of electronics based on memristive systems. *Nat. Electron*, 2018, **1**, P. 22–29.

[3] Zhang Y., Wang Z., Zhu J., Yang Y., Rao M., Song W., Zhuo Y., Zhang X, Cui M., Shen L., Huang R., Yang J.J. Brain-inspired computing with memristors: challenges in devices, circuits, and systems. *Appl. Phys. Rev.*, 2020, **7**, P. 011308.

[4] Velichko A., Belyaev M., Boriskov P. A Model of an Oscillatory Neural Network with Multilevel Neurons for Pattern Recognition and Computing. *Electronics*, 2019, **8**(1), P. 75.

[5] Strukov D.B., Snider G.S., Stewart D.R., Williams R.S. The Missing Memristor Found. *Nature*, 2008, **453**(7191), P. 80–83.

[6] Waser R., Dittmann R., Staikov G., Szot K. Redox-Based Resistive Switching Memories – Nanoionic Mechanisms, Prospects, and Challenges. *Adv. Mater.*, 2009, **21**(25-26), P. 2632–2663.

[7] Chua L. Resistance Switching Memories Are Memristors. *Appl. Phys. A*, 2011, **102**(4), P. 765–783.

[8] Chua L.O., Kang S.M. Memristive devices and systems. *Proc. IEEE*, 1976, **64**(2), P. 209–223.

[9] Du C., Ma W., Chang T., Sheridan P., Lu W.D. Biorealistic Implementation of Synaptic Functions with Oxide Memristors through Internal Ionic Dynamics. *Adv. Funct. Mater.*, 2015, **25**(27), P. 4290–4299.

[10] Pickett M.D., Medeiros-Ribeiro G., Williams R.S. A Scalable Neuristor Built with Mott Memristors. *Nat. Mater.*, 2012, **12**(2), P. 114–117.

[11] Yang J.Y., Pickett M.D, Li X., Ohlberg D.A.A., Stewart D.R., Williams S. Memristive switching mechanism for metal/oxide/metal nanodevices. *Nat. Nanotech.* 2008, **3**, P. 429–433.

[12] Illarionov G.A., Morozova S.M., Chrishtop V.V., Einarsrud M.-A., Morozov M.I. Memristive TiO_2: Synthesis, Technologies, and Applications. *Front. Chem.*, 2020, **8**, P. 724.

[13] Acharyya D., Hazra A., Bhattacharyya P. A journey towards reliability improvement of TiO_2 based resistive random-access memory: a review. *Microelectron. Reliab.*, 2014, **54**, P. 541–560.

[14] Xia Q., Robinett W.; W. Cumbie M., Banerjee N., J. Cardinali T., Joshua Yang J., Wu W., Li X., M. Tong W., B. Strukov D., S. Snider G., Medeiros-Ribeiro G., Williams S.R. Memristor?CMOS Hybrid Integrated Circuits for Reconfigurable Logic. *Nano Lett.*, 2009, **9**(10), P. 3640–3645.

[15] Jeong D.S., Thomas R., Katiyar R.S., Scott J.F. Overview on the Resistive Switching in TiO_2 Solid Electrolyte. *Integr. Ferroelectr.*, 2011, **124**(1), P. 87–96.

[16] Zhang F., Gan X., Li X., Wu L., Gao X., Zheng R., He Y., Liu X., Yang R. Realization of Rectifying and Resistive Switching Behaviors of TiO_2 Nanorod Arrays for Nonvolatile Memory. *Electrochem. Solid-State Lett.*, 2011, **14**(10), P. H422.

[17] Xia Q., Yang J.J. Memristive Crossbar Arrays for Brain-Inspired Computing. *Nat. Mater.*, 2019, **18**(4), P. 309–323.

[18] Ryu J.-H., Kim S. Artificial Synaptic Characteristics of TiO_2/HfO_2 Memristor with Self-Rectifying Switching for Brain-Inspired Computing. *Chaos, Solitons and Fractals*, 2020, **140**, P. 110236.

[19] Ismail M., Chand U., Mahata C., Nebhen J., Kim S. Demonstration of Synaptic and Resistive Switching Characteristics in W/TiO_2/HfO_2/TaN Memristor Crossbar Array for Bioinspired Neuromorphic Computing. *J. Mater. Sci. Technol.*, 2022, **96**, P. 94–102.

[20] Fu T., Liu X., Gao H., Ward J.E., Liu X., Yin B., Wang Z., Zhuo Y., Walker D.J.F., Joshua Yang J., Chen J., Lovley D.R., Yao J. Bioinspired Bio-Voltage Memristors. *Nat. Commun.*, 2020, **11**(1), P. 1861.

[21] Roncador A., Jimenez-Garduco A.M., Pasquardini L., Giusti G., Cornella N., Lunelli L., Potrich C., Bartali R., Aversa L., Verucchi R., Serra M.D., Caponi S., Iannotta S., Macchi P., Musio C. Primary Cortical Neurons on PMCS TiO_2 Films towards Bio-Hybrid Memristive Device: A Morpho-Functional Study. *Biophys. Chem.*, 2017, **229**, P. 115–122.

[22] Gupta I., Serb A., Khiat A., Zeitler R., Vassanelli S., Prodromakis T. Real-Time Encoding and Compression of Neuronal Spikes by Metal-Oxide Memristors. *Nat. Commun.*, 2016, **7**, P. 12805.

[23] Serb A., Corna A., George R., Khiat A., Rocchi F., Reato M., Maschietto M., Mayr C., Indiveri G., Vassanelli S., Prodromakis T. Memristive Synapses Connect Brain and Silicon Spiking Neurons. *Sci. Rep.*, 2020, **10**(1).

[24] Vidiš M., Plecenik T., Movško M., Tomavšec S., Roch T., Satrapinskyy L., Gran?i? B., Plecenik A. Gasistor: A Memristor Based Gas-Triggered Switch and Gas Sensor with Memory. *Appl. Phys. Lett.*, 2019, **115**(9), P. 93504.

[25] Sahu D.P., Jammalamadaka S.N. Detection of Bovine Serum Albumin Using Hybrid TiO_2 + Graphene Oxide Based Bio – Resistive Random Access Memory Device. *Sci. Rep.*, 2019, **9**(1), P. 16141.

[26] Haidry A.A., Ebach-Stahl A., Saruhan B. Effect of Pt/TiO_2 Interface on Room Temperature Hydrogen Sensing Performance of Memristor Type Pt/TiO_2/Pt Structure. *Sensors Actuators B Chem.*, 2017, **253**, P. 1043–1054.

[27] Vilmi P., Nelo M., Voutilainen J.-V., Palosaari J., Pörhönen J., Tuukkanen S., Jantunen H., Juuti J., Fabritius T. Fully Printed Memristors for a Self-Sustainable Recorder of Mechanical Energy. *Flex. Print. Electron.*, 2016, **1**(2), P. 25002.

[28] Senthilkumar V., Kathalingam A., Kannan V., Rhee J.-K. Observation of Multi-Conductance State in Solution Processed Al/a-TiO$_2$/ITO Memory Device. *Microelectron. Eng.*, 2012, **98**, P. 97–101.

[29] Yoshida C., Tsunoda K., Noshiro H., Sugiyama Y. High Speed Resistive Switching in Pt/TiO$_2$/TiN Film for Nonvolatile Memory Application. *Appl. Phys. Lett.*, 2007, **91** (22), P. 223510.

[30] Park J., Jung S., Lee J., Lee W., Kim S., Shin J., Hwang H. Resistive Switching Characteristics of Ultra-Thin TiOx. *Microelectron. Eng.* 2011, **88**(7), P. 1136–1139.

[31] Do Y.H., Kwak J.S., Hong J.P., Jung K., Im H. Al Electrode Dependent Transition to Bipolar Resistive Switching Characteristics in Pure TiO$_2$ Films. *J. Appl. Phys.*, 2008, **104**(11), P. 114512.

[32] Wei Z., Kanzawa Y., Arita K., Katoh Y., Kawai K., Muraoka S., Mitani S., Fujii S., Katayama K., Iijima M., Mikawa T., Ninomiya T., Miyanaga R., Kawashima Y., Tsuji K., Himeno A., Okada T., Azuma R., Shimakawa K., Sugaya H., Takagi T., Yasuhara R., Horiba K., Kumigashira H., Oshima M. Highly Reliable TaOx ReRAM and Direct Evidence of Redox Reaction Mechanism. In 2008 IEEE International Electron Devices Meeting; 2008, P. 1–4.

[33] Yang J.J., Zhang M.-X., Strachan J.P., Miao F., Pickett M.D., Kelley R.D., Medeiros-Ribeiro G., Williams R.S. High Switching Endurance in TaOx Memristive Devices. *Appl. Phys. Lett.*, 2010, **97**(23), P. 232102.

[34] Tao D.W., Chen J.B., Jiang Z.J., Qi B.J., Zhang K., Wang C.W. Making reversible transformation from electronic to ionic resistive switching possible by applied electric field in an asymmetrical Al/TiO$_2$/FTO nanostructure. *Appl. Surf. Sci.*, 2020, **502**, P. 144124.

[35] Hu L., Han W., Wang H. Resistive switching and synaptic learning performance of a TiO$_2$ thin film based device prepared by sol-gel and spin coating techniques. *Nanotechnology*, 2020, **31**, P. 155202.

[36] Dai Y., Bao W., Hu L., Liu C., Yan X., Chen L., et al. Forming free and ultralow-power erase operation in atomically crystal TiO$_2$ resistive switching. *2D Materials*, 2020, **4**, P. 025012.

[37] Xiao M., Musselman K.P., Duley W.W., Zhou N.Y. Resistive switching memory of TiO$_2$ nanowire networks grown on Ti foil by a single hydrothermal method. *Nano-Micro Lett.*, 2017, **9**, P. 15.

[38] Dongale T.D., Shinde S.S., Kamat R.K., Rajpure K.Y. Nanostructured TiO$_2$ thin film memristor using hydrothermal process. *J. Alloy. Compounds.*, 2014, **593**, P. 267–270.

[39] Abunahla H., Mohammad B., Mahmoud L., Darweesh M., Alhawari M., Jaoude M.A., et al. Memsens: memristor-based radiation sensor. *IEEE Sens. J.*, 2018, **18**, P. 3198–3205.

[40] Illarionov G.A., Kolchanov D.S., Mukhin I.S., Kuchur O.A., Zhukov M.V., Sergeeva E., et al. Inkjet assisted fabrication of planar biocompatible memristors. *RSC Adv.*, 2019, **9**, P. 35998–36004.

[41] Vilmi P., Nelo M., Voutilainen J.V., Palosaari J., Pörhönen J., Tuukkanen S., et al. Fully printed memristors for a self-sustainable recorder of mechanical energy. *Flex. Print. Electron.*, 2016, **1**, P. 025002.

[42] Szot K., Speier W., Bihlmayer G., Waser R. Switching the electrical resistance of individual dislocations in single-crystalline SrTiO$_3$. *Nature Mater.*, 2006, **5**(4), P. 312–320.

[43] Yang J., Miao F., Pickett M.D., Ohlberg D.A.A., Stewart D.R., Lau C.N., Williams R.S. The mechanism of electroforming of metal oxide memristive switches. *Nanotechnology*, 2009, **20**(21), P. 215201.

[44] Jang M.H., Agarwal R., Nukala P., Choi D., Johnson A.T.C., Chen I.-W., Agarwal R. Observing Oxygen Vacancy Driven Electroforming in Pt-TiO$_2$-Pt Device via Strong Metal Support Interaction. *Nano Lett.*, 2016, **16**(4), P. 2139–2144.

[45] Münstermann R., Yang J.J., Strachan J.P., Medeiros-Ribeiro G., Dittmann R., Waser R. Morphological and electrical changes in TiO$_2$ memristive devices induced by electroforming and switching. *Physica Status Solidi (RRL) - Rapid Research Letters*, 2010, **4**(1-2), P. 16–18.

[46] Prusakova V., Dire S., Collini C., Pasquardini L., Vanzetti L., Resta G., Pederzolli C., Lorenzelli L. Optimisation and Memristive Response of Sol-Gel Derived TiO$_2$ thin films. In Proc. XVIII AISEM Annual Conference. AISEM 2015, IEEE Inc. 2015.

[47] Schroeder H., Jeong D.S. Resistive switching in a Pt/TiO$_2$/Pt thin film stack – a candidate for a non-volatile ReRAM. *Microelectronic Engineering*, 2007, **84**(9-10), P. 1982–1985.

[48] Waser R., Aono M. Nanoionics-Based Resistive Switching Memories. *Nanosci. Technol. A Collect. Rev. from Nat. Journals*, 2009, P. 158–165.

[49] Kwon D.-H., Lee S., Kang C.S., Choi Y.S., Kang S.J., Cho H.L., Sohn W., Jo J., Lee S.-Y., Oh K.H., Noh T.W., De Souza R.A., Martin M., Kim M. Unraveling the Origin and Mechanism of Nanofilament Formation in Polycrystalline SrTiO$_3$ Resistive Switching Memories. *Adv. Mater.*, 2019, **31**(28), P. 1901322.

[50] Kim K.M., Choi B.J., Koo B.W., Choi S., Jeong D.S., Hwang C.S. Resistive Switching in Pt/Al$_2$O$_3$/TiO$_2$/Ru Stacked Structures. Electrochem. *Solid-State Lett.*, 2006, **9**(12), P. G343.

[51] Schroeder H., Jeong D.S. Resistive switching in a Pt/TiO$_2$/Pt thin film stack – a candidate for a non-volatile ReRAM. *Microelectron. Eng.*, 2007, **84**, P. 1982.

[52] Münstermann R., Yang J.J., Strachan J.P., Medeiros-Ribeiro G., Dittmann R. and Waser R. Morphological and electrical changes in TiO$_2$ memristive devices induced by electroforming and switching. *phys. stat. sol. (RRL)*, 2010, **4**, P. 16–18.

[53] Yuzhakov V., Chang H.-C., Miller A. Pattern Formation during Electropolishing. *Phys. Rev. B*, 1997, **56**, P. 12608–12624.

[54] Yuzhakov V.V., Takhistov P.V., Miller A.E., Chang H.-C. Pattern Selection during Electropolishing Due to Double-Layer Effects. Chaos Interdiscip. *J. Nonlinear Sci.*, 1999, **9**(1), P. 62–77.

NANOSYSTEMS: PHYSICS, CHEMISTRY, MATHEMATICS, 2021, 12 (6), P. 792–798

Effect of fuel type on solution combustion synthesis and photocatalytic activity of $NiFe_2O_4$ nanopowders

K. D. Martinson[1], V. E. Belyak[2], D. D. Sakhno[2],
N. V. Kiryanov[2], M. I. Chebanenko[1], V. I. Popkov[1]

[1]Ioffe Institute, St. Petersburg, 194021, Russia

[2]Saint Petersburg State Institute of Technology, 26 Moskovsky prospect, St. Petersburg, 190013, Russia

martinsonkirill@mail.ru

PACS 61.46.+w, 75.50.Bb, 75.60.-d **DOI 10.17586/2220-8054-2021-12-6-792-798**

Nickel ferrite nanopowders were obtained under conditions of solution combustion with the addition of various types of organic fuels (glycine, ascorbic acid, oxalic acid, and malic acid) and studied as photocatalysts in the photodegradation of methylene blue. Photocatalytic measurements were carried out under the action of visible light in model dye solutions. The highest photocatalytic activity was found in the case of a sample synthesized using malic acid as a fuel and in which the largest specific surface area (128.1 m^2/g) and the smallest particle size (18 nm) were observed. The obtained dependences of the photocatalytic activity of the synthesized samples demonstrate its strong dependence on morphological and structural parameters. Thus, with an increase in the particle size and a decrease in the specific surface area, a decrease in the efficiency of a photocatalyst based on nickel ferrite is observed. In addition, the use of various types of fuels made it possible to obtain aggregates of various shapes and sizes up to several tens of micrometers. The resulting rate constants were established to vary from 0.00756 to 0.00867 min^{-1}.

Keywords: nickel ferrite, solution combustion synthesis, nanocrystals, photocatalysts, methylene blue.

Received: 6 September 2021

Revised: 1 December 2021

1. Introduction

In recent years, a large amount of research has been directed to the study of ferrites of various structures and compositions due to the combination of their unique magnetic and electromagnetic properties [1–3]. Thus, classical spinel ferrites are widely used in various fields of production of electrical equipment [4], magnetic storage media [5], and sensors [6]. In addition, to date, new areas of application of this type of materials have begun to appear, related to medicine, catalysis, biotechnology, etc. [7–9]. Special attention is paid to using ferrites as photocatalysts in various reactions of photodegradation under visible light [10, 11] due to the possibility of their magnetic separation caused by pronounced ferrimagnetic behavior [12]. The importance of these processes lies in the possibility of removing various types of organic pollutants from natural or industrial water sources and converting solar energy into chemical energy [13]. Most often, single-component semiconductors or conductors based on heterostructures such as zinc and titanium oxides together with bismuth oxide are used as materials for photocatalysis [14–16].

Among all the variety of spinel ferrites, nickel ferrite stands out, which has pronounced photocatalytic properties [17, 18]. The functional properties of $NiFe_2O_4$ primarily depend on the features of its crystal structure. Nickel ferrite belongs to the class of inverted spinels and its general structure can be written as follows: $([Fe^{3+}]_A[Ni^{2+},Fe^{3+}]_B)_2O_4$. It is known that, depending on the synthesis conditions, Ni^{2+} cations can be located in both tetrahedral and octahedral positions, thereby changing the cation distribution [19]. This, in turn, can significantly affect both the magnetic and photocatalytic properties of the obtained samples [20]. To date, a large number of works have been published in which nickel ferrite nanoparticles were synthesized by sol-gel method [21], hydrothermal method [22], solution combustion method [23], mechanochemical synthesis [24], etc. A distinctive feature of the above methods is the ability to carry out the targeted synthesis of nanostructures with controlled particle size and shape as well as morphological and structural features [25]. Different varieties of solution combustion methods stand out, which, due to their simplicity [26] and the possibility of industrial scaling [27], are one of the most popular methods for obtaining nanostructured spinel ferrites of various compositions [28]. An important property of combustion methods is the large number of synthesis parameters, the variation of which makes it possible to change the structural and functional characteristics of the resulting powders across a wide range of values. In addition, this synthesis method is capable of providing the obtained products in high purity [29].

One of the key parameters of the solution combustion synthesis is the choice of organic fuel acting as both a chelating agent and a resource that ensures the course of the autoignition process. At present, a large number of various organic substances are known that can act as a fuel, among which glycine, ascorbic, oxalic, and malic acids are distinguished [30]. Each of these compounds has its effect on the initial reaction solution and provides different values of the crystallinity degree and particle size of the synthesized product. It is known that for catalysts and photocatalysts, morphological features are especially important, including the values of specific surface area and average particle size, on which their functional properties largely depend [31]. Often, within the framework of the classical single-phase method of solution combustion, even due to the selection of various types of organic fuels, it is difficult to obtain particles with a size less than 15–20 nm and a specific surface area of more than 40–50 m^2/g. To solve this problem, the authors of this work proposed a two-stage synthesis technique based on thermal treatment of X-ray amorphous combustion products, which consists in the synthesis of the initial powder with a significant lack of fuel and further mild heat treatment at 500–700 °C. This technique has been repeatedly and successfully used to synthesize many systems of REE orthoferrites and spinel ferrites and has shown its high efficiency, including for the production of thermocatalytic and photocatalytic materials [32–34].

Therefore, the presented work is devoted to the study of the photocatalytic activity of pure nickel ferrites synthesized by the solution combustion method with the addition of various types of organic fuels (with their significant deficiency) and heat-treated at 600 °C. All synthesized samples were investigated by XRD, SEM, EDX, and ASA methods, and their photocatalytic activity was tested using the model photodegradation of methylene blue.

2. Experimental

The following compounds were chosen as the initial reagents for the synthesis: $Ni(NO_3)_2{\cdot}6H_2O$ (puriss., NevaReactiv), $Fe(NO_3)_3{\cdot}9H_2O$ (puriss., NevaReactiv), CH_2NH_2COOH (puriss., NevaReactiv), $C_6H_8O_6$ (puriss., NevaReactiv), $C_2H_2O_4$ (puriss., NevaReactiv) and $C_4H_6O_5$ (puriss., NevaReactiv). The starting reagents were taken following the reaction of the formation of the final product. Organic fuels were utilized in a 2.5-fold excess compared to reaction stoichiometry to obtain a completely X-ray amorphous powder.

The reaction solution was prepared by dissolving the reagents in 50 ml of distilled water with constant mechanical stirring and heating to 25 °C. To prevent the hydroxide precipitation of transition metals, the solution was acidified with a small amount of 3M HNO_3. After complete dissolution of the initial reagents, the solution obtained in this way was placed on a hot plate until the water was completely removed. After reaching the autoignition point, abundant evolution of gaseous reaction products and the formation of a brown solid product were observed. The synthesized powder was mechanically ground and thermally treated aerobically at 600 °C for 6 hours to remove unreacted organics and form a crystalline phase. The synthesis procedure is described in more detail in [35].

The obtained $NiFe_2O_4$ nanopowders were analyzed by powder X-ray diffractometry, scanning electron microscopy, energy-dispersive spectroscopy, and adsorption-structural analysis. Powder X-ray diffractometry was performed using a Rigaku SmartLab 3 diffractometer using the Rigaku SmartLab Studio II software package and an ICDD PDF 2 powder database. Scanning electron microscopy and energy dispersive spectroscopy were performed using a Tescan Vega 3 SBH instrument equipped with an Oxford INCX X-ray spectral microanalysis attachment. The adsorption-structural analysis was carried out using a Micromeritics ASAP 2020 instrument. Spectrophotometric measurements were carried out using a Shimadzu UV-1800 spectrophotometer. Methylene blue was chosen as a model dye. The 25 ppm dye stock solution was prepared in 50 ml of distilled water. Photocatalytic tests were carried out by adding a single number of synthesized powders to dye solutions and spectrophotometric analysis of a 5 ml sample in 10-minute steps.

3. Results and discussion

Figure 1 shows diffraction patterns of nickel ferrite samples synthesized by the solution combustion method with the addition of various types of organic fuels (glycine, ascorbic acid, oxalic acid, and malic acid). The data obtained indicate that in all synthesized samples, a pure phase of nickel ferrite is observed. According to the Scherrer formula, the average crystallite size of the synthesized ferrites was calculated, which ranged from 18 to 27 nm. The smallest size is observed in the case of the sample synthesized with the addition of malic acid (18 nm), while the largest is in the sample obtained using glycine (27 nm). It should be noted that the samples synthesized with the addition of oxalic acid and ascorbic acid had an average crystallite size close to that of malic acid, which is 20 and 21 nm, respectively. The absence of visible displacements of the main diffraction maxima and the equality of the unit cell parameters of all synthesized powders (8.338(5)-8.339(1) Å) make it possible to assert that their crystal structure is identical.

The elemental analysis and morphology of the synthesized $NiFe_2O_4$ samples were studied by energy dispersive analysis and scanning electron microscopy (SEM). SEM micrographs of the samples are shown in Fig. 2.

According to EDX data, all the obtained powders correspond to the calculated composition within the error of the determination method (Fe:Ni = 50:50 at. %). According to the obtained micrographs, the morphology of nickel ferrite changes significantly depending on the type of fuel used. So, in the case of glycine, large aggregates with a size of

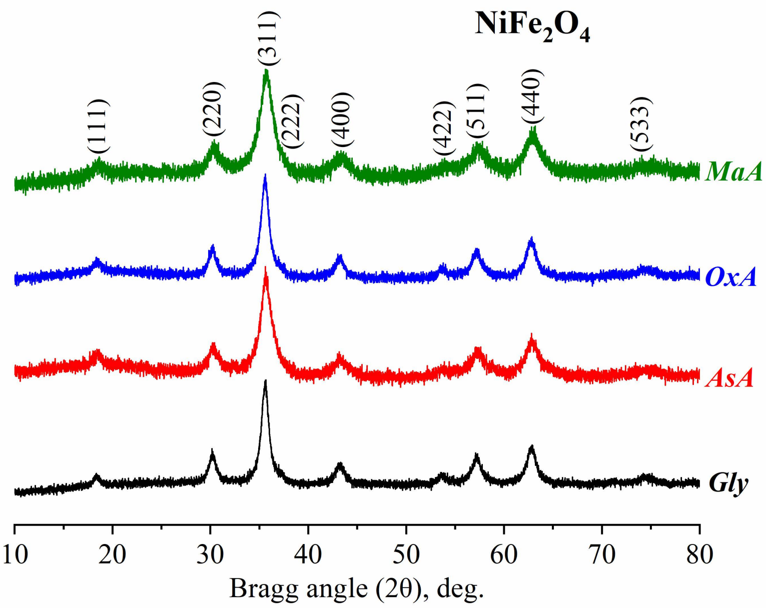

FIG. 1. PXRD patterns of the NiFe$_2$O$_4$ synthesized by the solution combustion method using glycine (Gly), ascorbic acid (AsA), oxalic acid (OxA), and malic acid (MaA)

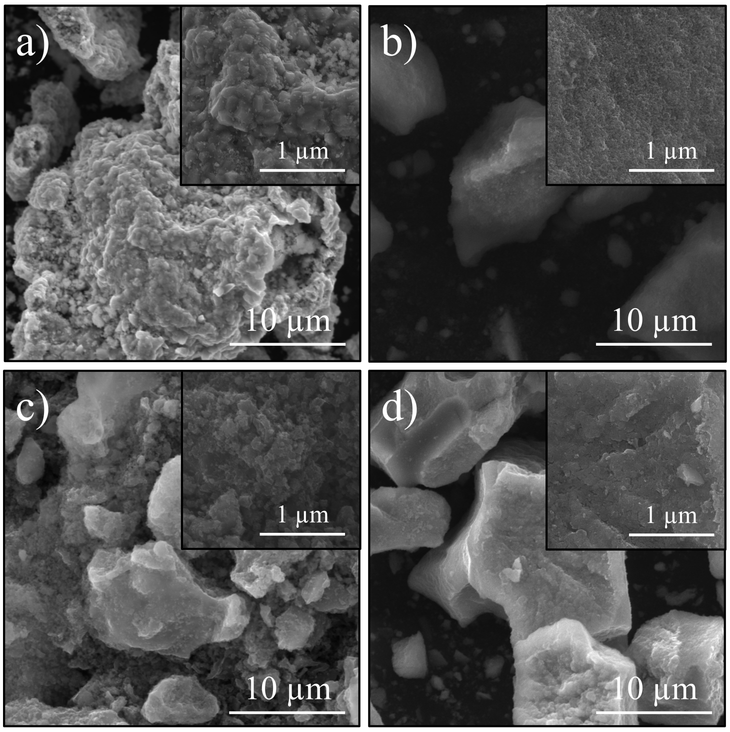

FIG. 2. SEM images of the NiFe$_2$O$_4$ nanopowders synthesized using solution combustion and different fuels – glycine (a), ascorbic acid (b), oxalic acid (c), and malic acid (d)

10–20 microns are formed, consisting of well-sintered particles of submicron and nanometer sizes with a pronounced shape. In turn, the rest of the samples consist of particles of a much smaller size and have aggregates of a different shape and smaller size. An exception is a sample obtained with ascorbic acid, which has individual aggregates up to 35–40 microns in diameter, which, however, consist of particles of much smaller size than in the case of glycine.

The specific surface area of the synthesized powders was determined according to the data of low-temperature sorption-desorption of nitrogen, the results of which are shown in Fig. 3. It follows from the obtained data that all isotherms correspond to IV-type with hysteresis loops belonging to the H3-type according to the IUPAC classification. This appearance of the isotherms allows us to conclude that the obtained samples are highly porous, which is also confirmed by the data of scanning electron microscopy.

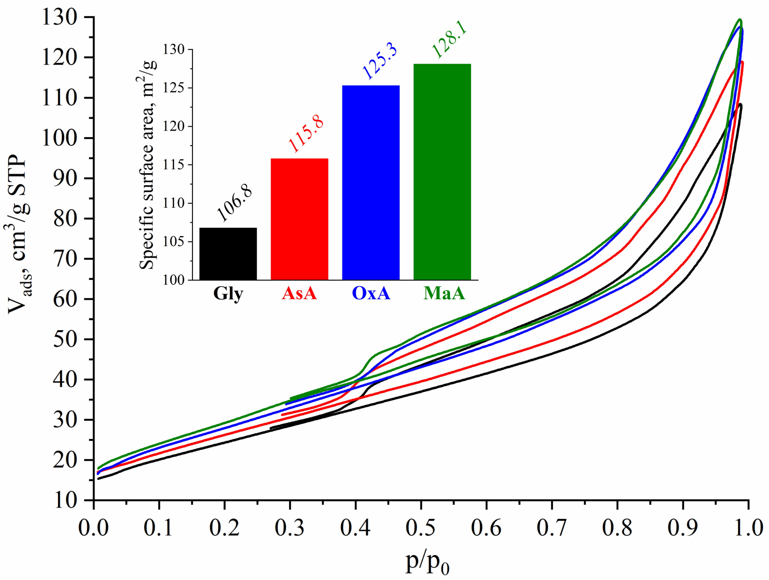

FIG. 3. Low-temperature nitrogen adsorption-desorption isotherms of synthesized nickel ferrite

The specific surface area calculated using the BET model was from 106.8 to 128.1 m^2/g, depending on the composition of the initial reaction medium. The smallest values were found in the case of nickel ferrite synthesized under the conditions of glycine-nitrate combustion, which agrees with the data of average crystallite size (the largest average crystallite size was observed for this sample). The most developed morphology and high specific surface area were observed for the samples synthesized with the addition of malic and oxalic acid (128.1 and 125.3 m^2/g, respectively). It should be noted that this regularity is also explained by the average crystallite size, which reached the smallest values in these two cases. A slight decrease in the specific surface area for a sample burned in the presence of ascorbic acid is explained by the peculiarity of its morphology and the presence of large aggregates up to 40 μm in size in its composition (Fig. 2b).

Photocatalytic reactions involving nickel ferrite are described in detail in the literature. Excited electrons present in the valence region pass into the conduction band, thus forming radicals of the O^{2-} type due to interaction with O_2 molecules. At the same time, water molecules can react with the formed vacant holes in the valence band and form hydroxyl radicals of the ·OH type having high activity and capable of adsorbing various organic pollutants on their surface. In this work, methylene blue was chosen as a model dye to evaluate the photocatalytic activity of nickel ferrite nanopowders.

Figure 4 show the raw results of photocatalytic tests of the synthesized samples. According to the data obtained, one absorption peak of the dye at 660 nm was observed in all samples. With the inclusion of UV light, the peaks under the action of the present catalysts began to gradually decrease, which confirms the photocatalytic activity of all synthesized powders. The most intense decrease was observed in the initial period of UV treatment (transition from 0 to 10 minutes). Then, the decrease in the peaks slowed down, which is explained by the attainment of equilibrium and the peculiarity of the filling of active centers on the surface of the photocatalysts.

The percentage of decomposition of dyes ranged from 82.3 to 86.4 %, depending on the type of fossil fuel used to synthesize nickel ferrite nanoparticles (Fig. 5). The highest values were observed in samples obtained using malic acid and oxalic acid due to the high specific surface area and small particle size. In turn, the sample synthesized with glycine showed the worst indicators of photocatalytic activity, which, nevertheless, remained at a sufficiently high

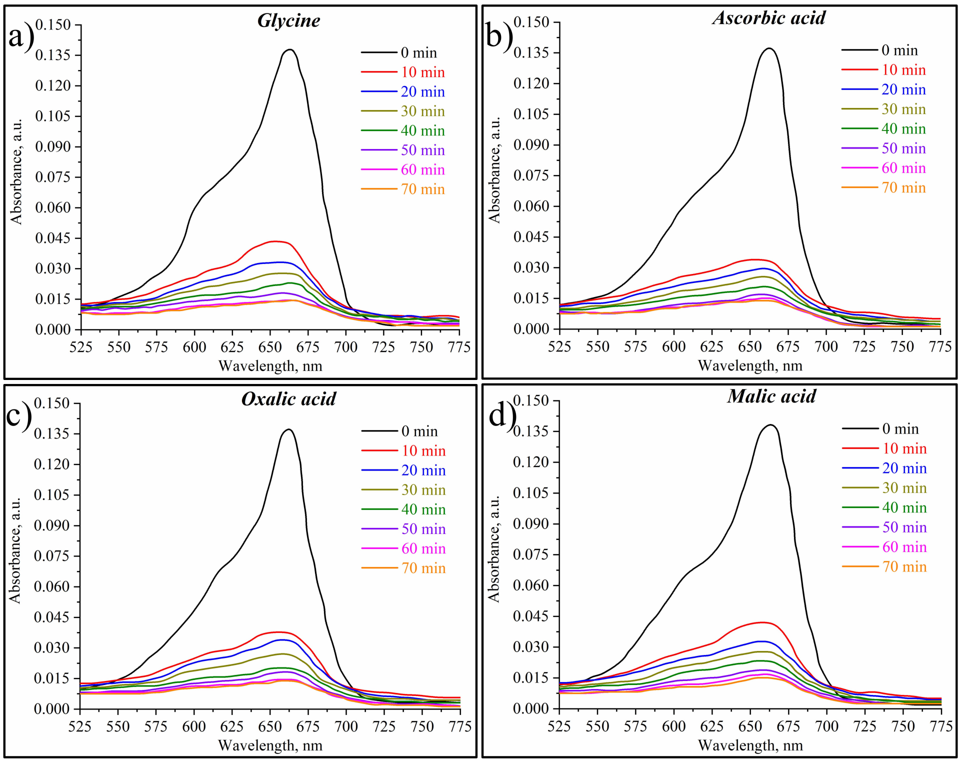

FIG. 4. Photodegradation of methylene blue over $NiFe_2O_4$ samples synthesized using: glycine (a), ascorbic acid (b), oxalic acid (c), and malic acid (d)

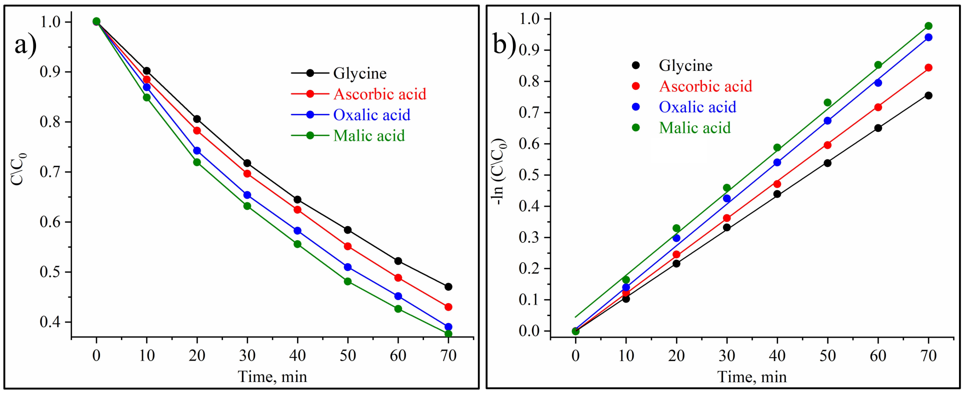

FIG. 5. Initial (a) and logarithmic (b) kinetic curves of methylene blue photodegradation over $NiFe_2O_4$ samples synthesized using different fuels

level. The band gap was determined by the diffusion reflectance spectroscopy and it turned out to be identical for all synthesized samples (2.31 eV). The obtained values of the band gap are in good agreement with the literature [36].

The calculation of the pseudo-first-order rate constant (Fig. 6) showed that its highest values are achieved for the samples obtained under combustion conditions with the addition of malic acid (0.00867 min^{-1}), while the smallest values are observed for the sample synthesized with glycine (0.00756 min^{-1}). The obtained data are in good agreement with the data on the average crystallite size and specific surface area presented earlier and confirm that the samples synthesized with the addition of oxalic and malic acids are the most promising as photocatalysts.

4. Conclusion

Thus, in this work, nanostructured nickel ferrites were obtained using a solution combustion technique and various types of organic fuels (glycine, ascorbic acid, oxalic acid, malic acid). It was shown that the morphology significantly changes depending on the composition of the initial reaction medium and can correspond to aggregates in the range of

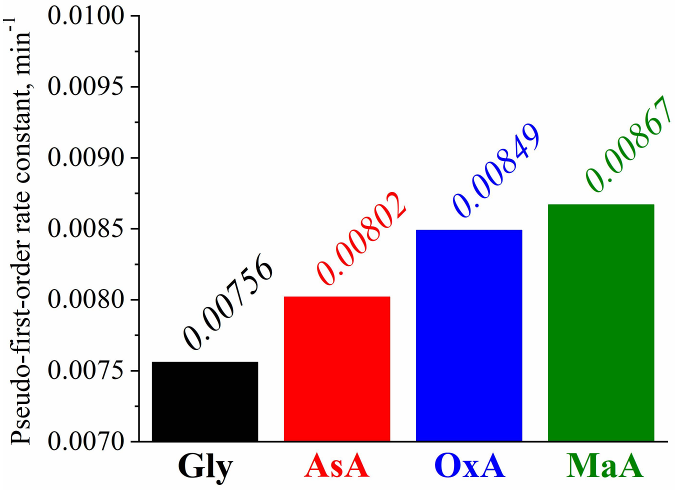

FIG. 6. Pseudo-first-order rate constant of nickel ferrite samples synthesized using glycine (Gly), ascorbic acid (AsA), oxalic acid (OxA), and malic acid (MaA)

values from 5 to 40 μm. The highest specific surface area and the smallest particle size were found in samples obtained using oxalic acid and malic acid. Analysis of photocatalytic activity showed high efficiency of all synthesized samples in photodegradation of methylene blue reactions.

References

[1] Kurian M., Thankachan S., Structural diversity and applications of spinel ferrite core-shell nanostructures – a review. *Open Ceramics*, 2021, **8**, P. 100179.

[2] Ranga R., Kumar A, Kumari P, Singh P., Madaan V., Kumar K., Ferrite application as an electrochemical sensor: a review. *Materials Characterization*, 2021, **178**, P. 111269.

[3] Houbi A., Aldashevich Z.A., Atassi Y., Telmanovna Z.B., Saule M., Kubanych K., Microwave absorbing properties of ferrites and their composites: a review. *Journal of Magnetism and Magnetic Materials*, 2021, **529**, P. 167839.

[4] Almessiere M.A., Slimani Y., Trukhanov A.V., Sadaqat A., Korkmaz A.D., Algarou N.A., Aydin H., Baykal A., Toprak M.S., Review on functional bi-component nanocomposites based on hard/soft ferrites: structural, magnetic, electric and microwave absorption properties. *Nano-Structures and Nano-Objects*, 2021, **26**, P. 100728.

[5] Harris V.G., Geiler A., Chen Y., Yoon S.D., Wu M., Yang A., Chen Z., He P., Parimi P.V., Zuo X., Patton C.E., Abe M., Acher O., Vittoria C., Recent advances in processing and applications of microwave ferrites. *Journal of Magnetism and Magnetic Materials*, 2009, **321**, P. 2035–2047.

[6] Petrila I., Tudorache F., Effects of sintering temperature on the microstructure, electrical and magnetic characteristics of copper-zinc spinel ferrite with possibility use as humidity sensors. *Sensors and Actuators A: Physical*, 2021, **332**, P. 113060.

[7] Rana G., Dhiman P., Kumar A., Vo D.-V. N., Sharma G., Sharma S., Naushad M., Recent advances on nickel nano-ferrite: a review on processing techniques, properties and diverse applications. *Chemical Engineering Research and Design*, 2021, **175**, P. 182–208.

[8] Tikhanova S.M., Lebedev L.A., Martinson K.D., Chebanenko M.I., Buryanenko I.V., Semenov V.G., Nevedomskiy V.N., Popkov V.I., The synthesis of novel heterojunction h-$YbFeO_3$/o-$YbFeO_3$ photocatalyst with enhanced Fenton-like activity under visible-light. *New Journal of Chemistry*, 2021, **45**, P. 1541–1550.

[9] Amiri M., Eskandari K., Salavati-Niasari M., Magneticxally retrievable ferrite nanoparticles in the catalysis application. *Advances in Colloid and Interface Science*, 2019, **271**, P. 101982.

[10] Kalam A., Al-Sehemi A.G., Assiri M., Gaohui D., Ahmad T., Ahmad I., Pannipara M., Modified solvothermal synthesis of cobalt ferrite ($CoFe_2O_4$) magnetic nanoparticles photocatalysts for degradation of methylene blue with H_2O_2/visible light. *Results in Physics*, 2018, **8**, P. 1046–1053.

[11] Irfan S., Zhuanghao Z., Li F., Chen Y.-X., Liang G.-X., Luo J.-T., Ping F., Critical review: bismuth ferrite as an emerging visible light active nanostructured photocatalyst. *Journal of Materials Research and Technology*, 2019, **8**, P. 6375–6389.

[12] Shih Y.-J., Su C.-C., Chen C.-W., Dong C.-D., Synthesis of magnetically recoverable ferrite (MFe_2O_4, M = Co, Ni and Fe)-supported TiO_2 photocatalysts for decolorization of methylene blue. *Catalysis Communications*, 2015, **72**, P. 127–132.

[13] Sonu, Sharma S., Dutta V., Raizada P., Hosseini-Bandegharaei A., Thakur V., Nguyen V.-H., VanLe Q., Singh P., An overview of heterojunctioned $ZnFe_2O_4$ photocatalyst for enhanced oxidative water purification. *Journal of Environmental Chemical Engineering*, 2021, **9**, P. 105812.

[14] Sansenya T., Masri N., Chankhanittha T., Senasu T., Piriyanon J., Mukdasai S., Nanan S., Hydrothermal synthesis of ZnO photocatalyst for detoxification of anionic azo dyes and antibiotic. *Journal of Physics and Chemistry of Solids*, 2022, **160**, P. 110353.

[15] Reddy K.M., Devaraju J., Kinetics of Photo Fenton Process and Ag-TiO_2 photocatalyst under UV-light. *Materials Today: Proceedings*, 2019, **17**, P. 234–238.

[16] Song C., Wang L.-J., Sun S.M., Wu Y., Xu L.-J., Gan L., Preparation of visible-light photocatalysts of Bi_2O_3/Bi embedded in porous carbon from Bi-based metal-organic frameworks for highly efficient Rhodamine B removal from water. *New Carbon Materials*, 2020, **35**, P. 609–618.

[17] Atacan K., Guy N., Cakar S., Ozacar M., Efficiency of glucose oxidase immobilized on tannin modified $NiFe_2O_4$ nanoparticles on decolorization of dye in the Fenton and photo-biocatalytic processes. *Journal of Photochemistry and Photobiology A: Chemistry*, 2019, **382**, P. 111935.

[18] Shokri A., Using $NiFe_2O_4$ as a nano photocatalyst for degradation of polyvinyl alcohol in synthetic wastewater. *Environmental Challenges*, 2021, **5**, P. 100332.

[19] Cvejic Z., Durdic E., Ivandekic G.I., Bajac B., Postolache P., Mitoseriu L., Srdic V.V., Rakic S., The effect of annealing on microstructure and cation distribution of $NiFe_2O_4$. *Journal of Alloys and Compounds*, 2015, **649**, P. 1231–1238.

[20] Dumitrescu A.M., Samoila P.M., Nica V., Doroftei F., Iordan A.R., Palamaru M.N., Study of the chelating/fuel agents influence on $NiFe_2O_4$ samples with potential catalytic properties. *Powder Technology*, 2013, **243**, P. 9–17.

[21] Majid F., Rauf J., Ata S., Bibi I., Malik A., Ibrahim S.M., Ali A., Iqbal M., Synthesis and characterization of $NiFe_2O_4$ ferrite: sol-gel and hydrothermal synthesis routes effect on magnetic, structural and dielectric characteristics. *Materials Chemistry and Physics*, 2021, **258**, P. 123888.

[22] Kesavan G., Nataraj N., Chen S.-M., Lin L.-H., Hydrothermal synthesis of $NiFe_2O_4$ nanoparticles as an efficient electrocatalyst for the electrochemical detection of bisphenol A. *New Journal of Chemistry*, 2020, **44**, P. 7698–7707.

[23] Martinson K.D., Cherepkova I.A., Panteleev I.B., Popkov V.I., Single-step solution-combustion synthesis of magnetically soft $NiFe_2O_4$ nanopowders with controllable parameters. *International Journal of Self-Propagating High-Temperature Synthesis*, 2019, **28**, P. 266–270.

[24] Yang H., Zhang X., Ao W., Qiu G., Formation of $NiFe_2O_4$ nanoparticles by mechanochemical reaction. *Materials Research Bulletin*, 2004, **39**, P. 833–837.

[25] Hajalilou A., Mazlan S.A., A review on preparation techniques for synthesis of nanocrystalline soft magnetic ferrites and investigation on the effects of microstructure features on magnetic properties. *Applied Physics A*, 2016, **122**, P. 680.

[26] Martinson K.D., Cherepkova I.A., Sokolov V.V., Formation of cobalt ferrite nanoparticles via glycine-nitrate combustion and their magnetic properties. *Glass Physics and Chemistry*, 2018, **44**, P. 21–25.

[27] Aruna S.T., Mukasyan A.S., Combustion synthesis and nanomaterials. *Current Opinion in Solid State and Materials Science*, 2008, **12**, P. 44–50.

[28] Martinson K.D., Panteleev I.B., Shevchik A.P., Popkov V.I., Effect of the Red/Ox ratio on the structure and magnetic behavior of $Li_{0.5}Fe_{2.5}O_4$ nanocrystals synthesized by solution combustion approach. *Letters on Materials*, 2019, **9**, P. 475–479.

[29] Khort A., Roslyakov S., Loginov P., Solution combustion synthesis of single-phase bimetallic nanomaterials. *Nano-Structures & Nano-Objects*, 2021, **26**, P. 100727.

[30] Lazarova T., Georgieva M., Tzankov D., Voykova D., Aleksandrov L., Cherkezova-Zheleva Z., Kovacheva D., Influence of the type of fuel used for the solution combustion synthesis on the structure, morphology and magnetic properties of nanosized $NiFe_2O_4$. *Journal of Alloys and Compounds*, 2017, **700**, P. 272–283.

[31] Kharisov B.I., Dias H.V.R., Kharissova O.V., Mini-review: ferrite nanoparticles in the catalysis. *Arabian Journal of Chemistry*, 2019, **12**, P. 1234–1246.

[32] Popkov V.I., Martinson K.D., Kondrashkova I.S., Enikeeva M.O., Nevedomskiy V.N., Panchuk V.V., Semenov V.G., Volkov M.P., Pleshakov I.V., SCS-assisted production of $EuFeO_3$ core-shell nanoparticles: formation process, structural features and magnetic behavior. *Journal of Alloys and Compounds*, 2021, **859**, P. 157812.

[33] Martinson K.D., Ivanov A.A., Panteleev I.B., Popkov V.I., Effect of sintering temperature on the synthesis of LiZnMnFe microwave ceramics with controllable electro/magnetic properties. *Ceramics International*, 2021, **47**, P. 30071–30081.

[34] Martinson K.D., Sakhno D.D., Belyak V.E., Kondrashkova I.S., $Ni_{0.4}Zn_{0.6}Fe_2O_4$ nanopowders by solution-combustion synthesis: influence of Red/Ox ratio on their morphology, structure, and magnetic properties. *International Journal of High-Temperature Synthesis*, 2020, **29**, P. 202–207.

[35] Martinson K.D., Kozyritskaya S.S., Panteleev I.B., Popkov V.I., Low coercivity microwave ceramics based on LiZnMn ferrite synthesized via glycine-nitrate combustion. *Nanosystems: Physics, Chemistry, Mathematics*, 2019, **10**, P. 313–317.

[36] Amulya M.A.S., Nagaswarupa H.P., Kumar M.R.A., Ravikumar C.R., Prashantha S.C., Kusuma K.B., Sonochemical synthesis of $NiFe_2O_4$ nanoparticles: characterization and their photocatalytic and electrochemical applications. *Applied Surface Science Advances*, 2020, **1**, P. 100023.

NANOSYSTEMS: PHYSICS, CHEMISTRY, MATHEMATICS, 2021, 12 (6), P. 799–807

The influence of condition of the monazite structured $La_{0.9}Y_{0.1}PO_4$ nanocrystals sintering on thermal and mechanical properties of the material

M. O. Enikeeva[1,2,*], O. V. Proskurina[1,2], E. S. Motaylo[2], D. P. Danilovich[2], V. V. Gusarov[1]

[1]Ioffe Institute, 26, Politekhnicheskaya St., 194021, St. Petersburg, Russia

[2]Saint Petersburg State Institute of Technology, 26, Moskovsky Ave., 190013, St. Petersburg, Russia

enikeevamo@gmail.com

DOI 10.17586/2220-8054-2021-12-6-799-807

A lanthanum orthophosphate- and yttrium-based monazite structured $La_{0.9}Y_{0.1}PO_4$ nanocrystalline material was synthesized. The influence of the thermal treatment temperature on its thermal and mechanical properties has been determined. It was shown that the hydrothermal treatment of coprecipitated phosphates at 230 °C for 110 minutes yielded monazite structured nanoparticles with the crystallite size of about 16 nm. Nanopowder thermal treatment for 20 min in the annealing-quenching mode at 1000–1400 °C resulted in obtaining compact materials, the porosity of which varied from 52 to 27% with the grain growth from ∼20 to ∼100 nm. Active sintering occurred at temperatures above 1300 °C. Nanocrystalline materials obtained by heat treatment at 1200 °C with a grain size of ∼40 nm have a porosity of 42%, microhardness of H_v(25 °C) = 4±0.5 GPa, thermal conductivity λ(25 °C) = 0.4 $W\cdot m^{-1}\cdot K^{-1}$, and can be used as thermal insulation material.

Keywords: hydrothermal treatment, lanthanum and yttrium orthophosphates, thermal diffusivity, specific heat capacity, thermal conductivity.

Received: 25 November 2021

Revised: 6 December 2021

1. Introduction

Many modern functional materials are produced from complex oxide compounds, e.g. ferrites, tungstates, phosphates and others [1–5]. Various branches of modern industry require materials with thermal insulation and barrier properties [6–9]. In this regard, rare earth element (*RE*) orthophosphates with monazite and zircon type structures are promising [10–14]. Monazites structured *RE* orthophosphates have a high melting temperature (T_m ∼2173–2345 K) [15,16], low water solubility [17], high isomorphic capacity [18–21], resistance to aggressive media [22] and radiation damage [23–25]. The physicochemical properties of *RE* orthophosphates determine the great interest in the study of materials based on them. The mechanical and thermal properties influence the long-term stability, thermal insulation properties and integrity of ceramic products.

Functional materials are obtained on the basis of individual *RE* orthophosphates, solid solutions, including nanocrystalline ones [26–35]. *RE* orthophosphate nanoparticles are of scientific interest to researchers, both from the fundamental and from practical points of view. A thorough study of the mechanisms of formation and stability of *RE* orthophosphate phases will help broaden their potential application in modern technology. At present, the obtaining of monazite *RE*PO_4 (*RE*= La – Gd) based materials are aimed at producing composites for the radioactive waste form [21,36–39], thermal barrier coatings [11,12], and for the manufacture of luminescent materials [26,40].

Pre-ceramic powders synthesis is an important stage for obtaining functional materials. The hydrothermal treatment synthesis makes it possible to obtain monazite structured single-phase nanopowders without their subsequent thermal treatment [41–43]. Under hydrothermal conditions, the process of structural transformation of the rhabdophane structured $La(Y)PO_4 \cdot nH_2O$ solid solutions into monazite structured $La(Y)PO_4$ solid solutions occurs at lower temperatures (T ≈180 °C) than during aerobic calcination (T ≥500 °C) [21,44,45]. Besides, hydrothermal conditions ensure the obtaining of nanocrystalline powders and their greater uniformity in size and composition.

In the literature sources, one can find studies on the obtaining of non-porous macrocrystalline materials based on phases with monazite- or zircon-type structures by high-temperature calcination of rhabdophane structured phases [20, 36, 38]. The obtaining of nanocrystalline powders under hydrothermal conditions and subsequent sintering of the pressed samples in the annealing-quenching mode make it possible to produce porous nanocrystalline materials. Porous ceramics based on monazite structured phases can be considered as a thermal insulating material, since it can potentially have low thermal conductivity.

Despite numerous papers on the synthesis and study of the properties of materials based on monazite structured phosphates [5,16,46–48], there are practically no studies concerning nature-like nanocrystalline single-phase materials with yttrium or other *RE* additives.

Due to the above reasons, it is urgent to study the effects that the sintering temperature of monazite structured $La_{0.9}Y_{0.1}PO_4$ nanocrystalline pre-ceramic powders have on the thermal and mechanical properties of nature-like nanomaterials obtained from them.

2. Experimental

Monazite structured $La_{0.9}Y_{0.1}PO_4$ polycrystalline pre-ceramic nanopowders were synthesized in two stages. At the first stage, a solution of ammonium dihydrogen phosphate $NH_4H_2PO_4$ was added to a solution of lanthanum nitrate hexahydrate $La(NO_3)_3 \cdot 6H_2O$ (puriss.) and yttrium nitrate hexahydrate $Y(NO_3)_3 \cdot 6H_2O$ (puriss.) with constant stirring. The ratio of the reagent solutions was selected to ensure the stoichiometry specified for the reaction products. The resulting suspension with pH=1 was stirred for 15 minutes and placed in a Teflon liner of a steel autoclave (at 0.7 autoclave capacity). The autoclave was heated to 230 °C inside the furnace at $\sim$10 MPa inside the autoclave. The autoclave was kept in the furnace for 110 minutes at this temperature. After heat treatment, the autoclave was taken out from the furnace and naturally cooled down to room temperature. The solid phase was separated from the solution by decantation and rinsed with distilled water. The powder was dried at 85 °C for 48 hours.

The powder was molded into cylindrical pellets with an average diameter of 15 mm and a thickness of about 1.5 mm by uniaxial dry pressing at 4 MPa.

Sample sintering was carried out in the annealing-quenching mode as follows: the pressed tablets were placed in a heated furnace in a platinum crucible: sample 1 at 1000 °C, sample 2 at 1100 °C, sample 3 at 1200 °C, sample 4 at 1300 °C, and sample 5 at 1400 °C for 20 min for all samples. Then the samples were taken out and cooled down to room temperature (25 °C).

The X-ray phase analysis of the samples employed powder diffractograms recorded on a Rigaku SmartLab 3 powder diffractometer ($Cu_{K\alpha}$ emission) in the 2θ=10–80° angle range with a step of 0.01° and a scanning rate of 0.8°/min. The monazite phase was identified using the PDF 2 database. The average crystallite sizes were determined using the SmartLab Studio II software from Rigaku for all the peaks, using the Halder-Wagner method and taking into account the instrumental broadening of the instrument. The same SmartLab Studio II software was used to plot a lognormal crystallite size distribution for the monazite 020 peak.

The elemental composition and morphological features of powders and sintered samples were determined using a Tescan Vega 3 SBH scanning electron microscope (Tescan, Czech Republic) with an x-act detector Oxford Instruments (Oxford Instruments, United Kingdom) attachment for the X-ray spectral microanalysis. Due to the overlapping of the energy lines of the yttrium Lα-series (1.922 keV) and the phosphorus Kα-series (2.013 keV), the analysis of the nanopowder composition was carried out in the range up to 20 keV in 4–5 different regions, and the resulting value was obtained by averaging the obtained data.

The samples microhardness was determined by a PMT-3 microhardness tester (LOMO, Russia) by pressing a tetrahedral diamond pyramid in (Vickers method) at a load of 200 g for 10 s. At least five measurements were done for each sample.

The thermal properties of the materials were determined by the laser flash method using the LFA 457 MicroFlash (Netzsch, Germany) in the 25–825 °C range.

The specific heat values of the monazite structured $La_{0.9}Y_{0.1}PO_4$-based materials (at 25–825 °C) were processed by the least squares method to obtain the coefficients a, b and c according to the Mayer-Kelly equation $C_p = a + bT + cT^{-2}$ [49].

3. Results and discussion

The elemental analysis of the powder obtained by hydrothermal treatment at 230 °C for 110 minutes showed that the (La+Y):P atomic ratio is 48:52 (±1-2%), and the La:Y atomic ratio is 9:1 (±1-2%), i.e., it can be considered as corresponding to the $La_{0.9}Y_{0.1}PO_4$ stoichiometry within the error of the method.

The X-ray diffraction data on the initial powder and cylindrical pellets sintered from it (samples 1–5) are shown in Fig. 1. All samples have a monazite structure (PDF 00-012-0283). The monazite phase unit cells in all the samples have practically the same parameters: a=6.8147±0.0025 Å, b=7.0416±0.0050 Å, c=6.4916±0.0050 Å, V=303.32 Å^3, and $\rho_{calc.}$=5.0104 g/cm^3.

Figure 2 shows the dependence of the average crystallite size of the $La_{0.9}Y_{0.1}PO_4$ solid solution on the ceramics sintering temperature. The average crystallite size of the $La_{0.9}Y_{0.1}PO_4$ phase after hydrothermal treatment is about 16 nm. When sintering samples in the 1000–1200 °C range for 20 minutes (samples 1, 2, and 3), the average crystallite size gradually increases to 40 nm. An increase in the sintering temperature to 1300–1400 °C (samples 4, 5) leads to a sharp increase in the crystallite size up to 100±10 nm. The observed dependence allows one to conclude that the process of sintering and grain growth activates in the 1200 °C$< T <$1300 °C range.

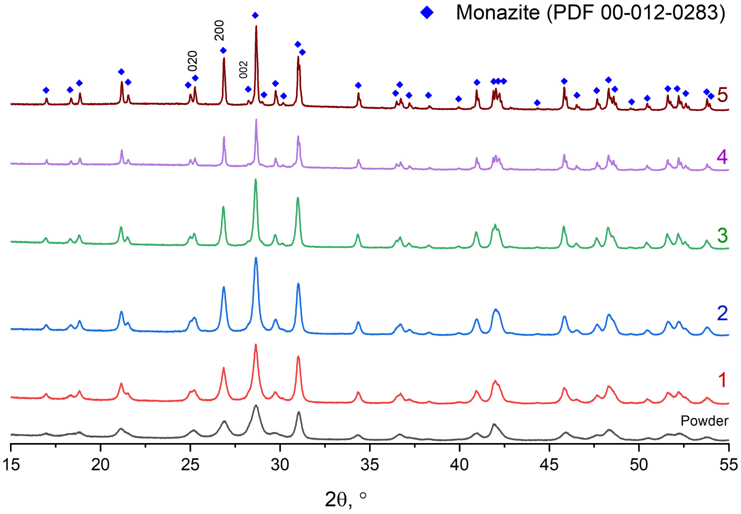

FIG. 1. X-ray diffraction patterns of the nanocrystalline powder (Powder) and samples after heat treatment at 1000 (1), 1100 (2), 1200 (3), 1300 (4), and 1400 °C (5)

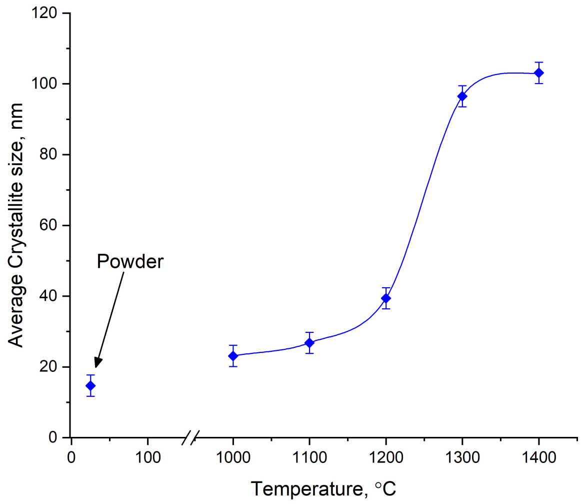

FIG. 2. Dependence of the average crystallite size on the sintering temperature

Figure 3 shows the crystallites size distribution for the initial powder and sintered samples, determined from the profile of the 020 peak of the monazite phase. It follows from the obtained data that crystallites of the initial powder have a narrow size distribution. The thermal treatments at 1000 °C and 1100 °C (samples 1 and 2) lead to an insignificant broadening of the distribution, while the heat treatment at 1200 °C (sample 3) broadens the size distribution of crystallites more noticeably, and the size distribution broadens significantly at 1300 °C and 1400 °C (samples 4 and 5).

Figure 4 demonstrates images of chips and polished sections of the samples sintered at 1000–1400 °C (specimens 1–5). The images of splinters (Fig. 4 a,c,e) and polished sections (Fig. 4 b,d,f) of samples 1–3 clearly show the fibrous microstructure of the samples formed by anisotropic nanoparticles of $La_{0.9}Y_{0.1}PO_4$ monazite. The images of splinter from samples 1 and 2 demonstrate a significant fraction of voids between the chaotically stacked monazite nanoparticle agglomerates. The topography of the polished sections from samples 1 and 2 (Fig. 4 b,d) has a similar appearance. Microstructural changes in the material begin at $T \approx 1200$ °C, the agglomerated fibers in its polished section (Fig. 4 f) are less pronounced than in the case of samples 1 and 2 (Fig. 4 b,d) obtained at lower temperatures.

The analysis of changes in the microstructure of materials after sintering, revealed by studies on a scanning electron microscope (SEM), and of the data on the crystallites growth during thermal treatment, allows a conclusion that

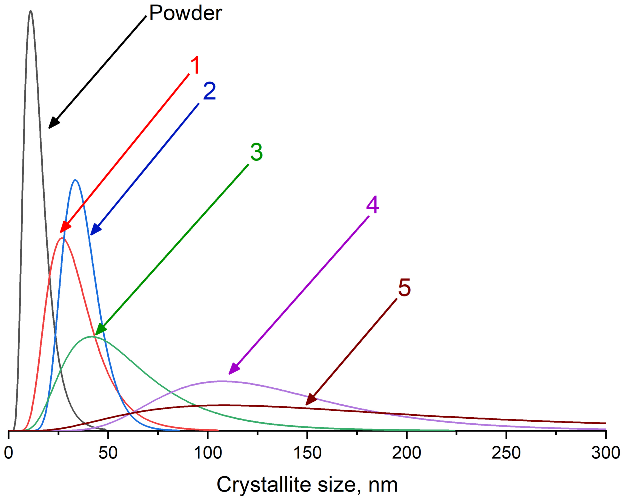

FIG. 3. Size distribution of crystallites of the initial powder (Powder) and samples after heat treatment at 1000 (1), 1100 (2), 1200 (3), 1300 (4), and 1400 °C (5)

TABLE 1. Characteristics of the $La_{0.9}Y_{0.1}PO_4$-based materials

Sample	Sintering temperature, °C	Bulk density ρ, g/cm^3	Porosity P, %	λ ($T = 25$°C), W·m^{-1}·K^{-1}
Compacted powder	–	2.242	55.3	–
1	1000	2.389	52.3	0.12±0.08
2	1100	2.767	44.8	0.42±0.08
3	1200	2.871	42.7	0.45±0.08
4	1300	3.627	27.6	1.35±0.08
5	1400	3.646	27.2	1.39±0.08

the activation of sintering and recrystallization processes lies in the temperature range of 1200–1300 °C. It should be noted that the obtained temperature range correlates well with the melting point value for the surface (nonautonomous) phase, calculated using the expression proposed in [50, 51].

Fig. 4 g,i shows the microstructure of samples 4 and 5 obtained at temperatures ≥1300 °C, which differs from samples 1, 2, and 3 by the absence of a fibrous structure. Due to a sharp increase in the contact area of grain boundaries and their recrystallization, pore formation occurs in the samples. In the image of the material obtained at 1300 °C (Fig. 4 h), the pore size varies in the range from 50 nm to several μm, which confirms active sintering of this material. An increase in the sintering temperature to up to 1400 °C leads to an increase in the pore size up to 3–5 μm (Fig. 4 j).

Table 1 presents the values of the total porosity and apparent density of the samples (powder and samples 1–5). As a result of dry uniaxial pressing of the powder at 4 MPa, the resulting material has a total porosity of $P = 55\%$ before the high-temperature treatment. Sintering at temperatures ≤1200 °C reduces the total porosity of the samples down to $P = 42\%$. The obtained values of the total porosity are consistent with the qualitative SEM data (Fig. 4 a–j) for samples 1–3, which show a large fraction of voids between the agglomerated $La_{0.9}Y_{0.1}PO_4$ monazite nanoparticles. As a result of an increase in the sintering temperature up to 1300 and 1400 °C (samples 4, 5), the material compactness increases to an apparent density of 3.65 g/cm^3, and the total porosity decreases down to $P \sim 27\%$.

Figure 5 shows the dependence of microhardness (H_v) at 25 °C on total porosity (P) of the samples (Table 1). A decrease in the total porosity of the material from 52% to 27%, which leads to an increase in H_v from 5±0.5 GPa to 17±0.5 GPa, shows that intense sintering and an increase in the hardness of porous materials based on a monazite structured $La_{0.9}Y_{0.1}PO_4$ solid solution occurs at temperatures ≥1300 °C. The obtained porous nanocrystalline materials have lower microhardness values than the known lanthanum orthophosphate-based monazite ceramics [46]. This is due to the difference in the microstructure and functional purpose of these materials. Large porosity and small microhardness values of the synthesized materials are due to the fact that this work was aimed at studying the possibility

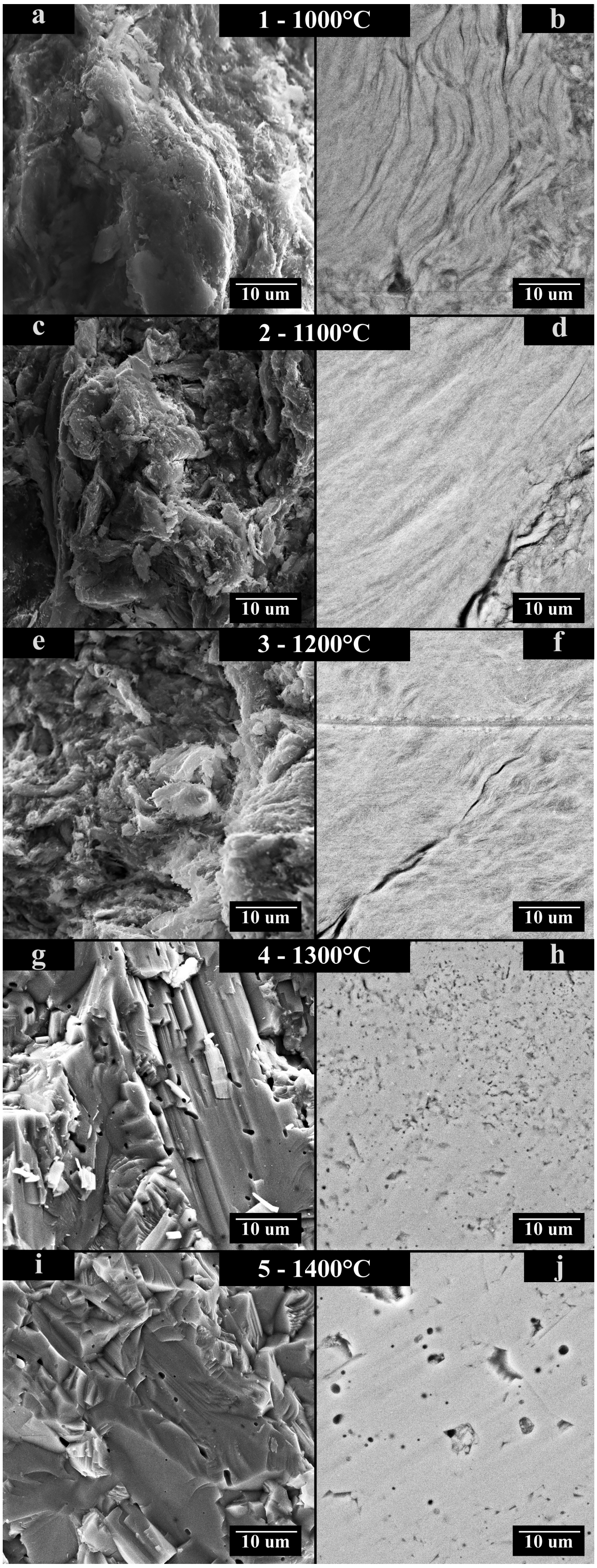

FIG. 4. SEM micrographs of samples heat treated at temperatures 1000 (1), 1100 (2), 1200 (3), 1300 (4) and 1400 °C (5): (a,c,e,g,i) splinters of cylindrical samples; (b,d,f,h,j) – polished sections of samples

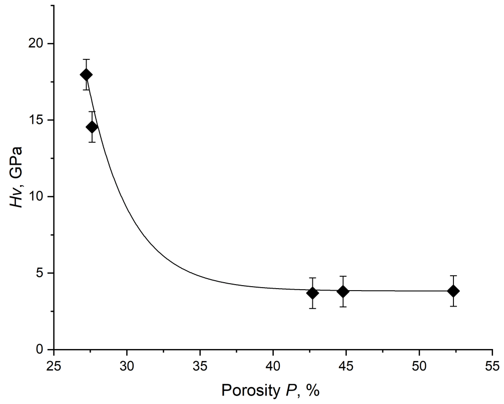

FIG. 5. Dependence of microhardness H_v on the total porosity P of the $La_{0.9}Y_{0.1}PO_4$-based materials

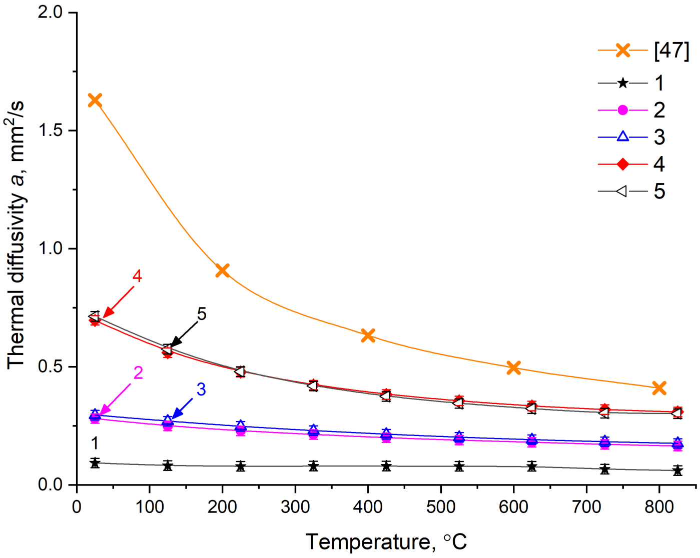

FIG. 6. Materials thermal diffusivity a after heat treatment at 1000 (1), 1100 (2), 1200 (3), 1300 (4), and 1400 °C (5)

of obtaining heat-insulating monazite structured *RE* phosphate-based materials, in contrast to the above works focused on obtaining non-porous ceramic materials for the radioactive waste form.

The dependence of thermal diffusivity (a) of materials (samples 1-5) on temperature ($T = 25 - 825$ °C) is shown in Fig. 6. For all the samples, a decrease in the a coefficient with the increasing temperature is inherent. The values of thermal diffusivity for samples 1–3 with total porosity of P=52–44% (Table 1) is lower than those for the samples with total porosity of $\approx 27\%$ (samples 4, 5). The materials obtained at 1000–1200 °C displayed an almost linear character of the temperature diffusivity dependence on temperature; the values of a do not exceed 0.3 mm^2/s. As a result of material sintering and compaction, an increase in the thermal diffusivity occurs over the entire investigated temperature range. The obtained values depend on the total porosity and the size of the contact boundaries formed during the pressing of the powder. Fig. 6 shows that $a(T)$ values coincide within the error for samples 4 and 5 sintered at T =1300 °C and T =1400 °C, which is confirmed by their almost identical total porosity of $\sim 27\%$. The highest thermal diffusivity for the produced materials is 0.70±0.02 mm^2/s at T =25 °C for the samples obtained at 1300–1400 °C. The values of thermal diffusivity for the $LaPO_4$ monazite-based dense materials decrease monotonically from 1.629 mm^2/s (T=20 °C) down to 0.410 mm^2/s (T=800 °C) [47]. The minimum difference between the values of a obtained in the present study and those given in the literature is observed at high temperatures: a(800 °C)=0.410 mm^2/s ($P_{calc.}$=0%), and a(825 °C)=0.302±0.020 mm^2/s (sample 5, $P \sim 27\%$) in the present study.

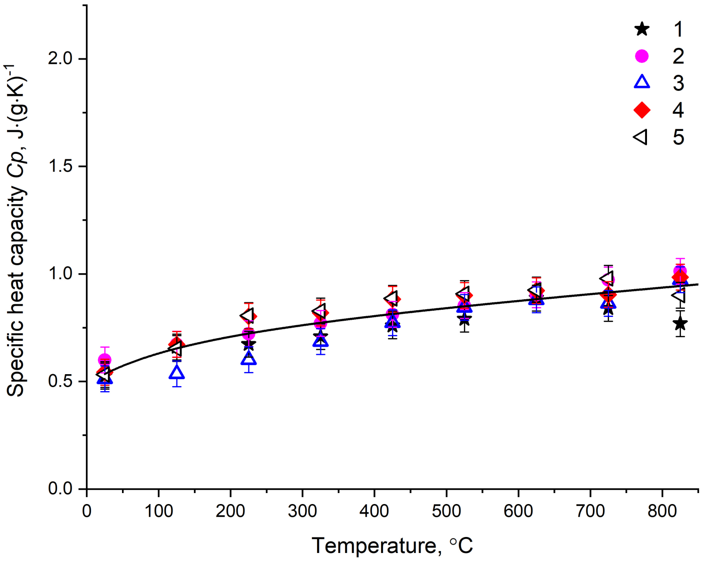

FIG. 7. Specific heat capacity (C_p) of the monazite structured $La_{0.9}Y_{0.1}PO_4$-based materials

Hence, it can be concluded that the thermal diffusivity, most likely, is less dependent on the total porosity of the monazite-based material.

The specific heat values of the sintered samples in Fig. 7 were calculated using the Mayer-Kelly empirical dependence equation ($C_p = a + bT + cT^{-2}$), the coefficients in which were determined from experimental data in the 25–825 °C range ($a = 0.66 \pm 0.06$, $b = (2.7 \pm 0.6) \cdot 10^{-4}$, $c = (-18.6 \pm 5.3) \cdot 10^3$). The specific heat values obtained for the monazite structured $La_{0.9}Y_{0.1}PO_4$-based material are higher than those for individual lanthanum orthophosphate with the same structure [30,47,48]. The character of $C_p(T)$ dependence is in good agreement with the authors' data for the monazite structured lanthanum orthophosphate, differing by 0.1–0.3 J·(g·K)$^{-1}$, which may be due to the presence of yttrium in the phase.

The values of thermal conductivity coefficient λ of samples 1-5 at T =25 °C are presented in Table 1. The compaction of the $La_{0.9}Y_{0.1}PO_4$-based materials by increasing the processing temperature leads to an increase in the thermal conductivity from 0.12±0.08 W·m^{-1}·K^{-1} at $P = 52.3\%$ up to 1.35 ± 0.08 W·m^{-1}·K^{-1} for samples 4 and 5 with a total porosity of ≈27%.

4. Conclusion

Pre-ceramic nanocrystalline powders have been obtained on the basis of a monazite structured $La_{0.9}Y_{0.1}$ PO_4 solid solution. The powders are represented by quasi-one-dimensional particles with a crystallite size of about 16 nm. The nanoparticles were synthesized under hydrothermal conditions at 230 °C and a processing time of 110 minutes. The heat treatment of compacted nanocrystalline $La_{0.9}Y_{0.1}PO_4$ powder by the annealing-quenching method in the 1000–1400 °C range for 20 minutes resulted in polycrystalline compact materials with a total porosity of 27 to 52%. It is shown that the activation of nanopowder sintering and crystallite growth occurs in the 1200–1300 °C range, which correlates with the melting temperature of the surface (nonautonomous) phase.

The dependence of the thermophysical characteristics and microhardness of the material on the porosity has been determined. The maximum microhardness (H_v) value of 17±0.5 GPa was obtained for the material with the lowest porosity. It was shown that the values of thermal diffusivity (a) of a material with total porosity (P) of 27% decreased monotonically with an increase in temperature from a (T = 25 °C)= 0.70 ± 0.02 mm^2/s to a (T = 825 °C)= 0.30 ± 0.02 mm^2/s. It was determined that the specific heat capacity of the monazite structured $La_{0.9}Y_{0.1}PO_4$-based material is higher than that of an individual lanthanum orthophosphate. The thermal conductivity of materials $\lambda(T = 25$ °C) varies depending on the porosity within a wide range from 0.12 ± 0.08 W·m^{-1}·K^{-1} at P ≈52% to 1.35 ± 0.08 W·m^{-1}K^{-1} at P ≈27%.

Acknowledgement

The X-ray diffraction studies, determination of thermal diffusivity, examination by scanning electron microscopy, and the elemental analysis of samples were carried out on the instruments of the Engineering Center of the St. Petersburg State Technological Institute (Technical University).

The present work was financially supported by the Russian Foundation for Basic Research (Project No. 18-29-12119).

References

[1] Lomanova N.A., Tomkovich M.V., Danilovich D.P., Osipov A.V., Panchuk V.V., Semenov V.G., Pleshakov I.V., Volkov M.P., Gusarov V.V. Magnetic characteristics of nanocrystalline $BiFeO_3$-based materials prepared by solution combustion synthesis. *Inorg. Mater.*, 2020, **56**(12), P. 1271–1277.

[2] Martinson K.D., Kondrashkova I.S., Omarov S.O., D.A. Sladkovskiy D.A., Kiselev A.S., Kiseleva T.Yu., Popkov V.I. Magnetically recoverable catalyst based on porous nanocrystalline $HoFeO_3$ for processes of n-hexane conversion. *Advanced Powder Technology*, 2020, **31**(1), P. 402–408.

[3] Lomakin M.S., Proskurina O.V., Sergeev A.A., Buryanenko I.V., Semenov V.G., Voznesenskiy S.S., Gusarov V.V.Crystal structure and optical properties of the Bi–Fe–W–O pyrochlore phase synthesized via a hydrothermal method. *Journal of Alloys and Compounds*, 2021, **889**, P. 161598.

[4] Maslennikova T.P., Osipov A.V., Mezentseva L.P., Drozdova I.A., Kuchaeva S.K., Ugolkov V.L., Gusarov V.V. Synthesis, Mutual Solubility, and Thermal Behavior of Nanocrystals in the $LaPO_4$–YPO_4–H_2O System. *Glass Physics and Chemistry*, 2010, **36**(3), P. 351–357.

[5] Gavrichev K.S., Ryumin M.A., Tyurin A.V., Gurevich V.M., Komissarova L.N.. Refined heat capacity of $LaPO_4$ in the temperature range 0–1600K. Thermochimica Acta, 2008, **474**(1–2), P. 47–51.

[6] Clarke D.R., Phillpot S.R. Thermal barrier coating materials, *Materials Today*, 2005, **8**(6), P. 22–29.

[7] Chen D., Dambra C., Dorfman M. Process and properties of dense and porous vertically-cracked yttria stabilized zirconia thermal barrier coatings, *Surface and Coatings Technology*, 2020, **404**, P. 126467.

[8] Chen Y., Wang N., Ola O., Xia Y., Zhu Y. Porous ceramics: Light in weight but heavy in energy and environment technologies, *Materials Science and Engineering: R: Reports*, 2021, **143**, P. 100589.

[9] Mehboob G., Liu M.-J., Xu T., Hussain S., Mehboob G., Tahir A. A review on failure mechanism of thermal barrier coatings and strategies to extend their lifetime, *Ceramics International*, 2020, **46**(7), P. 8497–8521.

[10] Orlova A.I., Orlova V.A., Orlova M.P., Bykov D.M., Stefanovskii S.V., Stefanovskaya O.I., Nikonov B.S. The crystal-chemical principle in designing mineral-like phosphate ceramics for immobilization of radioactive waste. *Radiochemistry*, 2006, **48**, P. 330–339.

[11] Li M, Yuxian C., Lei G., Chenglong Z., Yuchen Z., Sixian H., Fuxing Y. Preparation of plasma sprayed nanostructured GdPO4 thermal barrier coating and its hot corrosion behavior in molten salts. *Ceram. Int.*, 2017, **43**(10), P. 7797–7803.

[12] Zhao Z., Heng C., Huimin X., Fu-Zhi D., Xiaohui W., Peng Z., Yanchun Z. $(La_{0.2}Ce_{0.2}Nd_{0.2}Sm_{0.2}Eu_{0.2})PO_4$: A high-entropy rare-earth phosphate monazite ceramic with low thermal conductivity and good compatibility with Al_2O_3. *J. Mater. Sci. Technol.*, 2019, **35**(12), P. 2892–2896.

[13] Monazite-based thermal barrier coatings: US6863999B1 USA F01D5/288, Sudre O.H., Marshall D.B., Morgan P.E.D. patent holder: Teledyne Scientific and Imaging LLC, 2005.

[14] Montel J.M., Glorieux B., Seydoux-Guillaume A.-M., Wirth R. Synthesis and sintering of a monazite–brabantite solid solution ceramic for nuclear waste storage. *J. Phys. Chem. Solids*, 2006, **67**(12), P. 2489–2500.

[15] Hikichi Y., Nomura T. Melting Temperatures of Monazite and Xenotime. *J. Am. Ceram. Soc*, 1987, **70**(10), P. 252–253.

[16] Galahov F.Y. Diagrammy sostoyaniya sistem tugoplavkih oksidov: spravochnik. V. 5. Dvojnye sistemy ch. 2. [State diagrams of refractory oxides]. Leningrad, Nauka, 1986, **5**, 359. (in Russian)

[17] Van Hoozen C.J., Gysi A.P., Harlov D.E. The solubility of monazite ($LaPO_4$, $PrPO_4$, $NdPO_4$, and $EuPO_4$) endmembers in aqueous solutions from 100 to 250°C. *Geochim. Cosmochim. Acta*, 2020, **280**, P. 302–316.

[18] Gratz R., Heinrich W. Monazite-xenotime thermobarometry; experimental calibration of the miscibility gap in the binary system $CePO_4$ –YPO_4. *Am. Mineral*, 1997, **82**(7), P. 772–780.

[19] Podor R., Cuney M., Nguyen T.C. Experimental study of the solid solution between monazite-(La) and $(Ca_{0.5}U_{0.5})PO_4$ at 780°C and 200 MPa. *Am. Mineral.*, 1995, **80**(11), P. 1261–1268.

[20] Huittinen N., Arinicheva Y., Kowalski P.M., Vinograd V.L., Neumeier S., Bosbach D. Probing structural homogeneity of $La_{1-x}Gd_xPO_4$ monazite-type solid solutions by combined spectroscopic and computational studies. *J. Nucl. Mater.*, 2017, **486**, P. 148–157.

[21] Zeng P., Teng Y., Huang Y., Wu L., Wang X. Synthesis, phase structure and microstructure of monazite-type $Ce_{1-x}Pr_xPO_4$ solid solutions for immobilization of minor actinide neptunium. *J. Nucl. Mater.*, 2014, **452**(1–3), P. 407–413.

[22] Arinicheva Y., Gausse C., Neumeier S., Brandt F., Rozov K., Szenknect S., Dacheux N., Bosbach D., Deissmann G. Influence of temperature on the dissolution kinetics of synthetic $LaPO_4$-monazite in acidic media between 50 and 130°C. *J. Nucl. Mater.*, 2018, **509**, P. 488–495.

[23] Ewing R.C., Wang L. Phosphates as nuclear waste forms. *Rev. Mineral.*, 2002, **48**(1), P. 673–699.

[24] Grechanovsky A.E., Eremin N.N., Urusov, V.S. Radiation resistance of $LaPO_4$ (monazite structure) and $YbPO_4$ (zircon structure) from data of computer simulation. *Phys. Solid State*, 2013, **55**(9), P. 1929–1935.

[25] Schlenz H., Heuser J., Neumann A., Schmitz S., Bosbach D. Monazite as a suitable actinide waste form. *Z. Kristallogr.*, 2013, **228**(3), P. 113–123.

[26] Yang Z., Yuan G., Duan X., Liang S., Sun G. HDEHP assisted solvothermal synthesis of monodispersed *RE*PO$_4$ (*RE* = La–Lu, Y) nanocrystals and their photoluminescence properties. *New J. Chem.*, 2020, **44**(11), P. 4386–4393.

[27] Kenges K.M., Proskurina O.V., Danilovich D.P, Aldabergenov M.K., Gusarov V.V. Influence of the conditions for preparing $LaPO_4$-based materials with inclusions of the LaP_3O_9 phase on their thermal and mechanical properties. *Russ. J. Appl. Chem.*, 2018, **91**(9), P. 1538–1548.

[28] Thust A., Arinicheva Y., Haussühl E., Ruiz-Fuertes J., Bayarjargal L., Vogel S.C., Neumeier S., Winkler B. Physical properties of $La_{1-x}Eu_xPO_4$, $0 \leq x \leq 1$, monazite-type ceramics. *J. Am. Ceram. Soc.*, 2015, **98**(12), P. 4016–4021.

[29] Thust A., Hirsch A., Haussühl E., Schrodt N., Loison L., Schott P., Peters L., Roth G., Winkler B. Physical properties and microstructures of $La_{1-x}Pr_xPO_4$ monazite-ceramics. *Phys. Chem. Miner.*, 2018, **45**(4), P. 323–332.

[30] Min W., Daimon K., Matsubara T., Hikichi Y. Thermal and mechanical properties of sintered machinable $LaPO_4$–ZrO_2 composites. *Mater. Res. Bull.*, 2002, **37**(6), P. 1107–1115.

[31] Colomer M.T. Effect of Sr^{2+} doping on sintering behavior, microstructural development and electrical properties of $LaPO_4 \cdot nH_2O$ nanorods prepared by drymechanical milling. *Int. J. Hydrogen Energy*, 2018, **43**(29), P. 13462–13474.

[32] Arinicheva Y., Clavier N., Neumeier S., Podorb R., A.Bukaemskiy A., M.Klinkenberg M., Roth G., Dacheux N., Bosbach D. Effect of powder morphology on sintering kinetics, microstructure and mechanical properties of monazite ceramics. *J. Eur. Ceram. Soc.*, 2018, **38**(1), P. 227–234.

[33] Proskurina O.V., Sivtsov E.V., Enikeeva M.O., Sirotkin A.A., Abiev R. Sh., Gusarov V.V. Formation of rhabdophane-structured lanthanum orthophosphate nanoparticles in an impinging-jets microreactor and rheological properties of sols based on them. *Nanosyst. Physics, Chem. Math*, 2019, **10**(2), P. 206–214.

[34] Li P., Zhang Y., Zhang L., Li F., Guo Y., Li Y., Gao W. Phase control of Eu^{3+}-doped YPO_4 nano-/microcrystals. *Cryst. Growth Des.*, 2017, **17**(11), P. 5935–5944.

[35] Ugolkov V.L., Mezentseva L.P., Osipov A.V., Popova V.F., Maslennikova T.P., Akatov A.A., Doil'nitsyn V.A. Synthesis of Nanopowders and Physicochemical Properties of Ceramic Matrices of the $LaPO_4$–YPO_4–(H_2O) and $LaPO_4$–$HoPO_4$–(H_2O) Systems. *Russian Journal of Applied Chemistry*, 2017, **90**(1), P. 28–33.

[36] Terra O., Clavier N., Dacheux N., Podorb R. Preparation and characterization of lanthanum–gadolinium monazites as ceramics for radioactive waste storage. *New J. Chem.*, 2003, **27**(6), P. 957–967.

[37] Deschanels X., Seydoux-Guillaume A.M., Magnin V., Mesbah A., Tribet M., Moloney M.P., Serruys Y., Peuget S., Swelling induced by alpha decay in monazite and zirconolite ceramics: A XRD and TEM comparative study. *J. Nucl. Mater.*, 2014, **448**(1–3), P. 184–194.

[38] Martel L., Islam Md. A., Popa K., Vigier J.-F., Colineau E., Bolvin H., Griveau J.-C. Local structure and magnetism of $La_{1-x}M_xPO_4$ (M=Sm, ^{239}Pu, ^{241}Am) explained by experimental and computational analyses. *J. Phys. Chem.*, 2021, **125**(40), P. 22163–22174.

[39] Morgan P.E.D., Marshall D.B. Ceramic composites of monazite and alumina. *J. Am. Ceram.*, 1995, **78**, P. 1553–1563.

[40] Wu J., Jia H., Li M., Liu Z. Influence of pH on nano-phosphor YPO_4:2%Sm^{3+} and luminescent properties. *Appl. Phys. A*, 2020, **126**(2), P. 87.

[41] Enikeeva M.O., Kenges K.M., Proskurina O.V., Danilovich D.P., Gusarov V.V. Influence of hydrothermal treatment conditions on the formation of lanthanum orthophosphate nanoparticles of monazite structure. *Russ. J. Appl. Chem.*, 2020, **93**(4), P. 540–548.

[42] Fan W., Song X., Bu Y., Sun S., Zhao X. Selected-control hydrothermal synthesis and formation mechanism of monazite- and zircon-type $LaVO_4$ nanocrystals. *J. Phys. Chem. B*, 2006, **110**(46), P. 23247–23254.

[43] Bryukhanova K.I., Nikiforova G.E., Gavrichev K.S. Synthesis and study of anhydrous lanthanide orthophosphate (*Ln* = La, Pr, Nd, Sm) nanowhiskers. *Nanosyst. Physics, Chem. Math*, 2016, **7**(3), P. 451–458.

[44] Rafiuddin M.R., Grosvenor A.P. A structural investigation of hydrous and anhydrous rare-earth phosphates. *Inorg. Chem.*, 2016, **55**(19), P. 9685–9695.

[45] Hirsch A., Kegler P., Alencar I., Ruiz-Fuertes J., Shelyug A., Peters L., Schreinemachers C., Neumann A., Neumeier S., Liermann H., Navrotsky A., Roth G. Structural, vibrational, and thermochemical properties of the monazite-type solid solution $La_{1-x}Pr_xPO_4$. *J. Solid State Chem.*, 2017, **245**, P. 82–88.

[46] Perri Ere L., Bregiroux D., Naitali B., Audubert F., Champion E., Smith D.S., Bernache-Assollant D. Microstructural dependence of the thermal and mechanical properties of monazite *Ln*PO_4 (*Ln*= La to Gd). *J. Eur. Ceram. Soc.*, 2007, **27**(10), P. 3207–3213.

[47] Du A., Wan C., Qu Z., Pan W. Thermal Conductivity of Monazite-Type *RE*PO_4 (*RE*=La, Ce, Nd, Sm, Eu, Gd). *J. Am. Ceram. Soc.*, 2009, **92**(11), P. 2687–2692.

[48] Du A., Wan C., Qu Z., Pan W. Effects of texture on the thermal conductivity of the $LaPO_4$ Monazite. *J. Am. Ceram. Soc.*, 2010, **93**(9), P. 2822–2827.

[49] Maier C.G., Kelley K.K. An equation for the representation of high-temperature heat content data. *J. Am. Chem. Soc.*, 1932, **54**(8), P. 3243–3246.

[50] Gusarov V.V., Suvorov S.A. Melting points of locally equilibrium surface phases in polycrystalline systems based on a single volume phase. *J. Appl. Chem. of the USSR*, 1990, **63**(8), P. 1560–1565.

[51] Gusarov V.V. The thermal effect of melting in polycrystalline systems. *Thermochim. Acta*, 1995, **256**(2), P. 467–472.

NANOSYSTEMS: PHYSICS, CHEMISTRY, MATHEMATICS, 2021, 12 (6), P. 808–817

Application of biosynthesized nano-catalyst for biodiesel synthesis and impact assessment of factors influencing the yield

C. P. Gandhi[1], Rajni Garg[2], Nnabuk Okon Eddy[3]

[1]Department of Mathematics, Rayat Bahra University, Mohali, Punjab, 140301, India
[2]Department of Chemistry, Rayat Bahra University, Mohali, Punjab, 140301, India
[3]Department of Pure and Industrial Chemistry, University of Nigeria, Nsukka, Enugu State, 410001, Nigeria
cchanderr@gmail.com, rajnigarg@science.org.in, okon.nnabuk@unn.edu.ng

DOI 10.17586/2220-8054-2021-12-6-808-817

This study presents a green process to synthesize biodiesel using biosynthesized nano-catalyst and a novel methodology for analyzing the impact of influencing factors – methanol/oil ratio, the concentration of nano-catalyst, temperature, and time of reactions- on the yield of biodiesel obtained by heterogeneous nano-catalyst-based transesterification reaction. Nano-calcium oxide (nano-CaO) was obtained as a heterogeneous nano-catalyst using waste eggshells. Waste cooking oil was treated with methanol and nano-catalyst at varying methanol: oil ratios (4 – 14:1), nano-catalyst concentration (0.5 – 2 %), time of reaction (3 – 4.5 hrs), and temperature (50 – 65 °C). The superiority and effectiveness of the proposed transesterification indices were accomplished making use of Deluca and Termini fuzzy entropy weighted indexes to obtain optimal reaction conditions with 95.49 % biodiesel yield.

Keywords: nano-catalyst, biodiesel, transesterification, fuzzy entropy, neutrosophic entropy.

Received: 17 September 2021

1. Introduction

Worldwide consumption of energy is progressing especially in the transportation sector which is solely dependent upon petroleum-based non-renewable resources of energy [1]. These resources are the primary source of increasing environmental pollution due to the emission of carbon dioxide from vehicular exhausts in addition to the greenhouse effect [2]. The resulting environmental degradation and the expected energy depletion require the continuous search for alternative energy resources if the quality of the environment must be maintained [3]. Consideration of the energy policy review indicates that India and several nations of the world are facing great challenges towards alternative and sustainable energy resources that are eco-friendly, less expensive, biodegradable, and easily available [4]. Consequently, the search for biofuels such as biogas, hydrogen cells, and biodiesel has attracted intense research interest because of the potential of green chemistry usage [5]. Biodiesel has emerged as a sulfur-free, bio-degradable, cost-effective, non-toxic, and more reliable option among the alternative sustainable fuels [6]. It is miscible in diesel at all proportions and is favored as a blending constituent of automotive fuel due to its very high cetane value and high lubricity [7]. It can be obtained as fatty acid alkyl esters employing transesterification of cheap resources viz oils and fat with alcohols (ethanol/methanol) or alkoxides and homogeneous or heterogeneous catalyst with the production of glycerol as a by-product [8]. Vegetable oil is commonly obtained from oil crops such as coconut, sunflower, canola, palm, mustard, soybean, flax, rapeseed, jatropha, hemp, and rice bran, etc. India has a great potential for production of biodiesel with vast production of oil crops in the wasteland and forest area. In the global society, efforts are ongoing toward reducing dependency on fossil fuels and reducing production costs for biodiesel by opting for low-cost and easy to obtain feedstock and catalysts [9]. Many researchers have used vegetable oils in the form of raw, non-edible and waste oils obtained from various oil processing units as well as from household and locally available food ventures [10].

It has been found that heterogeneous catalysts exhibit better performance compared to homogeneous catalysts. The major factor includes the high production cost during industrial production on large scale due to the involvement of the multistep purification process and difficulties to remove the byproducts such as glycerol formed during the reaction. Treatment of the effluent resulted from this process also adds to the cost [11]. Further, all the conventional feedstock including non-edible oils with high content of fatty acids can not be used in the homogeneous esterification due to the possibility of soap formation that leads to loss of yield and adds to the separation issue of byproducts. Hence, researchers are seeking economically viable and alternative methods for the production of biodiesel [12]. However, the greatest advantage of heterogeneous catalysts is the ease of separation while the disadvantage is limited activity and selectivity. Heterogeneous (solid) catalyst-based transesterification offers future hope to current challenges because solid catalysts are required in a lesser amount compared to conventional catalysts and can be easily separated and be re-used. Also, the solid catalyst can be fabricated and tailored as per the requirement to increase the catalytic properties.

Various solid catalysts including metal oxide and alumina/silica supported metal oxide catalysts have been explored by researchers [13]. Several reports are available with usage of CaO as a heterogeneous nano-catalyst. Animal eggshells are a rich source of calcium carbonate that can be easily converted to nano-CaO. Throughout the world, eggshells of chicken, duck, and snails are discarded as waste and their improper disposal leads to environmental pollution that results in various health hazards. Hence, the use of waste eggshells for the generation of nano-CaO as a heterogeneous nano-catalyst is an eco-friendly step [14]. Likewise, edible oil is processed in various food processing units especially in the kitchen and restaurants for frying purposes. After frying, edible oil becomes unfit for consumption and is discarded and is known as waste cooking oil (WCO). This oil is rich in free fatty acids and may be successfully employed to obtain biodiesel using nano-CaO based heterogeneous transesterification [15].

Production of biodiesel is dependent upon many factors including methanol/oil ratio, temperature, the concentration of nano-catalyst, time of reaction, extent of stirring, etc. [16]. Subsequently, Yi et al. approached the enduring Karl's Pearson's coefficient formula and designed the optimal reaction conditions responsible for transesterification reaction [17]. However, the correlation coefficient formula has some limitations as it can be only used for studying interrelation and thus leads to a non-significant curvilinear relationship between two variables. The fuzzy set theory proposed by Zadeh has been proven as an indispensable tool for optimizing energy-related problems [18]. Ovchinnikov elaborated many impressions of fuzzy sets (FSs), one of which corresponds to the representation of membership degree or grade of the underlying FS [19]. Since then, FSs have been extended into a variety of equivalents and more quantified information is provided by the neutrosophic set (NS) contribute in comparison with the existing fuzzy set theory [20]. Moreover, the NS theory has the potential of predicting optimal reaction conditions under heterogeneous catalyzed transesterification reactions. To handle and solve these problematic issues, an effort is accomplished in this pathway by establishing a novel neutrosophic entropy-based methodology which can play a crucial role for the classification of influencing factors (i) methanol/oil ratio (ii) concentration of nano-catalyst (iii) temperature and (iv) time of reactions, responsible for optimal biodiesel yield, obtained by heterogeneous nano-catalyst-based transesterification reaction. The underlying neutrosophic entropy-based methodology provides remarkable yield information confirming the optimum parameters. The results of this underlying study are superseded as below.

Section 2 provides the details of the materials and procedures employed in performing the reaction. Section 3 introduces the projected methodology for constructing fuzzy entropy weighted waste cooking oil transesterification index (FCOTI), single-valued neutrosophic entropy weighted waste cooking oil transesterification index (SCOTI), and Deluca and Termini fuzzy entropy-based weighted waste cooking oil transesterification index (ECOTI) respectively. Section 4 provides the details for the characterization of the prepared nano-catalyst and biodiesel. It also provides the applicability and remarkability of the underlying methodology by identifying the most influencing reaction set, responsible for the optimum biodiesel yield whereas Section 5 finally summarizes the study. The basic terminology of fuzzy and neutrosophic entropy measures, required for the successive progress of the underlying study has been given in supplementary information.

2. Materials and methods

2.1. Materials

WCO, procured from the resident food vendors, was utilized as resource material for the reaction. Waste chicken eggshells, collected from the local food junctions, were used to develop the heterogeneous nano-catalyst. All the chemicals of analytical grade were acquired from Merck, Mumbai, and were utilized without any additional processing or purification.

2.2. Collection of reaction sets

A heterogeneous nano-catalyst based on waste eggshells was developed by the procedure given in literature [21]. Methanol has been used as a solvent and co-reactant. After washing, drying, and grinding, the eggshells were calcined to obtain nano-CaO as a nano-catalyst. The nano-catalyst was characterized by FTIR (Model Perkin Elmer Spectrum 400 FT-IR Spectrometer) operating with a resolution of 2 cm^{-1} (range 4000 – 400 cm^{-1}) and XRD (Model PANalytical X'Pert Pro) operating at a voltage of 45 kV with a current of 35 mA using Cu-Kα radiation ($K = 1.5406$ Å) and 2θ ranging from 20 – 80° at a continuous speed of 0.045° per min. Waste cooking oil was subjected to filtration for the removal of any insoluble impurities and was pre-treated with anhydrous sodium sulfate before heating at 100 °C. The reaction was executed in a batch reactor supported with a thermostatic water bath and magnetic stirrer by varying methanol: oil ratio (4 – 14:1), nano-catalyst concentration (0.5 – 2 %), time of reaction (3 – 4.5 hrs.), and temperature (50 – 65 °C) as per reaction sets and a constant stirring was maintained.

After the separation of glycerol, the by-product, the % yield of biodiesel was determined using the standard equation [22]. The biodiesel so obtained was characterized by FTIR (Model Perkin Elmer Spectrum 400 FT-IR

Spectrometer) and GC-MS analysis (Model THERMO Scientific Trace 1300GC) operating at conditions as shown in Table 1.

TABLE 1. GC-MS Conditions for the analysis of essential oils

GC Condition	
Injection Temperature	280 °C
Injection Mode	Split
Column Flow (Helium)	1.21 mL/min
Split Ratio	5
Injection Volume	1 μL

MS Conditions (EI mode at 70 eV)	
Ion Source Temperature	200 °C
Interface Temperature	280 °C
Solvent Cut Time	2.2 min
Start Time	2.5 min
End Time	55 min
Start m/z	40
End m/z	700

Oven Temperature Program		
Rate (°C/min)	Temperature (°C)	Hold Time (min)
	60	1
5	220	2
5	280	8

3. Normalization of monitored biodiesel yield

Suppose the number of parameters (influencing factors) under study is denoted by "n". Let the number of reaction sets to be optimized is denoted by "m". Let r_{ji} denote the monitored biodiesel yield of the j^{th} influencing factor at i^{th} reaction set. To diminish the errors created by the various influencing factor, it becomes essential for us to normalize each monitored biodiesel yield. If V_{ji} denotes the normalization construction function for a typical j^{th} influencing factor at a particular i^{th} reaction set, then:

$$V_{ji} = \frac{r_{ji} - \min r_{ji}}{\max r_{ji} - \min r_{ji}}, \tag{1}$$

where j runs over 1 to n and i over 1 to m.

3.1. Determination of fuzzy and neutrosophic entropy weights

In the existing literature of Information theory, many fuzzy entropy (FE) measures have been investigated and characterized by researchers, but with some faults and limitations. De Luca and Termini suggested the first non-additive FE measure as follows [23]:

$$H_F^d\left(C_{FS}^b\right) = -\frac{1}{\log m}\sum_{j=1}^{n}\Big[\tilde{\mu}_{C^b}(p_j)\log\tilde{\mu}_{C^b}(p_j) + \left(1-\tilde{\mu}_{C^b}(p_j)\right)\log\left(1-\tilde{\mu}_{C^b}(p_j)\right)\Big], \tag{2}$$

where m is a fixed natural number.

The fuzzy entropy $H_F^d\left(C_{FS}^b\right)$ has been found capable of optimizing the uncertainty problems associated with various aspects of the environment, pollution, and energy-saving resources. Unfortunately, the FE measure is facing a major drawback with assumption $0 \times \log 0 = 0$. Due to this reason, this fuzzy entropy faced intrinsic conflicts and hence indicated uncertainty and elusiveness in the quality evaluation. To overcome this problematic situation and to meet the exigency, we have been able to establish Neutrosophic fuzzy entropy (NTFE) and applied it for identifying the most influencing reaction sets responsible for the optimal bio-diesel yield. Let T_{ji} denote the amount of fuzziness (concentration) based on the truth membership degree of j^{th} persuading factor at the i^{th} reaction set. Then:

$$T_{ji} = \frac{V_{ji}}{\sum\limits_{j=1}^{n} V_{ji}}, \tag{3}$$

where j runs over 1 to n and i over 1 to m.

(a) The weights W_{ji}^{1} of j^{th} influencing factors at i^{th} reaction set can be determined as follows. Let m be the number of reaction sets, then:

$$W_{ji}^{1} = \frac{1 - H_{ji}^{1}}{\sum\limits_{j=1}^{n} H_{ji}^{1}}, \tag{4}$$

where

$$H_{ji}^{1} = -\frac{1}{\log m} \sum_{j=1}^{n} \Big[T_{ji} \log T_{ji} + (1 - T_{ji}) \log (1 - T_{ji}) \Big]. \tag{5}$$

(b) The weights W_{ji}^{2} of j^{th} influencing factors at i^{th} reaction set employing the proposed trigonometric FE measure (1) can be determined as follows. Let m be the number of reaction sets, then:

$$W_{ji}^{2} = \frac{1 - H_{ji}^{2}}{\sum\limits_{j=1}^{n} H_{ji}^{2}}, \tag{6}$$

where

$$H_{ji}^{2} = -\tan\left(\frac{1}{m}\right) \sum_{j=1}^{n} \left[\tan\left(\frac{2}{\sqrt{2} + \sqrt{T_{ji}} + \sqrt{(1 - T_{ji})}} \right) - \tan\left(\frac{2}{\sqrt{2} + 1} \right) \right].$$

(c) Let $F_{ji} = 1 - V_{ji}$ and $I_{ji} = 1 - V_{ji} - F_{ji}$ denote the amount of fuzziness (concentration) based on falsity and indeterminacy membership degree of j^{th} influencing factor at i^{th} reaction set respectively. Then, the weights $W_{ji}^{(3)}$ of j^{th} influencing factors at i^{th} reaction set employing the proposed Single Valued Neutrosophic Entropy (SVNE) measure can be determined as follows. Let m be the number of reaction sets, then:

$$W_{ji}^{(3)} = \frac{1 - H_{ji}^{3}}{\sum\limits_{j=1}^{n} H_{ji}^{3}}, \tag{7}$$

where

$$\begin{aligned} H_{ji}^{3} = \tan\left(\frac{1}{m}\right) \sum_{j=1}^{n} \Bigg[& 3\tan\left(\frac{2}{\sqrt{2}+1}\right) - \tan\left(\frac{2}{\sqrt{2} + \sqrt{I_{ji}} + \sqrt{1 - I_{ji}}} \right) \\ & - \left(\frac{2 + V_{ji} + F_{ji}}{3} \right) \tan\left(\frac{1 + V_{ji} + F_{ji}}{\sqrt{2} + \left(\sqrt{V_{ji}} + \sqrt{F_{ji}}\right)\left(\sqrt{V_{ji} + F_{ji}}\right)} \right) \\ & - \left(\frac{4 - V_{ji} - F_{ji}}{3} \right) \tan\left(\frac{3 - V_{ji} - F_{ji}}{\sqrt{2} + \left(\sqrt{1 - V_{ji}} + \sqrt{1 - F_{ji}}\right)\left(\sqrt{2 - V_{ji} - F_{ji}}\right)} \right) \Bigg]. \end{aligned} \tag{8}$$

3.2. Calculation of relative sub-indices of each influencing factor at various reaction sets

Two types of sub-indices, absolute and relative, are being used by eminent researchers. Since absolute (or relative) sub-indexing approaches are fully independent (or dependent) on quality standards, the relative sub-indexing approach has been empowered in this study.

Let Q_{ji} = The relative sub-indices, S_{ji} = The maximum monitored biodiesel yield, and c_{ji} =The monitored biodiesel yield of the j^{th} influencing factor at i^{th} reaction set consecutively. Then, the relative sub-indexing of each influencing factor concerning various reaction sets in this study has been assigned by:

$$Q_{ji} = \frac{c_{ji}}{S_{ji}} \times 100, \tag{9}$$

where j runs over 1 to n and i over 1 to m.

3.3. Constructions of ECOTI, FCOTI and SCOTI

The existing Deluca–Termini fuzzy entropy, proposed fuzzy trigonometric entropy and SVNE weighted waste cooking oil transesterification indices (ECOTI, FCOTI and SCOTI) can be computed employing the following equations:

$$\text{ECOTI at } i^{th} \text{ reaction set} = \sum_{j=1}^{n} W_{ji}^{1} Q_{ji}, \tag{10}$$

$$\text{FCOTI at } i^{th} \text{ reaction set} = \sum_{j=1}^{n} W_{ji}^{2} Q_{ji}, \tag{11}$$

$$\text{SCOTI at } i^{th} \text{ reaction set} = \sum_{j=1}^{n} W_{ji}^{3} Q_{ji}. \tag{12}$$

The maximum ECOTI, FCOTI, or SCOTI score for a typical influencing factor at a particular reaction set is designated as the most influencing reaction set.

4. Results and discussion

4.1. Characterization of nano-catalyst

The X-ray diffraction patterns of nano-CaO have been plotted in Fig. 1. The narrow and intense peaks in the patterns can be attributed to the crystalline nature (calcite) of nano-CaO [24]. The diffraction patterns clearly show that the nano-catalyst showed characteristic peaks for CaO at 2θ equal to 31.5, 37.5, 46.4, 51.1, 52.3, 55.2, and 58.1° [25]. The prepared nano-catalyst was also characterized using FTIR analysis as shown in Fig. 2. A band at 3267.67 cm^{-1} corresponded to the O-H stretching while two bands around 1439.41 and 438.43 cm^{-1} were attributed to Ca–O bending [26]. The FTIR features shown by the nano-catalyst in our study are consistent with the already reported data in the literature [27].

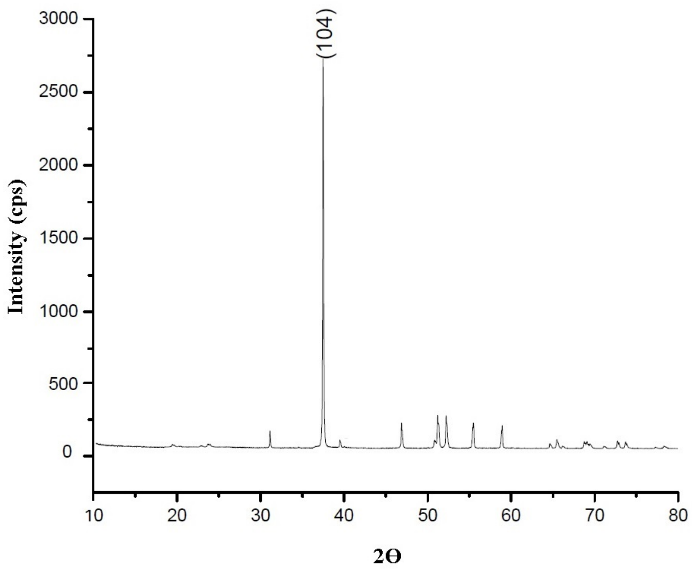

FIG. 1. X-ray Diffraction pattern for nano-CaO

4.2. Characterization of biodiesel

The biodiesel composition in terms of fatty acid methyl esters was identified by a pattern of mass fragmentation and the retention time of GCMS analysis. Fig. 3 shows the composition of the biodiesel produced under optimized conditions and confirms the completion of the transesterification reaction. The results found were consistent with previously reported results [28].

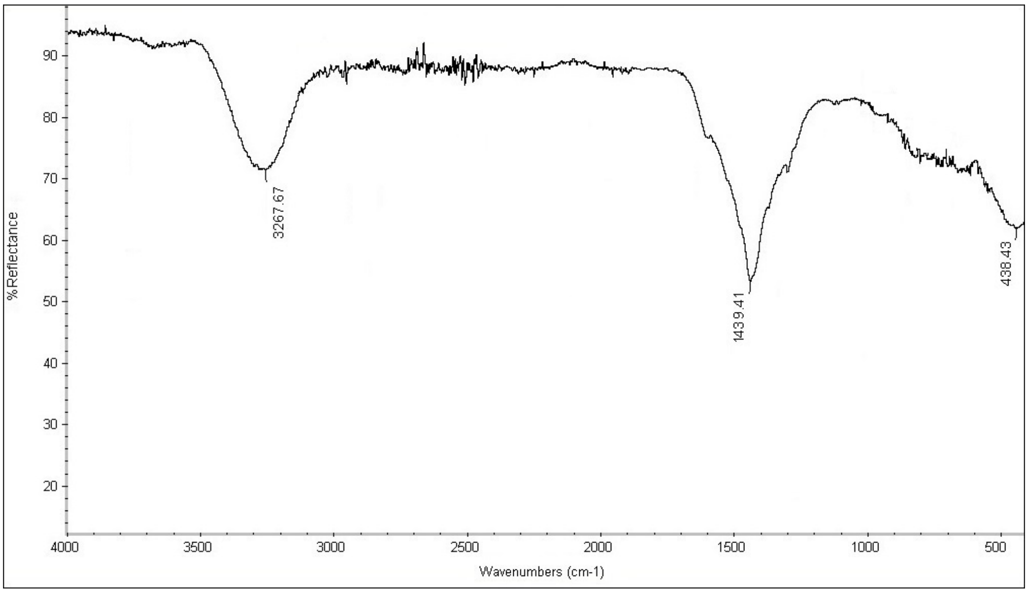

FIG. 2. FTIR spectrum for nano-CaO

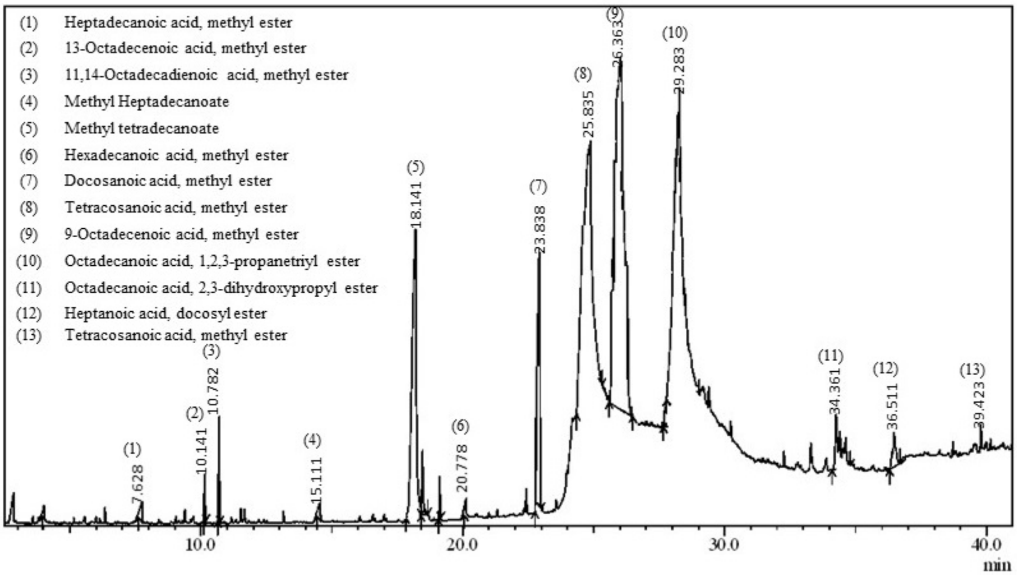

FIG. 3. GCMS for biodiesel

Functional group analysis of biodiesel was explored by FTIR as represented in Fig. 4. The most intense peak at 1755.96 cm^{-1} was assigned to CO stretching in esters [29, 30]. The absorption bands corresponding to the asymmetric bending of methyl groups of esters in the biodiesel were observed at 1639.41 cm^{-1} while that for stretching vibrations of methoxy groups were observed at 1239.85 cm^{-1} [31, 32]. The axial deformation of CH_2 bond was indicated by absorption bands at 2911.66 cm^{-1} [28, 33]. The absorption band at 2407.14, and 2170.60 cm^{-1} corresponded to stretching vibrations of C–O while O–H stretching vibration was observed as a weak absorption band at 3400.91 cm^{-1} [34]. The absorption bands at 628.59 cm^{-1} corresponded to CH_2 and CH_3 bending vibrations [28].

4.3. Identification of most influencing reaction set through ECOTI, FCOTI, and SCOTI

To predict the most influencing reaction set responsible for the optimum bio-diesel yield employing the proposed methodology has already been explained. The number of influencing factors in this study is four $(n = 4)$ and the number of transesterification reaction sets is eleven $(m = 11)$ for the concentration of nano-catalyst, temperature, and time of reaction, and ten $(m = 10)$ for methanol/oil ratio. We have been able to evaluate Deluca and Termini [23] fuzzy

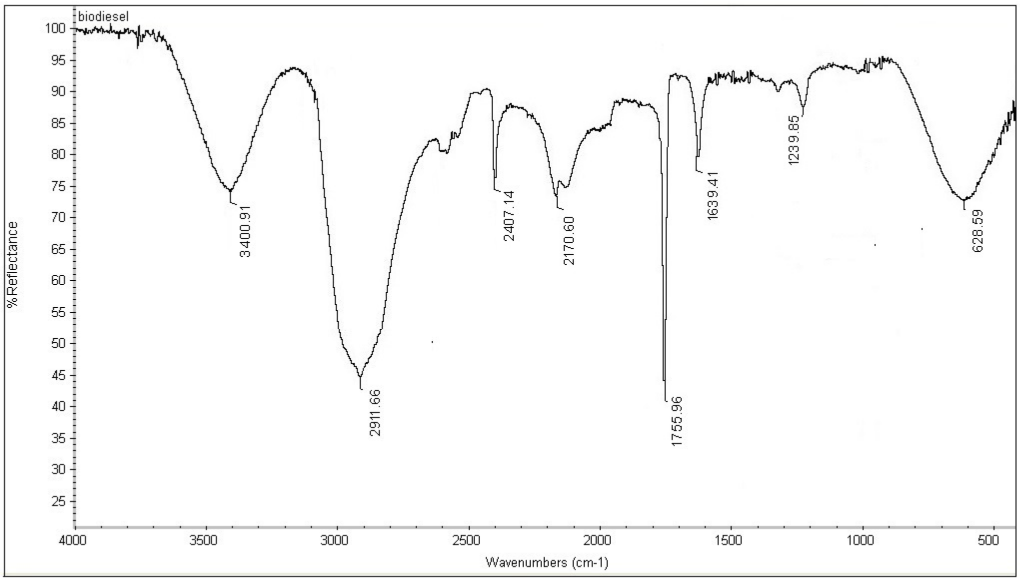

FIG. 4. FTIR spectrum for biodiesel

entropy-based weighted waste cooking oil transesterification index (ECOTI) employing equation (11) concerning each influencing factor at various reaction sets as summarized in Table 2. A careful analysis of the results depicted in Table 2 along with Fig. 5(a) reveals that, like the proposed fuzzy and SVNE measures, for the variation of (i) concentration of nano-catalyst (ii) temperature (iii) time of reaction and (iv) methanol:oil ratio, the reaction sets RS_8, RS_{19}, RS_{30}, RS_{35} were found to be the most influencing ones owing to their maximum ECOTI scores. The desired TFE weighted waste cooking oil transesterification index (FCOTI) can be evaluated employing equation (12). The results have been depicted in Table 2 along with Fig. 5(b), revealing that for the variation of concentration of nano-catalyst, temperature, time of reaction, and methanol: oil ratio, the reaction sets RS_8, RS_{19}, RS_{30}, RS_{35} were found to be the most promising ones owing to their maximum FCOTI scores. Following the proposed methodology and resulting equation (13), the desired trigonometric SVNE weighted waste cooking oil transesterification index (SCOTI) concerning each influencing factor at various reaction sets is summarized in Table 2. The subsequent analysis of the results depicted in Table 2 along with Fig. 5(c) reveals that for the variation of concentration of nano-catalyst, temperature, time of reaction, and methanol: oil ratio, the reaction sets RS_8, RS_{19}, RS_{30}, RS_{35} were found to be the most influencing ones owing to their maximum ECOTI scores.

The previous discussion reveals that for the variation in methanol: oil ratio with variation in concentration of nano-catalyst from 0.5 – 2 %, the reaction set RS_8 was found to be most influencing, owing to its maximum ECOTI, FCOTI, and SCOTI scores. Similarly, for the variation in methanol: oil ratio with variation in temperature of transesterification from 50 – 65 °C, the reaction set RS_{19} was found to be most effective owing to its maximum ECOTI, FCOTI, and SCOTI scores. Also, for the variation in methanol: oil ratio with variation in time of esterification from 3 – 4.5 hrs., the reaction set RS_{30} was found to be most effective owing to its maximum ECOTI, FCOTI, and SCOTI scores. These reaction sets involve the use of methanol: oil ratio as 11:1 which means that the optimized methanol: oil ratio for best yield of biodiesel is 11:1.

During the study of the effect of nano-catalyst concentration, temperature, and time of reactions at constant methanol: oil ratio, it was observed that the reaction set corresponding to the nano-catalyst concentration as 1 %, reaction temperature as 60 °C, and reaction time as 4.5 hrs., was found to be most effective, owing to its maximum ECOTI, FCOTI, and SCOTI scores resulting in 95.49 % biodiesel yield. It is therefore concluded that during the optimization analysis, the methanol: oil ratio has been the most influencing factor. This is due to the reason that for transesterification reaction, excess methanol is required for obtaining maximum yield (methanol being the co-reactant for the reaction). For a particular methanol: oil ratio, the temperature is the most influencing factor followed by nano-catalyst concentration and time of reaction owing to their highest ECOTI, FCOTI, and SCOTI scores. However, for the optimized value of nano-catalyst concentration and time of reaction, a slight decrease of reaction temperature 55 °C was observed followed by an increase of reaction temperature 65 °C indicating that at the optimized value of nano-catalyst concentration and reaction time, temperature change can be afforded. However, all four factors are interdependent and can be suitably varied at particular methanol: oil ratios to obtain the best yield of biodiesel.

TABLE 2. FCOTI, SCOTI and ECOTI Score for (i) Methanol: Oil Ratio (MR) with the variation of nano-catalyst (Cat), temperature (Temp.) and time of reactions

FCOTI Score							
RSs	Nano-catalyst	RSs	Temp.	RSs	Time	RSs	MR
RS_1	0.0000	RS_{12}	0.0000	RS_{23}	0.0000	RS_{34}	357.83
RS_2	305.80	RS_{13}	307.83	RS_{24}	294.78	RS_{35}	367.57
RS_3	312.72	RS_{14}	316.63	RS_{25}	302.84	RS_{36}	361.33
RS_4	320.19	RS_{15}	324.50	RS_{26}	310.46	RS_{37}	360.21
RS_5	327.81	RS_{16}	331.51	RS_{27}	316.71	RS_{38}	357.39
RS_6	342.00	RS_{17}	343.71	RS_{28}	330.05	RS_{39}	364.27
RS_7	350.00	RS_{18}	350.09	RS_{29}	337.19	RS_{40}	364.15
RS_8	359.44	RS_{19}	359.58	RS_{30}	347.12	RS_{41}	0.0000
RS_9	356.95	RS_{20}	358.13	RS_{31}	345.09	RS_{42}	347.07
RS_{10}	354.30	RS_{21}	356.35	RS_{32}	341.65	RS_{43}	359.97
RS_{11}	352.80	RS_{22}	354.67	RS_{33}	339.19		

SCOTI Score							
RSs	Nano-catalyst	RSs	Temp.	RSs	Time	RSs	MR
RS_1	0	RS_{12}	0	RS_{23}	0	RS_{34}	358.73
RS_2	305.8	RS_{13}	307.82	RS_{24}	294.78	RS_{35}	367.57
RS_3	312.73	RS_{14}	316.63	RS_{25}	302.84	RS_{36}	362.71
RS_4	320.21	RS_{15}	324.5	RS_{26}	310.47	RS_{37}	360.64
RS_5	327.83	RS_{16}	331.51	RS_{27}	316.73	RS_{38}	356.22
RS_6	342.06	RS_{17}	343.72	RS_{28}	330.11	RS_{39}	365.22
RS_7	349.99	RS_{18}	350.07	RS_{29}	337.2	RS_{40}	363.09
RS_8	359.44	RS_{19}	359.58	RS_{30}	347.12	RS_{41}	0
RS_9	357.3	RS_{20}	358.28	RS_{31}	345.83	RS_{42}	347.22
RS_{10}	354.52	RS_{21}	356.37	RS_{32}	342.35	RS_{43}	360.55
RS_{11}	353.01	RS_{22}	354.71	RS_{33}	340.02		

ECOTI Score							
RSs	Nano-catalyst	RSs	Temp.	RSs	Time	RSs	MR
RS_1	0.0000	RS_{12}	0	RS_{23}	0.0000	RS_{34}	357.51
RS_2	305.78	RS_{13}	307.82	RS_{24}	294.79	RS_{35}	367.57
RS_3	312.68	RS_{14}	316.63	RS_{25}	302.82	RS_{36}	360.97
RS_4	320.15	RS_{15}	324.5	RS_{26}	310.44	RS_{37}	360.13
RS_5	327.78	RS_{16}	331.51	RS_{27}	316.68	RS_{38}	357.70
RS_6	341.97	RS_{17}	343.71	RS_{28}	330.03	RS_{39}	364.36
RS_7	350.00	RS_{18}	350.09	RS_{29}	337.19	RS_{40}	364.09
RS_8	359.44	RS_{19}	359.58	RS_{30}	347.12	RS_{41}	0.0000
RS_9	356.95	RS_{20}	358.13	RS_{31}	345.08	RS_{42}	346.96
RS_{10}	354.29	RS_{21}	356.35	RS_{32}	341.61	RS_{43}	359.86
RS_{11}	352.79	RS_{22}	354.67	RS_{33}	339.11		

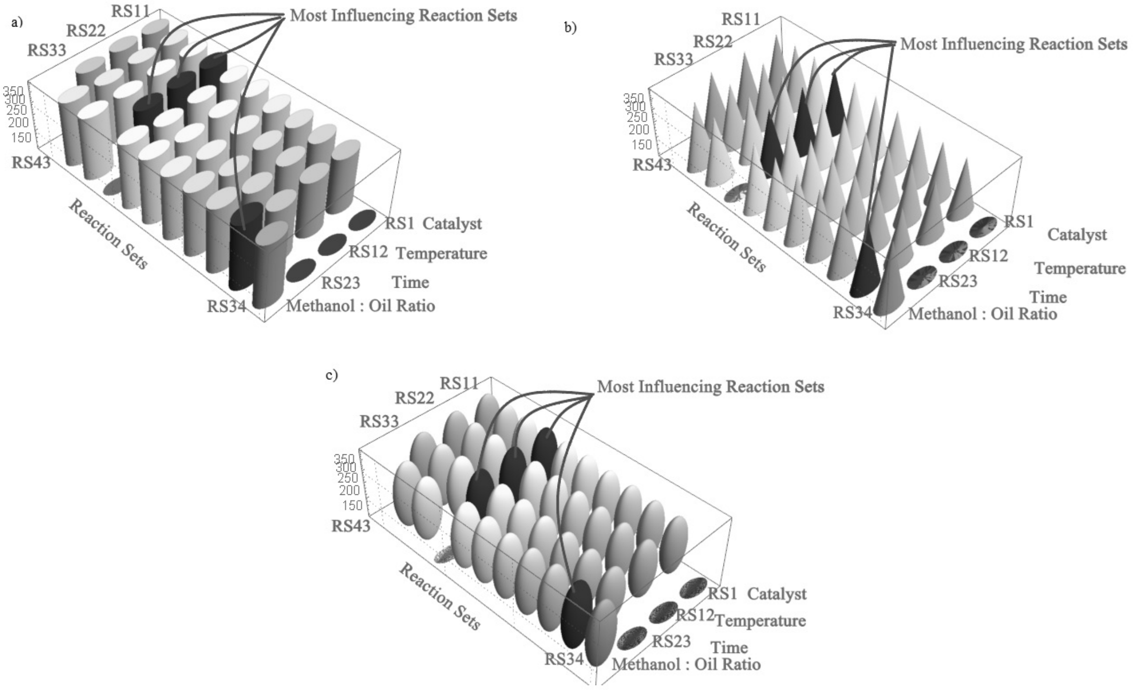

FIG. 5. Identification of Most Influencing Reaction Sets Employing a) ECOTI; b) FCOTI; c) SCOTI

5. Conclusion

This study investigates the synthesis of biodiesel using bio-synthesized nano-CaO as a nano-catalyst and employs a novel trigonometric fuzzy and SVNE-based methodology for evaluating the impact of various influencing factors (i) methanol/oil ratio (ii) concentration of nano-catalyst (iii) temperature and (iv) time of reaction on the biodiesel yield obtained through a heterogeneous nano-catalyst-based transesterification reaction. The proposed trigonometric entropy measures are deployed for constructing fuzzy entropy weighted waste cooking oil transesterification index (FCOTI) and SVNE weighted waste cooking oil transesterification index (SCOTI) respectively. The maximum FCOTI or SCOTI score concerning each influencing factor at various reaction sets indicated that the optimum methanol: oil ratio under the variation of nano-catalyst concentration from 0.5 – 2 % and the temperature variation from 50 – 65 °C comes out to be 11:1 to provide the maximum yield of biodiesel. Further, out of the next three parameters, the effect of temperature is more prominent to obtain the best yield of biodiesel followed by nano-catalyst and time of reaction. If nano-catalyst and time are suitably controlled within the range of optimum values, the reaction temperature doesn't significantly affect the reaction yield. The classification of various influencing factors obtained through the proposed FCOTI and SCOTI coincides with the existing Deluca and Termini fuzzy entropy-based weighted waste cooking oil transesterification index (ECOTI). This confirms that the optimum parameters are nano-catalyst concentration value of 1 %, reaction temperature as 60 °C, methanol: oil ratio as 11:1, and reaction time as 4.5 hrs.

References

[1] Sodhi A.K., Tripathi S., Kundu K. Biodiesel production using waste cooking oil: a waste to energy conversion strategy. *Clean Technologies and Environmental Policy*, 2017, **19** (6), P. 1799–1807.

[2] Caliskan H., Mori K. Thermodynamic, environmental and economic effects of diesel and biodiesel fuels on exhaust emissions and nano-particles of a diesel engine. *Transportation Research Part D: Transport and Environment*, 2017, **56** , P. 203–221.

[3] Yesilyurt M.K. A detailed investigation on the performance, combustion, and exhaust emission characteristics of a diesel engine running on the blend of diesel fuel, biodiesel and 1-heptanol (C7 alcohol) as a next-generation higher alcohol. *Fuel*, 2020, **275**, 117893.

[4] Alagh Y.K. India 2020. *J. of Quantitative Economics*, 2006, **4** (1), P. 1–14.

[5] Lam M.K., Lee K.T., Mohamed A.R. Homogeneous, heterogeneous and enzymatic catalysis for transesterification of high free fatty acid oil (waste cooking oil) to biodiesel: A review. *Biotechnology Advances*, 2010, **28** (4), P. 500–518.

[6] Martínez A., Mijangos G.E., et al. A novel green one-pot synthesis of biodiesel from Ricinus communis seeds by basic heterogeneous catalysis. *J. of Cleaner Production*, 2018, **196**, P. 340–349.

[7] Udo G.J., Etesin U.M., et al. GCMS and FTIR Spectroscopy Characterization of Luffa Cylindrica Seed Oil and Biodiesel Produced from the oil. *Communication in Physical Sciences*, 2020, **5** (3), P. 378–390.

[8] Fangsuwannarak K., Wanriko P., Fangsuwannarak T. Effect of Bio-polymer Additive on the Fuel Properties of Palm Biodiesel and on Engine Performance Analysis and Exhaust Emission. In: *Energy Procedia*, 2016, **100**, P. 227–236.

[9] Ogunkunle O., Ahmed N.A. A review of global current scenario of biodiesel adoption and combustion in vehicular diesel engines. *Energy Reports*, 2019, **5** , P. 1560–1579.

[10] Ihoeghian N.A., Usman M.A. Exergetic evaluation of biodiesel production from rice bran oil using heterogeneous catalyst. *J. of King Saud University – Engineering Sciences*, 2020, **32** (2), P. 101–107.

[11] Mohd Noor C.W., Noor M.M., Mamat R. Biodiesel as alternative fuel for marine diesel engine applications: A review. *Renewable and Sustainable Energy Reviews*, 2018, **94**, P. 127–142.

[12] Degirmenbasi N., Coskun S., Boz N., Kalyon D.M. Biodiesel synthesis from canola oil via heterogeneous catalysis using functionalized CaO nanoparticles. *Fuel*, 2015, **153**, P. 620–627.

[13] Marwaha A., Rosha P., et al. Biodiesel production from Terminalia bellerica using eggshell-based green catalyst: An optimization study with response surface methodology. *Energy Reports*, 2019, **5** , P. 1580–1588.

[14] Ayoola A.A., Fayomi O.S.I., et al. Impact assessment of biodiesel production using CaO catalyst obtained from two different sources. *Cogent Engineering*, 2019, **6** (1), 1615198.

[15] Degfie T.A., Mamo T.T., Mekonnen Y.S. Optimized Biodiesel Production from Waste Cooking Oil (WCO) using Calcium Oxide (CaO) Nano-catalyst. *Scientific Reports*, 2019, **9** (1), 18982.

[16] Mansir N., Teo S.H., et al. Modified waste egg shell derived bifunctional catalyst for biodiesel production from high FFA waste cooking oil. A review. *Renewable and Sustainable Energy Reviews*, 2018, **82**, P. 3645–3655.

[17] Wei Y., Zhang J., Zhang M., Zhang Y.D. Analysis on Factors Affecting Biodiesel Production Rate Based on Probability Theory. *Advanced Materials Research*, 2013, **860–863** , P. 1030–1034.

[18] Zadeh L.A. Fuzzy sets. *Information and control*, 1965, **8** , P. 338–353.

[19] Ovchinnikov S. An Introduction to Fuzzy Relations. In: *Fundamentals of Fuzzy Sets*. 2015, P. 233–243.

[20] Smarandache F.A. *Unifying Field In Logics: Neutrosophic Logic. Neutrosophy, Neutrosophic Set, Neutrosophic Probability*, American Research Press, Rehoboth, 2000.

[21] Tshizanga N., Aransiola E.F., Oyekola O. Optimisation of biodiesel production from waste vegetable oil and eggshell ash. *South African Journal of Chemical Engineering*, 2017, **23** , P. 145–156.

[22] Santya G., Maheswaran T., Yee K.F. Optimization of biodiesel production from high free fatty acid river catfish oil (Pangasius hypothalamus) and waste cooking oil catalyzed by waste chicken egg shells derived catalyst. *SN Applied Sciences*, 2019, **1** (2), P. 1–9.

[23] De Luca A., Termini S. A definition of a nonprobabilistic entropy in the setting of fuzzy sets theory. *Information and Control*, 1972, **20** (4), P. 301–312.

[24] Wei Z., Xu C., Li B. Application of waste eggshell as low-cost solid catalyst for biodiesel production. *Bioresource Technology*, 2009, **100** (11), P. 2883–2885.

[25] Fayyazi E., Ghobadian B., et al. Optimization of Biodiesel Production over Chicken Eggshell-Derived CaO Catalyst in a Continuous Centrifugal Contactor Separator. *Industrial & Engineering Chemistry Research*, 2018, **57** (38), P. 12742–12755.

[26] Borah M.J., Das A., et al. Transesterification of waste cooking oil for biodiesel production catalyzed by Zn substituted waste egg shell derived CaO nanocatalyst. *Fuel*, 2019, **242**, P. 345–354.

[27] Ngadi N., Sulaiman S., Abd Rahman R., Lani N.S. Production of biodiesel from palm oil using cockle shell waste as heterogeneous catalyst. *Jurnal Teknologi*, 2017, **79** (5), P. 183–188.

[28] Purandaradas A., Silambarasan T., et al. Development and quantification of biodiesel production from chicken feather meal as a cost-effective feedstock by using green technology. *Biochemistry and Biophysics Reports*, 2018, **14**, P. 133–139.

[29] Meena Devi R., Subadevi R., Paul Raj S., Sivakumar M. Comparative Studies on Biodiesel From Rubber Seed Oil Using Homogeneous and Heterogeneous Catalysts. *Int. J. of Green Energy*, 2015, **12** (12), P. 1215–1221.

[30] Brito G.M., Chicon M.B., et al. Eco-green biodiesel production from domestic waste cooking oil by transesterification using LiOH into basic catalysts mixtures. *J. of Renewable and Sustainable Energy*, 2020, **12** (4), 043101.

[31] Mumtaz M.W., Adnan A., et al. Response Surface Methodology: An Emphatic Tool for Optimized Biodiesel Production Using Rice Bran and Sunflower Oils. *Energies*, 2012, **5** (9), P. 3307–3328.

[32] Rabelo S.N., Ferraz V.P., Oliveira L.S., Franca A.S. FTIR Analysis for Quantification of Fatty Acid Methyl Esters in Biodiesel Produced by Microwave-Assisted Transesterification. *Int. J. of Environmental Science and Development*, 2015, **6** (12), P. 964–969.

[33] Touqeer T., Mumtaz M.W., et al. Fe_3O_4-PDA-Lipase as Surface Functionalized Nano Biocatalyst for the Production of Biodiesel Using Waste Cooking Oil as Feedstock: Characterization and Process Optimization. *Energies*, 2019, **13** (1), 177.

[34] Hangun-Balkir Y. Green Biodiesel Synthesis Using Waste Shells as Sustainable Catalysts with Camelina sativa Oil. *J. of Chemistry*, 2016, **2016**, P. 1–10.

NANOSYSTEMS:

PHYSICS, CHEMISTRY, MATHEMATICS

INFORMATION FOR AUTHORS

The journal publishes research articles and reviews, and also short scientific papers (letters) which are unpublished and have not been accepted for publication in other magazines. Articles should be submitted in English. All articles are reviewed, then if necessary come back to the author to completion.

The journal is indexed in Web of Science Core Collection (Emerging Sources Citation Index), Chemical Abstract Service of the American Chemical Society, Zentralblatt MATH and in Russian Scientific Citation Index.

Author should submit the following materials:

1. Article file in English, containing article title, the initials and the surname of the authors, Institute (University), postal address, the electronic address, the summary, keywords, MSC or PACS index, article text, the list of references.
2. Files with illustrations, files with tables.
3. The covering letter in English containing the article information (article name, MSC or PACS index, keywords, the summary, the literature) and about all authors (the surname, names, the full name of places of work, the mailing address with the postal code, contact phone number with a city code, the electronic address).
4. The expert judgement on possibility of publication of the article in open press (for authors from Russia).

Authors can submit a paper and the corresponding files to the following addresses: nanojournal.ifmo@gmail.com, popov1955@gmail.com.

Text requirements

Articles should be prepared with using of text editors MS Word or LaTex (preferable). It is necessary to submit source file (LaTex) and a pdf copy. In the name of files the English alphabet is used. The recommended size of short communications (letters) is 4-6 pages, research articles– 6-15 pages, reviews – 30 pages.

Recommendations for text in MS Word:

Formulas should be written using Math Type. Figures and tables with captions should be inserted in the text. Additionally, authors present separate files for all figures and Word files of tables.

Recommendations for text in LaTex:

Please, use standard LaTex without macros and additional style files. The list of references should be included in the main LaTex file. Source LaTex file of the paper with the corresponding pdf file and files of figures should be submitted.

References in the article text are given in square brackets. The list of references should be prepared in accordance with the following samples:

[1] Surname N. *Book Title*. Nauka Publishing House, Saint Petersburg, 2000, 281 pp.
[2] Surname N., Surname N. Paper title. *Journal Name*, 2010, **1** (5), P. 17-23.
[3] Surname N., Surname N. Lecture title. In: Abstracts/Proceedings of the Conference, Place and Date, 2000, P. 17-23.
[4] Surname N., Surname N. Paper title, 2000, URL: http://books.ifmo.ru/ntv.
[5] Surname N., Surname N. Patent Name. Patent No. 11111, 2010, Bul. No. 33, 5 pp.
[6] Surname N., Surname N. Thesis Title. Thesis for full doctor degree in math. and physics, Saint Petersburg, 2000, 105 pp.

Requirements to illustrations

Illustrations should be submitted as separate black-and-white files. Formats of files – jpeg, eps, tiff.

NANOSYSTEMS:

PHYSICS, CHEMISTRY, MATHEMATICS

Журнал зарегистрирован
Федеральной службой по надзору в сфере связи, информационных технологий и массовых коммуникаций
(свидетельство ПИ № ФС 77 - 49048 от 22.03.2012 г.)
ISSN 2220-8054

Учредитель: федеральное государственное автономное образовательное учреждение высшего образования
«Санкт-Петербургский национальный исследовательский университет информационных технологий, механики и оптики»

Издатель: федеральное государственное автономное образовательное учреждение высшего образования
«Санкт-Петербургский национальный исследовательский университет информационных технологий, механики и оптики»

Отпечатано в Учреждении «Университетские телекоммуникации»
Адрес: 197101, Санкт-Петербург, Кронверкский пр., 49

Подписка на журнал НФХМ
На первое полугодие 2022 года подписка осуществляется через
ОАО «АРЗИ», подписной индекс Э57385